



MONASH University

Theoretical and Experimental Development and Application of Pressuremeter Test (PMT) with Case Study of Victorian Brown Coal Open-Pit Mining

Zhan Tang

Master of Engineering (UNSW Australia, 2014)

Bachelor of Engineering (Jinan University, 2012)

A thesis submitted for the degree of Doctor of Philosophy at

Monash University in 2018

Faculty of Science

Abstract

The Pressuremeter Test (PMT) is an in-situ geotechnical field investigation method that provides evaluations of in-situ horizontal stress and essential geotechnical parameters such as shear strength and shear modulus. Due to its versatility, PMT is a widely used tool for the investigation of various types of cohesive and non-cohesive soils in civil-geotechnical projects. However, despite wide application of PMT in civil-geotechnical projects, the method is not broadly applied in open-pit mining. It is believed that there are two main issues which may affect the interpretation reliability of PMT results conducted in open-pit mines. One is the in-situ horizontal stress anisotropy induced by mining and the other is the tensile strength of the rock mass.

The present PhD study aims at describing the effect of the above-mentioned issues on the results of PMT conducted in the largest Victorian brown coal open-pit mine. In this research, two laboratory scale tests were designed, developed and conducted. The first is a small-scale Anisotropic Pressuremeter Chamber Test to investigate the effect of stress anisotropy on shear strength and shear modulus interpreted from PMT results, while the second is the Unconfined Expansion Test (UET) to study the tensile strength of Victorian brown coal as an intermediate geotechnical material. These two laboratory tests were paralleled with Finite Element Method (FEM) and eXtended Finite Element Method (XFEM) analyses, respectively, for modelling of internal stresses and tensile failure.

Laboratory chamber test on sand indicated that when cavity pressure increased, the interpreted unload-reload shear modulus (G_{ur}) increased accordingly. However, the variation of cavity pressure did not affect the interpreted friction and dilation angles. The laboratory findings explained that in-situ stress variation affects G_{ur} . Whilst the resistance of shear stress during in-situ PMTs, whether it is undertaken by undrained shear strengths of cohesive materials or by friction angle of cohesion-less materials, seemed to be unaffected by in-situ stress variation.

The UET results showed that tensile strength of Victorian natural brown coal at zero confining pressure sit between 114kPa and 155kPa. The UETs benefited the research by helping with determining the minimum depth for conducting full-size PMT at the mine while avoiding tensile failure.

The laboratory and field techniques for shear resistances measurements can be applied in mining excavation design against shear failure. The techniques for unload-reload shear modulus measurements can be applied in future studies of stress-strain development on the

material due to mining activities. The laboratory techniques of tensile strength measurements can be applied in determining in-situ PMTs depths.

Finally, a series of full-size PMTs were conducted at the mine in two locations one at the mine floor and the other one behind the mine batter. The interpretation of the test results provided valuable geotechnical information such as the in-situ horizontal stress profile and shear strength parameters which can be used in future stability analyses of open-pit batters using FEM.

Publications during enrolment

Tang, Z., Tolooiyan, A., & Mackay, R. (2017). Unconfined Expansion Test (UET) for measuring the tensile strength of organic soft rock. *Computers and Geotechnics*, 82, 54-66.

Dyson, A. P., **Tang, Z.**, & Tolooiyan, A. (2018). Use of stochastic XFEM in the investigation of heterogeneity effects on the tensile strength of intermediate geotechnical materials. *Finite Elements in Analysis and Design*, 145, 1-9.

Thesis including published works declaration

I hereby declare that this thesis contains no material which has been accepted for the award of any other degree or diploma at any university or equivalent institution and that, to the best of my knowledge and belief, this thesis contains no material previously published or written by another person, except where due reference is made in the text of the thesis.

This thesis includes two original papers published in peer reviewed journals. The idea, development and writing up of the first paper in the thesis was the principal responsibility of myself, Zhan Tang. The idea, development and writing up of the second paper in the thesis was the principal responsibility of Mr Ashley P. Dyson with my collaboration. Both of us at the time of publication were working within the GHERG, Federation University Gippsland Campus (former Monash University Gippsland Campus) under the supervision of Dr. Ali Tolooiyan.

(The inclusion of co-authors reflects the fact that the work came from active collaboration between researchers and acknowledges input into team-based research.)

In the case of appendix my contribution to the work involved the following:

Thesis Chapter	Publication Title	Status	Nature and % of student contribution	Co-author name(s) Nature and % of Co-author's contribution	Co-author(s), Monash student Y/N*
Appendix I	Unconfined Expansion Test (UET) for measuring the tensile strength of organic soft rock	Published	60%. Concept, laboratory testing, numerical model, collecting data and writing	1) Dr. Ali Tolooiyan, Concept, laboratory testing, numerical model, writing 30% 2) Prof. Rae Mackay, writing 10%	No
Appendix II	Use of stochastic XFEM in the investigation of heterogeneity effects on the tensile strength of intermediate geotechnical materials	Published	20%. Concept, numerical model, collecting data and writing	1) Mr. Ashley P. Dyson, Concept development, numerical model, writing 60% 2) Dr. Ali Tolooiyan, numerical model, writing 20%	No

I have renumbered sections of submitted or published papers in order to generate a consistent presentation within the thesis.

Student signature:



Date: 07/09/2018

The undersigned hereby certify that the above declaration correctly reflects the nature and extent of the student's and co-authors' contributions to this work. In instances where I am not the responsible author I have consulted with the responsible author to agree on the respective contributions of the authors.

Main Supervisor signature:



Dr Ali Tolooiyan

Date: 07/09/2018

Acknowledgements

There is a long list of people during the last four years who made me from zero to the dissertation submission. I try to cover all of them in the acknowledgements.

First, I would like to express sincere gratitude to my main supervisor, Doctor Ali Tolooiyan, for more than his academic expertise in regard to the area of my research. Throughout his supervision, Doctor Ali Tolooiyan continuously showed his patience, mindfulness, perseverance and generosity and conveyed them to me. Without his guidance, encouragement and support, I would not have achieved this submission.

My gratitude also goes to my second supervisor, Doctor Jianfeng Xue, for giving me the chance to start my research, and for his academic supports and advice during my study.

I would thank the former head of GHERG, Professor Rae Mackay, for his helps regarding my research funding, publications, conferences and thesis structure.

A special gratitude goes to our technician, Wayne Prowie, for his great technical support in designing, developing and maintaining all the laboratory equipment involved in this research.

The research of the thesis is funded by Geotechnical and Hydrogeological Engineering Research Group (GHERG) based on Federation University Gippsland Campus (former Monash University Gippsland Campus). I would like to say thank you to all former and current members from GHERG: Ashley, Kaveh, Negin, Mojtaba, Mohsen, Tahereh, Jack, Tristen, Luke, Catherine, Chow, Salma. I would also appreciate members from both universities who provided supports for initiating, continuing and finishing my study.

I would like to appreciate my family members. I would thank my father, Jiandong Tang, for setting-up professional model as a geotechnical engineer for me. I would thank my mother, Xiaohong Cai, for encouraging me to take all the adventures of my study. I am always proud of being your son. I would also thank my partner, Qin Shao, for her caring in every aspect of my life.

This thesis engaged professional proofreading from confidential editors from Scribbr (www.scribbr.com) in assist to the improvements not beyond language issues such as spelling, grammar, academic style, sentence structure, punctuation, word choice, incorrect and unclear words or sentences.

Table of Contents

1. Introduction-----	1
1.1. Background-----	1
1.2. Problem Definition-----	1
1.3. Research Hypothesis-----	2
1.3.1. Shear Modulus and Shear Strength in Slope Stability-----	2
1.3.2. Tensile Failure and in-situ Horizontal Stress in Open-pit Mining-----	2
1.3.3. Overview of Hypothesis-----	3
1.4. Introducing the Pressuremeter Test to the Project-----	3
1.4.1. Overview-----	3
1.4.2. Anisotropy Impact on the Pressuremeter Test Measurement-----	4
1.5. Research Objective-----	5
1.6. Research Methodology-----	5
1.6.1. Overview-----	5
1.6.2. Anisotropic Stress Analysis-----	5
1.6.3. Tensile Strength Analysis-----	6
1.6.4. Numerical Modelling-----	7
1.6.5. Auxiliary Laboratory Tests-----	8
1.6.6. Field Pressuremeter Test-----	8
1.7. Thesis Outline-----	9
2. State of the Art of In-situ Pressuremeter Testing-----	11
2.1. Introduction-----	11
2.2. Pressuremeter Test Background-----	11
2.2.1. Menard Pressuremeter (MPM)-----	11
2.2.2. Self-boring Pressuremeter (SPB)-----	12
2.2.3. Push-in Pressuremeter (PIP)-----	13
2.2.4. Other Types of Pressuremeters-----	13
2.2.5. Pressuremeter Probe-----	14
2.2.6. Bottom Components of Different Types of Pressuremeter Probes-----	17
2.2.7. Pressuremeter Test Preparation-----	21
2.2.7.1. Pre-test Inspection-----	21
2.2.7.2. Initial Volumetric (Radial) Reading and Zero-pressure Verifications-----	22
2.2.7.3. System Compliance Calibration-----	23
2.2.7.4. Membrane Resistance Calibration-----	24
2.2.8. Test Execution-----	24
2.2.8.1. Menard Pressuremeter (MPM) Probe Installation-----	24

2.2.8.2. Self-boring Pressuremeter (SBP) Probe Installation-----	25
2.2.8.3. Push-in Pressuremeter (PIP) Probe Installation-----	26
2.2.8.4. Probe Expansion (Pressure-controlled and Strain-controlled)-----	26
2.2.8.5. Unload-reload Cycle-----	28
2.2.9. Result Processing-----	28
2.2.9.1. Synopsis of Result Processing-----	28
2.2.9.2. Data Correction-----	28
2.2.9.3. Application of the Corrected Pressure-Radial Strain Curves-----	31
2.2.9.4. Application of the Corrected Pressure-Volumetric Strain Curves-----	32
2.2.9.5. Conversions between ε_c and ε_v -----	32
2.2.10. Result Analysis-----	33
2.2.10.1. Graphical based method-----	33
2.2.10.2. Numerical based method-----	34
2.3. Parameter Interpretations-----	35
2.3.1. Interpretation for Sandy (Granular) Materials-----	35
2.3.1.1. General Characteristics-----	35
2.3.1.2. Stress-strain relationship-----	35
2.3.1.3. Friction and Dilation Angle-----	36
2.3.1.4. In-situ Horizontal Stress-----	38
2.3.1.5. Unload-reload Stiffness-----	39
2.3.2. Interpretation for Cohesive Materials and Soft rock-----	40
2.3.2.1. General Characteristics-----	40
2.3.2.2. Stress-strain Relationship-----	41
2.3.2.3. Undrained Shear Strength-----	42
2.3.2.4. In-situ Horizontal Stress-----	44
2.3.2.5. Unload-reload Stiffness-----	45
2.3.2.6. Limit Pressure-----	45
2.3.2.7. Pressuremeter Test in Soft rock-----	46
2.4. Pressuremeter Chamber Tests-----	47
2.4.1. Brief Introduction-----	47
2.4.2. Methodology-----	47
2.4.2.1. Test Preparation-----	47
2.4.2.2. Apply Boundary Condition-----	48
2.4.2.3. Test Execution, Data Acquisition and Analysis-----	48
2.4.3. Limitation of Pressuremeter Chamber Test-----	49
2.5. Tension Failure in IGMs-----	49

2.5.1. Background-----	49
2.5.2. Conventional Tensile Strength Tests and Their Limitations-----	49
2.5.2.1. Direct Tensile Test (DTT)-----	49
2.5.2.2. Brazilian Test (BT)-----	50
2.6. Conclusion and Discussion-----	52
2.6.1. Conclusion of the Chapter-----	52
2.6.2. Research Gap-----	53
3. Laboratory Experiment: Design and Numerical Analysis-----	54
3.1. Introduction-----	54
3.2. Miniature Scale Pressuremeter Probe-----	54
3.2.1. Apparatus Set-up-----	54
3.2.2. Slenderness Ratio-----	55
3.2.3. Expansion Mechanism-----	56
3.3. Anisotropic Pressuremeter Chamber-----	57
3.3.1. Limitation of the Cylindrical Chamber-----	57
3.3.2. Anisotropic Horizontal Stresses Conversion-----	57
3.3.3. Development of the Anisotropic Pressuremeter Chamber-----	58
3.3.4. Advantages of the Anisotropic Pressuremeter Chamber-----	59
3.3.5. Chamber-Probe Size Ratio-----	59
3.3.6. Chamber Assembly-----	62
3.3.6.1. Air Cushions-----	62
3.3.6.2. Compression Plates-----	63
3.3.6.3. Chamber Frame-----	65
3.3.6.4. Transparent Plate-----	68
3.3.6.5. Top Webbing-----	68
3.3.6.6. Installation-----	69
3.3.7. Loading Mechanism-----	70
3.3.7.1. Air Pressure Regulating System-----	71
3.3.7.2. Horizontal Confinement-----	72
3.3.7.3. Vertical Confinement-----	72
3.3.8. Chamber Calibration Equipment-----	73
3.3.8.1. Miniature Pressure Transducer-----	73
3.3.8.2. Data Acquisition Box-----	74
3.3.8.3. Transducer Holder-----	75
3.3.9. One Dimensional Calibration-----	76
3.3.9.1. Setup Introduction-----	76

3.3.9.2. Air Pressure versus Confining Pressure-----	78
3.3.9.3. Transducer Voltage versus Transducer Measured Pressure-----	79
3.3.10. In-chamber Calibration-----	80
3.3.10.1. Setup Introduction-----	80
3.3.10.2. Calibration Procedure-----	82
3.3.10.3. Data Processing-----	83
3.3.10.4. Results-----	83
3.3.11. Stress around the Pressuremeter Test Cavity-----	84
3.3.11.1. Stress Difference Justification-----	84
3.3.11.2. Hypothesis and Plane Strain Solution-----	84
3.3.11.3. Isotropic Solution-----	85
3.3.11.4. Anisotropic Solution (Simplified)-----	87
3.3.12. Finite Element Simulation of Pressuremeter Chamber Testing-----	87
3.3.12.1. Purpose and Goal-----	87
3.3.12.2. Geometry and Material Property Definition-----	88
3.3.12.3. Meshing-----	90
3.3.12.4. Material Properties-----	93
3.3.12.5. Finite Element Parts Assembly-----	94
3.3.12.6. Constraints-----	94
3.3.12.7. Surface Interactions-----	96
3.3.12.8. Boundary Conditions-----	97
3.3.12.9. Fluid Cavity Creation-----	98
3.3.12.10. Fluid Cavity Properties-----	98
3.3.12.11. Pre-test Confining Pressures-----	99
3.3.12.12. Applying Thermal Expansion-----	99
3.3.12.13. Simulation Result-----	100
3.3.12.14. Discussion-----	109
3.4. Conclusion-----	109
4. Laboratory Test Programme-----	111
4.1. Anisotropic Pressuremeter Chamber Tests-----	111
4.1.1. Introduction-----	111
4.1.2. Test Design-----	112
4.1.3. Test Material and Specimen Preparation-----	113
4.1.3.1. Material Characteristics-----	113
4.1.3.2. Material Compaction-----	114
4.1.4. Calibration and Installation-----	116

4.1.4.1. Hose Calibration-----	116
4.1.4.2. Membrane Calibration-----	120
4.1.4.3. Probe Installation-----	121
4.1.4.4. Top Webbing Installation-----	124
4.1.5. Pressuremeter Test Procedure-----	125
4.1.5.1. Apply Air Pressure-----	125
4.1.5.2. Apply Cavity Expansion-----	129
4.1.5.3. Data Acquisition, Corrections, and Post-processing-----	134
4.1.6. Interpretation-----	137
4.1.6.1. Unload-Reload Stiffness-----	137
4.1.6.2. Friction Angle-----	137
4.1.6.3. Dilation Angle-----	139
4.1.7. Test results-----	140
4.1.7.1. Corrected Pressure VS. Volumetric Strain Curves-----	140
4.1.7.2. Interpretation Summary-----	144
4.1.8. Comparison and Conclusion-----	144
4.1.8.1. Unload-reload Stiffness (G_{ur}) in Isotropic Condition-----	144
4.1.8.2. Friction Angle (ϕ) in Isotropic Condition-----	145
4.1.8.3. Dilation Angle (ψ) in Isotropic Condition-----	146
4.1.8.4. Comparison of ϕ from Isotropic Tests with Direct Shear Tests-----	147
4.1.8.5. Unload-reload Shear Modulus in Anisotropic Conditions-----	150
4.1.8.6. Friction Angle and Dilation Angle in Anisotropic Condition-----	151
4.2. Unconfined Expansion Test-----	153
4.2.1. Introduction-----	153
4.2.2. Theoretical Background-----	153
4.2.3. Test Material-----	156
4.2.4. Specimen Preparation-----	157
4.2.5. Determination of Loading Rate-----	157
4.2.6. UET Setup-----	159
4.2.7. Results-----	160
4.2.8. Determination of Energy Release Rate-----	162
4.2.9. XFEM analysis-----	165
4.2.10. Comparison with traditional methods-----	170
5. Pressuremeter Tests at the Yallourn Open-pit Brown Coal Mine-----	174
5.1. Introduction-----	174
5.2. Equipment-----	174

5.3. Borehole Drilling-----	175
5.4. Pressuremeter Testing-----	176
5.4.1. Probe Expansion-----	176
5.4.2. Unload-reload Cycle-----	176
5.5. Test Results and Parametric Interpretations-----	177
5.5.1. Stress-strain Curves-----	177
5.5.2. Parameter Interpretations-----	177
5.5.2.1. In-situ Horizontal Stress-----	177
5.5.2.2. Undrained Shear Strength-----	180
5.5.2.3. Unload-reload Shear Modulus-----	182
5.6. Conclusion-----	183
6. Summary and Recommendations-----	185
6.1. Research Conclusion-----	185
6.2. Research Findings-----	186
6.2.1. Anisotropic Pressuremeter Chamber-----	186
6.2.2. Unconfined Expansion Test-----	187
6.2.3. In-situ Pressuremeter Test-----	187
6.3. Discussions and Recommendations-----	188
Reference-----	189
Appendix I-----	195
Appendix II-----	208

1. Introduction

1.1. Background

The Latrobe Valley region in the Victoria state is a major brown-coal-mining region in Australia. In Latrobe Valley, large-scale, open-pit excavation is the only method of brown coal mining. The Yallourn open-pit mine, introduced in Section 5.1 as a good illustration of open-pit excavation in Latrobe Valley, reaches approximately 80m below ground level. Failure of open-pit wall (batter) is identified as one of the major hazards of open-pit excavation (Singh et al., 2011). Some aspects related to the brown coal open-pit excavation design have not been systematically investigated in the region.

1.2. Problem Definition

Simmons and Simpson (2006) state that failure modes of an open-pit excavated batter can vary based on the characteristics of the ground material. Typically, clay and soft rock brown coal are the most common ground materials found from a brown coal open-pit mine. Previous geotechnical investigations for open-pit excavation batter design, such as Fernando and Nag (2003), emphasise shear strength analysis, which is most suitable for the open-pit excavation of cohesive soils (e.g. clay). More recent in-situ investigations, such as Zhao and You (2017), show that mechanism of the tensile failure of the soft rock (e.g. brown coal) is an underlying geotechnical hazard of open-pit excavation batter. The tensile failure occurs when the tensile strength of brown coal is reached (Tolooiyan et al., 2014). However, none of the previous in-situ and laboratory tests have evaluated brown coal's tensile strength in randomly initiated radial cracking, which is a common cracking scenario during in-situ pressuremeter testing in soft rock.

The addressed problems of current research can be distinguished by laboratory and in-situ tests. In laboratory tests, the problems addressed are the impact of the anisotropy of the in-situ horizontal stresses at rest on the interpretation of pressuremeter results (Section 4.1) and the initiation of tensile failure of brown coal (Section 4.2). In in-situ tests, the problems addressed are the in-situ horizontal stress and ground-material parameters in the open-pit mine (Section 5.9) and impacts of anisotropy of in-situ horizontal stress on the in-situ test results (Section 5.10).

1.3. Research Hypothesis

1.3.1. Shear Modulus and Shear Strength in Slope Stability

Describing the parameters of the in-situ ground materials related to their shear failure is essential to geotechnical investigation in open-pit mining. This is because the shear failure is a common geotechnical hazard found in of open-pit excavated wall (Drucker and Prager (1952). The shear modulus and shear strength parameters have essential roles in shear failure analysis.

In Limit Equilibrium Analysis (LEM), idealised collapse body is defined by its margin. The margin called the ‘shear surface’. The safety of open-pit excavation is achieved by comparing ground material’s shear strength parameters and shear stresses at the field. As an example, in Mohr-Coulomb failure criterion, the shear strength parameters of the material, the undrained shear strength, friction angle, define the shear failure envelope. A shear failure occurs when this shear failure envelope is exceeded by the Mohr circle that represents the stress condition. For sandy material, since the undrained shear strength is mostly negligible, the failure is mostly governed by friction angle. Whereas for clay, the undrained shear strength is the more significant governing factor among the two shear strength parameters.

Another common failure analysis method is called the Shear Strength Reduction (SSR). The method considers material’s stress-strain behaviour by using iterative numerical modelling to calculate the critical Factor of Safety (FoS). In this case the shear modulus needs to be take into consideration for numerical simulations of material’s stress-strain behaviour.

1.3.2. Tensile Failure and in-situ Horizontal Stress in Open-pit Mining

The mineral brown coal in Victoria is regarded as organic soft rock (Tolooiyan et al., 2014). For the organic soft rock, the measurement of shear modulus and shear strength parameter can be disturbed by the tensile failure. Therefore, in addition to geotechnical investigation for the shear failure Section 1.3.1, consideration of material’s tensile failure is necessary for the research.

In-situ horizontal stress is another consideration for the research. In open-pit excavated batter, due to the existence of joints and stress relief, in-situ horizontal stress cannot be empirically evaluated as a stress component of the total vertical stress by the surcharge and soil unit weight (Hoek et al., 2002). In the brown coal open-pit mine of

the research, both the in-situ horizontal stress and its possible impact on the measurement of shear modulus and shear strength parameter are to be studied.

1.3.3. Overview of Hypothesis

This research implements in-situ and laboratory methods to estimate the material characteristics of soil and brown coal in the open-pit mining area. These in-situ material characteristics are shear modulus, friction and dilation angles (for non-cohesive materials) and undrained shear strength (for cohesive materials). In-situ testing can be applied to verify measurements because it minimises disturbance to the sampling. For brown coal that is regarded as cohesive organic soft rock, both the shear failure mode and the brittle failure mode need to be examined (Tang et al., 2017). Specifically, the in-situ horizontal measurement should consider the possible anisotropy of the horizontal stresses, which could have been affected by excavation and other mining activities in open-pit excavated batter.

1.4. Introducing the Pressuremeter Test to the Project

1.4.1. Overview

The pressuremeter test is a universal in-situ testing method for measuring the properties of soil developed by Menard (1957). The aim of the pressuremeter is to perform cylindrical cavity expansion in the soil cavity using a hydraulic fluid or gas. The soil-resistant pressure and the cavity-expansion volume (or radius) are recorded during the test. After calibration and correction, the data is plotted as the curve of pressure (stress) versus strain. By empirical, analytical or numerical explanations, the stress-strain curve can be used for the interpretation of geotechnical characteristics of the test material. The pressuremeter test has been widely applied in foundation design, pavement engineering and in-situ geotechnical investigation processes for measuring a ground material's characteristics and in-situ stress distribution.

The pressuremeter test was implemented for this research project for four purposes. First, the pressuremeter test was applied to obtain the in-situ horizontal stress in the open-pit. Second, based on the parameter interpretations, the in-situ elastic stress-strain parameter (shear modulus) and the plasticity-strength parameters of soil (the undrained shear strength for clay and coal) can be directly obtained. These parameters are useful supplements to both simple and sophisticated laboratory testing methods such

as direct-shear testing, tri-axial testing and laboratory pressuremeter chamber testing which both ignore the scale effect. Mair and Wood (1987) state that simple laboratory estimations cannot determine in-situ boundary conditions and avoid disturbances to the sampling, while sophisticated laboratory tests are time-consuming and costly. Third, in-situ pressuremeter testing eliminates material disturbances that are generated by sample extraction and preparation (Palmer, 1971). Therefore, the results from a pressuremeter test are applied to describe the realistic behaviour of the material at the site. Fourth, for the interpretation of the material's elastoplasticity, results from the pressuremeter tests were plotted to observe the stress-strain relationship. This stress-strain relationship can be fitted by different models. The models then provide one with an describing of the material's quasi-static behaviour.

1.4.2. Anisotropy Impact on the Pressuremeter Test Measurement

The in-situ pressuremeter test has never been performed on Victorian brown coal. As a result, describing the potential interference factors of pressuremeter testing measurements, especially the factors that are typically found in the brown coal mine area, is a prerequisite for implementing in-situ testing.

The in-situ horizontal stress measurement applied in the current research project is used to (1) better demonstrate the in-situ stress conditions of a brown coal mine and (2) to better study the sensitivity of the material parameter to the anisotropy of in-situ horizontal stress conditions. The conventional cavity expansion hypothesis for the pressuremeter testing study is used on the basis of isotropic in-situ horizontal stress at rest. The conventional hypothesis assumes that the ground material on the side-wall of the in-situ test cavity is subjected to uniform earth pressure in all radial directions before cavity expansion. As a result, a pressuremeter test usually estimates the uniform in-situ horizontal stress at rest by providing the value of the 'lift-off pressure' in the stress-strain curve.

The in-situ pressuremeter behind the open-pit excavated batter may not be subjected to uniform horizontal stresses. The likelihood of anisotropic in-situ horizontal stress around the test cavity is based on (1) the stress relief of open-pit excavation, (2) groundwater level variations and (3) the presence of joints in soft rock. In the anisotropic stress condition, the cavity side-wall is subjected to non-uniform radial confinement. The associated stress-strain behaviour during the pressuremeter test

differs from the isotropic stress condition. Eventually, this anisotropy can cause a variation in the parametric interpretation of test results.

Due to the uncertainty of the impact of anisotropy, in-situ horizontal stress estimation based on the in-situ pressuremeter test in a brown coal open-pit area can be misleading. Therefore, it is necessary to describe the potential impact of anisotropy on the horizontal stress estimation in the laboratory before performing an in-situ test.

1.5. Research Objective

This research project uses cavity expansion theory to develop two laboratory tests to describe the two major impacts found from brown coal open-pit mining area on the in-situ pressuremeter test measurement. These two major potential impacts are (1) tensile failure and (2) the anisotropy of the in-situ horizontal stresses. On the basis of the laboratory results, this research project obtained the characteristics of soil and soft rock and in-situ stress conditions based on in-situ pressuremeter testing.

1.6. Research Methodology

1.6.1. Overview

The present research project is mainly based on laboratory and in-situ tests, which are complemented by numerical Finite Element Modelling (FEM) and analytical solutions. This research project has developed two new laboratory testing methods for achieving the first and second research objectives. The anisotropic pressuremeter chamber test was developed for describing the impact of anisotropic horizontal stresses on the interpretation of pressuremeter testing results. The Unconfined Expansion Test (UET) was designed to evaluate the tensile strength of brown coal without the predefined failure plane. The first in-situ pressuremeter test on Victorian brown coal was performed at the final stage of the research and is explained with a full description of the in-situ geotechnical background, equipment specification and installation, test execution and the presentation of test results.

1.6.2. Anisotropic Stress Analysis

As mentioned in Section 1.2.1.2, the in-situ boundary condition in brown coal open-pit mines is unpredictable before in-situ testing. Therefore, it is recommended that the study of the impact of anisotropy of in-situ stresses on pressuremeter testing be

studied prior to the field testing. This can be done by pre-defining isotropic/anisotropic confining pressures in the laboratory and performing a parametric analysis.

As described in Section 2.4, laboratory chamber testing is known to be reliable for studying issues relevant to in-situ boundary conditions for pressuremeter testing. This author studies the drawbacks of the axisymmetric design of the conventional chambers presented in Section 2.4.3 and introduces a newly designed isotropic-anisotropic cubic chamber in Section 3.3.

Since the cubic chamber can simulate various in-situ stress conditions by making independent adjustments in three principal directions, miniature pressuremeter tests were performed in isotropic and anisotropic confining stresses conditions in the chamber and are discussed in Section 4.1. Isotropic tests provide parametric studies to ensure the accuracy of simulations of the in-situ stress conditions by the chamber. The anisotropic tests provide an describing of the sensitivity of the interpreted parameters in accordance to the anisotropy.

1.6.3. Tensile Strength Analysis

Using the same miniature expansion probe for the isotropic/anisotropic pressuremeter chamber testing, the author developed a stress-controlled, UET for the thick-walled cylindrical specimen, described in chapter 4.1. The test material is the saturated natural brown coal specimen from the Yallourn open-pit mine where the field pressuremeter test is considered to be conducted at. The UET was performed in unconfined boundary condition, using an axisymmetric simplified geometrically designed and uniformly radial pressurisation strategy. As a result, a random crack could be made in the weak zone of the natural specimen and propagated without limitations from the test's boundary condition. Results from the UET are representative of the strength of the non-artificial (randomly initiated) failure surface of brown coal.

The UET was developed to evaluate brown coal's tensile strength on the radial failure surface. This failure scenario is commonly found in in-situ pressuremeter tests for soft rock. The results of the UET were compared to the results from the two conventional tensile test methods, the DTT and BT. The comparison was performed by an eXtended Finite Element Method (XFEM) simulation, described in section 4.2.12 to demonstrate the advantage of using the UET for brown coal material.

1.6.4. Numerical Modelling

The author carried out several FEM XFEM simulations using the ABAQUS FEM programme in this research project for different purposes. The FEM models were built to (1) simulate the excess pore-pressure generated by the UET and the Semi-circular Bending Test and (2) observe the stress distribution inside the material during the tests. The XFEM models are dedicated to simulating the material's fracture behaviours. The purposes of the models in this dissertation are demonstrated as follows:

- (1) The three dimensional FEM of the laboratory pressuremeter chamber test model was built for the observation of the stress distribution in horizontally isotropic and anisotropic boundary conditions (Section 3.3.12.8).
- (2) The three dimensional FEM of the UET was built to simulate excess pore-pressure during UET testing. The purpose of the simulation is to optimise the UET expansion rate (Section 4.2.7).
- (3) The semi-two-dimensional XFEM of the UET was built to simulate crack initiation and propagation. The purpose of the simulation is to (1) examine the tensile strength, shear modulus and fracture parameters of the specimen (2) analyse stress development along with the specimen's deformation and (3) compare the simulated measurement with conventional tensile tests (Section 4.2.11).
- (4) The three-dimensional FEM of the Semi-circular Bending Test was built to simulate excess pore-pressure during the SCB test. The purpose of the simulation is to optimise the laboratory test rate (Section 4.2.10).
- (5) The three-dimensional XFEM of the direct tension test (DTT) was built to simulate the test procedure and specimen failure. The purpose of the simulation is to (1) demonstrate the stress concentration issue of the DTT due to the shape of the specimen and (2) compare the simulated measurements of tensile strength with the UET and the Brazilian test (BT) (Section 4.2.12)
- (6) The three-dimensional XFEM of the BT was built to simulate the specimen's fracture behaviours during the test. The purpose of the simulation is to (1) demonstrate the stress concentration issue of the BT due to the stress conversion, and (2) compare the simulated measurement of tensile strength with the UET and DTT (Section 4.2.12)

1.6.5. Auxiliary Laboratory Tests

The author carried out the standard direct shear test to determine the shear strength of the sand that was also used in the chamber pressuremeter test (Section 4.1.3.1). Three direct shear tests were performed with normal stresses in accordance to the specified horizontally isotropic confining pressures in the chamber pressuremeter test. The shear strength parameters from the direct shear tests were then used to verify the interpretation results from isotropic chamber testing. The purpose of the test is to demonstrate the capability and accuracy of the newly designed chamber in estimating shear strength parameters.

The Semi-Circular Bending (SCB) test was applied to evaluate the fracture toughness of the brown coal. The result was used to calculate the critical energy release rate of the UET test brown coal, which was then applied as the fracture parameter for the XFEM simulations of the newly developed and conventional tensile tests.

1.6.6. Field Pressuremeter Test

In-situ pressuremeter testing on Victorian brown coal was carried out in the Yallourn open-pit mine. Both the brown coal and the inter-seam materials (mostly clay) were tested. The tests were performed in two multi-purpose bore-holes: one is behind the batter and the other is in the mine floor. Based on the UET results and bore-logging data, the research optimises the test depths to prevent disturbances to the results from the brown coal's tension failure. The test depths behind the batter range from 40m to 120m, while the depths in the mine floor ranges from 17m to 40m below the ground level.

The high-capacity, gas-inflated, Menard-type rock pressuremeter probe with four radial deformation feeler arms was chosen as the test probe. The pressuremeter test bore-holes were created prior to probe installation by geotechnical drilling. Before the installation of the pressuremeter probe, system compliance and membrane resistance were calibrated.

The in-situ pressuremeter tests adopt the pressure-controlled pressurisation method. Each test consists of one stress-holding procedure followed by one unload-reload cycle. The unload-reload cycle was used to determine the linear stress-strain graph to estimate the shear modulus. The other soil properties interpreted from the tests are in-situ horizontal stress at rest and undrained shear strength.

1.7. Thesis Outline

The structure of the thesis is illustrated by the flowchart Figure 1.1. The thesis consists of six chapters:

Chapter 1 consists of the introduction of the project. The first section starts with the research background (location and topic) and the research problem. The second section includes the problem definition, which is identified as the parametric analysis of soil and weak rock for geotechnical investigation for open-pit mining excavation for the brown coal open-pit mining. The third section shows the research hypothesis. This section lists considerations of potential failures of materials of soil (Section 1.3.1) and soft rock (Section 1.3.2) respectively. Section 1.3.3 demonstrates the reason that both soil and soft rock should be taken into account when a brown coal open-pit excavated batter is studied. Section 4 introduces the pressuremeter tests into the project and demonstrates research gaps. Section 5 shows the research objective. This is followed by the introduction of the research methodology in Section 6.

Chapter 2 presents the literature review of this thesis. The first part provides the background of pressuremeter testing. The second part explains the parameter interpretation methods associated with different types of materials. The third part introduces existing pressuremeter chamber tests and their limitations on the present research project. The fourth part introduces conventional tensile strength testing and limitations for determining the tensile strength of brown coal. The fifth part is the conclusion of the literature review.

Chapter 3 introduces the development of the test instrument. This development procedure is a vital part of the research project. The first subchapter introduces the construction of the miniature pressure probe for both the UET and the pressuremeter chamber test. The second subchapter introduces the designed isotropic/anisotropic pressuremeter chamber. This section includes the concept of the test, the construction of the chamber, the internal pressure calibration procedure, stress concentration analysis and the FEM analysis of stress distribution in accordance with isotropic and anisotropic confining pressures.

Chapter 4 introduces the two laboratory tests. The first subchapter demonstrates laboratory anisotropic pressuremeter chamber testing on medium grain sand. The subchapter starts with test design. The next section describes the preparation, which includes the specimen preparation and equipment calibration. The introduction of the

test procedure and parametric interpretations is found in the next section. The last two sections of the first subchapter are the parameter comparison and conclusion. The second subchapter describes UET of brown coal. The subchapter starts with the introduction and theory. Then the subchapter introduces the the test brown coal and specimen preparation. The subchapter then describes the test rate and the test procedure. The UET and its results are showed in the next section. This is followed by the XFEM comparison between the UET and the conventional tensile measurement techniques.

Chapter 5 describes the in-situ pressuremeter test perfored in the Yallourn open-pit brown coal mine. First, the test background is introduced, which includes the purpose of the test, followed by the illustration of the test procedure of the in-situ pressuremeter test. Thereafter, the test procedures are described. This is followed by the illustration of the in-situ pressuremeter test results of different test materials.

Chapter 6 firstly concludes the research gap of implementing pressuremeter testing in brown coal mines. Then it concludes the two laboratory testing methods developed in the research. The chapter then reviews the in-situ pressuremeter testing carried out in the brown coal open-pit mines and the test result. Thereafter, the recommendation for the future work in the field of study is made in the chapter.

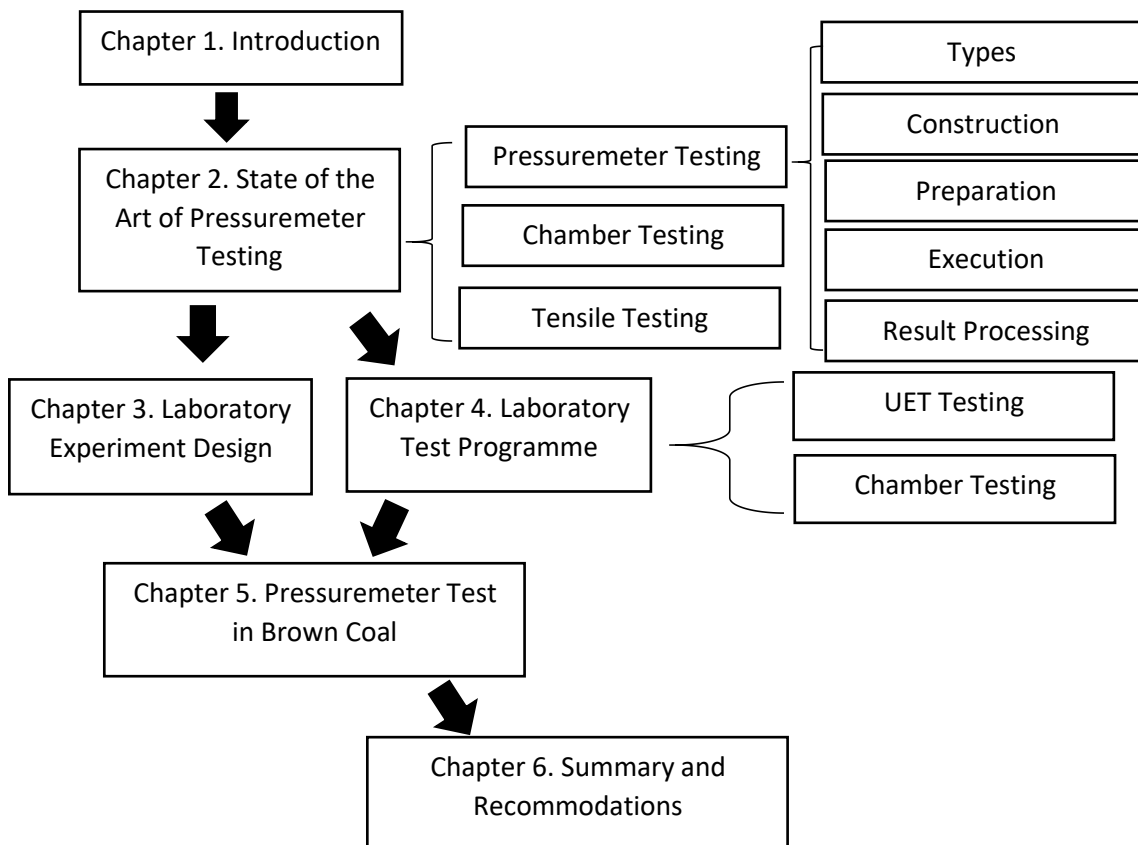


Fig.1.1. Thesis Outline Flowchart

2. State of the Art of In-situ Pressuremeter Testing

2.1. Introduction

This chapter is presented as the literature review chapter of the thesis. The chapter consists of five sections. Section 2.2 introduces the background for the pressuremeter test. Section 2.2.1 to Section 2.2.4 conclude different types of pressuremeter tests. Section 2.2.5 and Section 2.2.6 describe the differences of construction between different types of pressuremeter equipment. Section 2.2.7 and Section 2.2.8 are the procedures of pressuremeter test preparation and execution. Section 2.2.9 and Section 2.2.10 present the processing and analysis of the test curves. The parameters interpreted from the test results are summarized in section 2.3. Section 2.4 introduces the laboratory calibration chamber for the pressuremeter test analysis. This section illustrates the test development and the interpretation of the material parameters. Section 2.5 provides an overview of the principles of the conventional laboratory tensile strength testing techniques. Section 2.6 encompasses the content of the literature review and highlights the significance of the research.

2.2. Pressuremeter Test Background

2.2.1. Menard Pressuremeter (MPM)

Pressuremeter (PMT) testing is one of the most versatile types of in-situ testing for the interpretation of the geotechnical properties of soil, and it has been extensively applied in the evaluation of in-situ horizontal stresses. The first implementation of the pressuremeter test was introduced by Menard (1957). According to Menard's demonstration, the first pressuremeter probe is a device that consists of three hollow cylindrical cells and is sealed by an expandable rubber membrane sleeve. The test procedure can be demonstrated in two steps. The first step is the installation. The pressuremeter probe is lowered into the prepared cavity of the test soil. The second step is the expansion. The probe is expanded in the form of a 'Chinese lantern' along with the soil cavity, which can be regarded as cylindrical cavity expansion in small level of strain, using the hydraulic fluid. During the expansion, the measured pressure and volume (radius) strain are related to the geotechnical properties of the soil.

The generally accepted classification of the pressuremeter test is based on the method of installation. The pressuremeter test that is prepared by the pre-bored installation method, as was first developed by Louis Menard, is named the Menard

Pressure Meter (MPM) test. The MPM test was initially used for the estimation of the regional in-situ density of the soil. Thereafter, the three-cell structure of the MPM probe was simplified to the one-cell probe by Briaud and Shields (1979). The MPM test procedure was standardised by Briaud, Tucker et al. (1985).

Since the empirical equation was introduced into the interpretation of the MPM test curves by Gibson (1961), the MPM test has been carried out extensively to estimate soil parameters such as the undrained shear modulus, G , the undrained shear strength S_u , and the limit pressure, P_L . The interpretation methods were further studied using the analytical solutions of plane-strain cavity expansion (Ladanyi 1972, Palmer 1971). In addition, some of the analytical solutions were compared with the empirical solutions by Menard (1975).

Nowadays, the MPM test is one of the most common types of pressuremeter tests. This is attributed to its versatility. The MPM test is widely used in cohesive materials due to the ease of preparation of an undisturbed borehole. The preparation of the MPM borehole is excavated with the drilling rigs. Therefore, compared to other types of pressuremeter probes that can create test cavities with the probe itself, which is discussed later, the MPM probe is more adaptable for use in soft rock materials (Mair and Wood 1987). However, for cohesion-less materials such as sand, it is difficult to prepare boreholes with undisturbed walls due to the collapse of cavity after drilling. Hence, MPM tests in cohesion-less materials are prone to being imprecise.

2.2.2. Self-boring Pressuremeter (SPB)

Based on the illustration of the MPM test in cohesion-less materials, it can be described that disruption due to pre-boring the test cavity lowers the quality of the MPM test results. Therefore, a pressuremeter test with a self-boring probe is ideal for sandy materials. The pressuremeter test that applies the self-boring technique was first introduced by Wroth and Hughes (1972) and Baguelin, Jezequel et al. (1972). The technique was named the Self-Boring Pressuremeter (SBP) test. The major difference between MPM and SBP testing is the construction of the pressuremeter probe. The SBP probe has a unique rotary-cutting shoe and a slurry flushing channel at the bottom of the probe. The cutting shoe is driven by the drilling rig connected to the SBP probe. During probe installation, the rotary power from the drill is applied to the cutting shoe to crush the soil underneath the probe. The small pieces of soil particles are then flushed out by

the slurry flushing system (Windle and Wroth 1977). Since the bore-hole creation and probe installation take place simultaneously, disturbances from the test preparation of SBP are more likely minimised (Mair and Wood 1987).

Thanks to SBP test's advantage of an undisturbed pressuremeter test cavity, the test is widely implemented on the cohesion-less (sandy) materials for the interpretations of geotechnical parameters such as the friction angle (ϕ) and the dilation angle (ψ) (Hughes, Wroth et al. 1977). It is also found that the SBP test is compatible with the soft clay pressuremeter test. In addition to sandy materials and provides undisturbed parameter interpretations (Windle and Wroth 1977). Due to its versatility, the SBP test is extensively implemented in soft soil pile and foundation designs (Baguelin 1978, Potts and Martins 1982). The major drawback of the SBP test is that due to the capacity of the cutting shoe, the probe is unable to create a rotary bore-hole in rock, soft-rock, and soft-rock-like mineral materials.

2.2.3. Push-in Pressuremeter (PIP)

In order to better adapt the pressuremeter test for offshore application, the Push-in Pressuremeter (PIP) test was specifically developed by Henderson et al. (1979). Similar to the SPB probe, the PIP probe creates a test cavity during probe installation with its cutting shoe. The major difference can be found in the construction of the cutting shoe. The PIP is equipped with a non-rotary push-in cutting shoe. Therefore, the push-in force is applied during probe installation instead of the rotary driving force. Hence, the technique is most suitable under the bottom of the wireline drill (Fyffe et al. 1985). When well-performed tests are achieved with the MPM, SBP and PIP methods, parameter interpretations of the test curves are comparable (Powell and Uglow 1985).

2.2.4. Other Types of Pressuremeters

Hughes and Robertson (1985) introduced the installation technique to perform the pressuremeter test along with the cone penetration test. The technique is named the Full Displacement Pressuremeter (FDPM) test or Cone Pressuremeter Testing (Nutt 1993). The main use of the FDPM test is for the comparison between the soil properties obtained from the cone penetration test and from the pressuremeter test. However, disruption to the initial condition of the PMT test can be found due to cone penetration (Schnaid 1990).

Another type is the PENCEL Pressuremeter (PPMT) test. It is a pressuremeter test that applies the downscaled pressuremeter test probe. The PPMT was initially developed by Anderson (2001) for laboratory pressuremeter tests in the calibration chamber. Due to the advantage of its size, more recent research considers the PPMT test for pavement design (Shaban 2016).

2.2.5. Pressuremeter Probe

The initial design of Menard's Pressuremeter (MPM) probe consisted of three expansion cells (Mair and Wood 1987). The construction of the three-cell pressuremeter probe and its measurement devices are shown in Figure 2.1 (a). The total length and diameter of the pressuremeter probe are 420mm and 58mm, respectively (Cosentino et al. 2006). This original design provides for a length-to-diameter ratio, also named the slenderness ratio, of 7.2. In the lateral pressuremeter test study, much attention was paid to the sensitivity of the parametric interpretations corresponding to the slenderness ratio (Houlsby and Carter 1993, Shuttle and Jefferies 1996, Whittle 1999). Ajalloeian and Yu (1998) discovered the relationship between the different slenderness ratios and the accuracy of the parametric interpretations of the pressuremeter test. It was then concluded that the ideal slenderness ratio is between 6 and 6.5 (Briaud 2013).

In the pressuremeter probe, the three expansion cells expand together as a consequence of the applied hydraulic pressure. Of the three cells, the cells at the top and bottom are the guard cells. These two guard cells offer geometric protection against the non-cylindrical deformation of the main expansion cell in the middle. This non-cylindrical deformation at the top and bottom is regarded as the end effect during the pressuremeter test (Briaud 2013). The end effect was comprehensively described by Cunha (1994). The main expansion cell in the middle is also referred to as the measuring cell by Menard (1975). The volumetric strain and pressure increment of the measuring cell during cavity expansion are defined by the tester with the control system on the ground surface. It can be seen, based on Figure 2.1 (a), that the three-cell pressuremeter probe requires independent pressure valves and pressure gauges for the guard cells and the main cells, respectively. As a result, the calibration and test procedure for the three-cell pressuremeter test can be time-consuming.

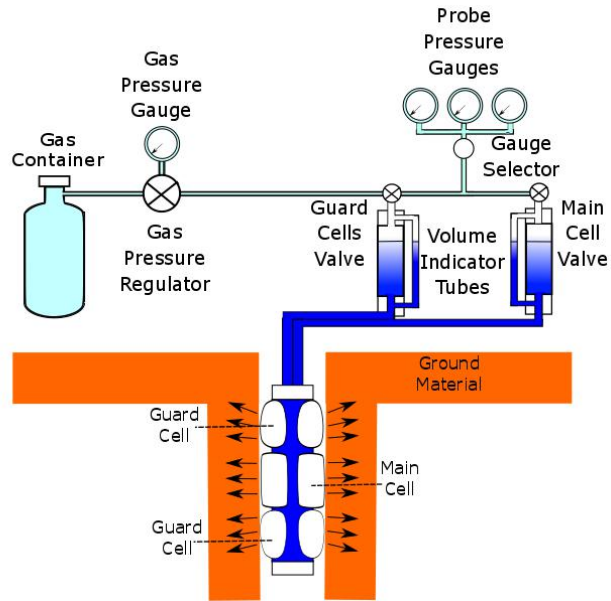
In order to improve the efficiency of the pressuremeter test, a single-cell design of the MPM type of pressuremeter testing probe was developed. The single-cell design

was named the monocell (Clarke and Gambin 1998). The diagram of the monocell pressuremeter probe is showed in Figure 2.1 (b). Briaud et al. (1985) address that with the proper test quality, the test results and interpreted parameters from three-cell pressuremeter testing and monocell pressuremeter testing should provide identical test results.

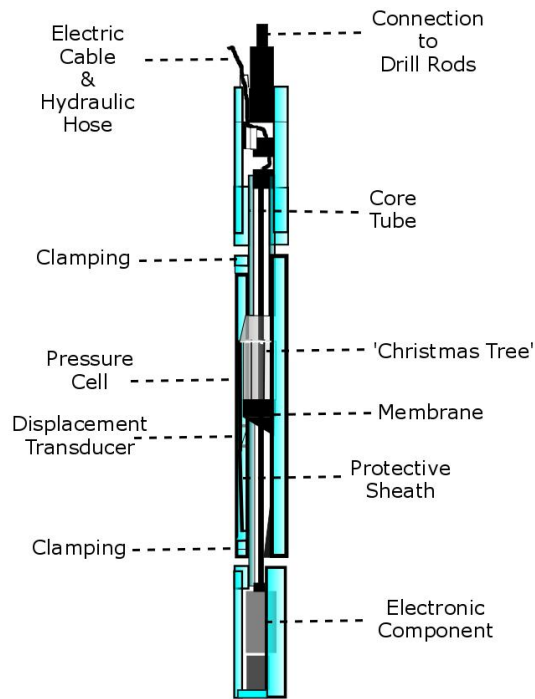
In order to overcome the error generated by both the end effect and the compressibility of the inflation fluid (or gas), some in-situ monocell pressuremeter probes are often equipped with three, four or six forms of strain gauges. As the radial strain is recorded by the strain gauges, the pressuremeter test method with strain gauges is referred to as the radius-measurement method (Mair and Wood 1987). In contrast, the pressuremeter test method without radial measurement is referred to as the volume-measurement method. A comparison between the two types of deformation measurements is shown in Table 2.1.

Inside the pressuremeter probe that uses the radius-measurement method, the strain gauges are located in the middle of the length of the pressuremeter probes. These strain gauges face towards different directions for the average measurement of the radial strain of the bore-hole. Inside the pressuremeter probe that uses the volume-measurement method, the volumetric strain is recorded based on the volume change of the injected fluid (or gas).

Sometimes, a protective sheath is added to the external surface of the pressuremeter cells in case the probe is damaged by the test material or is affected during installation. The protective sheath can be described as a group of steel strips on the exterior of the probe's membrane. The sheath structure is commonly found in the PIP and the SBP (Fyffe et al. 1985, Cunha 1994, Goh and Fahey 1996).



(a)



(b)

Fig.2.1. Pressuremeter probe diagrams of (a) 3-cell probe with physical pressure-strain measurement (Mair and Wood 1987), (b) monocell pressuremeter probe with electric pressure-strain measurement (Clarke 1994)

Table 2.1. Comparison between the two measurement types of pressuremeters

Pressuremeter Type	Volume-measurement	Radius-measurement
Inflation	Fluid	Fluid, gas
Deformation Measurement	Fluid volume gauge	Feeler-arms
Advantages	Does not require arm calibration	Overcome 'end effect'
Drawbacks	(1) Geometric 'end effect' (2) Requires volume losses calibration	Each feeler-arms requires calibration
Compatibility	Normal MPM, SBP, PIP	Soft rock PMT

2.2.6. Bottom Components of Different Types of Pressuremeter Probes

The bottom components of different types of pressuremeter probes are different. The Menard pressuremeter (MPM) probe has a flat-head bottom component, as Figure 2.1 shows. The design ensures that the disturbance and incline during installation in the pre-bored cavity is minimised.

The SBP is equipped with a rotary cutting shoe for the initial creation of the pressuremeter test cavity. Figure 2.2 displays the typical design of the SBP probe (Windle and Wroth 1977). The cutting shoe and the pressuremeter probe have the same measured diameter. This cutting shoe performs rotary soil cutting to create the pressuremeter cavity during probe installation. As mentioned earlier, both the rotary-cutting and the vertical advancing forces are generated by the drilling rig connected to the probe. This connection also conveys slurry flow. Slurry flow is applied to flush out the smashed soil from the bottom of the cavity when the probe is installed. During the installation, the oversized cavity should be avoided. Therefore, optimisations need to be made for (1) the rotation rate of the cutting shoe, (2) the speed at which the probe is lowered and (3) the flow rate of the slurry. Instead of the rotary cutting shoe, an alternative design called UBC SBP was presented by Cunha (1994). The UBC SBP probe is implemented with the mud-jetting bottom components, which replace the rotary cutting shoe on the general SBP probe.

In marine ground research and engineering, where pressuremeter tests are implemented in soil layers under the sea level, probe installation for these pressuremeter tests is different from the MPM and SBP tests. The PIP was especially designed for these purposes. Figure 2.3 shows the bottom component of the PIP probe (Fyffe, Reid et al. 1985). The general PIP probe features the protective sheath, as mentioned earlier in this section. At the bottom of the probe and the sheath, there is a push-in (non-rotary) cutting shoe with a diameter identical to the PIP. Using the push-in cutting shoe, the PIP probe can be installed into the cavities that the rotary drilling rig cannot reach to (e.g. the bottom of the marine wireline drilling) or the under-sized pre-drilled cavities.

The FDPM, also named the cone pressuremeter, is a combined structure of the Cone Penetration Testing (CPT) probe and the pressuremeter probe (Hughes and Robertson 1985). A demonstration of the FDPM that was presented by Schnaid (1990) is shown in Figure 2.3. The FDPM probe is connected to the CPT probe at the bottom. Both the FDPM probe and the CPT probe share the same diameter.

According to Cosentino et al. (2006), the PENCEL Pressuremeter (PPMT) probe is basically a down-sized cone-pressuremeter device commercially promoted by Roctest® especially for pressuremeter tests (e.g. laboratory chamber research, length to diameter ratio research). As shown in Figure 2.4, the PPMT probe is down-scaled to 34mm in diameter and 240mm in length. The difference between the PPMT and the FDPM is that cavity expansion during the PPMT test is indicated based on the volumetric strain, while the FDPM records cavity expansion based on its radial strain.

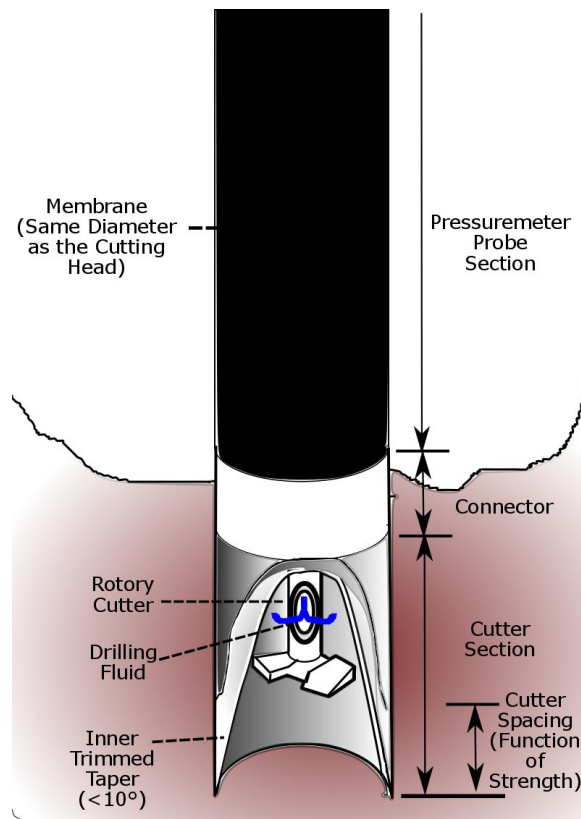


Fig.2.2. Self-boring pressuremeter cutting shoe diagram (Windle and Wroth 1977)

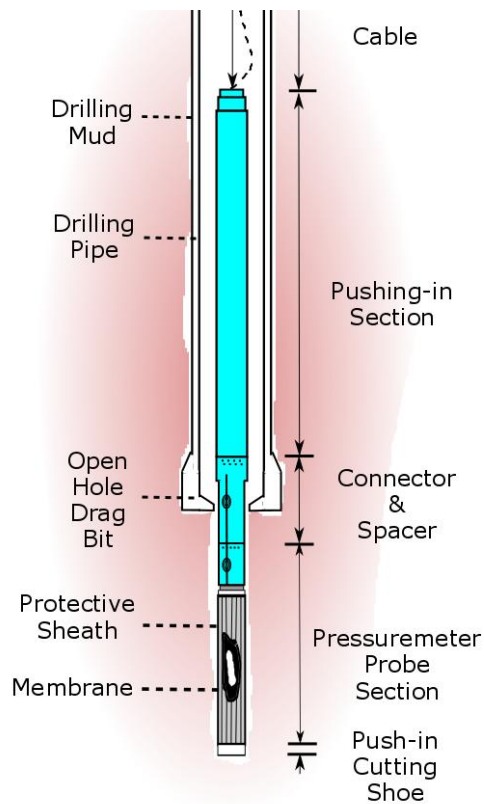


Fig.2.3. Push-in pressuremeter cutting shoe diagram (Fyffe, Reid et al. 1985)

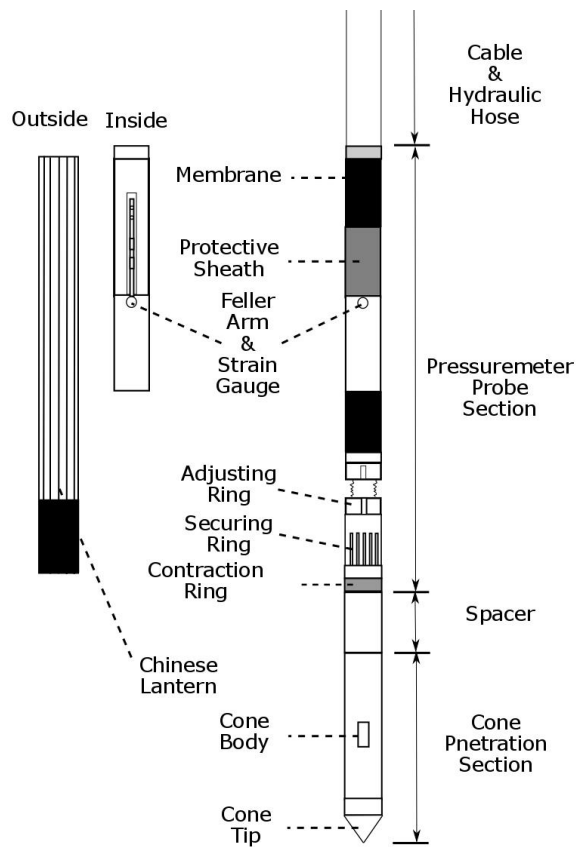


Fig.2.4.Demonstration of cone pressuremeter device (Schnaid 1990)

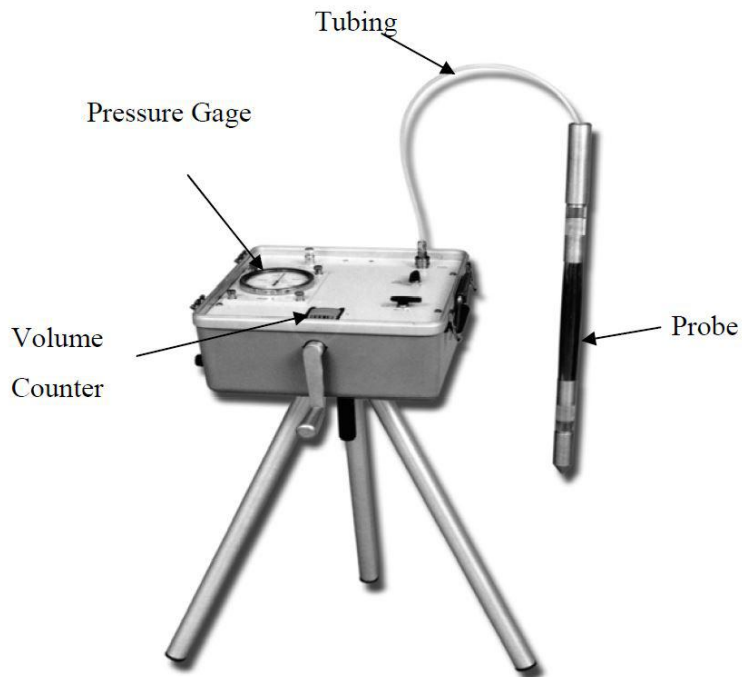


Fig.2.5. Demonstration of PENCEL pressuremeter device (Cosentino, Kalajian et al. 2006)

2.2.7. Pressuremeter Test Preparation

Preparation of the pressuremeter test includes the pre-test inspection and the system calibration. Preparation is essential for performing accurate pressuremeter tests. Mair and Wood (1987) highlight that the geotechnical parameters interpreted from non-calibrated pressuremeter tests are worthless. The inspection procedure examines both the saturation condition and leakage of the whole pressuremeter system (e.g. probe membrane, probe internal fluid circuits, pressure gauges, hydraulic pump, connection hoses), and verifies the zero-reading of both the volume and the pressure gauges (Briaud 1989). The system calibration procedure includes the system compliance calibration and the membrane resistance calibration. In conditions where the protective sheath is equipped with the probe, the expansion resistance of the protective sheath also needs to be calibrated (Cunha 1994).

2.2.7.1. Pre-test Inspection

The inspection has two stages. Stage one (saturation inspection) is only for the volumetric strain type pressuremeter. The inspection ensures the pressuremeter probe is fully saturated by the hydraulic fluid so that the error of volumetric expansion cannot occur due to the compressibility of the air. During the inspection, the pressuremeter probe is flushed with the hydraulic fluid (de-aired water, oil, etc.) with the bottom component of the probe open. This step expels the internal air of the system. When there is no visible air-bubble coming out of the system, the bottom component is closed to maintain the saturation of the hydraulic fluid at a low pressure. In the circumstance where the probe is fully protected by a confining tube (or calibration tube), Briaud and Shields (1979) suggest a 'squirt out' method. The method is performed by opening the valve suddenly after the system is pressurised at 1000kPa.

The inspection of leakage is conducted after the system saturation. During the leakage inspection, the pressuremeter probe is inserted into the tightly-fit calibration tube. Briaud (1989) notes that the design criteria for the calibration tube include the following: (1) the internal diameter of the calibration tube should be roughly 0.5% larger than the diameter of the deflated pressuremeter probe, and (2) the calibration tube should be thick enough so that the deformation of the tube at the calibration procedure is negligible. Briaud et al. (1985) explain that the next step of the leakage inspection is

pressurisation. In this step, the pressuremeter probe is pressurised up to the designed maximum pressure of the pressuremeter test at the designed test rate. During pressurisation, the pressure and volumetric (radial) strain are monitored and plotted onto a graph, as shown in Figure 2.6. The graph of a fully saturated, leakage-proof pressuremeter system satisfies the following requirements:

- (1) Volumetric strain (or converted volumetric strain from the radial strain) at the designed maximum pressure of the pressuremeter test is minimised.
- (2) Pressure-volumetric (radial) strain is linear once the ‘fully contacted’ stage is reached.

If the graph does not satisfy the listed criteria, the remedy can be achieved by (1) repeating the saturation process, (2) investigating the leakage positions and (3) replacing the calibration tube to reach the required rigidity.

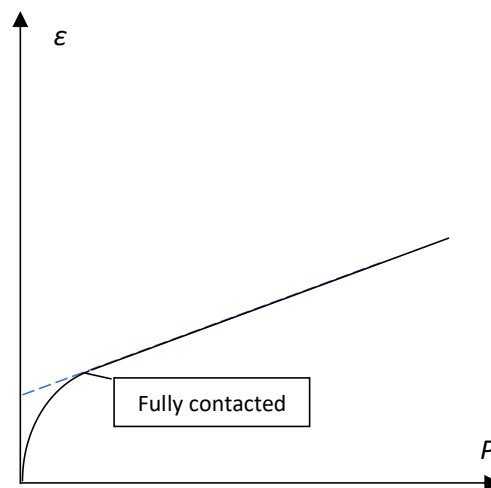


Fig.2.6. Saturation and leakage inspections

2.2.7.2. Initial Volumetric (Radial) Reading and Zero-pressure Verifications

When verifying the volumetric (radial) increment, one should consider the fact that the unconfined pressuremeter has a very sensitive and flexible membrane in its deflated condition. Therefore, without a proper definition of the initial volumetric (radial) reading, the calculated strain values are inaccurate. Briaud (1989) suggests that

verification of the initial volumetric (radial) reading is achieved by deflating the volume-measurement (radius-measurement) pressurised probe inside the rigid calibration tube until the probe can barely be withdrawn from the tube. The corresponding volumetric (or radial) readings are regarded as the initial readings of the pressuremeter probe.

Zero-pressure verification provides the offset of the hydraulic pressure required to settle the pressuremeter system to its pre-test conditions. This pressurisation stage is called the ‘preliminary expansion’ by Menard (1975). In cases where the protective sheath is applied (Briaud and Shields 1979), preliminary expansion also considers the initial expansion of the sheath. For one to conduct a zero-reading verification, the probe should be sealed and placed lower than the regulator on the control unit so that fluid head does not generate errors. Thereafter, the pressuremeter probe is pressurised to the initial volumetric (radial) reading from the previous step. The corresponding pressure can be regarded as the zero pressure of the pressuremeter test.

2.2.7.3. System Compliance Calibration

Mair and Wood (1987) introduced ‘volume losses’ calibration for the volume-measurement pressuremeter. In the radius-measurement pressuremeter, the ‘volume losses’ calibration is replaced by the ‘radius losses’. Generally, both the ‘volume losses’ and ‘radius losses’ calibrations are regarded as system compliance calibrations. According to Mair and Wood (1987) and Briaud et al. (1985), system compliance calibration is conducted due to (1) the flexibility of the hydraulic fluid/pneumatic gas conveying hose; (2) the compressibility of other connected components; and (3) the compressibility of the thickness of the membrane and the feeler arm under high pressure. Reasons (1) and (2) only apply to the volume-measurement pressuremeter. Factor (3) can be seen in high capacity pressure cases in the soft rock pressuremeter tests when a radius-measurement pressuremeter is used (Bacciarelli 1985).

During the system compliance calibration, the pressuremeter is inserted into a calibration tube. The calibration tube has a much higher elastic modulus than the pressuremeter system. Therefore, once the probe is pressurised, all the deformation is undertaken by the system compliance. The pressure rate for the calibration is identical to the pressure rate for the pressure control pressuremeter test. During calibration, system compliance deformation (volume or radius) at each pressure interval is plotted

against pressure. Based on the plot, the correlation of pressure against system compliance can be determined. In the pressuremeter test, the actual volumetric (or radial) strain can be derived by subtracting the corresponding system compliance strain value from each pressure reading.

2.2.7.4. Membrane Resistance Calibration

Membrane resistance can be regarded as the pressure requires expanding the membrane of the pressuremeter probe (or its protective sheath if present). During the pressuremeter test, due to the elasticity of the membrane (and the sheath), the resistance pressure increases along with the expansion of the probe. Without membrane resistance calibration, this resistance pressure cannot be distinguished from the result of the pressuremeter test.

To start membrane resistance calibration, the pressuremeter probe is deflated to the initial condition defined by step two. In the initial condition, Briaud (1989) suggests that one ‘work’ the rubber membrane by inflating and re-deflating the rubber membrane repeatedly at a fast rate. This procedure is performed to stretch the membrane to the test condition, in which the pressure-strain curve is repeatable. The pressuremeter probe is then expanded at the pressuremeter test rate. The pressure-strain correlation is then plotted as the result of membrane resistance calibration. Theoretically, the pressure increment correlates linearly with the volumetric (radius) strain of the probe, but due to the actual non-linear expansion of the probe, non-linear calibration is sometimes considered (Bacciarelli 1985). Based on the linear/nonlinear correlations obtained from the membrane calibration, the pressure, in accordance with the different volumetric (radial) strains of the pressuremeter probe, can be deducted. The actual cavity pressure during the pressuremeter test can be derived by subtracting the resistance pressure from the total pressure.

2.2.8. Test Execution

2.2.8.1. Menard Pressuremeter (MPM) Probe Installation

The MPM test probe is installed after the pre-bored cavity is formed at the test depth. Based on the guidance indicated by Finn et al. (1986) and Mair and Wood (1987), the inner-diameter of the pre-bored cavity should not exceed 10% of the MPM probe’s external diameter at the initial condition. The quality of the MPM test is highly

sensitive to the quality of the cavity boring. The oversized and undersized cavities can both cause significant errors in the test results.

Various types of drilling methods can be applied to achieve proper MPM test cavities in different ground materials. In situations where preparing a proper sized cavity is difficult, an undersized pilot bore-hole is pre-drilled. This undersized borehole is then enlarged through tubing, followed by the insertion of the MPM probe (Baguelin 1978). This method is usually performed in hard ground materials (e.g. rock and weak rock) or cohesion-less soil, where collapse happens (e.g. sand). For cohesive soil such as clay, the core-drilling technique is recommended for the MPM probe installation. However, during core-drilling, the circulation of the slurry should be minimised to reduce soil-softening. For soft clay, the pushing tube with the internal chamfer is recommended to avoid disturbances from rotary cutting and vibration. In extremely soft material (e.g. silt and loose sand), hand auguring is recommended to reduce 'wall erosion' (Mair and Wood 1987).

2.2.8.2. Self-boring Pressuremeter (SBP) Probe Installation

The SBP probe is installed during bore-hole creation through rotary drilling. Theoretically, SPB installation creates the test cavities without any disturbance. However, a certain degree of disturbance can still be found around the cavity due to the disturbances from the drilling execution (Windle and Wroth 1977). There are some factors of SBP drilling that can be controlled to minimise disturbances. First, the diameter of the cutting shoe should not be larger than the exterior diameter of the pressuremeter probe. Second, it is important to apply a constant pushing load and rotation rate during installation. Third, it is recommended that one minimise the pressure of the slurry fluid to reduce the disturbance from the flushing. Forth, it is recommended that one relax the soil before testing when the installation is finished (Mair and Wood 1987).

An alternative SBP installation technique introduced by Cunha (1994) replaces the rotary cutting installation with the ground jetting procedure. In this case, the disturbance generated by drilling is considered to be eliminated. However, jetting generates high fluid pressure on the soil, and hence is not recommended for materials with low permeability (Clarke 1996).

2.2.8.3. Push-in Pressuremeter (PIP) Probe Installation

In offshore implementations of pressuremeter testing, where neither SBP nor MPM techniques can be adapted to form the pressuremeter bore-hole, the PIP installation technique is specifically recommended. In addition to offshore implementations, the PIP technique is also applied in some soft sand onshore pressuremeter testing cases (Mair and Wood 1987). Similar to the SBP technique, PIP technique creates the cavity at the testing depth during bore-hole creation through pushing-in excavation. Before the installation, tube coring is normally performed up to the test depth Fyffe et al. (1985). An undersized borehole is then formed up to the test depth. The pressuremeter probe is then lowered to create a properly sized cavity. During the insertion, the vibrations form the main disturbance. Therefore, the applied pressure and rate for the pushing-in should be constant.

2.2.8.4. Probe Expansion (Pressure-controlled and Strain-controlled)

The expansion of the pressuremeter probe is specified through either the pressure-controlled method or the strain-controlled method. The test with an expansion limit and rate controlled by the monitored pressure variable is the pressure-controlled test. The test controlled by the monitored deformation (strain) variable is the strain-controlled test.

The data logging interval can also be defined by the corresponding variables that govern the expansion method or a specific time interval. For example, a pressure-controlled test can define the data logging interval as every 20kPa or every 10 seconds, while a strain-controlled test can define the data logging interval as every 5% of volumetric (or radial) strain or every 10 seconds. The suggested number of increments to complete the pressure-deformation graph in a typical pressuremeter test is seven to fourteen for the first loading phase (Briaud, 1989) or fifteen to twenty for the entire test procedure (Mair and Wood, 1987). A much higher definition can be achieved in modern pressuremeter tests. These high-definition graphs are significantly helpful in measuring the unload-reload stiffness and in curve-fitting the calibration and test graphs. However, the noise generated by the high frequency of data reading should be avoided through proper noise reduction (or curve smoothing) manners (Schnaid 1990).

For pressuremeter tests, each type of expansion controlling method has its advantages and drawbacks. Based on Briaud et al. (1985), the comparison between the

pressuremeter test conducted by two expansion methods is shown in Table 2.2. Generally, the pressure-controlled test is preferable for pressuremeter tests in materials of high stiffness (i.e. stiff clay, dense sand, soft rock and deep ground level). This is due to the fact that in these tests, the limit pressure of the probe is reached much earlier than the limit strain of the probe membrane. A further consideration is that since in stiff materials, the pressure increments in small strain levels are high, the strain-controlled test tends to generate over-discrete logging scatter. Therefore, the pressure-controlled test tends to result in smoother test curves in the small strain level in high stiffness materials. In contrast, strain-controlled tests are preferable in soft materials, such as some offshore material (Fyffe et al. 1985), loose sand (Schnaid 1990) and silt. In those cases, the limit strain of the probe membrane is easier to reach within the limit pressure of the probe. As a result, strain-controlled tests can better protect the equipment whilst providing smoother readings compared to pressure-controlled tests. In the cases where material creeping can affect the test results significantly, e.g., the tests on London clay presented by Windle and Wroth (1977), the strain-controlled method is applied due to the pore-pressure variation that can be governed by the defined strain rate.

For pressuremeter tests in which the ground conditions are unknown, the recommended method to select the appropriate pressuremeter test methods are in-situ bore-logging and sample coring to classify the in-situ material. These in-situ procedures can be accompanied by laboratory geotechnical testing so that one can better describe the properties of the material. Regardless of the pressuremeter test methods, probe expansion should reach a minimum of 10% of the radial strain for one to obtain meaningfully interpreted parameters (Cunha 1994). Additionally, pressuremeter capacity should be considered during the test design.

Table 2.2. Comparison between the two inflation techniques

Inflation Type	Pressure-controlled	Strain-controlled
Advantages	Data point is determined by limit pressure and test rate	Naturally reaches limit pressure
Disadvantages	Limit pressure is unknown	Discrete volume increment creates too few data points

2.2.8.5. Unload-reload Cycle

The unload-reload cycle is applied to estimate the unload-reload shear modulus (G_{ur}) of the material from the pressuremeter test. In early pressuremeter tests implementations, the elastic deformation stiffness of the material was represented by the shear modulus from the first expansion curve (Palmer 1971). However, the interpreted result from the first expansion curve was soon discovered to be unreliable. This is due to the fact that the first expansion curve is highly sensitive to probe installation (Briaud 1989). By contrast, the shear modulus from deflation and the second expansion phase represented by the unload-reload curve is completely free of disturbance from installation (Schnaid 1990). As a result, it is recommended that one evaluate the material's elasticity through the unload-reload shear modulus (Briaud et al. 1985).

The deflation (unloading) pressure/strain level to initiate the unload-reload phases has been debated by Mair and Wood (1987) and Briaud (1989). However, it is commonly agreed on that deflation (unloading) should start at a relatively high pressure/strain level, at which point the in-situ horizontal stresses at rest have minimum effect on the measurement. The pressure range in the unload-reload cycle, suggested by (Wroth 1982) also correlates with the stress/strain level of the deflation (unloading) phase.

2.2.9. Result Processing

2.2.9.1. Synopsis of Result Processing

This section introduces the procedures between the end of the pressuremeter test and the start of the geotechnical parameter interpretation of the pressuremeter test results. The raw pressuremeter test data is recorded as the total pressure change and the total strain during the test. Processing includes data correction and data conversion. The data correction process corrects the raw pressure and strain based on the actual cavity pressure and cavity strain. Data conversion makes turns the data into forms for parameter interpretations.

2.2.9.2. Data Correction

The raw results from the pressuremeter tests are the plots of total pressure and the total volume change or radial deformation. Subsequent to the calibration procedure

described in Section 2.2.7, there are normally two stress-strain curves from the calibration results ready for data correction. One of them is from the system compliance calibration result and the other one is from the membrane resistance calibration file. The system compliance calibration result is presented as the calibrated volume or radius ($dV_{calibration}$ or $dr_{calibration}$) versus the expansion pressure (P). In the graph, P usually sits on the Y-axis as the independent variable. Accordingly, either $dV_{calibration}$ or $dr_{calibration}$ sit on the X-axis as the dependent variable. If one looks at the dV - P curve as an example, the calibration process of the raw pressuremeter test stress-strain curve and the stress-strain curve from the system compliance calibration result use the total volume change, dV_{total} , minus the calibrated volume change to determine the actual volume change of the cavity, $dV_{calibration}$. The equation is defined as follows:

$$dV = dV_{total} - dV_{calibration} \quad \text{Eq.2.1}$$

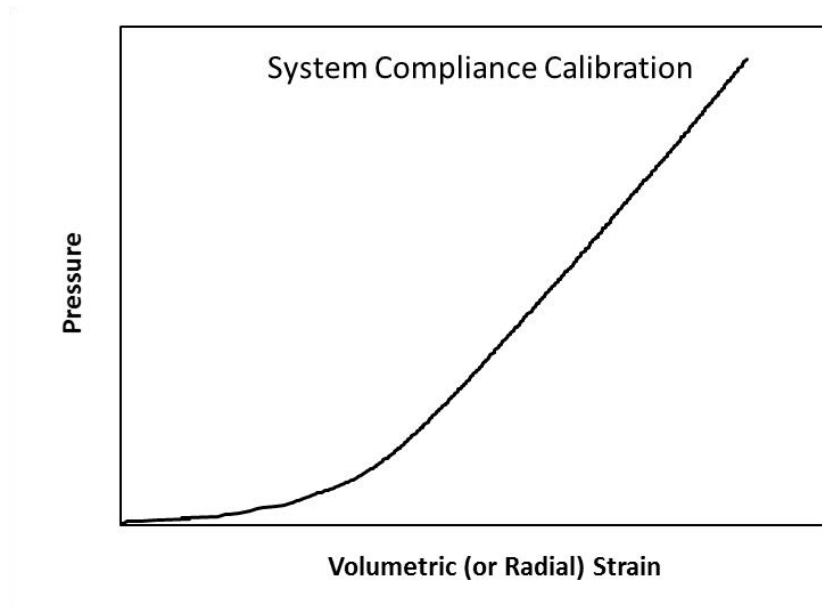
The membrane resistance calibration results are plotted as the membrane compliance pressure, $P_{membrane\ compliance}$ against the volume or radius deformation (dV or dr), in which $P_{membrane\ compliance}$ acts as the dependent variable on the Y-axis and either dV or dr acts as the independent variable. The pressure-strain correlation is typically linear based on the elasticity of rubber, with the exceptions of (1) significantly high-pressure tests, (2) the extra thick membrane (thickness > 1mm) and (3) the existence of the protective sheath. The correlation procedure for membrane resistance can be expressed as

$$P = P_{total} - P_{membrane\ compliance} \quad \text{Eq.2.2}$$

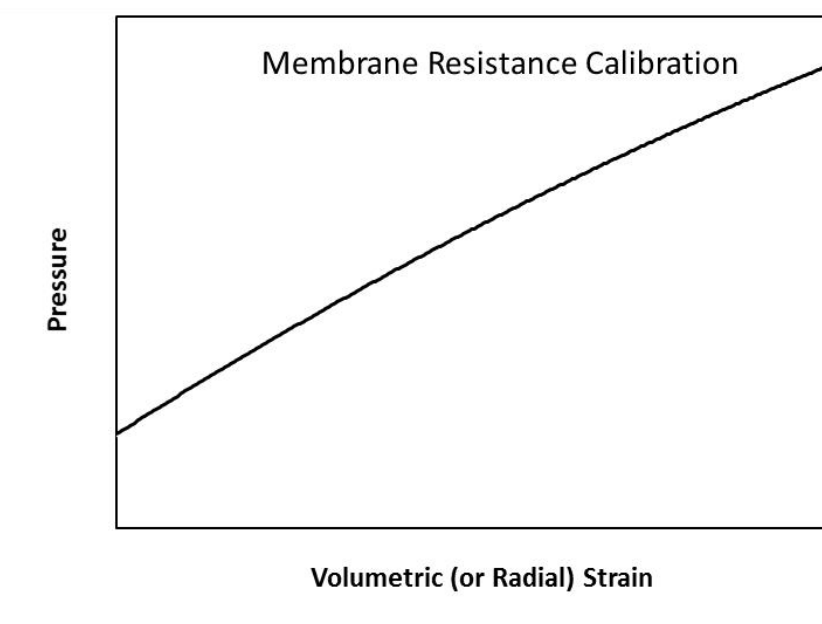
where P is the actual cavity pressure; P_{total} is the total pressure from the raw pressuremeter test data; and $P_{membrane\ compliance}$ is the corresponding membrane compliance pressure provided by the membrane calibration stress-strain curve.

The data correction is indicated in Figure 2.7. A common difficulty during data correction was dealing with the differences of reading intervals between the raw pressuremeter test data and the two calibration stress-strain curves. This is due to the fact that the defined interval for readings in the raw pressuremeter test data of both the pressure-controlled test and the strain-controlled test can only match one of the

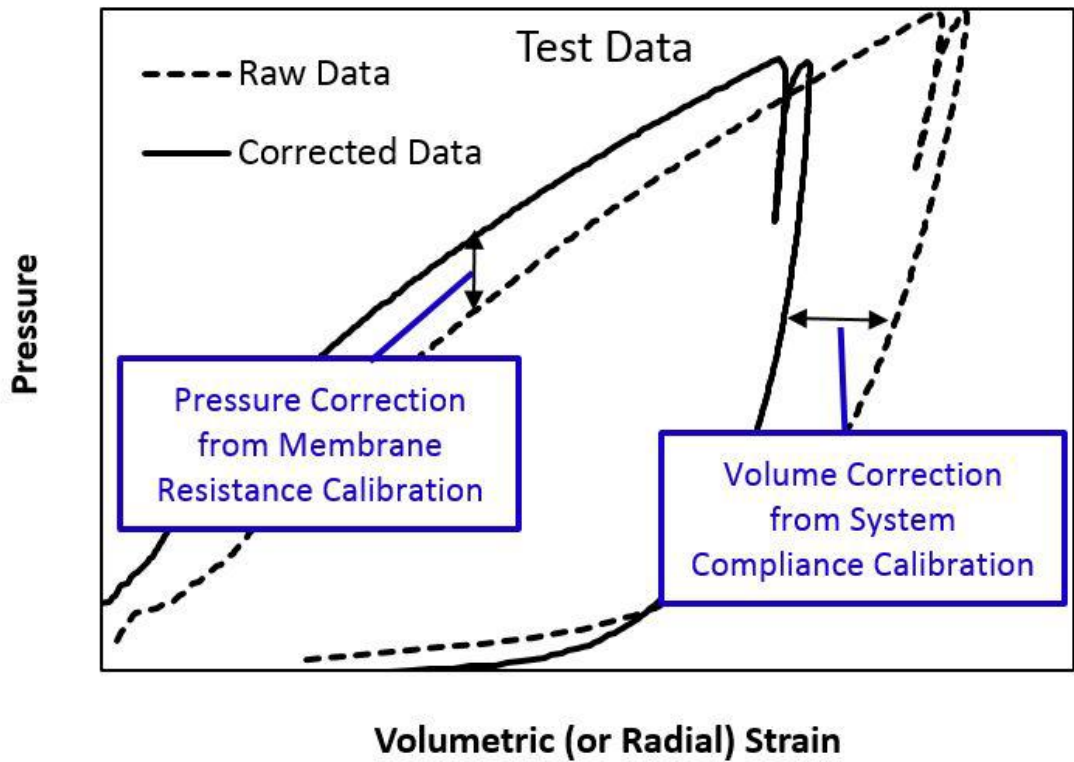
correspondent independent variables (X-axis) of the two calibration files. The solution is to discover the closed-form equations to curve-fit the two calibration data-plots (Briaud et al. 1985). For the membrane calibration, linear or low-order polynomial functions (≤ 3) are prone to be reliable in most cases. Nevertheless, the functions for the system compliance request a further study. Tang et al. (2017) applied a one-site total binding equation curve-fitting method, which shows consistent trends that are identical to the calibration data in high definition.



(a)



(b)



(c)

Fig.2.7. Data correction procedure: (a) system compliance data, (b) membrane resistance data, and (c) raw pressuremeter test correction

2.2.9.3. Application of the Corrected Pressure-Radial Strain Curves

In the $P-\varepsilon_c$ graph, the Y-axis normally stands for the pressure value, P , which represents the expansion pressure that acts on the cavity or the total stress applied on the soil cavity. The cavity strain, ε_c , as mentioned, represents the one-dimensional strain of the cavity, assuming the cavity expansion is performed in a plane-strain condition. The equation to express the correlation is

$$\varepsilon_r = \frac{dr}{r_0} = \varepsilon_c = \frac{dc}{c_0} , \quad \text{Eq.2.3}$$

where dr and r_0 are radial deformation and the radius of the deflated probe, dc and c_0 are the circumferential expansion and the initial cavity circumference, respectively.

If the $P-\varepsilon_c$ curves are converted into a logarithmic scale, $\ln(P)-\ln(\varepsilon_c)$, the gradient of the linear portion indicates the friction angle, ϕ , and the dilation angle, ψ (Hughes et al. (1977); Mair and Wood (1987) and Ajalloeian and Yu (1998)).

2.2.9.4. Application of the Corrected Pressure-Volumetric Strain Curves

In contrast to the radius-measurement type of pressuremeter testing, the volume-measurement type of pressuremeter testing can obtain the $P-\varepsilon_v$ curve directly from the corrected data. However, conversions need to be applied to the radius-measurement type of testing for the $P-\varepsilon_v$ curve, assuming the pressuremeter test is fully cylindrical cavity expansion.

In the $P-\varepsilon_v$ curve, the P value on the Y-axis stands for the cavity pressure or total stress of the soil around the cavity, and ε_v is the total volumetric strain of the cavity denoted as

$$\varepsilon_v = \frac{dV}{V_0}, \quad \text{Eq.2.4}$$

where dV and V_0 denote the total volume change of the cavity and the original cavity volume.

In the natural form, the $P-\varepsilon_v$ curve can be treated similarly to the $P-\varepsilon_c$ curves. In addition, the $P-\varepsilon_v$ curves can be used to derive the unload-reload shear modulus, G_u . If one converts ε_v to the logarithmic form, the $P-\ln(\varepsilon_v)$ curves can provide the gradient for the interpretation of the undrained shear strength, S_u , in cohesive materials (Mair and Wood 1987). The $P-\ln(\varepsilon_v)$ curve can also be applied to better estimate the limit pressure. AlZubaidi (2015) applied the $\ln(\varepsilon_v)-V$ graph and the $P-\ln(\varepsilon_v)$ graph to decide the initial state of cavity expansion and the in-situ horizontal stress at rest, σ_{h0} .

2.2.9.5. Conversions between ε_c and ε_v

It should be noted that both ε_c and ε_v have specific implementations for the parameter interpretations. The ε_c and ε_v are converted, assuming the pressuremeter test is performed as axisymmetric cylindrical cavity expansion. Based on this assumption, the conversion was developed by Palmer (1971) as

$$y_1 = \left(1 - \frac{\Delta V}{V_0}\right)^{-\frac{1}{2}} - 1, \quad \text{Eq.2.5}$$

where y_1 is the relative radial displacement of the cavity with regard to the initial cavity radius, r_0 , which can be further expressed as the cavity strain:

$$y_1 = \frac{r}{r_0} - 1 = \frac{\Delta r}{r_0} = \varepsilon_c \quad \text{Eq.2.6}$$

Mair and Wood (1987) state that the gradient of the P - ε_v curve is twice the gradient of the P - ε_c curve. Consequently, the conversion can be simplified as follows:

$$\varepsilon_v = 2\varepsilon_c \quad \text{Eq.2.7}$$

2.2.10. Result Analysis

2.2.10.1. Graphical based method

The results from PMT are plotted as a set of stress-strain readings (Briaud, 1989; Mair and Wood, 1987). Analytical functions are then made to approximate the graph of stress-strain readings to interpret the geometric parameters of the test cavity. These approximated functions are called closed-form equations or the closed-form solutions. In the closed-form solutions, by verifying the parameters to obtain the best-fitted curve, the anticipations of material parameters can be achieved. The early curve-fitting is found in research by Gibson (1961), of which the closed-form equation was established by assuming the PMT to be performed in linear-elastic-perfectly-plastic materials. Based on the curve-fitting, several parameters such as undrained shear strength and shear modulus can be interpreted from the PMT results. However, the early curve-fitting method was not suitable for non-linear-elastoplastic materials. This limitation was solved by the application of hyperbolic equation on the curve-fitting for the non-linear stress-strain behaviour of cohesive soil (Kondner et al. 1963). The hyperbolic curve-fitting method was further modified by adding empirical parameters for the adjustments of stress-strain curves regarding different initial PMT states (Arnold 1981). Despite the improvements of closed-form equation, the parametric verified from the curve-fitting technique was found to have a large range of error (Eldridge 1980). Therefore, the curve-fitting technique was initially not recommended for the pressuremeter testing (Briaud et al.

1985). Development has been continuously made on the curve-fitting technique for more reliable parameter interpretations. A significant development on the curve-fitting technique is the involvement of computer-calculation in curve-fitting to allow researchers to reduce the time of iterative calculations. One example of curve-fitting involves computerized calculation is the Computer-Aided Modelling (CAM) established by Jefferies (1988) who extensively analysed factors of the level of in-situ horizontal stress, the differences between initial shear modulus and unload-reload shear modulus and the anisotropy of undrained shear strength to improve the accuracy of the curve-fitting method developed by Gibson (1961). Cunha and Campanella (1998) found that with big data, this CAM method had a closest fitted curve at the parametric matching range between 5-10%. Another example of curve-fitting involves computerised calculation is the Semi-Analytical Method (SAM) developed by Anandarajah and Agarwal (1991). The SAM can interpret parameters from the non-linear-elastoplastic materials using Cam-clay model to obtain reliable material parameters from PMT results.

2.2.10.2. Numerical based method

In contrast to the graphical based method which focuses on parametric verification by matching the stress-strain graph from the PMT results with closed-form equations, the Finite Element Method (FEM) can be used in PMT analysis to take into account both geometry/boundary condition complexities and constitutive behaviour. For geometry/boundary condition complexities, an example of FEM for PMT analysis demonstrated by Randolph (1981) proved that the PMT problem can be studied by axisymmetric cylindrical cavity expansion FEM model. Based on the axisymmetric FEM model, Anandarajah and Agarwal (1991) changed the vertical surcharge condition and observed the FEM calculations to describe the in-situ vertical stress impacts on PMT results. The impacts of in-situ vertical stress were further studied by Monnet (2007, 2008, and 2012) who considered the ratio between in-situ horizontal stress and vertical stress, K_0 . Houlsby and Carter (1993) varied the slenderness ratio in the axisymmetric FEM to describe the correlations between slenderness ratio and interpreted parameters from PMT. Despite the axisymmetric cylindrical cavity expansion FEM, the three-dimensional FEM was also used in PMT analysis. Three-dimensional analysis can be very useful especially for the simulation of PMT test in rock mass. This to the fact that rock has generally anisotropic parameters such as Young's modulus, shear modulus,

tensile and compressive strengths. As an example, the three-dimensional FEM on rock PMT demonstrated by Sharo (2009) suggested that anisotropy of Young's modulus of rock can significantly affect the results PMT. To study the effect of constitutive model analysis of PMT, Vaziri and Wang (1993) assigned Mohr-Coulomb model parameter in axisymmetric FEM and found the calculation results matched the in-situ PMT on cohesive materials without strain-softening or strain-hardening behaviours. For cohesive materials with strain-softening and strain-hardening material, the FEM with assigned Cam-clay model was found to be applicable in the PMT analysis (Anandarajah and Agarwal 1991).

2.3. Parameter Interpretations

2.3.1. Interpretation for Sandy (Granular) Materials

2.3.1.1. General Characteristics

A typical stress-strain relationship of the pressuremeter test in the granular material was demonstrated by Mair and Wood (1987). Generally, the stress path of the sand pressuremeter test follows typical drained cavity expansion, which has three characteristics based on the material's properties.

First, in the small strain level, the sand cavity develops a non-linear stress-strain curve. The initial state of the pressuremeter stress-strain curve, especially from the MPM type of pressuremeter test, is highly subjective to disturbance to the cavity.

Second, in the large strain level, plasticity (failure) is due to the particle displacement due to frictional behaviour. Therefore, the undrained shear strength that can be interpreted from the cohesive material, S_u , cannot be derived from sand pressuremeter tests. Nevertheless, the pressuremeter test in sandy material can usually derive the material's internal friction angle, ϕ , instead.

2.3.1.2. Stress-strain relationship

Palmer (1971) first suggests using the pressuremeter interpretation for non-linear-elastic materials. Using the integration method, the stress-strain relationship is written as

$$p = \int_0^{y_1} \frac{1}{(1+x)^3} \left[1 - \frac{1}{(1+x)^2} \right]^{-1} \Phi(x) dx + \sigma_{h0} \quad , \quad \text{Eq.2.8}$$

where x is the integration variable form of r and can be expressed as

$$x = -1 + \left[1 - \frac{y_1(2+y_1)}{r^2} \right]^{-\frac{1}{2}}, \quad \text{Eq.2.9}$$

where y_1 , as mentioned, is the relative radial displacement of the cavity with regard to the initial cavity radius, r_0 and can be expressed as follows:

$$y_1 = \frac{r}{r_0} - 1 = \frac{\Delta r}{r_0} = \varepsilon_c \quad \text{Eq.2.10}$$

The function $\Phi(y_1)$ is the stress difference, which can be expressed as follows:

$$\Phi(y_1) = 2 \frac{dp}{d[\log(dV/V)]} \quad \text{Eq.2.11}$$

The alternative solution developed by Arnold (1981) applies the hyperbolic equation based on Kondner (1963). The stress-strain relationship in a non-linear elastic pressuremeter test (corrected) data in soft clay can be expressed as

$$\sigma_r = \sigma_{h0} + \frac{\varepsilon_r}{a+b\varepsilon_r}, \quad \text{Eq.2.12}$$

where σ_r is the radial stress applied on the soil cavity, σ_{h0} is the in-situ horizontal stress at rest, and ε_r is the radial strain. In this case, a and b are the parameters to fit the curve.

2.3.1.3. Friction and Dilation Angle

The friction angle is an essential shear strength parameter of the granular soil. In the conventional assumption of pressuremeter testing, the cavity expansion is performed in the infinite-length cylindrical cavity of a homogeneous medium, which can be simplified to the axisymmetric cavity expansion assumption. The two principal stresses are radial stress, σ_r , and circumferential stress (or so-called hoop stress), σ_θ . Shear stress, τ , takes the form of deviatoric stress and can be expressed as follows:

$$\tau = \frac{\sigma_r - \sigma_\theta}{2} \quad \text{Eq.2.13}$$

The Mohr-Coulomb failure criterion dictates that when shear occurs (material yields), the friction angle represents the gradient between the mean principal stress and the shear stress. In a small strain, the yield function can be writing as follows (Hughes et al. 1977):

$$\frac{\sigma_\theta}{\sigma_r} = \frac{1 - \sin\phi}{1 + \sin\phi} \quad \text{Eq.2.14}$$

Dilation indicates when there is positive volumetric strain during the material's shearing. This normally occurs in strain-hardening materials (e.g. dense sand). The gradient of the difference between a volumetric strain and shear strain is reflected by the dilation angle, ψ . Rowe (1962) defines the relationship between the dilation angle and friction angle as follows:

$$\psi = 2 \tan^{-1} \left[\frac{\tan(45^\circ + \frac{\phi}{2})}{\tan(45^\circ + \frac{\phi_{CV}}{2})} \right] - 90^\circ \quad \text{Eq.2.15}$$

Interpretations

Fiction angle interpretation can be achieved through the graphical interpretation of 'logarithm scale of pressure-strain curve', originally suggested by Hughes et al. (1977). Mair and Wood (1987) demonstrate the interpretation of the friction angle from the stress-strain curve. The initial state of the test is firstly determined in the corrected stress-strain curve. The data from beforehand is excluded from the analysis. Then, the graph is converted to the form of $\ln(P) - \ln(\epsilon_c)$. In this way, the graph becomes linear in the large strain level, which consequently provides the slope, S , indicating the friction angle. The expression illustrated by Hughes et al. (1977) is written as follows:

$$\sin \phi = S / [1 + (S - 1) \sin \phi_{CV}] \quad \text{Eq.2.16}$$

The parameter ϕ_{CV} is the constant volume friction angle, which can be estimated through laboratory direct shear testing.

The dilation angle can also be found with the slope from the $\ln(P)$ - $\ln(\varepsilon_c)$ curve. The expression is written as follows:

$$\sin\psi = S + (S - 1)\sin\phi_{CV} \quad \text{Eq.2.17}$$

It is essential to choose the right slope, S , to perform accurate interpretations of the friction and dilation angles. The slope is highly dependent on the determination of the initial state (or so-called the reference state) of the test. Considering the disturbance from the general types of pressuremeter tests, Mair and Wood (1987) recommend the trial and error method to determine the ideal initial state of the test.

In addition, after the slope is determined, the value of the friction and dilation angles are often overestimated. The correlation for a PMT probe with a slenderness ratio of six was developed by Yu (1994) with the following equation:

$$\frac{S_{d\infty}}{S_{d6}} = 1.19 - 0.058 \ln \frac{G}{p_0} \quad \text{Eq.2.18}$$

Based on the slenderness ratio, further correction of the slope, $S_{correct}$, was developed by (Ajalloeian and Yu 1998) as

$$\frac{S_{corrected}}{S} = 1 - \frac{D}{L}, \quad \text{Eq.2.19}$$

where D is the diameter of the PMT probe before expansion, and L is the length of the expansion portion of the PMT probe.

2.3.1.4. In-situ Horizontal Stress

The in-situ environment generates stresses within the soil in both vertical and horizontal directions. For normally-consolidated ground material, the in-situ vertical stress, σ_{v0} , can be obtained by summing the unit weight of the overburden material on top of the measured depth. However, it is more complicated to measure the horizontal stress, σ_{h0} . Knowing the horizontal pressure at any in-situ testing spot can help one obtain the parameter called ‘coefficient of in-situ stress at rest, K_0 ’. The value is defined as $K_0 = \frac{\sigma_{h0}}{\sigma_{v0}}$ (Jefferies 1988).

Interpretation

The pressuremeter test is capable of estimating the in-situ horizontal stress at rest based on the ‘lift-off’ pressure. The ‘lift-off’ pressure is defined as the cavity pressure at the initial (elastic) state of the cavity expansion during the test, which is also called the reference state. Since the in-situ horizontal stress is isotropic, the ‘lift-off’ pressure, p_0 , represents the in-situ horizontal stress at rest, $p_0 = \sigma_{h0}$.

The difficulties of observation of the reference state are dependent on the test type and the installation quality. Mair and Wood (1987) compare different test techniques for observing the p_0 . The MPM tends to create an oversized cavity. As a result, the determination of the reference state requires engineering judgements. The PIP tests, on the other hand, can either generate extra initial pressure that is greater than the ‘lift-off’ pressure or initiate plasticity around the cavity wall, which lowers the estimated p_0 . By comparison, the SBP technique is typically recommended for the estimation of p_0 .

However, even for the best-selected testing, the evaluation of p_0 is highly sensitive to the test condition and pore water pressure in achieving the ideal estimation. Mair and Wood (1987) suggest the ‘iteration method’, which performs interpretations for other soil parameters using different estimated p_0 values, and determines the most reasonable result.

2.3.1.5. Unload-reload Stiffness

Generally, the elastic behaviour of the soil in one dimension is directly reflected by Young’s Stiffness, E . In pressuremeter testing, based on the axisymmetric cavity expansion assumption, the cavity expansion develops two principal components, σ_r and σ_θ , and their associated axial strain, ε_r and ε_θ . The resultant tangential shear stress and shear strain can be more easily demonstrated through the total stress-strain graph than the single stress-strain component. As a result, the elasticity property estimated by the pressuremeter test is the shear modulus, G . The conversion between G and E of homogeneous material in plane strain condition can be written as

$$E = 2G(1 + \nu) , \quad \text{Eq.2.20}$$

where ν is the Poisson’s ratio of the material.

The elastic response of the soil starts immediately after the initiation of cavity expansion. It is widely observed that the shear modulus from the first loading phase is far less than the laboratory test result. This can be either due to the softening or plasticity that occurs around the cavity wall. Since the initial disturbance and plasticity are not reversible, the unload-reload cycle described in Section 2.2.8.5 typically correlates with the material elasticity (Schnaid et al. 2000). As a result, the much satisfactory elastic parameter can be indicated by the unload-reload shear modulus, G_{ur} . Attention needs to be paid to the stress-dependency of the stiffness, which means the value of G_{ur} is in accordance with the stress level of the unload-reload cycle.

Interpretations

After the test, based on Timoshenko (1940) and the graph conversion in Section 2.2.9, the shear modulus in the unload-reload cycle can be expressed as follows:

$$G_{ur} = \frac{1}{2} \frac{dP}{d\varepsilon_c} \quad \text{Eq.2.21}$$

Or

$$G_{ur} = \frac{dP}{d\varepsilon_v} \quad \text{Eq.2.22}$$

The equation means that the unload-reload stiffness can be obtained if one finds the gradient of the P - ε_v curve, or half of the gradient of the P - ε_c curve. However, the stress path in the unload-reload cycle is a ‘hoop’ instead of a straight line. A secant line is drawn in between the two intersections of unloading and reloading curves to determine the gradient,. The slope of the secant line can directly reflect the shear modulus.

2.3.2. Interpretation for Cohesive Materials and Soft rock

2.3.2.1. General Characteristics

The pressuremeter test in clay can be regarded as an undrained test as it does not give enough time for the drainage of excess pore water pressure. The stress path developed during the test has typical phases of elasticity, elasto-plasticity and perfect-

plasticity (Wroth and Hughes 1972). As a result, the undrained shear strength, S_u , presented by the cohesion of the material, is observable at the yield pressure of the test (Windle and Wroth 1977). Being an undrained test also means that the pressuremeter test in cohesive materials and soft rock has unchanged overall volume around the small-medium around the cavity (Clarke and Gambin 1998). As a result, the dilation behaviour is not observable in clay and soft rock pressuremeter testing. The conventional stress-strain analysis of pressuremeter test merely considers the compressive strain. Therefore, the tension interference, which can occur in soft rock, is not studied in the pressuremeter tests (Ladanyi 1967; Haberfield 1997).

Overall, the observed parameters from pressuremeter testing in cohesive material and soft rock are the undrained shear strength, S_u , the (undrained) shear modulus, G , the in-situ horizontal stress at rest, σ_{h0} , and the limit pressure, p_l . The main difficulties associated with the clay pressuremeter test were due to the low permeability of the material. The time-dependent dissipation of pore-pressure, U , has a significant effect on the test result (Jang et al. 2003) as well. For example, Campanella et al. (1990) and Prapaharan et al. (1990) discovered a disturbance in the SBP results on clay due to the fluid circulation in the installation procedure. Therefore, the MPM test is preferred for clay pressuremeter testing.

2.3.2.2. Stress-strain Relationship

Linear Elastic

Since the stress path of the pressuremeter test in cohesive material has the elasto-plastic transition. The development of a stress-strain relationship should start with elastic expansion. Shuttle and Jefferies (1996) express the stress-strain relationship during the elastic expansion as follows:

$$p = \sigma_{h0} + 2G \frac{\Delta V}{V} \quad \text{Eq.2.23}$$

Elasto-plastic

The common assumption for perfectly plastic clay is that it does not take any more stress (hardening) after failure. Based on this assumption, the material follows the Mohr-Coulomb failure criteria. Another failure model that is commonly used is the Drucker-Prager model. However, Durban and Papanastasiou (1997) have compared the

numerical solutions based on Mohr-Coulomb and Drucker-Prager criteria and found the results are very close. Based on the Mohr-Coulomb criteria, Windle and Wroth (1977) introduced the plasticity phase into the stress-strain relationship; the stress path is written as follows;

$$P = P_l + S_U \ln \left\{ \frac{\Delta V}{V} - \left(1 - \frac{\Delta V}{V} \right) \frac{\sigma_{ho}}{G} \right\} \quad \text{Eq.2.24}$$

The required parameters for defining the function are the in-situ horizontal stress at rest, the limit pressure, the undrained shear strength and the shear modulus. A simplified expression regardless of the limit pressure was demonstrated by Gibson (1961) and applied by Jefferies (1988) and Houlsby and Carter (1993) as

$$P = \sigma_{ho} + S_U \left\{ 1 + \ln \left(2 \frac{G}{S_U} \frac{\Delta V}{V} \right) \right\}, \quad \text{Eq.2.25}$$

where $\frac{G}{S_U}$ is the rigidity index defined by Whittle (1999). Vaziri and Wang (1993) defined the range of the plastic zone by comparing the close-form solutions, using Mohr-Coulomb criteria with the one-dimensional axisymmetric finite element modelling.

2.3.2.3. Undrained Shear Strength

The undrained shear strength, S_U , is the parameter that represents the material's undrained yielding and plasticity for a cohesive soil. Under the plane-strain assumption, shear stress develops along with the increase of the two principal stresses, σ_r and σ_θ . At the yield point, the peak shear stress denotes the undrained shear strength, which can be expressed as (Sharo 2009)

$$S_U = \frac{\sigma_{rp} - \sigma_{\theta p}}{2}, \quad \text{Eq.2.26}$$

where σ_{rp} and $\sigma_{\theta p}$ are the peak radial stress and circumferential (hoop) stress, respectively. Campanella et al. (1990) interpreted undrained shear strength by

considering the impact of shear strength and limit pressure, introducing the rigidity index, $N_p = f\left(\frac{G}{S_u}\right) = f(I_r)$. Undrained shear strength can be expressed as follows:

$$S_U = \frac{(P_l - P_{h0})}{N_p} \quad \text{Eq.2.27}$$

When the undrained shear strength is put into the total cavity pressure expression, plastic behaviour is found when the cavity pressure passes the yield pressure, p_y . The expression of p_y was suggested by (Marsland and Randolph 1977) as follows:

$$p_y = \sigma_{h0} + S_u \quad \text{Eq.2.28}$$

Then, the cavity pressure increases from the yield pressure to the limit pressure, assuming the shear strain is half of the cavity strain. The undrained shear strength involved at this stage can be expressed with the equation demonstrated by Windle and Wroth (1977) and Mair and Wood (1987) as follows:

$$p = p_l + S_u \ln(\varepsilon_v) \quad (p_y \leq p \leq p_l) \quad \text{Eq.2.29}$$

Based on the equation, it should be noted that undrained shear strength has a relationship with the slope of cavity pressure against the volumetric strain. Mair and Wood (1987) suggest that the peak slope indicates the derived undrained strength during cavity expansion.

Interpretation

Based on Equation 2.29, it can be seen that the undrained shear strength has a correlation with the ratio between the pressure and the natural logarithm scale of the volumetric strain. To derive undrained shear strength from the stress-strain curve, the first step is to obtain the $p-\varepsilon_v$ curve and convert it to the format of $p-\ln(\varepsilon_v)$. The next step is to choose the initial (reference) state of the volumetric strain that represents the initiation of cavity expansion. The third step is to take the tangential slope in each reading, which represents shear stress, as Figure 2.8 shows.

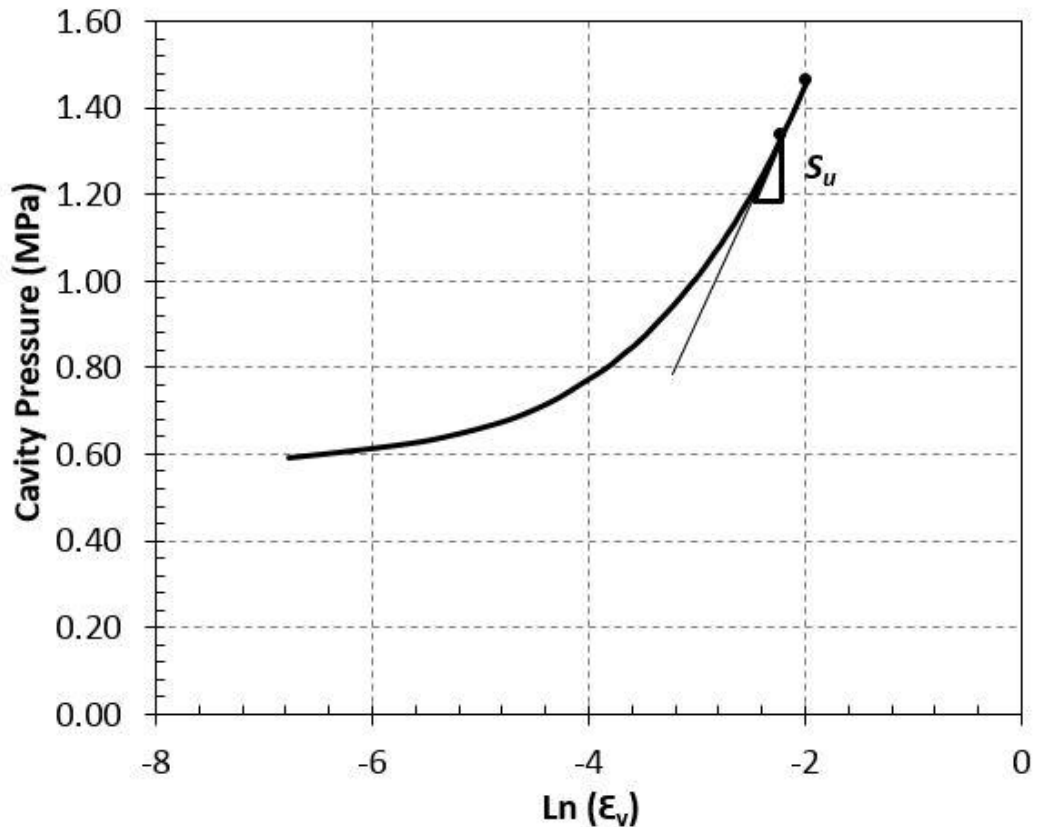


Fig.2.8. Interpretation of the undrained shear strength based on the pressuremeter curves

2.3.2.4. In-situ Horizontal Stress

The theory and methodology of interpreting the in-situ horizontal stress for clay and soft rock based on pressuremeter test results are generally identical to those in granular materials (discussed in Section 2.2.1.4).

One of the differences is that the MPM test is applicable to measuring the in-situ horizontal stress in clay and soft rock pressuremeter testing. In this case, the ‘lift-off’ pressure is denoted by the start point of the linear portion of the stress-strain graph. The graph before the linear portion denotes that the membrane is gradually getting in touch with the cavity side-wall due to the over-sizing installation of the MPM.

The other difference is that due to the pore-pressure increase during installation, cavity expansion should not start immediately after installation. It is recommended that one relax the soil until the excess pore-pressure settles back to the groundwater level. For obtaining accurate effective horizontal stresses, a device measurement of pore-pressure is suggested in clay and soft rock pressuremeter testing.

2.3.2.5. Unload-reload Stiffness

The theory and methodology of performing the unload-reload cycle in obtaining the unload-reload shear modulus, G_{ur} , in pressuremeter testing for sandy materials (Section 2.3.2) is discussed. There are two key points that need to be paid attention to when one is obtaining the high-quality unload-reload shear modulus for clay and soft rock.

First, in terms of the starting point of the unload-reload cycle, for materials that present linear-elasto-perfectly-plastic behaviour, Mair and Wood (1987) suggest that the cycle should not start in the vicinity of the yield pressure, p_y . Additionally, Briaud (1989) applies the unload-reload cycle at the end of the elastic expansion.

Second, in terms of the pressure range of the unload-reload cycle, the range suggested by Wroth (1982) and Mair and Wood (1987) is within two times the undrained shear strength. The minimum range was found by Briaud (1989) as half the magnitude of the undrained shear strength.

Unlike the stress-dependency of elasticity for granular materials, the unload-reload stiffness for the cohesive material is strain-dependent Wood (1990). As a result, care needs to be taken when observing the strain level in which the unload-reload cycle is initiated.

2.3.2.6. Limit Pressure

The limit pressure, p_l , indicates that all material in the test medium cannot take a further load (in compressive and shear ways). Theoretically, the limit pressure for the pressuremeter test is the pressure in accordance with 100% volumetric strain, ε_v , which is not practical in actual testing. Briaud et al. (1985) apply the functions to derive the limit pressures in both cylindrical and spherical cavity expansions, which can be written as follows:

$$P_l = P_{h0} + S_u \left(1 + \ln \frac{G}{S_u} \right) \quad (\text{cylindrical}) \quad \text{Eq.2.30}$$

and

$$P_l = P_{h0} + \frac{4}{3} S_u \left(1 + \ln \frac{G}{S_u} \right) \quad (\text{spherical}) \quad \text{Eq.2.31}$$

Mair and Wood (1987) simplified the cylindrical expression, replacing volumetric strain with the shear modulus and in-situ horizontal stress. The expression became:

$$p = p_l + S_u \ln(\varepsilon_v) \quad \text{Eq.2.32}$$

There are three major uses for estimating the limit pressure from pressuremeter testing. First, the bearing capacity for foundation engineering takes into account the limit pressure (Baguelin 1978). Second, for strain-hardening materials, the limit pressure helps the operator to determine the end of probe expansion in the test design. Third, the limit pressure is often used as the benchmark to back analysis other parameters (Yu 1994); Monnet (2008).

Interpretation

Generally, there are three ways to derive the limit pressure.

For the scenario in which σ_{h0} , G and S_u are obtained, Equation 2.31 can be used to directly derive the limit pressure.

For the scenario in which the ‘pressuremeter constant’, $N_p = 1 + \ln\left(\frac{G}{S_u}\right)$ is given, similar to the previous scenario, the limit pressure can be calculated using the following equation:

$$p_l = S_u N_p + \sigma_{h0} \quad \text{Eq.2.33}$$

For the scenario in which no associated parameters but the test result is present, the graphical method can be applied. The stress-strain curve is first converted to a p - $\ln(\varepsilon_v)$ curve. The curve is then extended to where ε_v is 100% ($\ln(\varepsilon_v)=0$). The corresponding pressure value can be regarded as the limit pressure.

2.3.2.7. Pressuremeter Test in Soft rock

Research on pressuremeter testing on soft rock (or organic soft rock) is very limited. The common analysis for soft rock pressuremeter testing assumes material behaviour is similar to cohesive material. However, actual soft rock failure behaviour may consist of both the shear-dominant ductile failure and the tension-dominant

fracture failure modes (Tolooiyan et al. 2014). Moreover, deformation stiffness, E , can vary in terms of compression and tension, and in different directions. Conventional analysis tends to neglect these features, which may lead to unreliable results.

A limited number of works on the rock-related pressuremeter studies solely address the issue of stiffness, especially in transverse pressuremeter tests (Isik et al. 2008; Sharo 2009). In terms of tensile interference, the impact on the stress-strain curve of pressuremeter tests was found by Ladanyi (1967) and Haberfield (1997). The existing solution is to introduce the tension cut-off parameter into the conventional failure model.

Describing cavity expansion in soft rock and organic soft rock also requires further works. Satapathy and Bless (1995) investigate the brittle failure in spherical cavity materials in the laboratory. The analysis assumes a homogeneous crack region around the cavity, which may not be similar in the cylindrical cavity expansion.

2.4. Pressuremeter Chamber Tests

2.4.1. Brief Introduction

The pressuremeter chamber test is performed in well-described material and boundary conditions. Therefore, the test can be used to study the theoretical or analytical interpretations (Juran and Mahmoodzadegan, 1989). Some research replaces field pressuremeter tests with the chamber test to derive soil parameters (Tan, 2005). The technique is also widely used in the analysis of other pressuremeter-related geometric problems (e.g. the slenderness ratio) that are not considered in theoretical or analytical studies (Schnaid 1990; Ajalloeian and Yu 1998).

2.4.2. Methodology

2.4.2.1. Test Preparation

In pressuremeter chamber tests, specimen preparation, cavity creation and probe installation are the necessary preparation steps prior to the application of boundary conditions. The sequence of preparation can vary in accordance with the type of chamber, test material and test technique. Juran and Mahmoodzadegan (1989) accommodated the specimen around the testing probe before the consolidation. Due to the high permeability of the material, the consolidation finished concurrently with the

application of boundary conditions. For low permeability materials, such as silt and clay, compaction is a pre-prerequisite (Tan 2005; Foriero and Ciza 2015).

2.4.2.2. Apply Boundary Condition

Generally, the pressuremeter chambers create boundary conditions by actively applying the confining pressures, which represent the in-situ stresses, onto the specimen. Different principles can be found in realising the confining pressures through various chamber designs:

Rigid side-wall: Fawaz, Boulon et al. (2002) use the air-rubber tubing on the top of the specimen to create the vertical boundary condition. The chamber sidewall is rigid. Therefore, the horizontal confining pressure is ‘passively’ provided by the confinement of the cylindrical side wall. The chamber is able to simulate the in-situ pressuremeter test in different depths by adjusting the vertical pressure. However, the horizontal stress cannot be changed independently.

Flexible side-wall: Juran and Mahmoodzadegan (1989), Bellotti et al. (1989), Schnaid (1990) and Ajalloeian and Yu (1998) use the flexible side confinement method to provide the independently adjustable horizontal confining pressure. For this method, a flexible membrane is placed between the rigid cavity side-wall and the specimen in the horizontal direction. Once the hydraulic fluid is injected into the membrane, the fluid pressure is distributed uniformly onto the specimen. The vertical confining pressure is provided by either a physical surcharge (Juran and Mahmoodzadegan 1989) or another hydraulic system (Schnaid 1990) so that the vertical and horizontal boundary condition can be regulated independently for simulating different coefficients of in-situ stresses, K_0 .

2.4.2.3. Test Execution, Data Acquisition and Analysis

The test and analysis procedure for pressuremeter chamber test is identical to the in-situ pressuremeter testing described in Section 2.2.8, Section 2.2.9 and Section 2.2.10. As probe installation is completed before the in-situ boundary condition is generated (Bellotti et al. 1989), the test scenario is close to the ideal SBP test, unless the specific type of pressuremeter test is studied (Schnaid 1990).

2.4.3. Limitation of Pressuremeter Chamber Test

The cylindrical design of the calibration chamber is dedicated for the independent adjustment of vertical and confining pressures. By creating horizontal pressure, the design solely allows for the provision of isotropic confining pressure, which matches the assumption of pressuremeter testing. In this condition, it is ascertained that the radial and circumferential stresses during the test develop uniformly in the specimen.

In most cases, the assumption of isotropic in-situ stresses matches the test scenario. However, likelihoods of anisotropic horizontal stresses can appear in complex test environments generated by open cut mining and other engineering activities. The impact of anisotropy in terms of horizontal boundary conditions cannot be studied in cylindrical chambers.

2.5. Tension Failure in IGMs

2.5.1. Background

As mentioned before, the tensile strength of soft rocks can influence the results of pressuremeter testing in these materials. Recent research has classified brown coal as an Intermediate Geotechnical Material (IGM) (Tolooiyan et al. 2014). The failure modes of IGMs include ductile failure and brittle failure. Undrained shear strength is usually greater than tensile strength. Depending on the loading scenario and the field condition, failure may occur once the tensile forces reach the tensile strength of the material.

Measuring the tensile strength in the laboratory can be achieved through the imposition of tensile stress, directly or indirectly, on a specimen through an applied load and the establishment of the stress required to cause tensile failure. The measured load limit, F , and the failure plane area, A , obtained from the test are used to calculate the tensile strength of the specimen with an equation of a general form, $\sigma_t = \alpha \frac{F}{A}$, where σ_t is tensile strength, and α is the test shape factor that converts the force into tensile force on the failure surface.

2.5.2. Conventional Tensile Strength Tests and Their Limitations

2.5.2.1. Direct Tensile Test (DTT)

General

The Direct Tension Test (DTT) is theoretically the simplest laboratory test for measuring tensile strength. It has been extensively used to investigate the tensile strength of unsaturated soils, over-consolidated clays, and cemented sands. Nevertheless, specimen preparation is not easy for these materials and the design of the test apparatus is a critical problem (Ajaz and Parry 1974; Lu et al. 2007; Tolooiyan et al. 2014; Vesga and Vallejo 2006). The specimen is typically a cylindrical or rectangular bar of the material. The bar is gripped at both ends, and the specimen is pulled apart at a known rate. Care with the grip and specimen design is essential to ensure uniform tensile stress across the specimen at the failure location.

Limitation

A difficulty associated with the DTT for IGMs is that the stress can be concentrated close to the grips and can lead to unpredictable and non-uniform failure plane locations. This makes it almost impossible to determine the test shape factor, α , required to calculate the tensile strength. Tolooiyan et al. (2014) adopted a notch around the midpoint of the specimen to force the specimen to fail on a predefined plane so that α is known. Although this technique produces measurable results, the nature of the result is unclear given the natural heterogeneity of IGMs. Under field conditions, tensile failure preferentially occurs on planes of weakness, but a predefined failure plane may not capture this tendency and can, therefore, lead to an overestimation of the effective tensile strength.

2.5.2.2. Brazilian Test (BT)

General

The Brazilian Test (BT), also called the indirect tensile test or the splitting tensile test, is an alternative to the tensile strength measurement technique. Cylindrical specimens with a diameter-to-thickness ratio of 2–2.5 are placed between two flat rigid loading plates that are parallel to the specimen's longitudinal axis. The plates compress the specimen at a specified rate. The compression loading is then converted into tensile stress on a diametric plane, perpendicular to the loading plates. For this test, the area, A , is equal to the thickness, t , multiplied by the diameter, D . The α factor has been determined to be $2(jk + 1)/\pi$, where k is the thickness-to-diameter ratio and j is an empirical factor (Yu et al. 2006). The tensile strength of the brittle material is normally

smaller than the compressive strength and, therefore, in the BT, tension fails the specimen.

Compared with the DTT, the BT is both easier in a practical sense and less expensive for specimen preparation. The validity of this test for rock materials has been debated (Colback 1966; Coviello et al. 2005; Hudson et al. 1972; Jaeger 1967; Jaeger and Hoskins 1966). Recent research confirms that a correction factor should be applied to BT results even for uniform materials (Tolooiyan et al. 2014; Yu et al. 2006).

Limitation

It is appropriate to observe here that comparisons of DTT and BT tests for different materials (Li and Wong 2013) lead to significant differences between the results of both tests types. In Table 2 of Li and Wong's paper (see Table 2.3), the BT results both underestimate and overestimate the results from the DTT for different materials, even though the correction factors identified by Tolooiyan et al. (2014) and Yu et al. (2006) suggest that the BT test for uniform materials should always underestimate true tensile strength. This difference may be due to the particular materials considered by Li and Wong (2013) or due to differences between the DTT results and the underlying true tensile strengths for these materials. Further studies would be needed to resolve this potential issue. However, it is important to note that the bias identified for the DTT also exists for the BT for fine-grained IGMs with oriented grain structures, as the failure plane is also predefined.

Table 2.3. Difference tensile strength measurements by BT and DTT (Li and Wong, 2013)

Rock type	Direct tensile strength (MPa)	Brazilian tensile strength (MPa)
Bowral trachyte	13.72	12.00
Gosford sandstone	3.59	3.72
Carrara marble	6.90	8.72
Barre granite	13.45	14.34

Indiana limestone	5.86	6.21
Sandstone	2.96 ± 0.51	7.80 ± 0.30
Vitosha syenite	20.50	21.05
Grey gypsum	1.75	1.99
White gypsum	1.42	1.29
Gravina calcarenite	0.69 ± 0.03	0.64 ± 0.10
Gasbeton	0.86 ± 0.08	0.54 ± 0.06
Ufalei marble	5.90 ± 2.66	6.90 ± 1.24
PP sandstone	6.49 ± 0.22	10.68 ± 0.70
SB marble	6.33 ± 0.62	8.02 ± 0.25
SB limestone	9.31 ± 0.65	10.90 ± 0.19

2.6. Conclusion and Discussion

2.6.1. Conclusion of the Chapter

The present chapter firstly reviews the historical background and the principles of executing the in-situ pressuremeter testing. The three major types of pressuremeter testing technique (MPM, SBP and PIP), including their construction and testing procedure is generally reviewed in Section 2.2.

The stress-strain correlation and the parametric interpretation methods regarding cohesionless and cohesive materials are covered in Section 2.3. For sandy (cohesionless) materials, the interpreted parameters are the friction and dilation angles, the in-situ horizontal stress and the stress-dependent unload-reload shear modulus. For cohesive material, the pressuremeter provides an evaluation of undrained shear strength, in-situ horizontal stress and the strain-dependent unload-reload shear modulus. The

chapter also addresses the limitation of research on pressuremeter testing in soft rock or organic soft rock, which the brown coal material belongs to.

Section 2.4 demonstrates the laboratory chamber study method for the pressuremeter testing.

Section 2.5 starts with the reason for considering tensile interference in brown coal pressuremeter tests research. Then it introduces the conventional methods (DTT and BT) to measure tensile strength and their limitations in obtaining reliable tensile strength from brown coal.

2.6.2. Research Gap

As discussed in Section 2.2, the procedures of equipment selection, test preparation, test execution and data processing of pressuremeter testing can differ in accordance with the test material. However, there has been no research focused on the pressuremeter testing in brown coal. The effects of in-situ stress conditions and the tensile behaviour of brown coal on the result of pressuremeter testing are needed to be studied.

The common laboratory pressuremeter chamber testing techniques cannot generate horizontal stress anisotropy, which can be common stress distribution scenario in open pit mining.

Two types of tensile strength testing (DTT and BT) are summarized in the chapter. These tests are found to have bias in measuring IGMs due to their predefined failure planes.

3. Laboratory Experiment: Design and Numerical Analysis

3.1. Introduction

This chapter presents the designs, calibrations and pre-test analysis of the main laboratory tests developed in the project. Introduced in Chapter 4, the laboratory tests include the anisotropic pressuremeter chamber test and the Unconfined Expansion Test (UET). These tests require the development of a miniature scale pressuremeter probe and an anisotropic pressuremeter chamber. Section 3.2 explains the design, characterisation and expansion mechanism of the probe. Section 3.3 overviews the development of the chamber. Which includes background, design, assembly, loading mechanism, calibration and ends with the analytical and numerical analysis of the internal stress of the chamber.

3.2. Miniature Scale Pressuremeter Probe

3.2.1. Apparatus Set-up

This section describes the external construction of the miniature pressuremeter probe. The probe was developed for the present research project for both the anisotropic pressuremeter chamber test and the unconfined expansion test. For the simplicity of design, the miniature pressuremeter probe is monocell as described in Chapter 2, which means there are no ‘guard cells’ on the edges of the probe. The expansion of the cylindrical membrane is measured by the volume transducer. The ratio between the length and diameter of the probe, also referred to as the ‘slenderness ratio’, is discussed in Section 3.2.2. For the anisotropic pressuremeter chamber test, minimising the expansion probe eliminates the effect of the finite boundaries of the chamber. For the unconfined expansion test, the miniature scale pressuremeter probe reduces the required size of the specimen.

The design of the pressuremeter probe comprises four major components. These are the Body, the Caps, the Nuts, and the Membrane. The Body of the pressuremeter probe is a stainless steel tube that supports other components and provides fluid channels for probe expansion. The total length of the tube is 102mm. From both sides of the tube, the diameter starts at 6mm and then gradually increases to 8mm cylindrically (see Figure 3.1). A 1mm-thick membrane (calibrated in Chapter 4) wraps tightly around the main body. This membrane is the expansion part, which examines the deformability of the specimen during tests. Two hollow metal caps with an internal

diameter of 6mm were placed at the two edges of the tube respectively. These caps are fixed by the nuts to provide fixity for the expansion membrane. Inside the caps, there are two rubber O-rings to seal the caps.

3.2.2. Slenderness Ratio

The slenderness ratio is the ratio between the length of the expanding portion (L) and the diameter of the probe (D), L/D . The variation of the slenderness ratio can affect the results of the chamber pressuremeter test and the unconfined expansion test. The idealised model applied to the interpretation of the pressuremeter test is based on the cylindrical cavity expansion of infinite depth by assuming the pressuremeter probe with $L/D=\infty$. In practice, however, due to the finite length of the commercial pressuremeter probe, the infinite cavity expansion model is replaced by a lantern shape expansion model, which combines cylindrical expansion (in the middle length) and spherical expansion (on both edges). As a result, the difference between the interpretations of the infinite and finite length cavity expansions needs to be studied.

Briaud and Audibert (1986) study the effect of the slenderness ratio by numerical simulation and recommended a slenderness ratio value of 6.5. For pressuremeter tests in sand, a slenderness of six was applied by Cunha (1994). The study using finite element modelling (FEM) had satisfactory results, showing that clay pressuremeter tests can be achieved with a slenderness ratio between 6 to 6.5 (Houlsby and Carter 1993). Further studies on the effects of the slenderness ratio on the parameter interpretations and their corrections were carried out by Ajalloeian and Yu (1998). Laboratory chamber tests allow researchers to simulate the pressuremeter test with slenderness ratios from five to ten (Fawaz et al 2002; Shaban 2016; Cosentino 2016; Schnaid 1990; Skandarajah 1992). In cases of high slenderness, the length of the probe is close to the total depth of the soil specimen in the chamber. Therefore, the pressuremeter test is more representative of the ideal, infinite length expansion scenario than the practical, finite length expansion scenario. For a better representation of the commercial pressuremeter test scenario, the present research project applies a slenderness ratio of 6.4. The expansion length of the probe is 64mm, as Figure 3.1 shows. The deflated probe has a total diameter of 10mm. With regard to the current design, the slenderness ratio's impact on the parameter interpretation is discussed in Section 4.1.

3.2.3. Expansion Mechanism

The internal structure of the pressuremeter probe provides enclosed fluid channels to achieve expansion. The inlet and outlet channels are opened from the top and bottom ends of the probe respectively (see Figure 3.2). Both channels are 3mm in diameter. The inlet channel is connected to the inlet hose. The calibration procedure for hose connection is described in Chapter 4. The outlet end of the channel is sealed by a screw during the test. This outlet channel is used to de-air the probe. The inlet and outlet channels have no direct connection, but each channel has two openings diametrically opposite to one another in the expansion portion of the Body. Therefore, as Figure 3.2 shows, the hydraulic fluid escapes from the internal Body through the inlet openings to saturate the membrane and then flush the air bubble out of the probe using the outlet openings. The distance between the two sets of openings from the inlet and outlet channels is 55.7mm. This distance allows better circulation of the water and allows for more uniform expansion of the probe. As a result, probe expansion can be regarded as cylindrical in terms of the strain level of all tests proposed in the present research project.

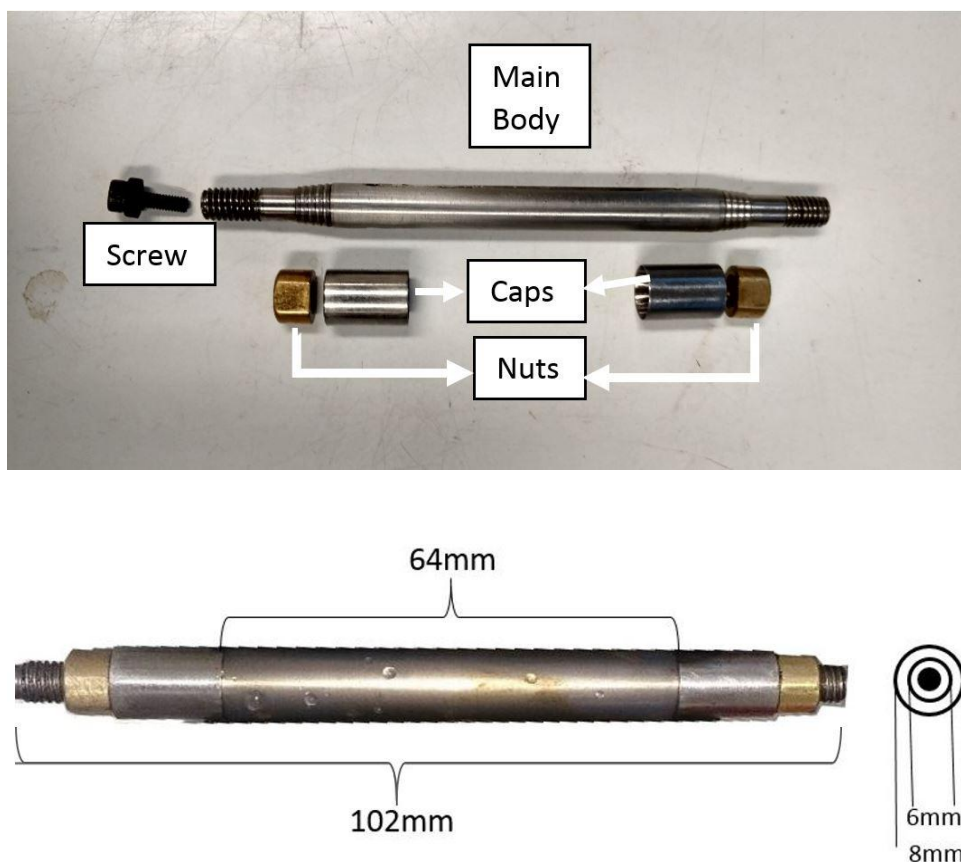


Fig.3.1. External view of the pressure probe

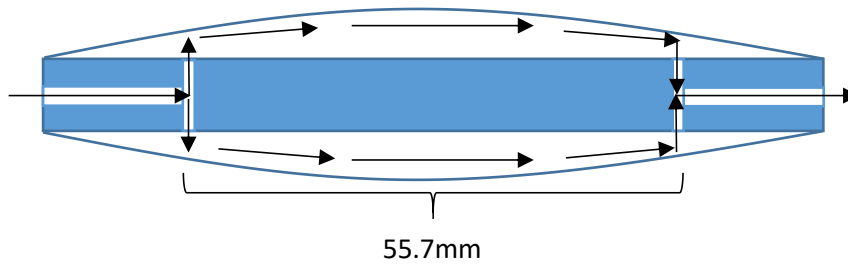


Fig.3.2. Internal construction and water flow of the pressure probe

3.3. Anisotropic Pressuremeter Chamber

3.3.1. Limitation of the Cylindrical Chamber

Previous research using conventional cylindrical pressuremeter chambers are reviewed in Section 2.4. In these cylindrical chambers, the in-situ horizontal stresses are generally simulated in two ways. The gravitational horizontal stresses (Read et al. 2009) are passively generated by the horizontal retaining pressure in response to the vertical surcharge. The non-gravitational horizontal stresses are actively generated by the hydraulic pressures around chamber. Due to the cylindrical axis-symmetry of the chamber, horizontal confining pressure needs to be isotropic around the specimen. Therefore, the cylindrical pressuremeter chamber study cannot simulate the circumstances of the pressuremeter test subjected to anisotropic horizontal stresses (Zhou et al. 2016). The assessment of the impact of in-situ stress anisotropy on the pressuremeter test's interpretations requires a new design of the pressuremeter chamber.

3.3.2. Anisotropic Horizontal Stresses Conversion

Anisotropic horizontal stresses are generated by tectonic stresses and a significant change in loading condition. Figure 3.3 shows the concept of stress conversion in pressuremeter tests in a plane strain condition. Vertical stress is commonly considered one of the principal directions of stress. The problem can be simplified in plan-view to purely discuss horizontal stresses. By using the simplified Euler-Cauchy stress principle in plan-view, horizontal stresses can be denoted based on the normal stress (σ), and the shear stress (τ) as σ_X , σ_Y , τ_{XY} , and τ_{YX} respectively. The principal XY-coordinate system is the system in which the shear stress components become zero ($\tau_{XY} = \tau_{YX} = 0$). The normal stress components σ_X and σ_Y in the in-plane principal coordinate system are the in-plane principal stresses. Based on the explanation, once the two in-plane principal

stresses are adjusted independently in the chamber, any isotropic/anisotropic in-situ horizontal stresses can be represented.

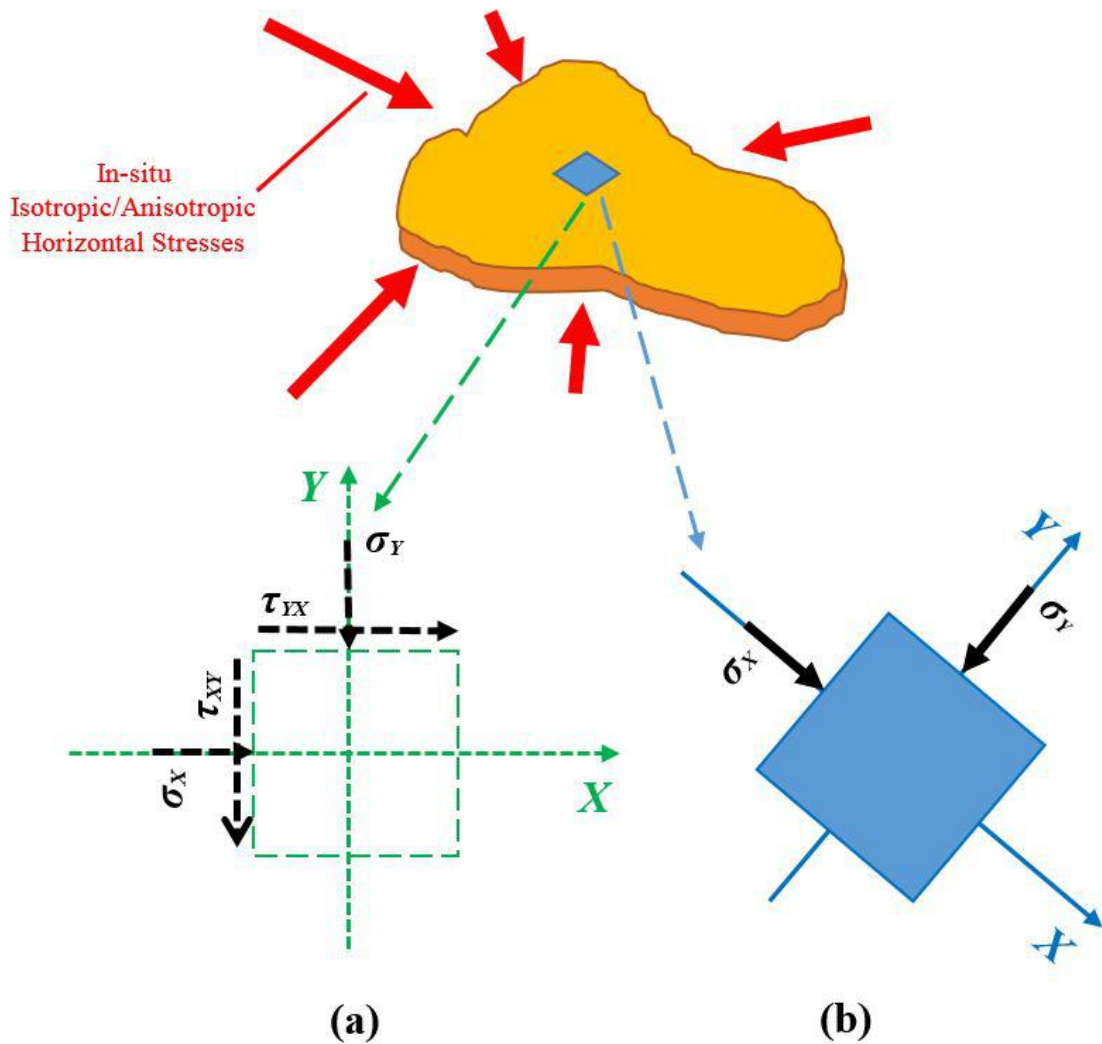


Fig.3.3. Two-dimensional stresses conversion of (a) random stresses coordinate system, and (b) principal stresses coordinate system.

3.3.3. Development of the Anisotropic Pressuremeter Chamber

It can be described, based on the stress conversion, that the in-plane principal stresses can be converted into in-situ horizontal stresses in any isotropic and anisotropic circumstance. Meanwhile, as mentioned, the out-of-plane principal stress (σ_z) is regarded as vertical stress (σ_v). Therefore, the author developed the anisotropic pressuremeter chamber using cubic geometry for the laboratory study. With cubic geometry, the new chamber is able to directly apply pressures to soil specimen in three orthogonal directions. The pressure applied vertically represents the vertical

(gravitational) surcharge conditions or test depth. Confining pressure applied on two orthogonal horizontal surfaces generate isotropic/anisotropic in-situ horizontal stress on the soil specimen in the form of in-plane principal stress.

The design of the cubic chamber needs the criteria for the pressuremeter chamber test:

- The pressures applied should be distributed uniformly and should be normal to the surface so that the applied pressures can be converted into normal stresses.
- Each surface pressure should be independently adjustable so that the chamber system can simulate different anisotropic confining conditions.

To meet the first criterion, the chamber comprises three flat compression sides that are orthogonal to one another. Each compression side is subjected to independent pneumatic pressures to confine the specimen. As a result, the compressive force is uniformly distributed by the plates. To meet the second criterion, the pneumatic pressures for the compression are consistently regulated by individual electronic air channels.

3.3.4. Advantages of the Anisotropic Pressuremeter Chamber

Compared with the conventional cylindrical chamber, the new design of the anisotropic pressuremeter chamber has the following advantages:

- Three air channels for confinement can independently generate/isolate confining pressures to satisfy the required test environment.
- The pneumatic system is much smaller than the conventional physical surcharge or hydraulic jack systems. This advantage makes the laboratory test more economical.
- In addition to the pressuremeter test study, the chamber can be further modified to satisfy different laboratory research topics, such as chamber studies for the cone penetration test and the miniature pile loading test.

3.3.5. Chamber-Probe Size Ratio

In contrast to the in-situ pressuremeter test, the boundary condition of the laboratory pressuremeter chamber test is limited by the finite geometry of the test chamber. Therefore, the test results' susceptibility to the boundary effect needs to be studied. The boundary effect is determined based on the ratio of the size of the chamber

to the size of the probe. For the cylindrical chamber, this ratio is defined by the ratio between the internal diameter of the chamber (D_c) and the external diameter of the expansion probe (D), (D_c/D). In the cubic chamber, designed for the present research project, the boundary effect is determined based on the ratio between the side length of the chamber (L_c) and the external diameter of the probe (D), (L_c/D).

Research on the ratio of L_c/D of 10 shows acceptable side boundary impact on the test results (Skandarajah 1992; Foriero et. al 2015). Further study on the variance of D_c/D (from 22 to 38) was done by Schnaid et. al (1991). All of these studies show that for loose and medium grain sand, once the ratio is adequate (more than 10), the boundary effect on the results of the chamber pressuremeter test is insignificant.

The present research project carries out a study on the size ratio of the cubic pressuremeter chamber through FEM. When the chamber is unloaded, the internal length of the cubic chamber, L_c , is designed as 300mm. As a result, the accommodated specimen in the chamber has a cross-section area of 300²mm² in plane. A probe with a diameter of 10mm, as described in Section 3.2, is installed in the middle of the specimen. With this setup, the size ratio for the cubic chamber pressuremeter test, L_c/D is 30. The test scenario is simulated through ABAQUS Finite Element Modelling (FEM). To generate the confining pressure on the specimen, the cavity of the cubic chamber is subjected to isotropic stresses in three principal directions, as illustrated in Section 3.3.1. The internal stress distribution on the specimen, especially the stress distribution around the cavity, is compared to the FEM simulation with a cylindrical chamber and an identical size ratio. As shown in Figure 3.4, the confining pressure distributed around the cylindrical and cubic chambers is identical. As a cylindrical chamber with $D_c/D=30$ is acceptable for the test material, the designed cubic chamber with a size ratio of 30 is considered to be acceptable.

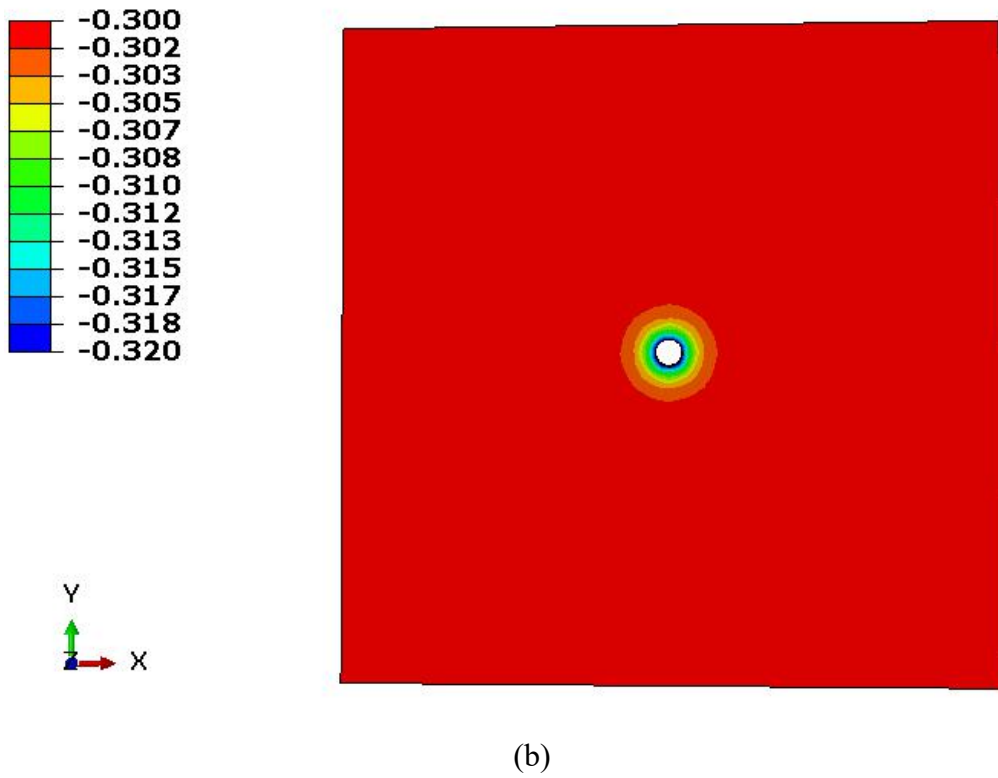
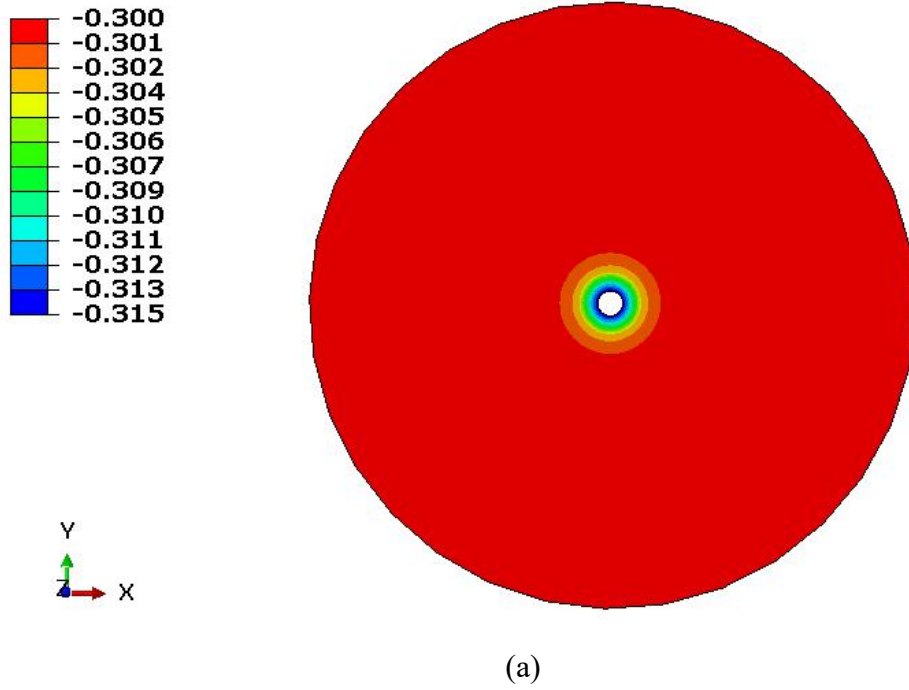


Fig.3.4. Confining pressure distributed by specimen
 (a) cylindrical chamber, (b) cubic chamber

3.3.6. Chamber Assembly

The section introduces the four major components in a cubic pressuremeter chamber. These components are (1) the air cushions, (2) the compression plates, (3) the chamber frame, (4) the transparent cap and (5) the top webbing.

3.3.6.1. Air Cushions

As mentioned in Section 3.3.3, there are three air cushions located between the chamber side-wall and the active compression plates. These air cushions are expandable according to the specific air pressure on their channel. Expansions of the air cushion are used to convert the pneumatic pressure into physical loading on the active compression plates to confine the specimen. The appearance of the air cushions is showed in Figure 3.5. These air cushions have a contact area of 320mm by 320mm. The thickness of the cushions is 25mm. At one of the four corners of each air cushion, there is a plug-in connector to connect the air hose. Each air cushion has a working pneumatic capacity of 800kPa. Compared with other physical loading chambers, such as the hydraulic jack pressuremeter chamber, the use of air cushions has an advantage in minimising the size of the chamber. Before the assembly, the three air cushions need to conduct a leakage check. As shown in Figure 3.6, a leakage check is conducted by inflating the air cushions submerged into the water. The appearance of an air bubble in the tank is a sign of air leakage.

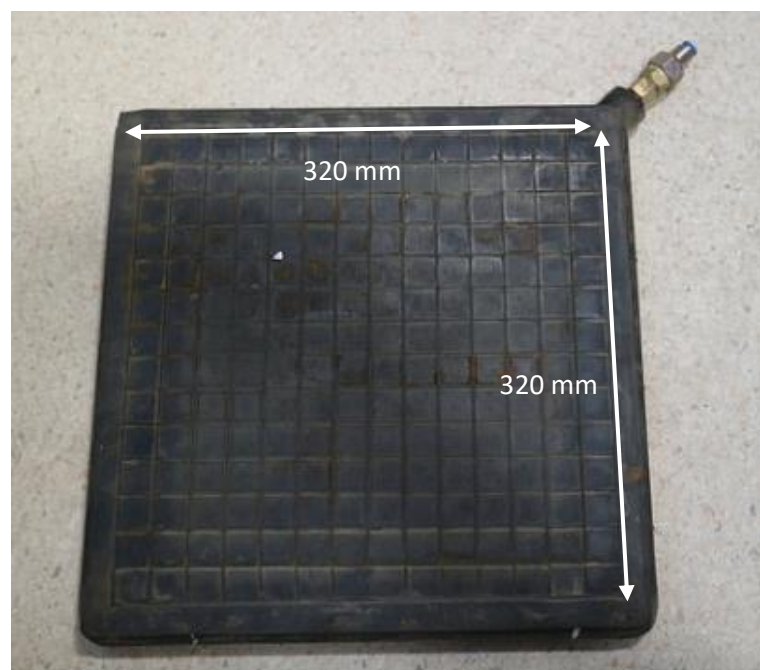


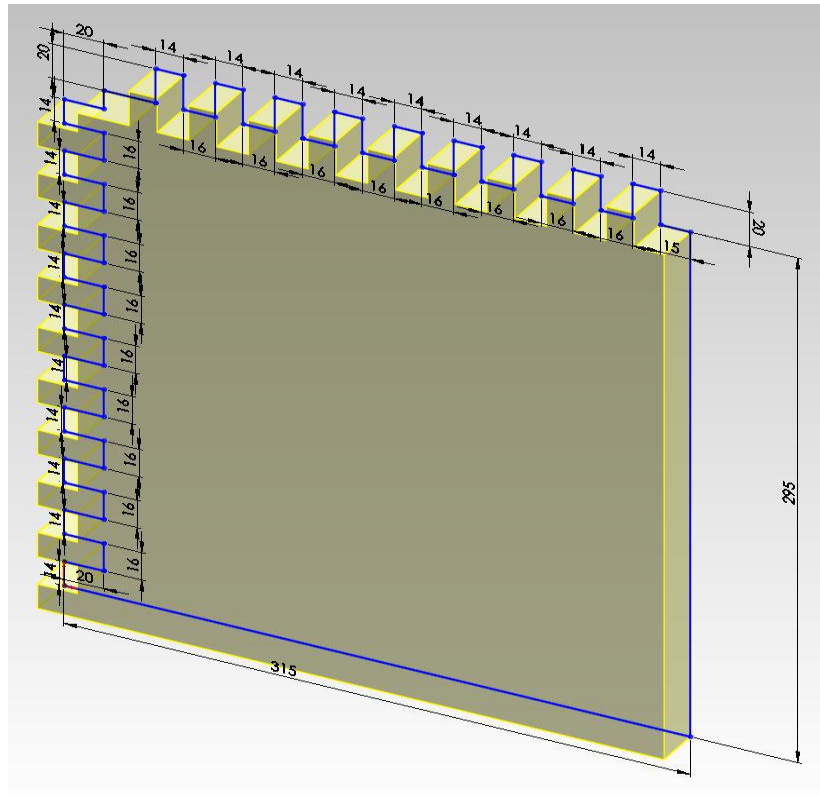
Fig.3.5. Air cushion in the anisotropic pressuremeter chamber



Fig.3.6. Leakage check for the three air cushions

3.3.6.2. Compression Plates

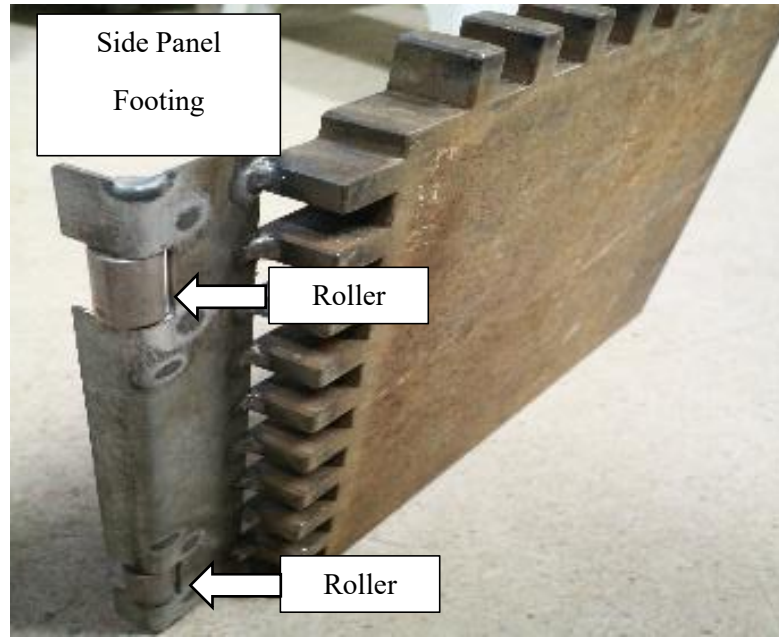
The compression plates are made of 25mm-thick steel plates. Each compression plate consists of a loading surface and structural slots. The two vertical-standing side compressions plates are also equipped with roller footings, as shown in Figure 3.7. The loading surface undertakes the conversion of pneumatic pressure from the air cushion behind the plate to physical confining loading by moving towards the specimen surface. The contact area between the loading surface and the specimen (excluding the slots) is about 300mm by 300mm. The structural slots are designed as two rows of 20mm-long and 14mm-wide slot-strips that lie perpendicularly along two fringes of the plates as shown in Figure 3.7. These structural slots interlock the plates against tangential sliding and tilting during the compression movements towards the specimen surface. The two compression plates that stand vertically are built for the generation of horizontal confining pressure. These plates are also equipped with 41mm-tall, 'L'-shaped roller footings for standing support. Each roller footing has two 31mm-wide rollers to reduce the friction between the footing and the bottom frame of the chamber.



(a)



(b)

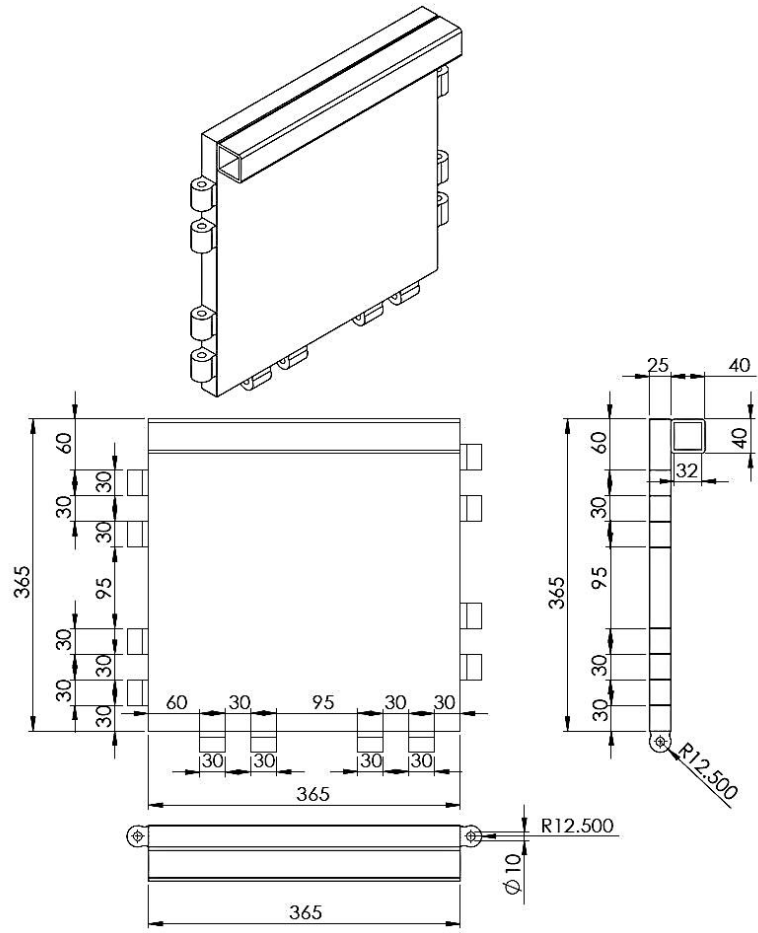


(c)

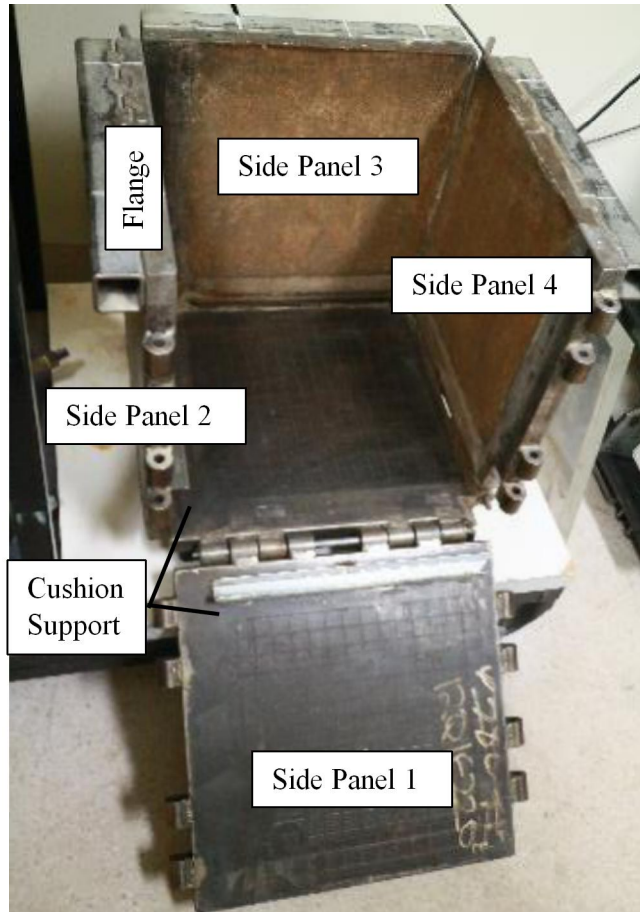
Fig.3.7. Illustration of the compression plates; (a) plate dimensions, (b) three compression plates overview, (c) roller footing for side plates

3.3.6.3. Chamber Frame

The chamber frame is the main structure of the anisotropic chamber, it is used to (1) accommodate specimen, air cushions and compression plates, (2) provide support for the top plate and top webbing, (3) provide confinement pressure on the passive boundaries of the specimen, and (4) allow external air hoses to connect with the air cushions. The chamber frame is constructed with five steel panels of 21mm thickness as Figure 3.8 shows. These panels are assembled by hinge joints with a diameter of 25 mm located on the fringes. There are four panels among them that are for the side panels. Their measurements are 365mm by 365mm. There is a 365mm-long rectangular hollow bar soldered on the top of each side panel. Each hollow bar has a 40mm×40mm cross-section. These hollow bars are the flanges for the installation of the transparent plate and the top webbing introduced later in this section. Of the four side panels, two of them are soldered with cushion supports. These cushion supports have inclined cuttings on their edges for the outlet of the air cushion hoses. The bottom panel is 365mm by 365mm, similar to the side panels. The bottom panel is equipped with four ground stands at the bottom, and the same inclined cutting from the two side panels.



(a)



(b)



(c)

Fig.3.8. Construction of the chamber frame; a) dimensions of the side panels, b) illustration of assembly, (c) after assembling the frame and air-cushions

3.3.6.4. Transparent Plate

The transparent plate is used to enclose the specimen from the top and observe the test procedure. Figure 3.9 shows the design of the transparent plate. The plate's measurements are 495mm by 495mm, with 25mm in thickness. An ovoid hole with a distance of 11mm minimum side-to-side is in the middle of the plate. The miniature pressuremeter probe is installed through the ovoid hole. It should be considered that the specimen is expected to move towards the passive corner due to isotropic/anisotropic pressurization inside the chamber. Therefore, the ovoid hole is offset from the centre towards the corner of the passive boundaries (see Figure 3.9). This offset provides slightly shifts the connection of the pressuremeter probe and the hydraulic hose during specimen deformation, so that cavity inclination is avoided.



Fig.3.9. Transparent plate and the ovoid hole

3.3.6.5. Top Webbing

The top webbing is used to reinforce the transparent cap. The webbing is shown in Figure 3.10. Around the mid-area of the frame is a 58mm-tall and 10mm-thick braze

tube with a diameter of 122mm to perform the vertical reinforcement for the testing area. The braze tube is offset from the central location to make it concentric with the ovoid hole of the transparent plate. The braze tube is connected with the 76mm-tall, 9mm-thick external flanging frame by four 9mm-thick auxiliary gussets. The external frame is strengthened by short gussets at its four corners. The flanging external frame has two handles for lifting and eight sockets (two on each side) for the U-clamp fixity.



Fig.3.10. Top webbing

3.3.6.6. Installation

The assembling of the chamber components is shown in Figure 3.11. The chamber frame is first assembled by getting eight 300mm-long rod-bolts through the aligned hinges on the side frames. The air cushions are then placed on the bottom and two sides of the frame. The hose connections on the cushions are placed on the inclined cuttings on the frame. The three active compression plates are then installed at the front of the cushion with slot structures interlocking with each other. After the specimen is filled into the chamber, the transparent plate is then placed on top. To prevent the escape of specimen particles and the damage of sand particles to the compressing plates,

the textile bag is applied to accommodate the specimen. When enclosing the transparent plate, the ovoid hole should be close to the two horizontal passive boundaries. Thereafter, the top webbing is installed on the transparent plate. During the installation, the braze tube should be concentric to the ovoid hole of the transparent plate. Finally, each side the flanges of the chamber frame, the transparent and the flanges of the top webbing are locked by two 25mm-thick U-clamps; hence a total number of eight U-clamps are used in the system. The sides of the transparent plate, the flanges of the top webbing and the chamber frame are aligned during locking. For the convenience of external air, water and electricity connections and test operations, the assembled chamber system is placed onto the mobile test platform as Figure 3.12 shows.

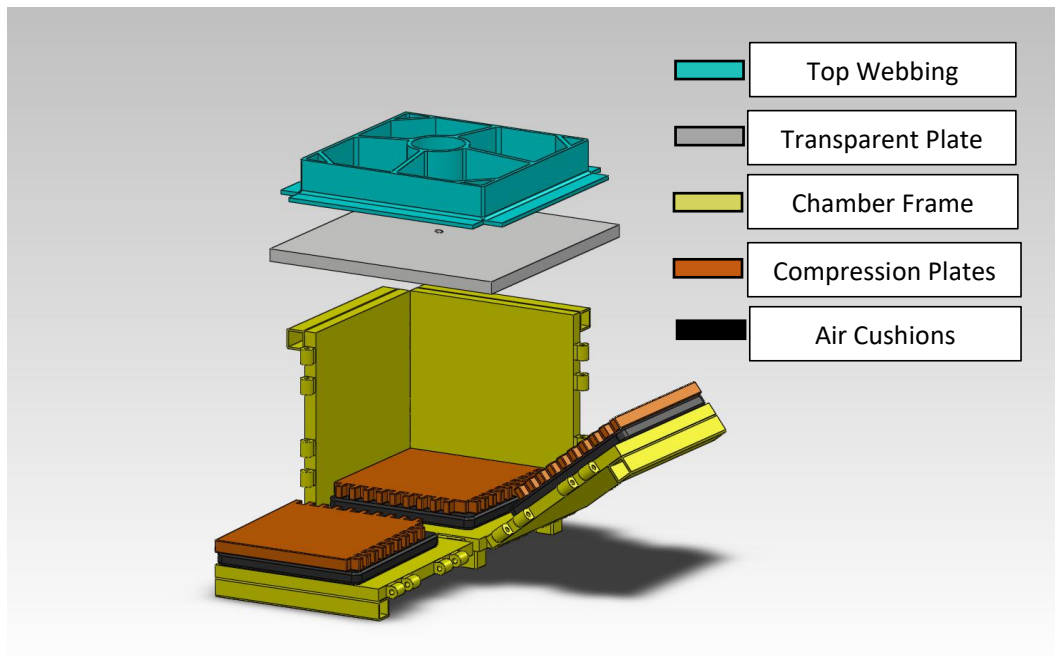


Fig.3.11. Assembling the anisotropic pressuremeter chamber

3.3.7. Loading Mechanism

External air pressure is separated to the three air cushions through the air pressure regulating system to generate expansions. These expanded air cushions push their attached compression plates to move horizontally or vertically, which cause horizontal and vertical confining pressures to act on the specimen.

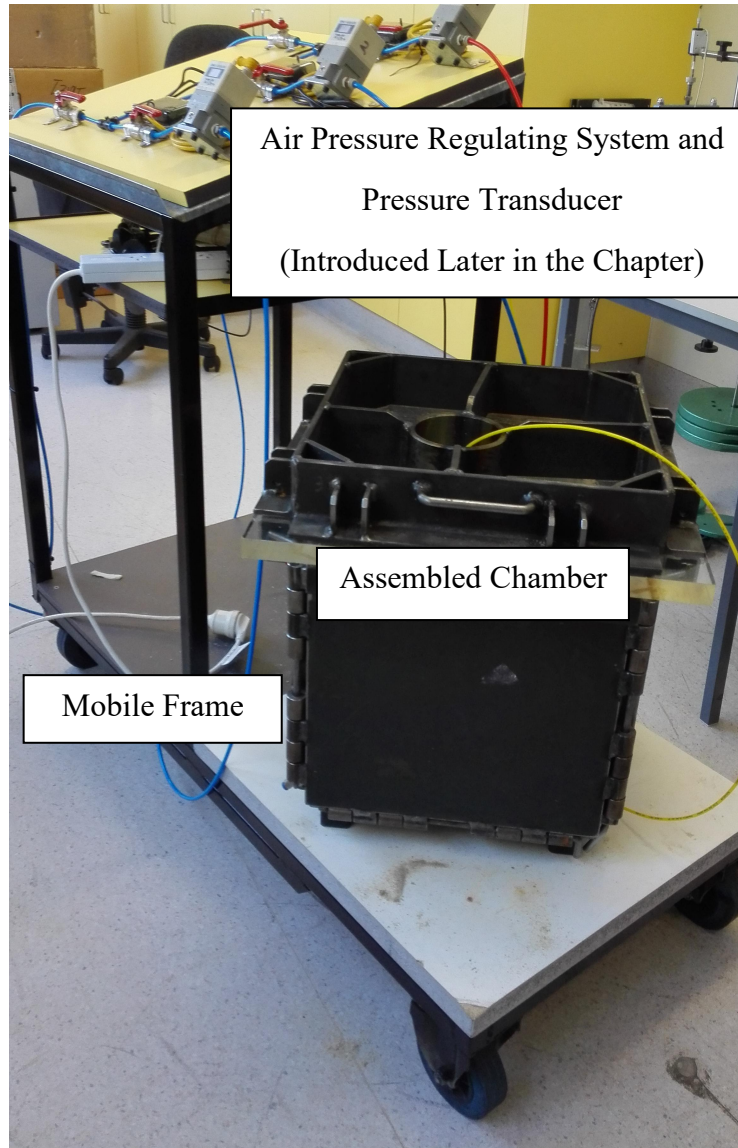


Fig.3.12 Assembled chamber and the test platform

3.3.7.1. Air Pressure Regulating System

The laboratory air supplier supplies pressurised air at constant 1000kPa. This pressurised air is conducted through three independent air regulating channels. Figure 3.13 shows one of the air regulating channels. In each channel, there is one electronic air pressure regulator (with the regulating capacity of 3000kPa). Regulators are connected to the voltage regulator. The voltage regulator controls the output pressure between 0 and 1000kPa by varying the voltage between 0 and 8 Volts. The regulated air pressure then goes to the air cushion that belongs to the regulated air channel to generate each principal direction of confining pressure on the specimen.

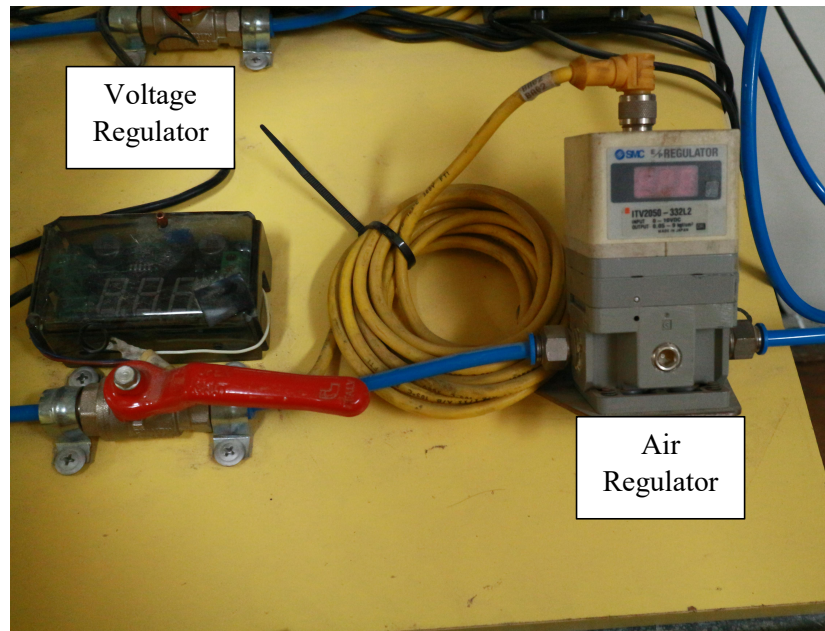


Fig.3.13. Illustration of an independent air regulating channel

3.3.7.2. Horizontal Confinement

It is explained in Section 3.3.3 that the anisotropic pressuremeter chamber can generate the isotropic and anisotropic confinements in two horizontal directions. In an isotropic circumstance, the air cushions behind the side compression plates are subjected to equalised air pressures. Therefore, the specimen is confined by the isotropic pressures in two principal directions. This confinement circumstance is similar to cylindrical chamber tests. In an anisotropic circumstance, the side air cushions are subjected to different air pressures, which drive the chamber to provide anisotropic horizontal confinements to the specimen in two principal directions.

3.3.7.3. Vertical Confinement

The regulating channel assigned to the bottom compression plate is dedicated to generating the active vertical confinement. This active vertical confinement is applied to the simulation of the variation of in-situ vertical stress once the consolidation history is studied. In the way of passive vertical confinement generation, the bottom air cushion is isolated. The vertical boundary condition is provided by the compressing plate and the top compartments. Therefore, the vertical stress is fully dependent on the Poisson's

ratio of the material. This method is suitable for studying cases where consolidation history is not within the interest of study, such as the present research project.

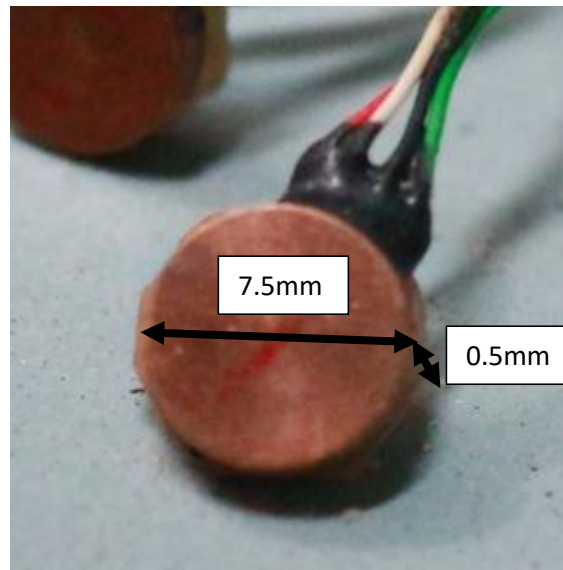
3.3.8. Chamber Calibration Equipment

There are two setups to calibrate the anisotropic pressuremeter chamber: the one dimensional setup and the in-chamber setup. The one dimensional calibration setup is the out-of-chamber setup. Introduced in Section 3.3.9, the one-dimensional calibration provides the correlations of: (1) the applied air pressure and the confining pressure on the specimen boundary and (2) the voltage output of the miniature transducers and their actual measured pressures. Introduced in Section 3.3.10, the in-chamber calibration provides the correlation between the applied pressure on the specimen boundary and the corresponding confining pressure of the pressuremeter test cavity. The equipment required to complete the calibration, three miniature transducers, one data acquisition box and a transducer holder.

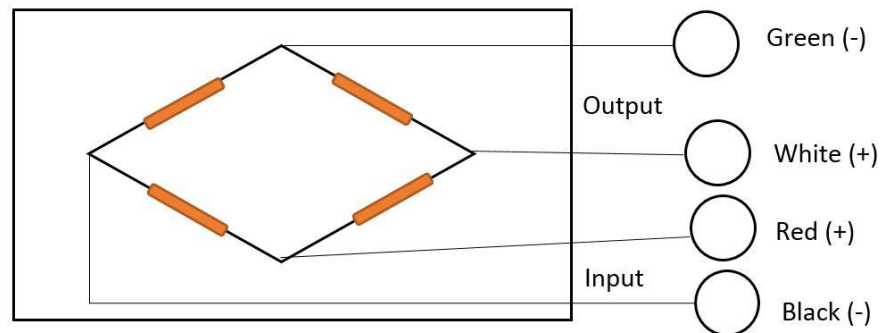
3.3.8.1. Miniature Pressure Transducer

The in-chamber calibration employs three miniature pressure transducers to measure internal stress inside the specimen. These transducers are calibrated during the one-dimensional calibration setup. The transducers are the PDA-1MPB transducers made by TML Corporation. These are the strain-sensing-type electric pressure cells with two circular surfaces with diameters of 7.5mm as shown in Figure 3.14 (a). The thickness of the transducers is 0.5mm. Each transducer is equipped with four electric wires, of which two wires (red and black) act as positive and negative power input wires connected to the adjustable DC power supplier to provide electric power. The other two wires (white and green) are the output signal wires connected to the Data Acquisition Box. When specific pressure is applied to each of the transducer surfaces, the internal circuit undertakes the loading by strain. The strain then changes their output voltage, which is then transmitted as electric signals to the Data Acquisition Box by the output wires. The internal circuits of the transducers are shown in Figure 3.14 (b). The transducers' capacity to measure pressure is from 50kPa to 3MPa, which fulfils the pressure requirement for the chamber calibrations. The maximum input voltage of each transducer is 2V. In this research project, a constant input power of 1.88V from the

adjustable power supplier is used for the calibrations. This input power is also connected to the Data Acquisition Box to monitor the undulation.



(a)



(b)

Fig.3.14. Miniature transducer: (a) exterior appearance and (b) interior circuits

3.3.8.2. Data Acquisition Box

The Data Acquisition Box is applied to monitor and record both the input and output DC signals from the three miniature pressure transducers. The applied DATAQ DI-710 Data Acquisition Box is a voltage monitoring device with sixteen input channels connected to the computer. The device is commanded by the WINDAQ software interface. The software allows manually operative functions to (1) activate and deactivate monitored channels, (2) set up gain for the input voltage, (3) adjust the reading rate (in Hz) and (4) output the recorded data to external software such as

Microsoft Excel for further processing. Figure 3.15 shows the Data Acquisition Box and the interface of WINDAQ software. There are a total number of thirty-two screw-terminal blocks that provide the sixteen channels. In the calibration setups, four channels are activated for the signal output of the three miniature transducers, and the other one is used for the power input. Considering the size of the record file, the signal reading rate of 1.3Hz is set in the WINDAQ software. This specific reading rate allows a data logging interval of 3.1 seconds.

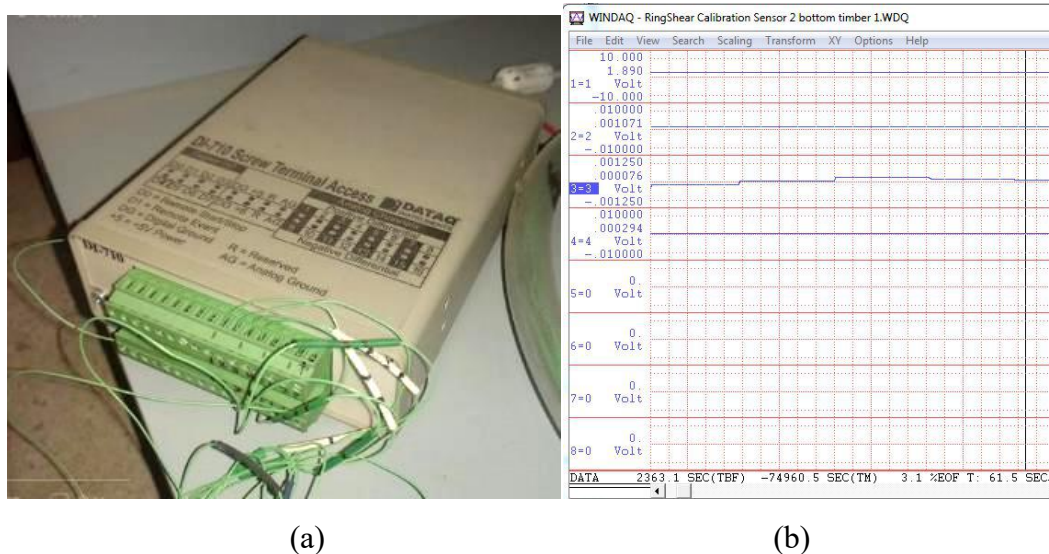


Fig.3.15. Data output from pressure measurement; (a) DATAQ acquisition box, and (b) WINDAQ software interface

3.3.8.3. Transducer Holder

The transducer holder is designed to place the three miniature pressure transducers in the middle of the specimen. The structure of the holder ensures that each of the transducers orients in one of the three principal directions corresponding to the confining pressures from the chamber. The holder is made by a hard plastic cube. The plastic cube has a side length of 30mm. Of the six surfaces of the cube, three orthogonal surfaces that accommodate the transducers are named surface 1, 2 and 3 respectively. These three surfaces are carved with cylindrical slots of a diameter of 8mm to accommodate the three transducers. To flatten the surfaces of the craved slots of the cube to allow better stress distribution to the transducers, three thin cylindrical metal pads of 7.5mm in diameter are placed in the three slots. The surface opposite to surface 1 (surface 4) is drilled from the centre. The drilled tunnel connects with the cutting on

the corner of surfaces 1, 2 and 3. This drilled tunnel forms the transducer-inlet tunnel so that the transducers going through the tunnel branch out to surfaces 1, 2 and 3 respectively. Each transducer is then pinned onto carved slots over metal pads. The deformable sides of the transducers face downward so that the surface remains flat. The three transducers are then sealed with the cube by tape as Figure 3.16 shows. Following this, the corner cutting is covered by a thin metal wedge to block soil particles. For the in-chamber calibration setup, a hollow-metal-tube is plugged into the opening on surface 4, acting as the extension for the transducer-inlet tunnel for the wires.

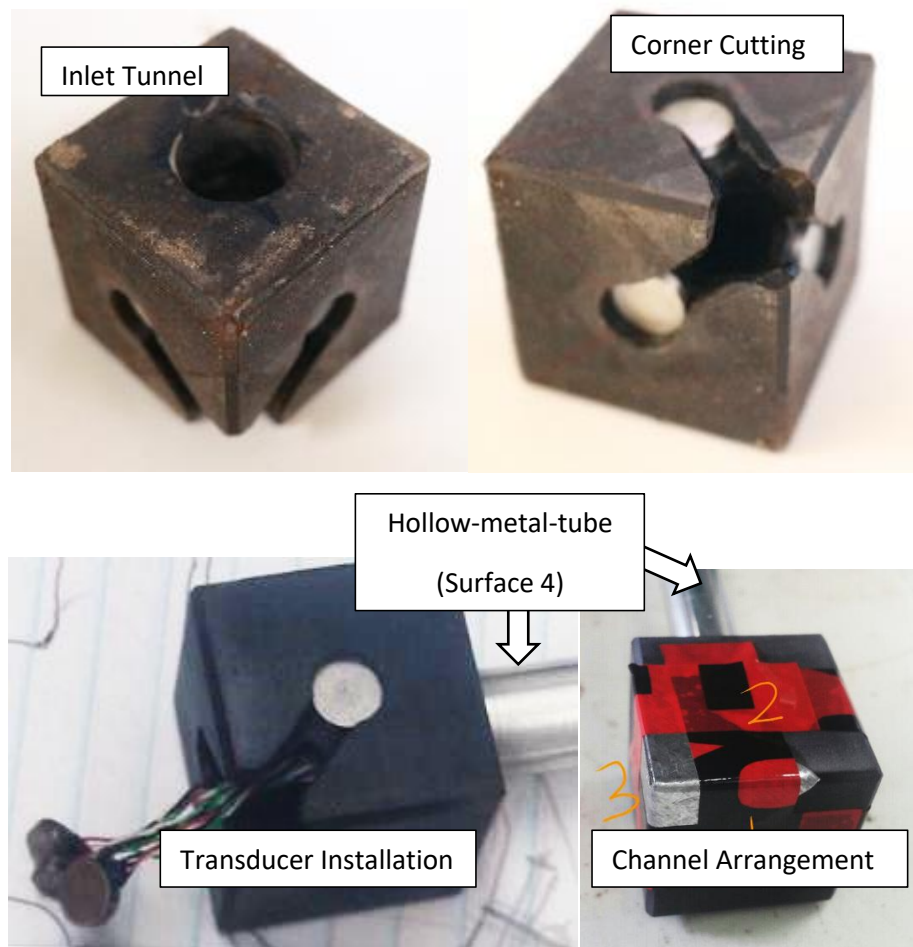


Fig.3.16. Transducer installation

3.3.9. One Dimensional Calibration

3.3.9.1. Setup Introduction

The calibration is conducted using a load frame. The air cushion undergoing calibration is placed at the bottom of the load frame and connected to the inlet air

monitored by a digital pressure gauge. As described in Section 3.3.7, each air cushion has its associated compression plate inside the anisotropic pressuremeter chamber.

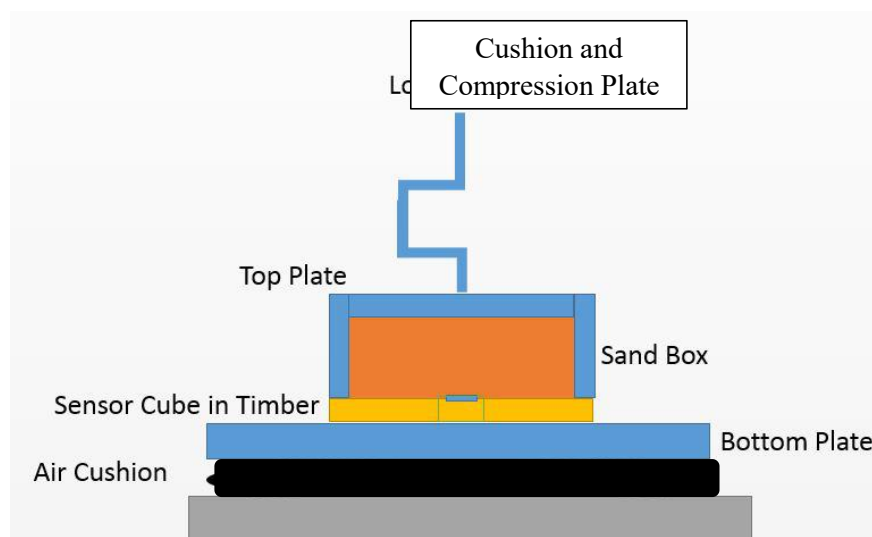
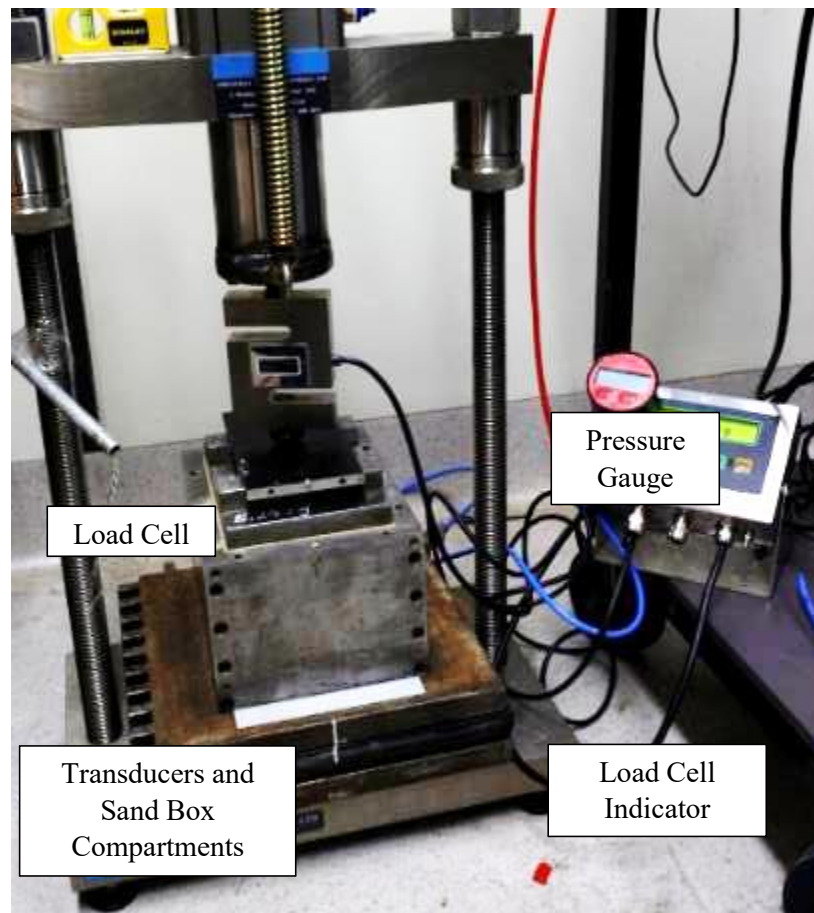


Fig.3.17. One dimensional calibration setup

In one dimensional setup, this associated compression plate is placed on top of the cushion undergoing calibration. The plate is overlain by a sand box, which

accommodates the nature-dense sand specimen. For the voltage-pressure calibration of the miniature pressure transducers, the three transducers - installed in the holder - are placed inside a hollow timber at the bottom of the sand box. Inside the timber, the transducer that faces a vertical direction should be the same transducer associated with the plate and cushion during the in-chamber calibration (describe in Section 3.3.10). There is a sand box lid that sits close to the external load cell of the frame. The load cell has its digital display to indicate the total loading, f , from the applied air pressure, P_a . The one-dimensional calibration setup is shown in Figure 3.17.

3.3.9.2. Air Pressure versus Confining Pressure

Applied air pressure, P_a (kPa), is adjusted between 100-600kPa. The load cell indicates the total loading in the vertical direction, f (kg). The surcharge weight, w (kg), is the additional surcharge over the cushion.

In the calibration, the internal pressure of the sandbox, P_s , can be determined by using the following equation:

$$P_s(kPa) = \frac{[f(kg)+w(kg)] \times 9.81 \left(\frac{N}{kg}\right)}{\text{Internal area of sand box (m}^2\text{)}} / 1000 \left(\frac{Pa}{kPa}\right) \quad \text{Eq.3.1}$$

In the chamber test, however, as the air cushion and the compression plate are both working inside the chamber, the specimen area should be the total area of the plate. The confining pressure in the chamber, P_c , can be expressed as follows:

$$P_c(kPa) = \frac{[f(kg)+w(kg)] \times 9.81 \left(\frac{N}{kg}\right)}{\text{Area of the compression plate (m}^2\text{)}} / 1000 \left(\frac{Pa}{kPa}\right) \quad \text{Eq.3.2}$$

Equation 3.2 shows that the confining pressure (P_c) correlates with surcharge weight (w). This surcharge weight (w) has two meanings in horizontal confining and vertical confining circumstances. For horizontal confining pressure calibrations, w is the weight of the sand box. For vertical confining pressure calibrations, w includes the total weight of the sand box and the compression plate. Therefore, a one dimensional calibration provides two correlations for horizontal confining and vertical confining circumstances respectively. By plotting the calculated confining pressure, P_c , against

applied air pressure, P_a , the correlations appear as two trend lines, as shown in Figure 3.18. These two trend lines can be expressed as follows:

$$P_c(kPa) = 0.578P_a(kPa) \text{ (for vertical confining pressure)} \quad \text{Eq.3.3}$$

$$P_c(kPa) = 0.5488P_a(kPa) \text{ (for horizontal confining pressure)} \quad \text{Eq.3.4}$$

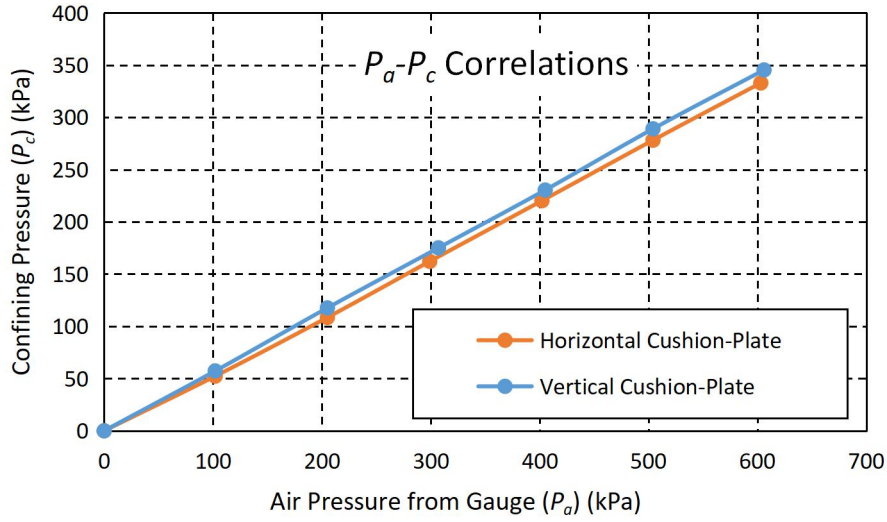


Fig.3.18. Correlations between air pressure (P_a) and confining pressure (P_c)

3.3.9.3. Transducer Voltage versus Transducer Measured Pressure

In a one dimensional calibration setup, the internal pressure of the sandbox, P_s (kPa), is equal to the pressure measured by the transducer undergoing calibration, P_t (kPa). However, the direct output of the transducer is expressed as voltage, V_o (V). By plotting the value of V_o against the P_t (P_s) for each transducer undergoing calibration, the correlations between the voltage output and the pressure on the transducer, V_o - P_t , can be shown, as in Figure 3.19.

It is notable that although in an unloading condition, the three transducers have different initial voltage readings. The gradients due to stress increment are identically linear. Using linear closed-form equations, the correlations can be expressed as follows:

$$P_t(kPa) = 433125 \left(\frac{kPa}{V} \right) \times V_o(V) - 460.5 (kPa) \text{ (for transducer 1)} \quad \text{Eq3.5}$$

$$P_t(kPa) = 454436 \left(\frac{kPa}{V} \right) \times V_o(V) + 329.31(kPa) \text{ (for transducer 2)} \quad \text{Eq.3.6}$$

$$P_t(kPa) = 520159 \left(\frac{kPa}{V} \right) \times V_o(V) - 155.63(kPa) \text{ (for transducer 3)} \quad \text{Eq.3.7}$$

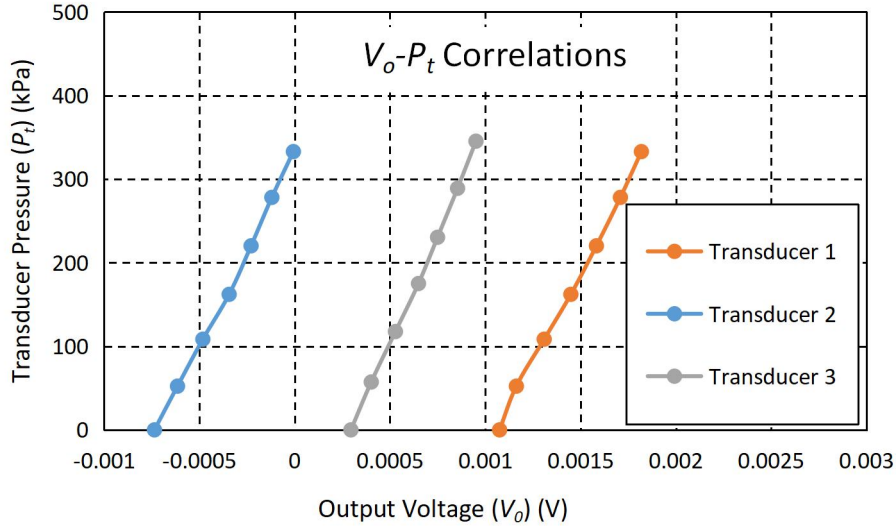


Fig.3.19. Output voltage (V_o) and transducer measured pressure (P_t) correlations

3.3.10. In-chamber Calibration

3.3.10.1. Setup Introduction

In the in-chamber calibration setup, each air cushion with its associated air channel, air regulator and compression plate are grouped as one ‘compression system’. Therefore, the chamber has three compression systems to create independent confining pressures in the three principal directions defined in Section 3.3.1. Vertical confining pressure is generated by System 1. Confining pressures in the horizontal X-axis and Y-axis are generated by System 2 and System 3 respectively. In-chamber calibration is conducted repeatedly, system by system. To start with Compression System 1 calibration, the chamber is installed based on the instructions in Section 3.3.6. All the components of Compression System 1 are connected and activated by connecting to the external air supplier. The two air cushions of the other two (horizontal) systems are removed from the chamber and replaced by five nuts that are 10mm in length behind each of their associated compression plates, as shown in Figure 3.20. These plates are fixed by adjustable G-clamps to prevent tilting during the specimen filling.



Fig.3.20. Preparation of in-chamber calibration (System 1)

The sand specimen is then filled inside the chamber with a textile bag to prevent its leakage. The first layer of the sand specimen is filled to half the height of the chamber, followed by a gentle plate-compaction. The transducer holder, which accommodates three transducers, with its metal tube for the wire extension, is then installed at the centre of the specimen surface. Since the calibration is for System 1, inside the transducer holder, transducer 1 should be located towards the bottom.

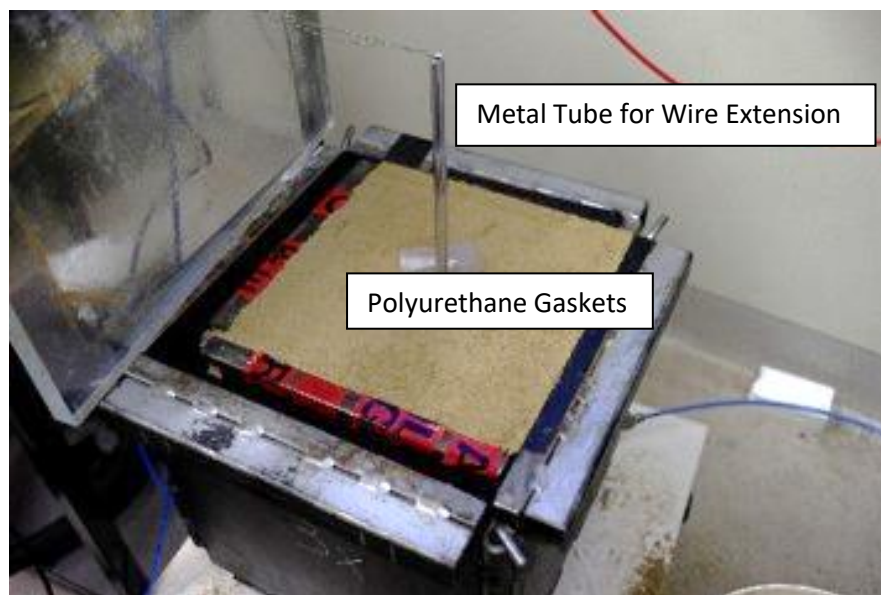


Fig.3.21. In-chamber calibration before top compartment installation

The sand specimen is then poured into the top of the chamber. The specimen surface is gently compacted by a metal plate again. Around the metal tube for the wire extension, there are two polyurethane gaskets embedding on the top of the specimen. The polyurethane gaskets are used to prevent the sand particles from leaving from the

gap between the metal tube and the opening of the transparent plate described in Section 3.3.6.4, while still providing space for the slight movement of the transducer holder with the metal tube. The described installation procedure is demonstrated in Figure 3.21. Following this procedure, the transparent plate and the top webbing designed in Section 3.3.6.5 are installed on the top of the chamber with its specimen. The flanges of the chamber and the top webbing are then fixed with eight U-clamps.

3.3.10.2. Calibration Procedure

After the setup, the pressure regulator for Compression System 1 is activated, and the other two regulators are fully closed. The pressure applied on cushion 1 is monitored with a pressure gauge. Pressurisation is similar to the one dimensional calibration, with applied air pressure, P_a , indicated by the gauge as increasing from 100kPa to 600kPa. In each increment, there is a 100kPa increase in applied air pressure and 15 minutes of time for the specimen to deform. The Data Acquisition Box is set to record the input voltage from the power supplier and the output voltages from the miniature transducer undergoing calibration (transducer 1). The reason for recording the input power is to monitor the consistency of the input voltage.

When Compression System 1 is calibrated, the chamber is re-assembled to initialise the calibration of Compression System 2. Compression System 2 is connected to the external air inlet. The other two Compression Systems (1 and 3) are disconnected from both power and air suppliers. The bottom cushion (cushion 1) is replaced by the five nuts of support for compression plate 1, similar to the horizontal compression plate supports applied in the Compression System 1 calibration as shown in Figure 3.20. The specimen filling, the installation of the transducers (including holder and metal tube wire extension) and the pressurisation procedure (for Compression System 2) are similar to Compression System 1 calibration. The measured voltage outputs are the power supplier voltage and transducer 2 voltage.

After calibration of Compression System 2, the chamber is re-assembled for the calibration of Compression System 3. Compression System 3 calibration involves the same procedure as was used for System 1 and System 2 calibrations, with all the activated components replaced with system 3 components. Additionally, the deactivated cushion 1 and cushion 2 are replaced by the five nut supports shown in Figure 3.20.

3.3.10.3. Data Processing

After the three stages of in-chamber calibration, the data is exported to Microsoft Excel for processing. Processing starts by extracting the voltage outputs of transducer 1 from system 1 calibration, transducer 2 from system 2 calibration and transducer 3 from system 3 calibration. The voltage outputs are then converted into pressure readings using Equation 3.5 (for system 1 calibration), Equation 3.6 (for system 2 calibration) and Equation 3.7 (for system 3 calibration) from the one dimensional calibration. To differentiate the transducer readings in the two calibrations, the P_t is represented by the in-chamber calibration pressure, P_{ti} . The applied pressure read by the pressure gauge is converted into pressure on the surfaces of the specimen using Equation 3.3 (for system 1) and Equation 3.4 (for system 2 and 3).

3.3.10.4. Results

The results from the in-chamber calibration are plotted as the compression pressure on the surface of the specimen, P_c , against the corresponding transducer measurement in the middle of the specimen, P_{ti} . The result is shown in Figure 3.22. It can be seen that each surface pressure on one side of the specimen is identical to the pressure in the middle of the specimen.

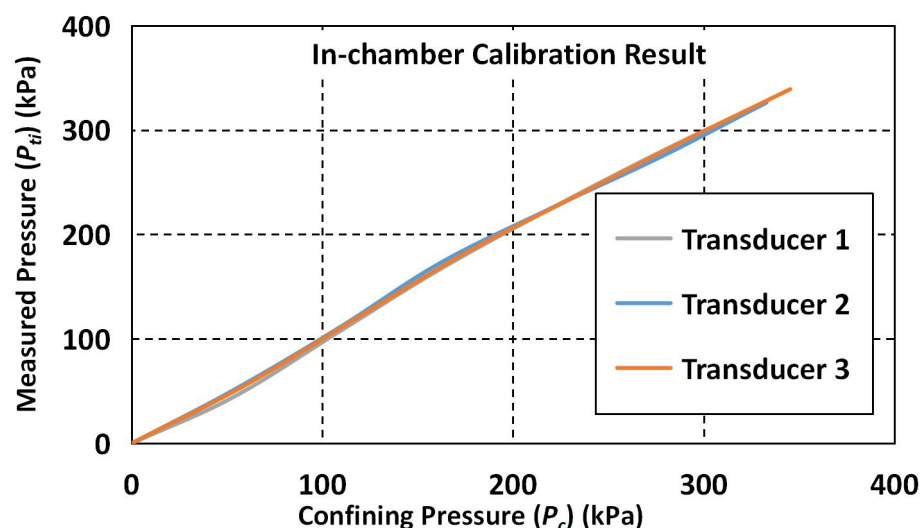


Fig.3.22. In-chamber calibration results

3.3.11. Stress around the Pressuremeter Test Cavity

The stress at the centre of the chamber centre, which is distributed around the cylindrical pressuremeter test cavity, is different from the confining pressure on the boundary. To explain this stress difference in detail, Section 3.3.11.1 states the problem of inequality between applied pressure and pressure in the soil around the cylindrical cavity. Section 3.2.11.2 shows the assumptions for analysis. Section 3.3.11.3 is the analytical solution for the cavity pressure.

3.3.11.1. Stress Difference Justification

When a cylindrical cavity is created inside the cubically shaped specimen, the pre-expansion internal boundary pressure around the cylinder can be different from the uniformly distributed pressure generated by the pressure plates. The cylindrical cavity pressure in chamber test refers to the in-situ stress for the parameter interpretations. Therefore the correlation between cylindrical cavity pressures and applied pressures on the specimen needs to be described.

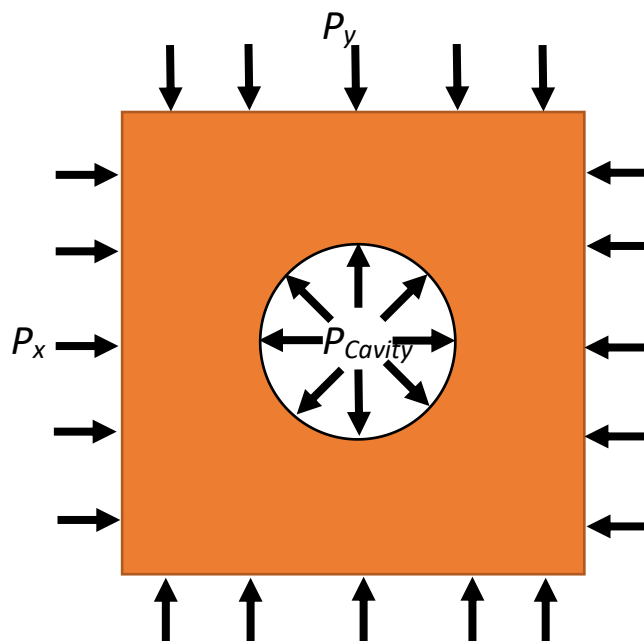


Fig.3.23. Plane-strain assumption for pressuremeter chamber test

3.3.11.2. Hypothesis and Plane Strain Solution

From the top view, the cylindrical cavity expansion problem can be simplified using the plane-strain assumption. As shown in Figure 3.23, the cylindrical cavity is

represented by the circular two-dimensional cavity. Assuming the cavity is fully touching the pressuremeter probe, the probe is represented by the fixity of the circumferential boundary of the cavity. The specimen inside the chamber is considered to be of square cube with infinite side-length. The material property of the specimen is assumed to be linearly elastic and homogeneous.

3.3.11.3. Isotropic Solution

The external boundary of the specimen is subjected to confining pressure from two principal directions, P_x and P_y . The internal boundary condition is created by the installation of the pressuremeter probe. The pre-expansion soil cavity is static. Therefore, before the expansion, based on static equilibrium, the cavity pressure, P_{Cavity} , is equal to the confining pressure around the cavity, P_c .

$$P_{Cavity} = P_c \text{ (at zero cavity deformation condition)} \quad \text{Eq.3.8}$$

It can be described that when the test starts, the cavity pressure becomes larger than the confining pressure around the cavity in the first static state $P_{Cavity} > P_c$. The cavity expands to compress the soil until another static equilibrium is reached (soil is assumed to be fully elastic). The opposite, as Figure 3.24 (a) shows, occurs if the internal boundary is removed. The cavity then shrinks until P_{Cavity} becomes zero for static equilibrium. Palmer (1971) expresses the static state at zero cavity pressure as the 'reference state'. If u represents the radial displacement of the cavity wall and a represents the original radius of the cavity before shrinkage, the strain of the cavity during shrinkage, ε , is expressed as follows:

$$\varepsilon = \frac{u}{a} \quad \text{Eq.3.9}$$

Yu (2000) states that the radial strain generated by the external boundary condition P_x and P_y , in a cylindrical cavity, can be expressed as follows:

$$\varepsilon = -\frac{1-\nu^2}{E} [(P_x + P_y) + 2(P_x - P_y) \cos 2\theta] \quad \text{Eq.3.10}$$

In this equation, θ is the angle between the P_x direction and the direction of radial displacement. In isotropic horizontal stress conditions, external confining pressure in two principal directions is equal ($P_x=P_y=P_e$). Therefore, the second part inside the square bracket of Equation 3.10 is equal to zero. Hence, the equation can be simplified as follows:

$$\varepsilon = -\frac{2P_e(1-\nu^2)}{E} \quad \text{Eq.3.11}$$

In this equation, ν and E are Poisson's ratio and Young's stiffness of material, respectively. Based on the previous explanation, the equation explains that the intensity of strain for the cavity pressure dropping from P to zero correlates with Poisson's ratio and Young's modulus. Based on Yu's deduction, tangential strain is negligible in this assumption.

In another words, if the down-sized cavity needs to be restored to a zero deformation condition, the same amount of pressure needs to be placed on the cavity as Figure 3.24 (b) shows. For linear elastic, homogeneous materials, the relationship between radial strain and radius stress can be explained by Young's modulus as follows:

$$E = \frac{\sigma}{\varepsilon} \quad \text{Eq.3.12}$$

In this case, the radial stress for restoring the initial volume around the cavity can be represented by cavity pressure:

$$\sigma = -P_{Cavity} \text{ (Negative sign due to the opposite directions of cavity pressure and radial stress)} \quad \text{Eq.3.13}$$

By combining Equation 3.11, Equation 3.12 and Equation 3.13 in an isotropic condition, the relationship between the isotropic external confining pressure, P_e , and the cavity pressure, P_{Cavity} , can be expressed as:

$$P_{Cavity} = 2P_e(1 - \nu^2) \quad \text{Eq.3.14}$$

Equation 3.14 expresses that the relationship between cylindrical cavity pressure and compression pressure in an isotropic stress condition is only dependent on Poisson's ratio of the material.

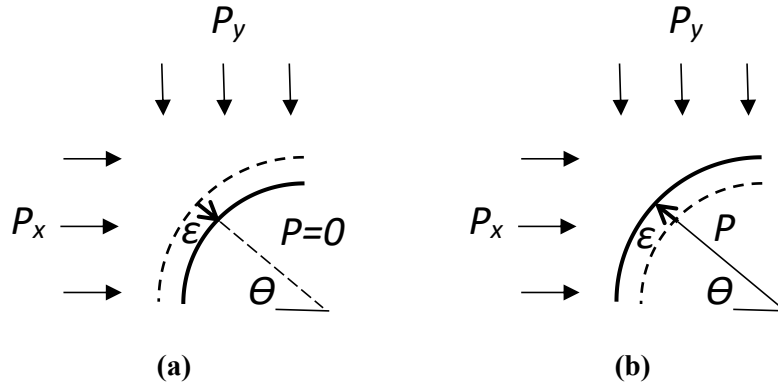


Fig.3.24 Cavity pressure-strain assumptions on (a) removed internal boundary and (b) restored internal boundary

3.3.11.4. Anisotropic Solution (Simplified)

For an anisotropic condition, although realistic anisotropic confining pressures generate an ‘ellipse’ deformation (Zhou et al., 2016), if the radial strain due to removal of the (or restoring) internal boundary is analysed in infinitesimal scale, the overall radial strain around the cavity can be replaced by the average strain generated by the mean principal confining pressure around the external boundary, P_{em} , where

$$P_{em} = \frac{P_x + P_y}{2} \quad \text{Eq.3.15}$$

Therefore, cavity pressure under an anisotropic condition can still use the correlation between Poisson’s ratio and cavity pressure from Equation 3.14 by replacing P_{em} with P_e . The cavity pressures estimated from isotropic and anisotropic compressions are verified with FEM in the next section.

3.3.12. Finite Element Simulation of Pressuremeter Chamber Testing

3.3.12.1. Purpose and Goal

There are two limitations on the analytical solutions of the cavity pressure in the chamber. First, the general analytical solutions are based on the plane strain condition. The two in-plane principal stresses are the radial and circumferential stresses. The out-of-plane principal stress is treated as the medium principal stress, acting perpendicular to the analysing plane, and the out-of-plane strain is simply regarded as zero. As a result,

the impacts of the length-to-diameter ratio of the probe and the vertical boundary condition in the chamber are ignored in the analytical solution. Second, the anisotropic solution is purely represented by the mean pressure. Hence, it is doubted that the analytical result is able to represent actual stress distribution around the probe in the real scenario.

As a result, FEM is built with ABAQUS 2017 FEM code to verify the calculated cavity stress from the analytical calculation. The FEM result also shows the stress distribution inside the specimen under isotropic/anisotropic testing conditions. Moreover, the results calculated by the FEM can address the stress distribution around the cylindrical cavity, which is then used in the parameter interpretations in isotropic/anisotropic pressuremeter chamber tests in Chapter 4.

3.3.12.2. Geometry and Material Property Definition

A comprehensive three-dimensional shape is built in the Computer-aided Engineering (CAE) interface of the ABAQUS 2017. The shape is shown in Figure 3.25. The shape consists of four parts. The first and second parts (indicated by the Bar and the Cap) are analytical rigid bodies that are considered non-deformable parts. The rigid body has no internal stresses. All the reaction forces, spatial displacements and boundary conditions are defined by reference points. As a result, these parts are excluded from the element stress-strain calculation by the programme to save calculation time. The third and fourth parts are the deformable parts (indicated as the Membrane and the Soil). These parts require element meshing, section assignment and definition of the material's elastic and plastic properties. These parts also have surface interactions for the stress and strain calculation between different instances. This is introduced later in this section.

The first part is the tube, which is the extension of the probe and is called the 'bar' in the CAE database. This part represents the connection between the flexible hydraulic hose and the miniature pressuremeter probe in the real test. It is created by rotating the analytical rigid shell axis-symmetrically so that the upper and bottom surfaces of the cylinder is sealed. The part is cylindrical with a radius of 5mm and length of 118mm.

The second part is another cylindrical rigid body that represents the non-expandable bottom component of the probe. The part is called the Cap in the model.

The generation of the Cap is identical to the Bar rigid part. It shares the same radius as the 'bar' with a length of 21mm.

The third part is a revolved, deformable shell-type of the section, which represents the expandable membrane of the pressuremeter probe. This part is named the Membrane. The part has a curved surface that has contact with the specimen to perform expansion and the top and bottom surfaces fixed with the Bar and the Cap, respectively. It has a radius of 5mm and length of 64mm. After generation, the centre of the part is assigned to a reference node, which acts as the reference point of the fluid cavity. The definition of the fluid cavity is introduced later in this chapter. The part is then partitioned into four spatial regions, using two spatial surfaces perpendicular to each other across the Z-axis. The term 'partition' in ABAQUS means the spatial segmentation of a part to (1) allocate a better boundary condition, (2) adjust the element-mesh generation independently, and (3) line up the shape with other parts that interact with the shape. In the Membrane, the partition is used to (1) define size/shape of the element mesh on the shell geometry for aligning with the elements in the soil specimen part (the fourth part) and (2) define a boundary condition for the fluid cavity.

The fourth part is a deformable solid-type of the section, which represents the specimen. This part is named the Soil in the model. A 300mm × 300mm square is extruded to a height of 300mm to define the part. The centre of the top surface is then cut with a radius of 5mm and 203mm-long cylindrical hole that acts as the cavity for assembling other parts. For better meshing, three spatial surfaces parallel to the X-Y plane of the Soil part are generated at the cross-sections of 118mm, 64mm and 21mm from the top. The spatial partition surfaces are in line with the Bar, the Membrane and the Cap respectively. As a result, the part is divided into four regions. The second region from the top is again sub-divided into four equivalent blocks and four spatial partition surfaces parallel to Z-axis. The advantages of these sub-divisions are to (1) align with the partitioned segments of the Membrane and (2) allow the assignment of hexagonal elements. The second advantage is described in the meshing introduction.

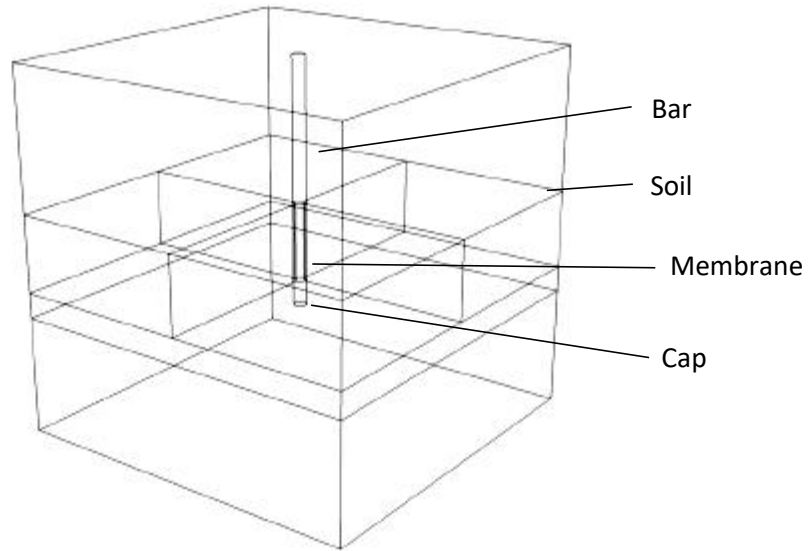


Fig.3.25. Geometry definition and partitions in FEM

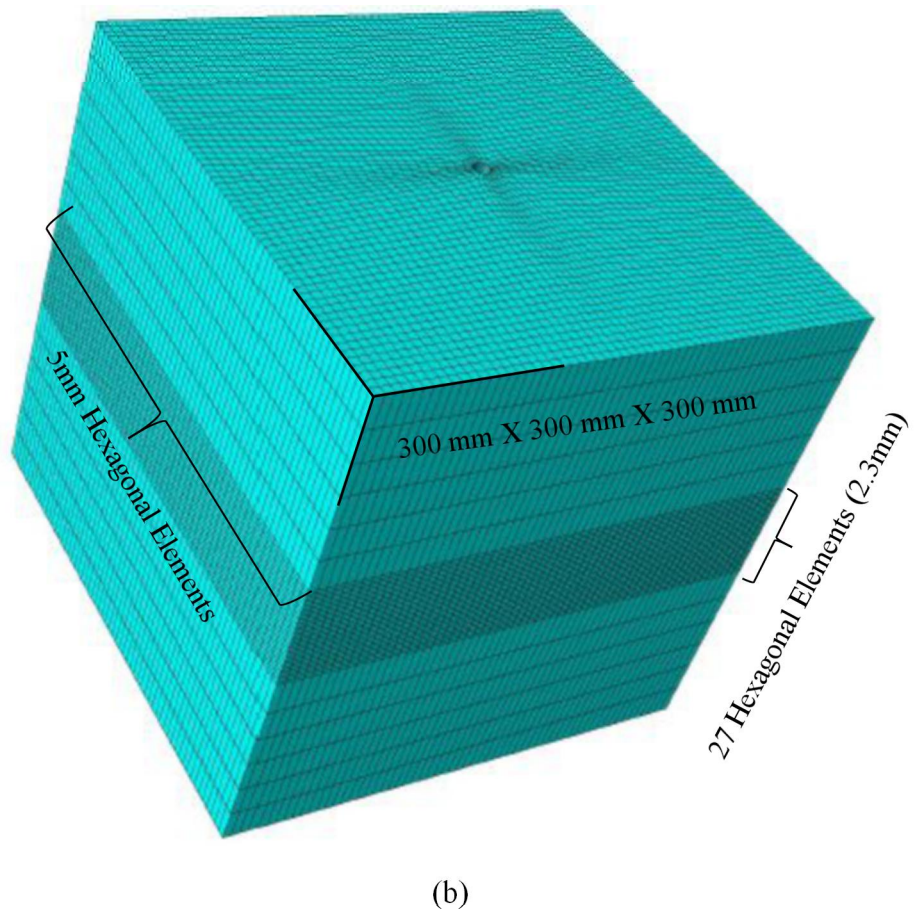
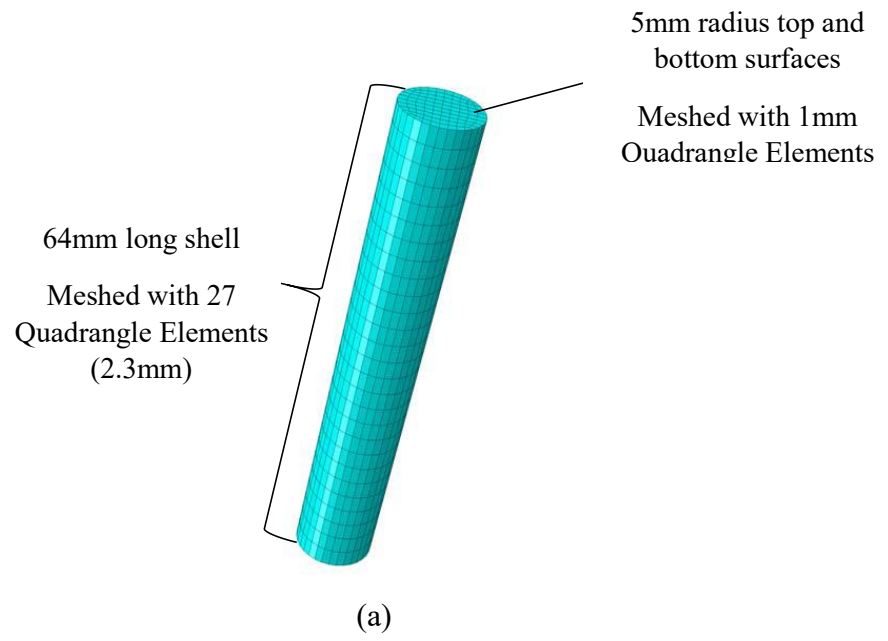
3.3.12.3. Meshing

To compute stress-strain relationships, the FEM programme needs to subdivide the non-rigid shapes (Membrane and Soil in this project) into smaller regions. These subdivided regions are the ‘elements’ for the simulation. The subdividing process is called ‘meshing’. The refinement of meshing, in FEM terms, means the number of smaller regions is subdivided into a nominated portion (the whole part or the partitioned segment) of the shape. Ideally, more refined meshing brings more accurate results up to a certain level. However, the computation is more time-consuming for, especially in three-dimensional simulations. Hereby, defining appropriate meshing in FEM is crucial to obtaining accurate yet achievable results. Well-defined meshing for the simulation of the chamber test is shown in Figure 3.26.

The Membrane meshes with conventional four-nodes linear quadrilateral shell elements (ABAQUS element S4R), which means that the stress and strain within the ‘element region’ are calculated with the linear properties of the internal four nodes at the four corners of the element. Based on the partition, the 64mm-long Membrane is divided into four equivalent quarter regions. Each quarter region is formed by a curved shell parallel to the Z-axis and two flat shells on the top and bottom. In the ABAQUS interface, the assignment of element side length or number of elements on the edge of the region is named ‘seed’. The top and bottom shells are seeded with an element size of 1, which means that the general side length of the element on the shell is roughly

1mm. The curved 'shell' is seeded with 27 elements in the longitude direction, which is equivalent to roughly 2.3mm of the element's side length on the curved shell. The meshing is displayed in Figure 3.26 (a). A total number of 1056 shell elements are generated on the Membrane.

The Soil meshes with two parts of 3D stress solid elements, the eight-nodes hexagonal elements (C3D8) and the six-node wedge elements (C3D6). These two types of elements are used in different partitioned regions. The partition region in line with the Membrane is meshed with eight-node, hexagonal elements so that the elements appearing on the cavity wall have quadrangle surfaces to contact the quadrangle elements on the curved surfaces of the Membrane. The top and bottom surfaces of this hexagonal-element region are seeded with a size of 5mm on the outer boundary [Figure 3.26 (b)] and 1mm elements around the cavity [Figure 3.26 (c)]. The longitude side of the region is seeded with 27 elements. This enrichment of element-mesh allows the elements size and number around the cavity to be equal to the elements of the 'membrane', while it reduces the number of the elements. There are three advantages to this enrichment. First, excessive slipping between the elements' nodes of the two parts (Membrane and Cube), which may lead to abortive calculation, is eliminated. Second, the ratios between side lengths from the internal boundary (1mm/2.3mm) and the external boundary (2.3mm /5mm) are maintained between 0.43 and 0.46 so that over-distortion in the simulation process is avoided. Third, the cost of calculation power is idealised. The rest of the elements are meshed with six-node wedge elements to reduce the computation cost. The size-seeding is automatically assigned and generated by the FEM programme. With this element definition and meshing, a total number of 139402 elements are generated in the Soil part.



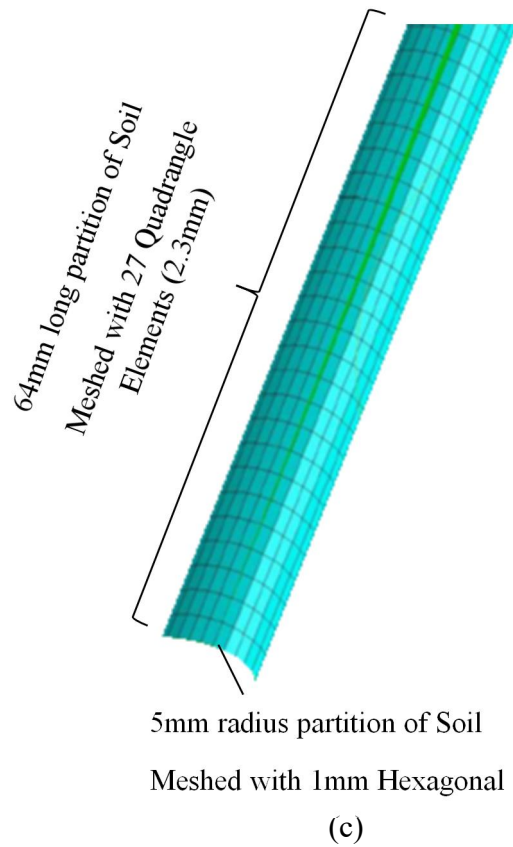


Fig.3.26. Element meshing demonstration of (a) The Membrane, (b) exterior of the Cube and (c) around the cavity of the Soil

3.3.12.4. Material Properties

The deformable parts, the Soil and Membrane, require property assignment to perform the stress-strain analysis. The material in the Soil is assumed to be linear elastic material with the Mohr-Coulomb failure criterion. The Membrane is defined as linear elastic. The material properties are suggested values based on empirical values and previous laboratory testings. The assigned properties are shown in table 3.1.

Table.3.1. Material properties for soil and membrane parts

Part	Soil	Membrane
Young's Modulus (MPa)	12	0.001
Poisson's Ratio	0.25	0.5
Friction Angle (°)	32	N/A
Dilation Angle (°)	0.01	N/A

3.3.12.5. Finite Element Parts Assembly

When the individual parts are built, meshed and assigned with different sections and material properties, the FEM programme needs the user to create instances from the meshed parts, followed by the assembly. Before the simulation, the FEM programme requires the user to state the following issues:

- (a) How are the parts positioned relative to each other?
- (b) How do the parts restrain each other in terms of motions?
- (c) How do the parts interact with each other during the simulation?

In ABAQUS 2017, these questions are answered with assembly, constraints and interactions, which are defined by the users.

The ‘assembly’ operation is the spatial organisation of the created parts along with their characteristics (element mesh, section properties, reference points and sets, datum coordinate systems, etc.) for the visualisation of the model in the FEM simulation (ABAQUS, 2017). This operation also allows users to activate/deactivate nominated parts in the modelling for specific purposes. The parts being included in the assembly are called instances. The assembly in the present simulation is based on the diagram in Figure 3.25.

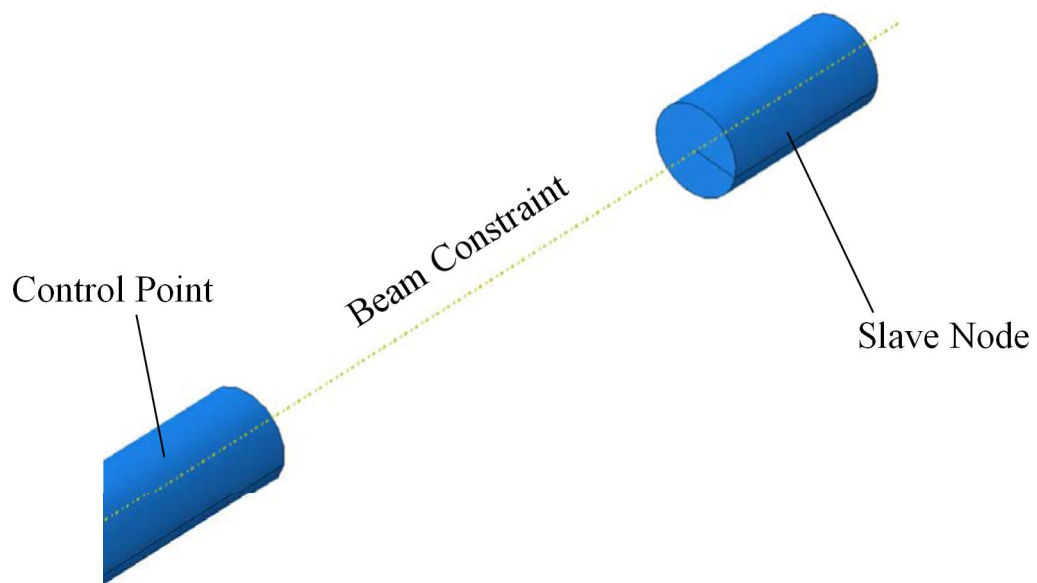
3.3.12.6. Constraints

The definition of ‘constraints’ in ABAQUS 2017 is the assignment of the suppositious restriction of the ‘relative Degree of Freedom (DOF)’ between the instances to govern the spatial motions. The present FEM simulation uses constraints to restrict the relative motions of the compartments of the probe and limit slipping between the probe and the cavity of the specimen. The types of constraint selected in the present simulation are Multiple Points Constraint (MPC) and the Tie constraint. The MPC constraints are used to define the compartments of the complex construction of the probe. The Tie constraint is used for limiting the relative motion between the curved surface of the Membrane and the cavity side-wall.

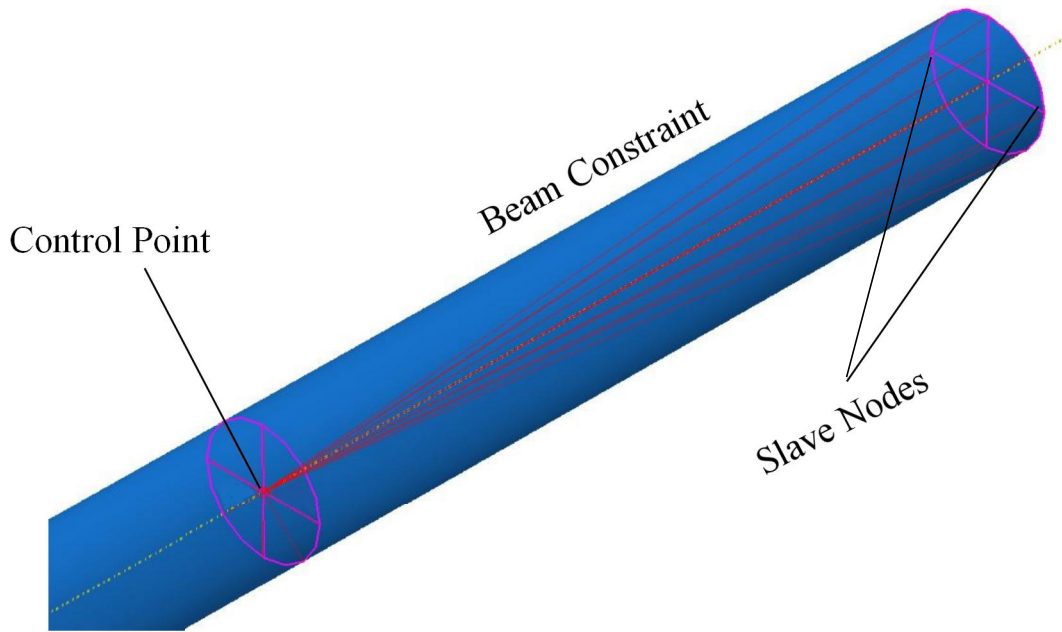
The MPC constraints are defined by nominating the spatial control point and the slave nodes to obey the selected type of restrictions of DOF. The control point has to be an individual node, but the slave nodes can be an individual node or sets of nodes. In this simulation, the first MPC is the Cap-to-Bar constraint [Figure 3.27 (a)]. Since both instances involved in the constraint are rigid instances, the constraint is defined by the

two reference points. In this MPC, the reference point of the Bar (at the bottom) is the control point, while the reference point of the Cap (at the top) is the slave node. The type of constraint is 'beam', which means no degrees of freedom relative to the control point are allowed to be activated on the slave nodes. The second MPC is the Membrane-to-Bar constraint. In this constraint, all the nodes at the top and bottom surfaces of the deformable Membrane are the slave nodes. The control point is again the reference point of the Bar [Figure 3.27 (b)]. The type of constraint is 'beam'. It restricts the change of the length and the rotation of the Membrane during simulation, especially in anisotropic stresses conditions.

The Tie constraint is a surface-based constraint. It maintains the relative positions in any DOF between the master and the slave surfaces during the simulation. The Tie constraint is defined between the Membrane-to-Cube surfaces in which the master surface is on the Membrane and the slave surface is on the Cube [Figure 3.27 (c)].



(a)



(b)



(c)

Fig.3.27. Constraint definitions of (a) Cap-Bar MPC 'beam' constraint (b) Membrane-Bar MPC 'beam' constraint and (c) Membrane-Cube Tie constraint

3.3.12.7. Surface Interactions

The material properties define the interaction between elements within the region of the part instance. However, when the FEM programme is solving the spatially overclosure of the surfaces of individual instance or a pair of instances, the elements belonging to the independent surfaces potentially have contact. Therefore, defining the

cross-surfaces interactions with normal and tangential properties can assist the solver in analysing the overclosure issue. In the present simulation, there are two interactions that need to be defined for the specimen cavity and the probe. The first interaction is the Bar-to-Soil interaction, which defines the interaction behaviour of the contact between the curved surface of the Bar and the cavity side-wall of the Soil. By parity of reasoning, the second interaction refers to the contact between the surface of the Cap and the cavity side-wall, which is named the Cap-to-Soil interaction. In both cases, the side-wall surface on the Soil acts as the slave surface, meaning the element nodes on the Soil surface cannot penetrate the Bar and the Cap. This definition is also based on the suggestion by ABAQUS that the surfaces on rigid bodies should always be the master surfaces.

In terms of interaction properties, the surface-pairs involved in the interactions are allowed to tangentially ‘slip’ against each other with a ratio between normal contact stress and friction (frictional coefficient) of 0.3. Normal contact is ‘hard’ contact, which means no penetration nor softening occur in the normal direction of the contact surfaces.

3.3.12.8. Boundary Conditions

In general, the boundary conditions are the specified variables on the nodes. In the present simulation, only the variables for the spatial motion (e.g. rotation and deformation) are considered. There are two boundary conditions that need to be specified in the model. First, the vertical displacements (Z-axis direction) of the top and bottom surfaces of the Soil part are fixed to zero. This is meant to simulate the chamber pressuremeter test in which the vertical compression is isolated. Second, the Bar is restricted to any movement during the test. In the three-dimensional simulation, this means that a total number six degrees of freedom (three for linear displacements U1, U2, U3 and three for rotational displacements UR1, UR2, UR3) are all set to zero on the reference point of the rigid Bar. This boundary condition means that no deformation is allowed to the miniature pressuremeter probe, apart from the expansion of the membrane. The horizontal movements of the Cube of the X-axis and Y-axis directions are defined by the confining pressures. In the initial stage (Step 1), these confining pressures are zero. A further application of isotropic/anisotropic pressures is introduced in Section 3.3.12.11.

3.3.12.9. Fluid Cavity Creation

In ABAQUS, the fluid cavity is a specified enclosed structure in the existing FEM model, which is assumed to be filled with a prescribed fluid (gas or liquid). The fluid cavity is built to simulate the relationship between the characteristics of the fluid inside the cavity (e.g. pressure, volume, and temperature) and the material behaviour outside of the cavity. As the fluid exchange can only be activated in ABAQUS explicit analysis, which is time consuming for the three-dimensional chamber analysis. The present research project applies the thermal expansion characteristic of the fluid to simulate probe expansion. The purpose is to simulate realistic probe expansion in the pressuremeter chamber test scenario and use the initial volumetric strain in the pressure-strain curve to obtain the estimated cavity pressure in all cases of confining pressures.

The first stage is used to define the fluid cavity in the expanding part Membrane of the model. There are two factors used to define the fluid cavity. These factors are the cavity point and the cavity surface. The cavity point is the reference point of the fluid cavity for the outputs, such as the hydraulic pressure and the fluid density. The cavity surface is the enclosed boundary of the cavity that interacts with the other assemblies outside the cavity. The cavity surface is also a boundary of the volume of fluid. In the present simulation, the cavity point is defined as the reference point at the centre of the Membrane. The cavity surface is defined as the internal surface of the Membrane.

3.3.12.10. Fluid Cavity Properties

The next stage is to define the properties of the fluid in the fluid cavity. The fluid is set as a hydraulic fluid. The bulk stiffness of the cavity fluid is defined as the water bulk stiffness (2.2×10^4 MPa). This bulk stiffness means that the compressibility of the fluid due to pressure is negligible. As a result, the fluid cavity can maintain its volume regardless of confining pressure unless thermal expansion is applied.

The fluid is assumed to have the significant characteristic of thermal expansion to generate probe expansion. As a result, the mean coefficient of thermal expansion is the next property that needs to be defined. In the ABAQUS manual, the function of expansion volumetric change fluid due to thermal expansion can be explained as follows:

$$V = V_0 [1 + 3\alpha(T - T_{ref}) - 3\alpha(T_0 - T_{ref})] \quad \text{Eq.3.16}$$

In this function, V is the final volume of the fluid cavity due to the thermal effect (in mm^3). V_0 is the original volume of the fluid cavity (in mm^3). T and T_0 are the defined temperature in the step and the temperature in the in the step prior to the current stage respectively. In ABAQUS, the default temperature is 0 with no unit. The variable, α , in the equation is the mean coefficient of thermal expansion.

The third stage involves defining zero initial cavity temperature and cavity pressure in the Predefined Field dialogue. The process provides the reference temperature and the initial state of pressure to the programme for the automatic computation of the thermal expansion of the fluid cavity in the Membrane.

3.3.12.11. Pre-test Confining Pressures

The horizontal confining pressure is defined in this stage (Step 2). The confining pressure is defined by ‘pressure’ type of loading (compression) on the four surfaces of Soil parallel to the Z-axis of the Cube. In accordance with the chamber test design, a total number of five cases of confining pressure are defined. In the three isotropic cases, the confining pressures applied on all the Soil part surfaces are defined as 150kPa, 225kPa and 300kPa, respectively. In the two anisotropic cases, the confining pressures parallel to Y-axis direction remain at 150kPa. The confining pressures parallel to X-direction are adjusted to 225kPa in case 1, and 300kPa in case 2. The same arrangement of confining pressure is also set in the laboratory chamber test, which is explained in Chapter 4. All of the confining pressure is set as static loading; as a result, the default ‘ramp’ amplitude is applied to the loading.

3.3.12.12. Applying Thermal Expansion

After the confining pressures are applied in the previous step, the next step (Step 3) is to modify the temperature in the Predefined Field dialogue. The temperature in the fluid cavity is raised to 0.14. Based on the thermal expansion relationship in Section 3.3.12.12, this temperature rise leads to a volume increase of the fluid cavity. Due to the interaction between the fluid cavity surface and the cavity of the Soil, the fluid pressure is also raised up to the ‘lift-off’ pressure that initialises the expansion. Similar to the in-situ pressuremeter test in an ideal condition (perfect installation, undisturbed cavity, continuous homogeneous specimen), this ‘lift-off’ pressure represents the cavity

pressure. As the probe continues to expand, the fluid pressure keeps rising due to the stiffness of the soil until the specimen reaches plasticity. All of this pressure increase is calculated by the FEM programme.

3.3.12.13. Simulation Result

The results of the FEM computation consist of two forms of output. These are the Field Output and the History Output. The Field Output is the visualised output of specified value, displayed by a legend or arrows, at the final stage of each calculation interval (named as time step in ABAQUS). In the present simulation, it is preferable to observe the overall stress distribution or the general trend of displacement of the model through the Field Output.

The History Output is the digital data of the historical development of the intensity of specified measurements. In one set of the History Output, the value of this specified measurement is normally plotted against the calculation time on the X-Y chart. The combinations of these charts are able to provide correlations between two measurements. The present simulation applied the History Output to study the relationship between the cavity pressure and the volumetric strain during cavity expansion.

Field Output 1: Deformation Due to Cavity Expansion in Isotropic Conditions

The specimen deformation in both pre-cavity-expansion and post-cavity-expansion states subjected to isotropic horizontal confining pressures ($P_x=P_y=150\text{kPa}$) is shown as the Field Output 1 in Figure 3.28. All of the plan-views from the figure are taken from the mid-high of the cavity. Figure 3.28 (a) shows the pre-cavity-expansion deformation of the specimen. Although the magnitude of displacement around the corner of the chamber shows a significantly large value, the remaining part of the specimen performs radial deformation, which is similar to the specimen confined by the cylindrical chamber. Figure 3.28 (b) is the absolute value of post-cavity-expansion deformation obtained by subtracting the pre-cavity-expansion deformation in Figure 3.28 (a) from the total value of post-cavity-expansion deformation. The absolute value indicates the specimen deformation purely subjected to the probe expansion, which has the highest value at the contact surface with the Membrane, and then drops gradually along the radius from the centre of cavity. Figure 3.28 (c) shows the absolute value of

post-cavity-expansion deformation in elevation-view. From the elevation-view, the cavity expansion behaves in a ‘Chinese Lantern’ shape (Mair and Wood 1987). In detail, the edges of the cavity perform spherical cavity expansion, and the mid-portion of the probe performs cylindrical cavity expansion. This appearance of cavity expansion agrees with the theoretical assumption of the cavity expansion with a pressuremeter probe of finite length. The results prove that all the interpretations of the conventional cylindrical chamber tests are applicable in the newly designed isotropic/anisotropic pressuremeter chamber tests subjected to isotropic confining pressures.

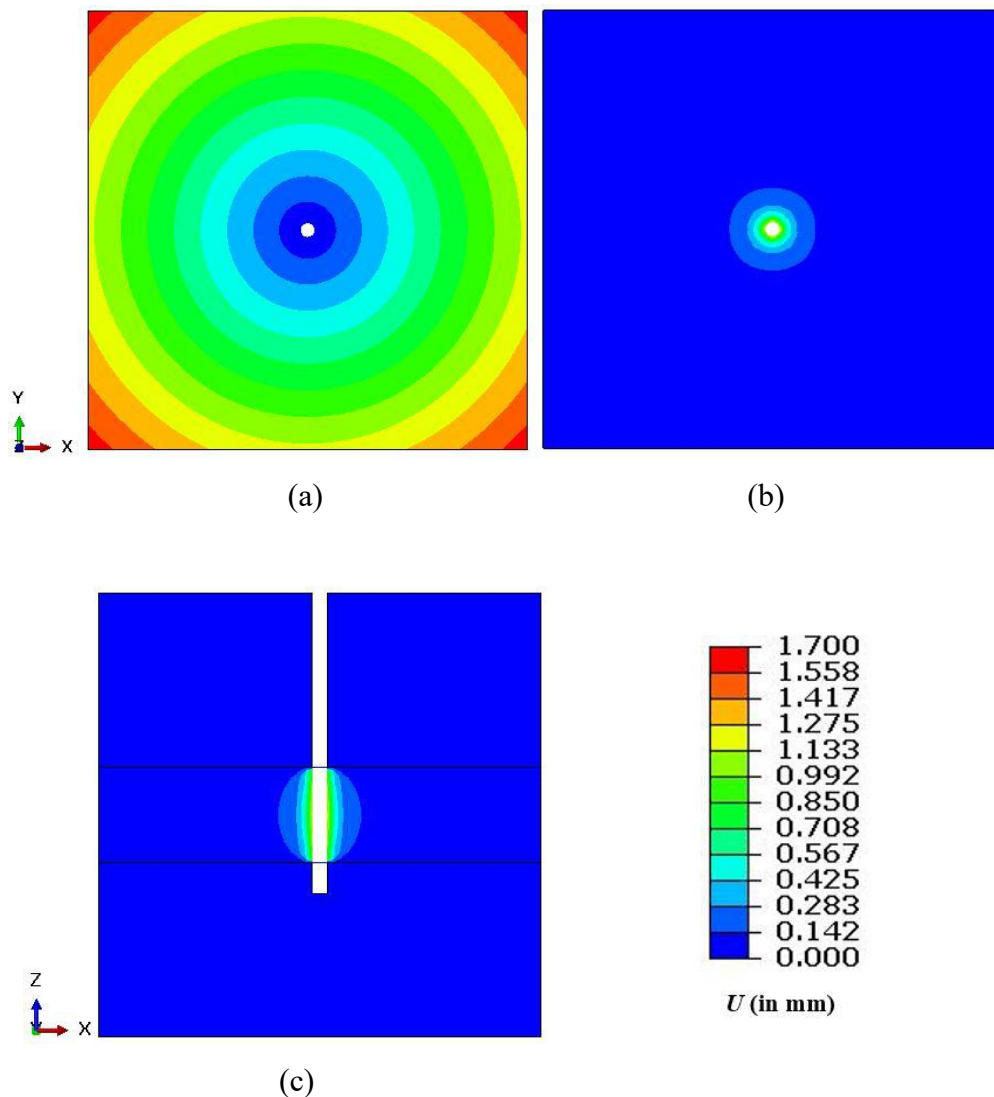
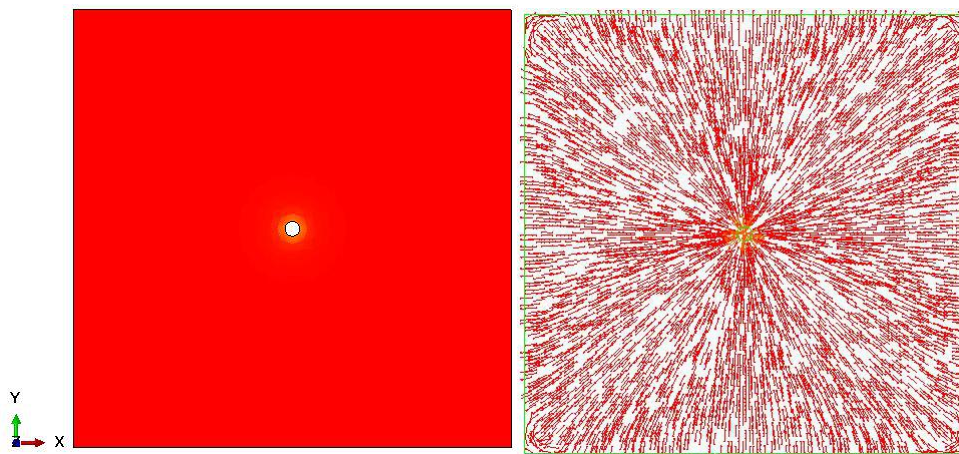


Fig.3.28. Deformation in isotropic condition ($P_x=P_y=150\text{kPa}$): (a) total value of pre-cavity-expansion in plan-view, (b) absolute value of post-cavity-expansion in-plan view, and (c) absolute value of post-cavity-expansion in elevation-view

Field Output 2: Stress Distribution Due to Cavity Expansion in Isotropic Conditions

The maximum principal stress distribution inside the specimen in both pre-cavity-expansion and post-cavity-expansion states subjected to isotropic horizontal confining pressures ($P_x=P_y=150\text{kPa}$) is shown as the Field Output 2 in Figure 3.29. The negative sign of the stress values indicates the internal stress is in compression. Therefore, the lower row in the legend shows higher value. Figure 3.29 (a) shows the pre-cavity-expansion maximum principal stress distribution in plan-view. The maximum principal stress distributes uniformly inside the specimen at around the isotropic confining pressure (150kPa), with the exception of slightly higher value at roughly 219kPa around the cavity as described in Section 3.3.11. The stress tensors are indicated in radial direction, which is the same as the specimen deformation direction. This means that before cavity expansion, the maximum principal stress in the chamber is the radial confining pressure applied on the cavity (and expansion probe). Figure 3.29 (b) shows the post-cavity-expansion stress distribution. The maximum principal stress value is increased to around 570kPa and limited by the plasticity of the material. Along radial direction, the maximum principal stress gradually decreases to the isotropic confining pressures on the boundary (150kPa). In the elevation-view around the cavity [Figure 3.29 (c)], the maximum principal stress is uniformly distributed around the mid-portion of the cavity, and spherically developed at edges.



(a)

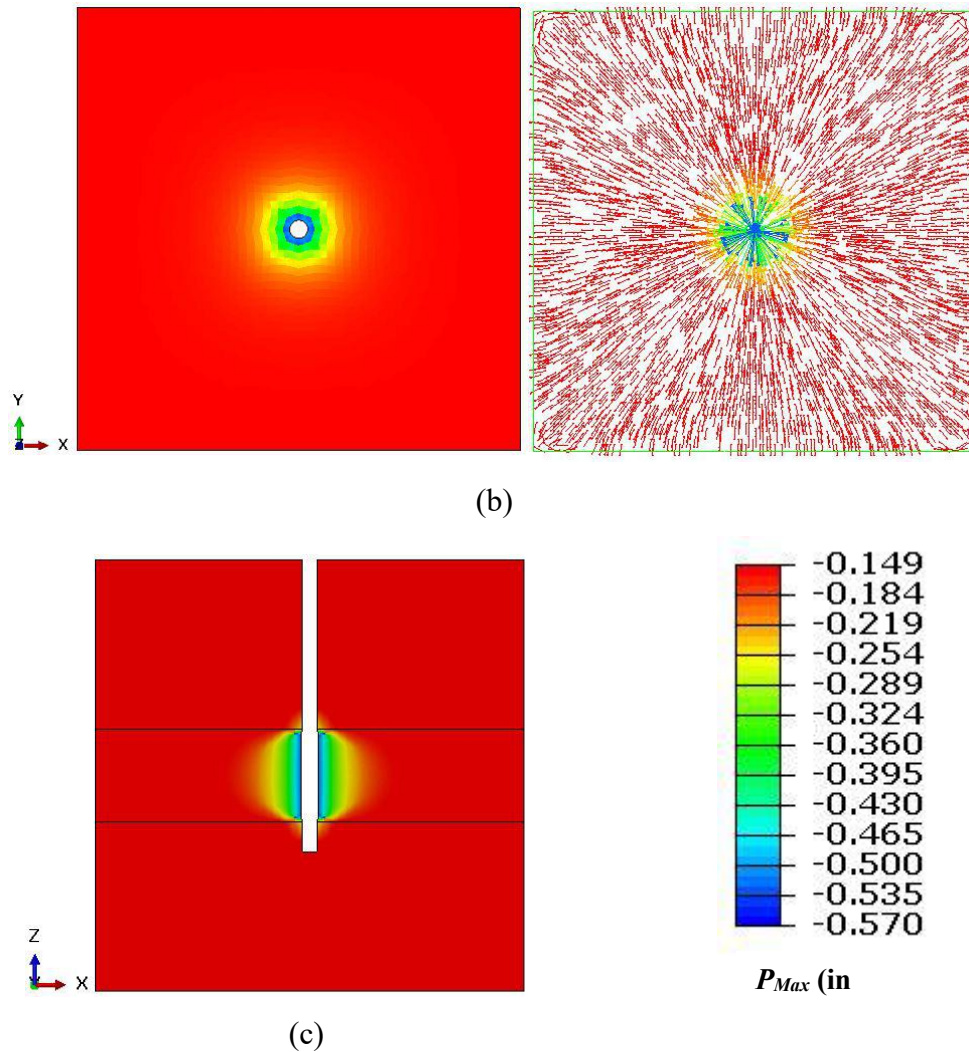


Fig.3.29. Maximum principal stress distribution in isotropic condition ($P_x=P_y=150\text{kPa}$):
 (a) pre-cavity-expansion value in plan-view, (b) post-cavity-expansion value in plan-view, (c) post-cavity-expansion value in elevation-view

Field Output 3: Deformation Due to the Cavity Expansion in Anisotropic Condition

The specimen deformation in both pre-cavity-expansion and post-cavity-expansion states subjected to anisotropic horizontal confining pressures ($P_x=300\text{kPa}$, $P_y=150\text{kPa}$) is shown in Field Output 3 in Figure 3.30. The pre-cavity-expansion deformation of the specimen is shown in Figure 3.30 (a). In anisotropic condition, the pre-cavity-expansion deformation is significantly different from the isotropic condition. The deformation is mainly controlled by the maximum confining pressure parallel to the X-axis (300kPa).

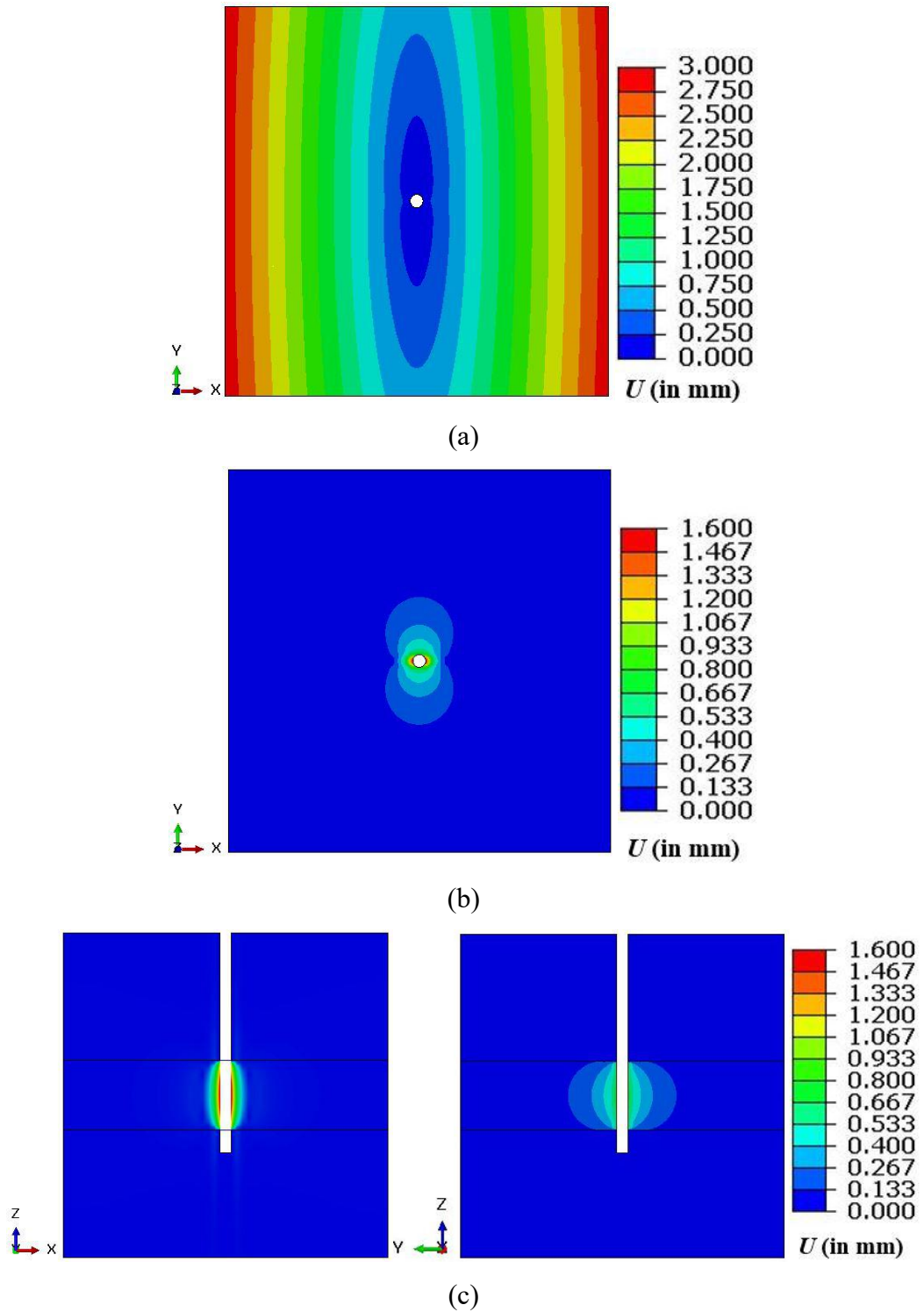


Fig.3.30. Deformation in anisotropic condition ($P_x=300\text{kPa}$, $P_y=150\text{kPa}$): (a) total value of pre-cavity-expansion in plan-view, (b) absolute value of post-cavity-expansion in plan view, and (c) absolute value of post-cavity-expansion in elevation-view

Figures 3.30 (b) and (c) show the absolute deformation of the specimen by subtracting the pre-cavity-expansion deformation from the total deformation after the

cavity expansion. The result shows the absolute specimen deformation due to cavity expansion. The maximum value of post-cavity-expansion deformation is parallel to the maximum confining pressure in X-axis (300kPa), with a magnitude nearly twice as the deformation parallel to the Y-axis (150kPa). However, the propagation of the absolute deformation is perpendicular to the maximum confining pressure (in X-axis).

Deformation of the contact between surfaces of the specimen and the probe is better demonstrated in Figure 3.31. As shown in this figure, the contact performs non-axisymmetric expansions in an ellipse appearance. More significant deformations are developed towards the maximum confining pressure (X-Axis). The behaviour is caused by the stress redistribution around the cavity, which can be analysed based on the stress distribution output.

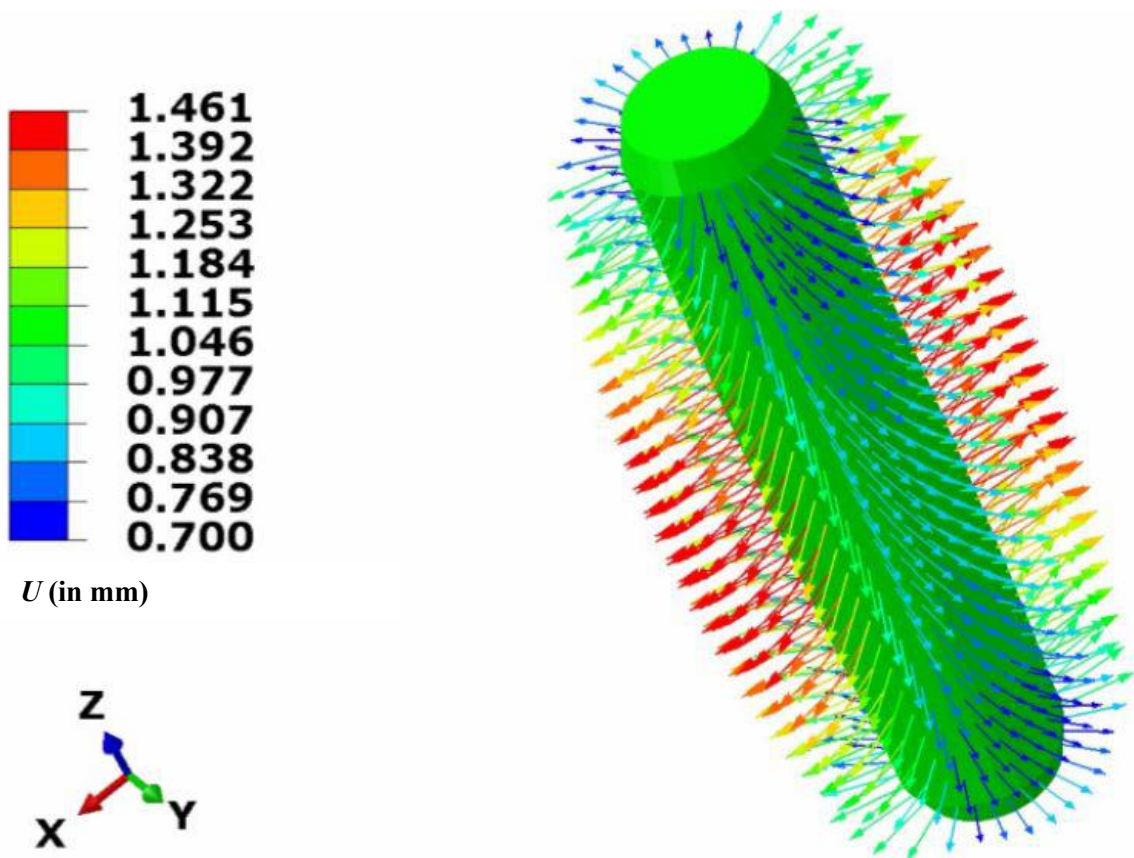
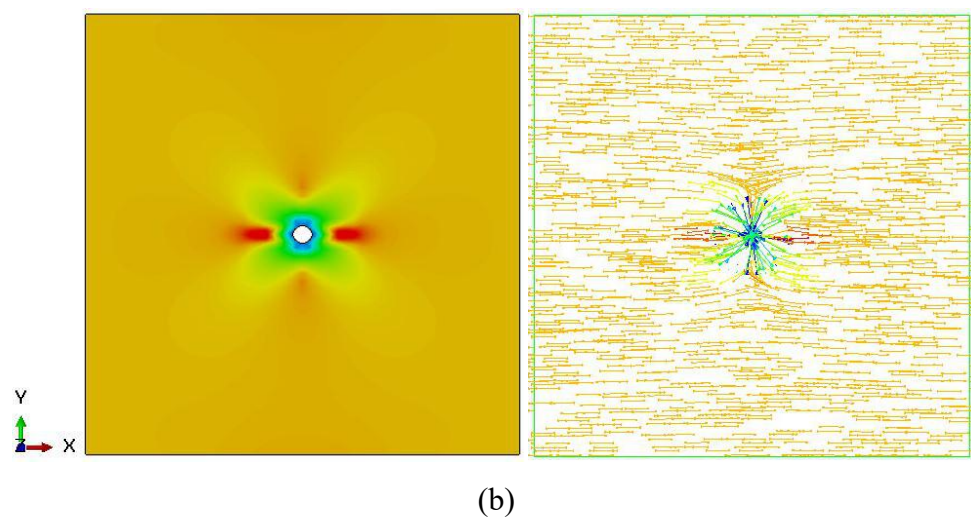
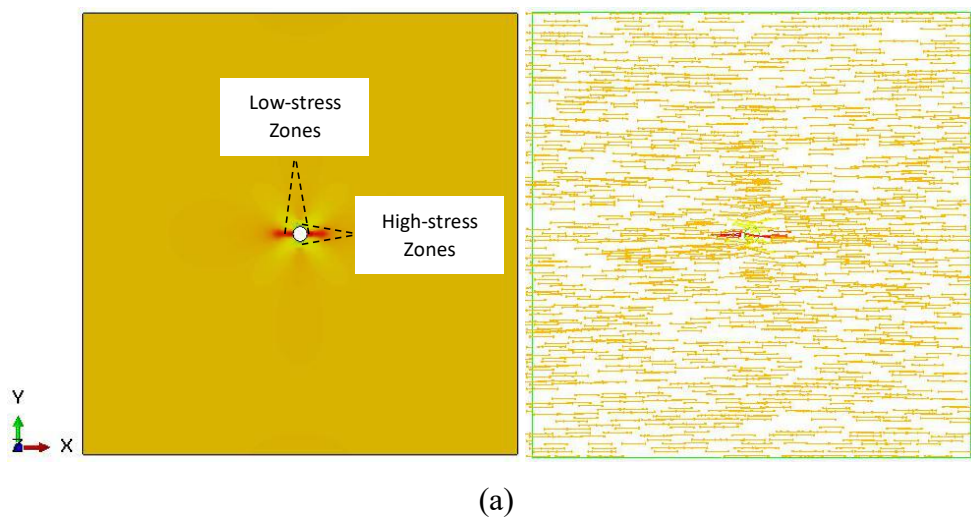


Fig.3.31. Membrane expansion under anisotropic confining pressure

Field Output 4: Stress Distribution Due to the Cavity Expansion in Anisotropic Condition

The maximum principal stress distribution in both pre-cavity-expansion and post-cavity-expansion states subjected to anisotropic confining pressures is shown in Figure

3.32. The negative sign from the legend indicates the stress is all in compression. Figure 3.32 (a) shows the pre-cavity-expansion stress distribution. Most region of the specimen has the maximum principal stress value equal to the maximum confining pressure (300kPa). As shown in the figure, two low-stress zones with maximum principal stress at around 210kPa can be found next to the cavity on the X-Axis of symmetry, while two high-stress zones with maximum principal stress at around 320kPa can be found on the Y-Axis of symmetry around the cavity. All the stress tensors orientate the maximum confining pressure directions. Figure 3.32 (b) shows the maximum principal stress re-distribution in post-cavity-expansion state. The orientation of the maximum principal stress around the cavity changes from the maximum confining pressure direction to the radial direction towards the cavity centre, with uniform magnitude at around 640kPa. The elevation-views [Figure 3.32 (c)] show identical stress distributions along the cavity longitude direction except both edges.



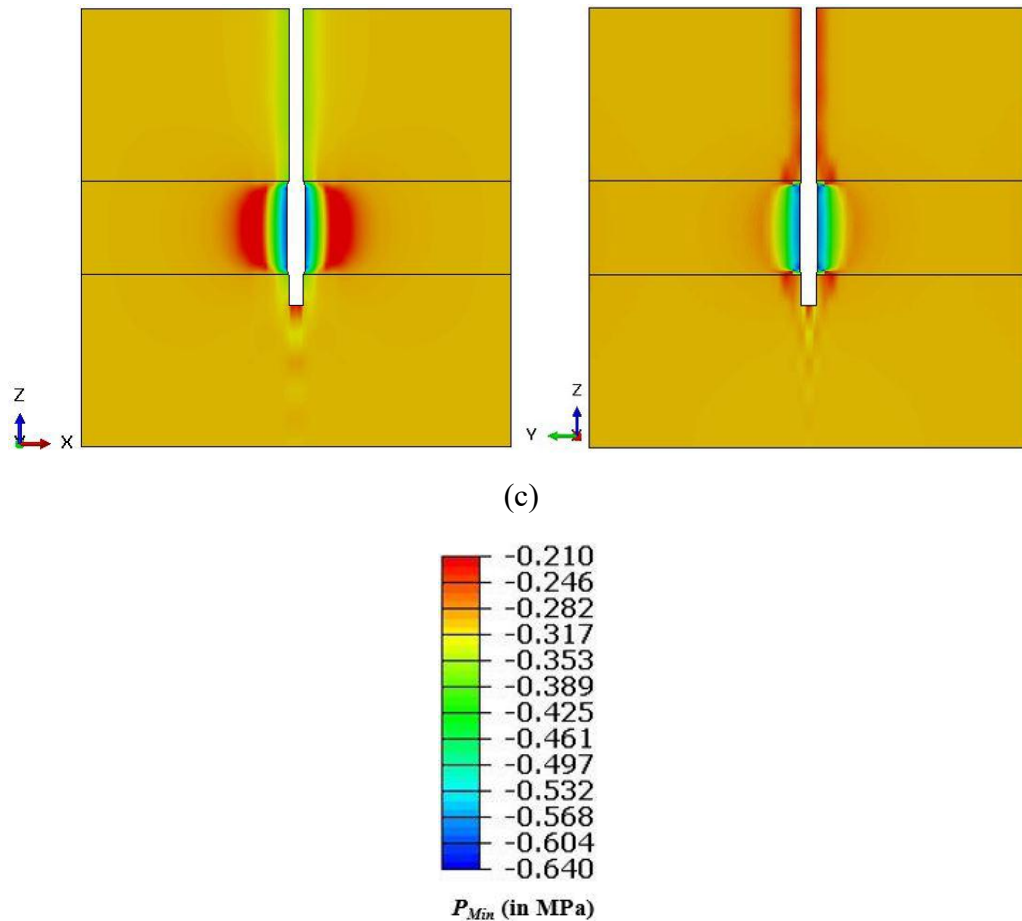


Fig.3.32. Maximum principal stress distribution in anisotropic condition ($P_x=300\text{kPa}$, $P_y=150\text{kPa}$): (a) pre-cavity-expansion value in plan-view, (b) post-cavity-expansion value in plan-view, (c) post-cavity-expansion value in elevation-view

History Output: Lift-off Pressures for the In-situ Stress Measurement

Analytical deduction in Section 3.3.11 suggests that there are differences between the confining pressure and the cavity pressure in isotropic/anisotropic pressuremeter chamber tests based on the plane-strain assumption. The Abaqus History Output in this section is used to verify the difference between the three-dimensional and finite length probe scenario. For this purpose, the volumetric expansions and the pressure increases of the fluid cavity are plotted to investigate the ‘lift-off pressure’ and estimate the cavity pressure.

In idealised pressuremeter testing, the probe has no volumetric expansion before the cavity pressure is reached by the probe. The pressure at the time when the probe expansion is initialised is called the ‘lift-off pressure’. Since the present FEM

simulation is similar to the realistic test condition, the fluid cavity pressure at the time when fluid cavity volume increases can reasonably represent the ‘lift-off pressure’.

Figure 3.33 shows the pressure-volume change curves from the History Output in all confining stress scenarios. The results show that the cavity pressures are higher than the confining pressures in all cases. The cavity pressure for each confining pressure scenario is shown in Table 3.2.

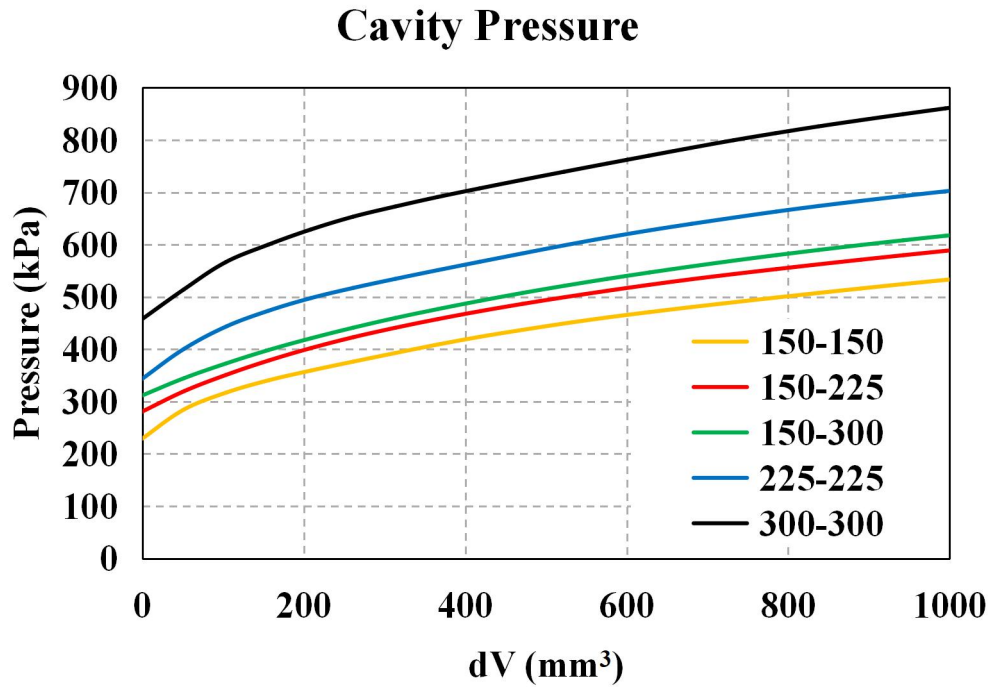


Fig.3.33. Pressure-volume change curves from the FEM history output

Table 3.2. Comparison between the confining pressures and the cavity pressure by the ‘lift-off’ method in FEM

P_x (kPa)	P_y (kPa)	$P_{average}$ (kPa)	$P_{lift-off}$ (kPa)	$P_{lift-off}$ Vs. P_x	$P_{lift-off}$ Vs. P_y	$P_{lift-off}$ Vs. $P_{average}$
150	150	150	228	+52%	+52%	+52%
150	225	187.5	280	+86.7%	+24.4%	+49.3%
150	300	225	311	+107.3%	+3.67%	+38.2%
225	225	225	342	+52%	+52%	+52%
300	300	300	456	+52%	+52%	+52%

3.3.12.14. Discussion

The stress concentration of the chamber-confining pressures around the cavity is investigated through three-dimensional finite element modelling. The concentrated cavity stress ($P_{lift-off}$), which is actually the magnitude of the concentrated stress around the cavity before expansion, is 52% higher than applied confining pressures in all the isotropic cases, $P_{lift-off}=1.52 \times P_x$ (or P_y). However, the analytical solution presented by Equation 3.14 in Section 3.3.11.2 using the same Poisson's ratio of 0.25 calculates the $P_{lift-off}$ of 87.5% rather 52%. The difference is due to the absence of the vertical stress-strain impact of the analytical solution.

The anisotropic confining stress provides stress-degradation zones near the cavity, as the Field Output shows. These stress-degradation zones reduce the concentration of stress around the cavity. Therefore, the effect of the stress concentration is less significant in anisotropic confining stress conditions. The larger difference between two principal confining pressures provides less disparity between the cavity pressure and the mean confining pressure.

3.4. Conclusion

The developments of miniature expansion probe and the cubic shape chamber, are introduced in this chapter. This starts from their backgrounds and concepts, then it moves to their constructions and fabrications. Finally, the chapter finishes with the calibration of the apparatus.

The miniature expansion probe developed in the project is meant for the use in both the chamber test and UET. This probe is much smaller than other pressuremeter probes reviewed in Chapter 2. For the chamber test, the down-sized cavity expansion reduces the boundary effects. For the UET, a down-sized probe means the reduced specimen size.

The anisotropic chamber is specially developed for the generation of stress anisotropy. Due to its shape and the use of pneumatic loading mechanism, the chamber is able to generate anisotropic stresses in the form of three independent orthogonal stresses. Despite the significance of anisotropy, the resultant cavity pressure, in terms of cylindrical cavity expansion during the pressuremeter test, is however revealed to be isotropic. The difference between applied pressure and cavity pressure is explained in

both analytical solutions and numerical simulations. The results of numerical simulations are applied as the reference pressure for the laboratory test programme.

4. Laboratory Test Programme

4.1. Anisotropic Pressuremeter Chamber Tests

4.1.1. Introduction

This section presents the pressure controlled laboratory pressuremeter tests in the anisotropic pressuremeter chamber. A dried, medium grain, semi-compacted sand is chosen as the test material. Both isotropic cases and anisotropic cases of horizontal confining pressures are considered. The chamber tests in this research aim at 3 goals:

First, in the isotropic horizontal confining pressure cases, the geotechnical parameters of the medium grain sand are interpreted. These parameters include (1) the unload-reload stiffness, G_{ur} , which can be converted to the sand shear modulus, G ; (2) the friction angle, ϕ ; and (3) the dilation angle, ψ . The unload-reload stiffness (G_{ur}) represents the elasticity of the soil. The friction angle (ϕ) represents the plastic behaviour of the test sand. The dilation angle (ψ) is a parameter represents the characteristic of the volumetric strain when material undergoes shear.

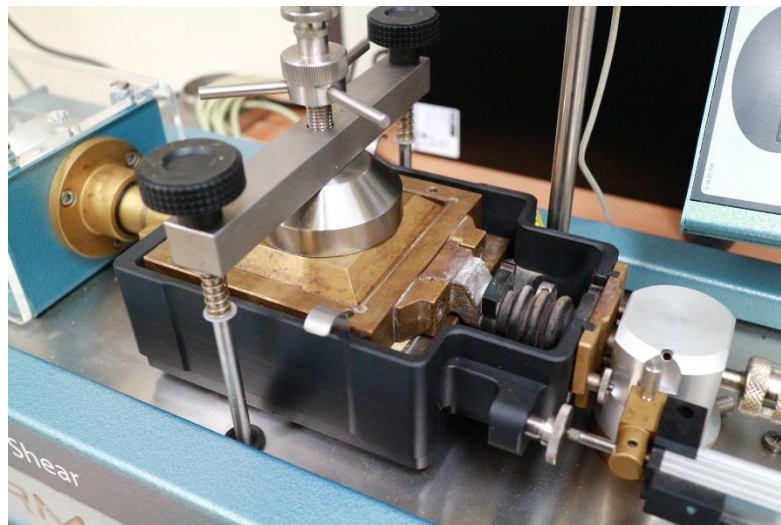


Fig.4.1. Standard direct shear test apparatus

Second, the friction angle interpreted from pressuremeter test results are verified by the friction angle from the direct shear tests. The direct shear test showed in Figure 4.1, is the standard test to estimate material's shear strength. The direct shear test is employed in this project to verify the friction and dilation angles from the pressuremeter chamber test. During the standard direct shear test, 3 normal stress levels corresponding to the horizontal isotropic confining pressures in the miniature

pressuremeter chamber tests are applied on the top of the sample. As a result, the peak and constant volume friction angles were obtained by plotting the shear stress versus the normal stress. The detail of the standard direct shear test and the verification results is concluded in Section 4.1.8.1.

Third, the ratio of the horizontal confining pressures in two principal directions was varied to study the impact of the anisotropy of the horizontal confining pressures on the interpretations of the sand parameters. The severity of the anisotropic impact on the interpreted results is to be described through this study. More precisely, the results from the research present whether the interpretation of the pressuremeter test is governed by the minimum horizontal stress, the maximum horizontal stress, or a combination of both.

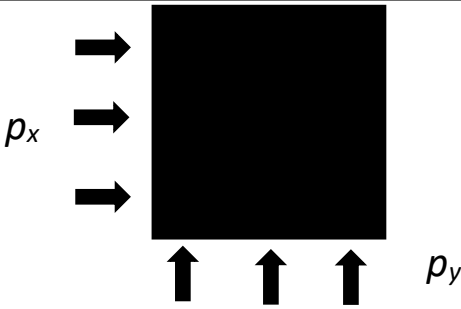
4.1.2. Test Design

Five test groups were set up with different horizontal confining pressures. Each group of test repeated three tests to ensure the consistency of the results. Isotropic horizontal pressures were applied to test groups 1, 2, and 3. In these tests, the horizontal confining pressures in two principal directions, P_x and P_y , were set to 150kPa in group 1, 225kPa in group 2, and 300kPa in group 3. The anisotropic horizontal pressures were applied to test groups 4 and 5. In these tests, one of the two horizontal confining pressures in the two principal directions, P_y , was maintained at 150kPa. The horizontal confining pressure in the other principal direction, P_x , was regulated at 225kPa in group 4, and 300kPa in group 5. These setups provided a horizontal stress ratio of 1.5 in group 4, and 2 in group 5.

This concentration of stress causes the difference between applied confining pressure and cavity pressure. This difference is presented in the finite element stress analysis in Section 1.3.1.2. Based on the finite element analysis, if the isotropic pressure is 150kPa, the actual stress around the cavity is 228kPa, giving the cavity a confining pressure 52% higher than the confining pressure applied on the specimen boundary.

The vertical confining pressure is achieved by fixing the bottom boundary. When the horizontal pressures are applied to pressurise the specimen, vertical deformation is prevented by the bottom (plate) and top (glass) boundaries of the chamber.

Table 4.1. Test plan and applied isotropic/anisotropic confining pressures



Group	P_x (kPa)	P_y (kPa)	P_x/P_y	Expected Cavity Pressure from FEM (kPa)	Number of Tests
1	150	150	1	228	3
2	225	225	1	342	3
3	300	300	1	456	3
4	225	150	1.5	280	3
5	300	150	2	311	3

4.1.3. Test Material and Specimen Preparation

4.1.3.1. Material Characteristics

The test material is a medium grain sand. Although the pressuremeter test can be applied to both sand and cohesive materials, there are two major reasons for using sand in the chamber tests. Firstly, the compaction of the cohesive specimen is time-consuming due to the time-dependent consolidation issue. In contrast, compaction for sandy material can be done instantly. Therefore, using sand to study the pressuremeter chamber test is more time efficient. Secondly, since the sand particles have no cohesion, they have more freedom to move during compaction. Therefore, it is easier to achieve homogeneous sand specimens than it is to achieve cohesive material specimens while preparing the samples. Before the test, the sand was oven dried. Given the small diameter of the pressuremeter probe (6mm), the sand was then sieved to under 2mm to obtain fine and very fine sand. The 0.0625mm (No.230) sieve is also used to exclude possible silt particles. The results of the sieve analysis are shown in Figure 4.2.

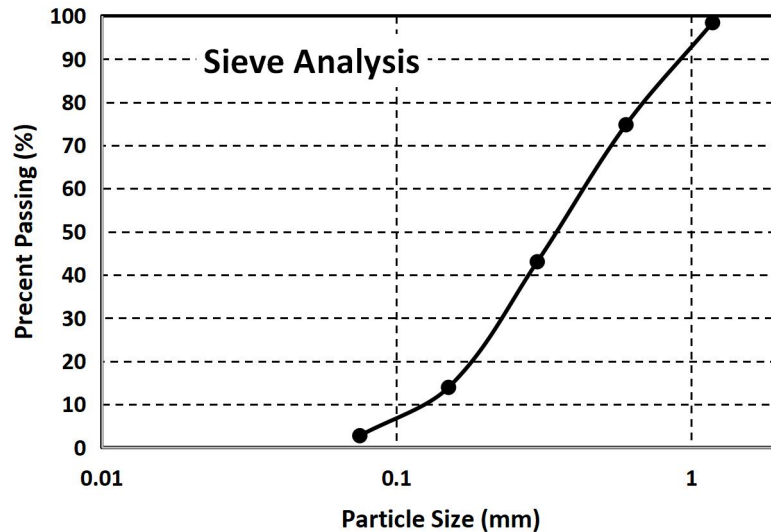


Fig.4.2. Particle size distribution of test sand

4.1.3.2. Material Compaction

Results from the pressuremeter test, including the material's parameters, were obtained based on interpretations of the pressure-strain graphs. In the pressuremeter test in sand, the two main factors that affect the shape of pressure-strain graphs are the (a) confining pressure and (b) density of the specimen. The specimen compaction method used for this research is the an vibration method. During the internal vibration compaction method, the vibratory rod is inserted into the specimen to vibrate the sand particles to a higher density. The vibratory rod goes through the length of the specimen. Therefore, the technique also allows for a uniform density along the vertical length of the specimen. The size of the rod is shown in Figure 4.3. Before the compaction, two movable side plates were fixed vertically and horizontally with their air cushions with G-clamps. As mentioned in the previous chapter, a textile bag was placed inside the chamber to prevent sand particles from leaking from the side of the chamber.

The chamber was first filled up with the sand specimen. Following this, 25 vibration holes were pre-located evenly on the surface of the specimen. Each hole is 5 cm from the next one. Gaps of 5 cm were added between the vibratory rod and all the sides of the chamber in order to avoid damage to the textile bag and the frame of the chamber. These gaps were marked with white tape (Figure 4.4). The pattern of vibration was unified from the bottom left corner to the upper right corner (Figure 4.5). The vibration rod was vertically inserted into the specimen and vibrated with the drill for 5 seconds. When the first 25 holes were vibrated, there was around 10 cm gap between

the surface of the specimen and the chamber surface due to the change in the local density. This settlement was recovered with the addition of around 500g of sand to the top before the second round of compaction. After four rounds of compaction, the settlement is negligible. The sand surface was then filled and trimmed with around one scoop (around 200g) of sand to align it with the chamber surface. After the compaction, the total weight of sand inside the chamber was around 51.9 kg, and the dimension of the chamber was 9000cm. The overall density of the sand inside the chamber after the compaction was 1922kg/m³.

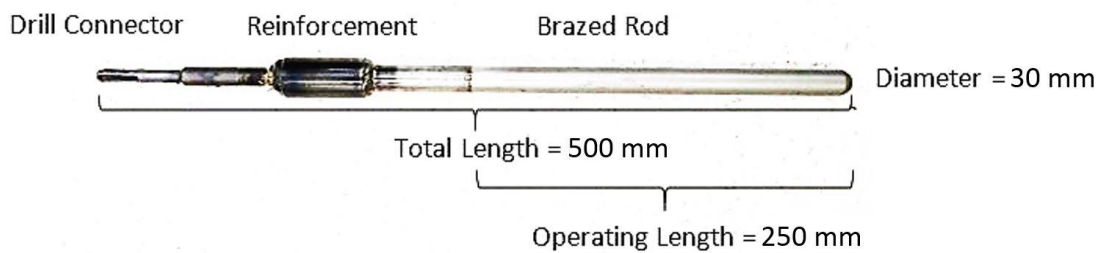


Fig.4.3. Vibratory hummer rod

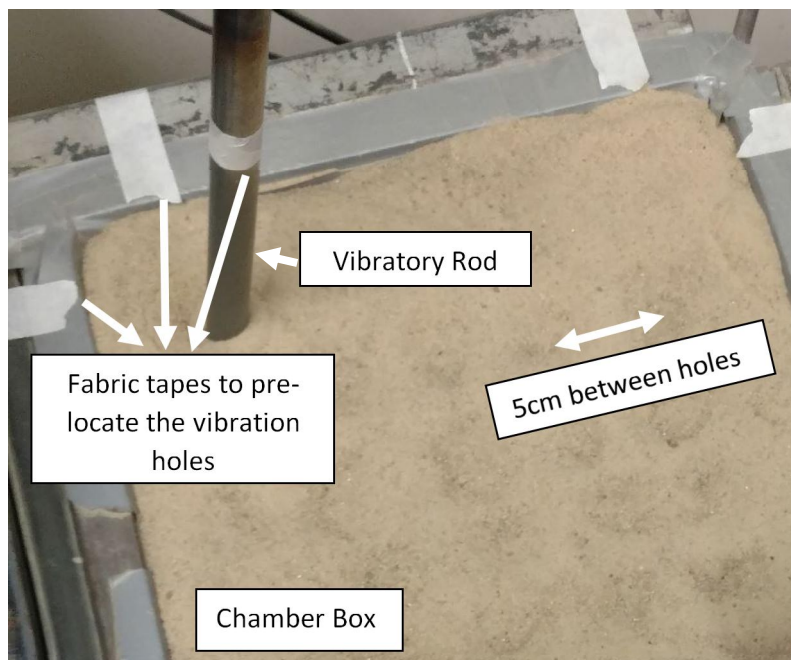


Fig.4.4. Internal vibration technique

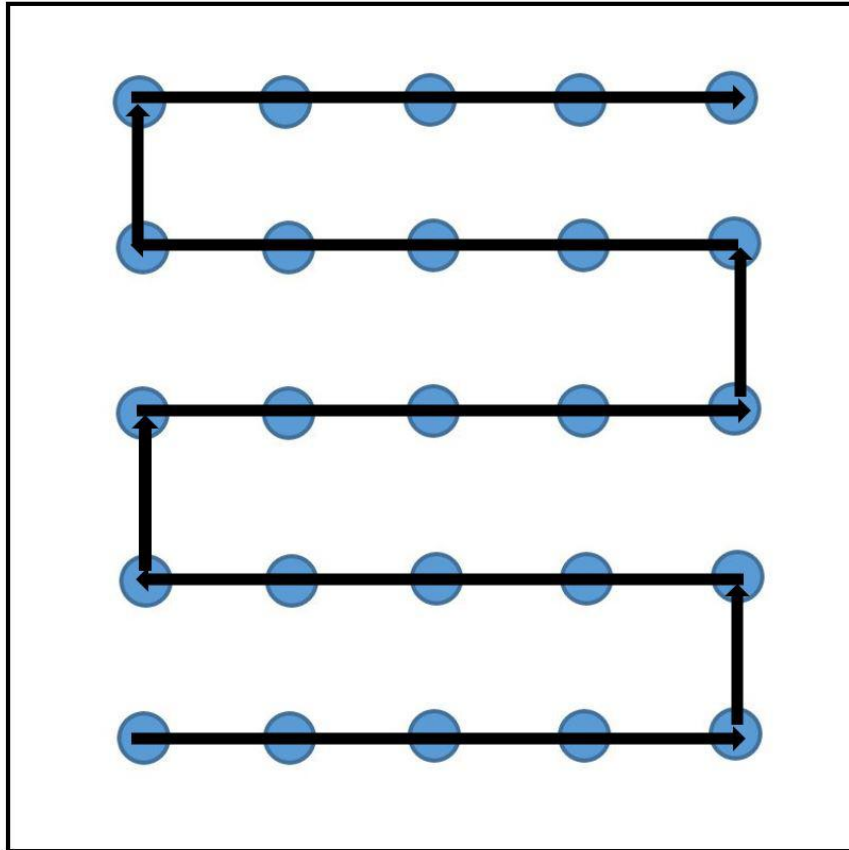


Fig. 4.5. Compaction pattern for sand specimen

4.1.4. Calibration and Installation

4.1.4.1. Hose Calibration

During the pressuremeter chamber test, probe expansion requires pressurised fluid from the pressure-volume transducer (introduced in Section 4.1.5). In addition, during the unloading steps, the discharged water is withdrawn by the transducer. The pressurised fluid is circulated by a special high-pressure hose that connects the pressure-volume transducer to the probe. Figure 4.6 shows the high pressure hose used for the test. The length of the hose is 2.4 m. The quick coupling for the transducer connection and the screw connection for the probe are excluded in the measurement. The internal diameter of the hose is 3.2 mm, allowing adequate flux for the expansion. The external diameter of the hose is 7.9 mm due to the braid for the reinforcement. The braided construction of the hose makes it achieve a pressure of 8 MPa of working capacity while minimising hose deformation during the test.

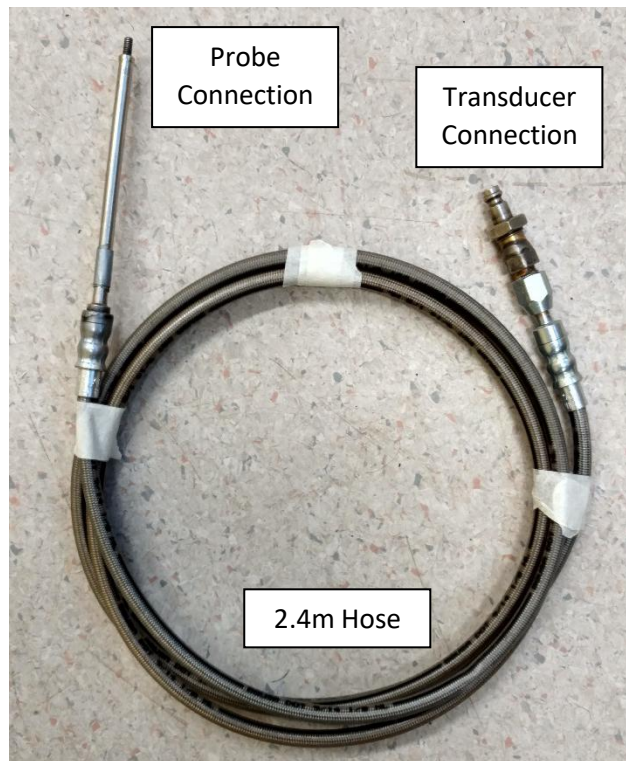


Fig.4.6. High pressure hose

When the hose is connected to the transducer and the probe, the installation may introduce air bubbles into the system. The air bubbles can significantly affect the quality of both the calibration and the test. Hence, the system needs to be de-aired right after installation. The first step of de-airing involves applying de-aired water to saturate the transducer, the hose, and the probe. After saturation, the system keeps being flushed by the de-aired water several times, eliminating trapped air bubbles. During flushing, the transducer needs to be shaken fully for a better result. When there are no more visible air bubbles, the de-airing is assumed to have finished.

Due to the elastic expansion of the hose, it is inevitable to have perimeter increments of the hose during pressurisation. As a result, an increasing amount of fluid is taken in by the hose expansion, thereby generating a volume measurement discrepancy. There is a discrepancy between the displayed volume lost from the transducer and the actual volumetric increase of the probe. In pressuremeter testing, such an error needs to be corrected through hose calibration. To prepare for hose calibration, the probe is inserted into the calibration hose, as shown in Figure 4.7. After de-airing, the probe is inserted into a rigid steel tube. During the insertion, lubricating grease is applied over the probe membrane to prevent the membrane from being

stretched. A series of pilot tests show that the change of pressure rate does not affect the calibration results. However, a slower pressure rate (less than 120kPa/min) provides enough pressure-volume readings for the development of a smooth calibration curve, which is explained later in this paper. In this setup, given that the membrane is fully confined by the rigid tube, the volume change was fully due to the hose expansion. Hose calibration is repeated several times to make sure that the results are similar each time. The calibration curves are shown in Figure 4.8.



Fig.4.7. Inserting probe into calibration hose

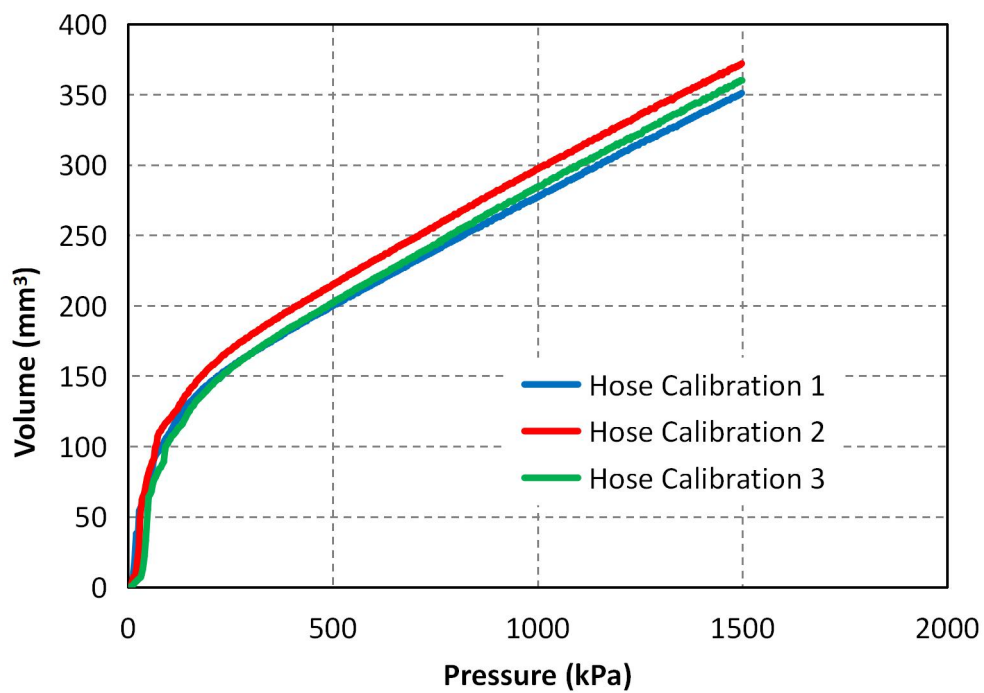


Fig.4.8. Hose calibration strain-stress curves

In hose calibration, the data points from the calibration are not identical to the pressure values from the real tests. Therefore, a pressure-volume change function needs to be built in order to obtain the correct hose expansion volume in accordance with the exact pressure readings of the real test. The graph in Figure 4.8 appears to be curved at a low pressure and linear at a high pressure. This trend can be fitted into the curve of a one-sided, total binding equation, which can be expressed as follows:

$$dV_{calibration}(ml) = B \frac{Pressure(kPa)}{C+Pressure(kPa)} + D \times Pressure(kPa) + E \quad \text{Eq. 4.1}$$

The $dV_{calibration}$ denotes the volume change from the hose expansion calibration on the Y-axis of the graph. The *Pressure* in the equation refers to the pressure reading on the X-axis of the graph. The maximum specific binding, B , and the equilibrium binding constant, C , define the shape of the curvature; the nonspecific binding, D , can adjust the slope of the linear portion. The amount of nonspecific binding, E , can shift the curve up and down. The total binding equation can adjust these four variables to achieve a fitted curve to the hose calibration results (Figure 4.9).

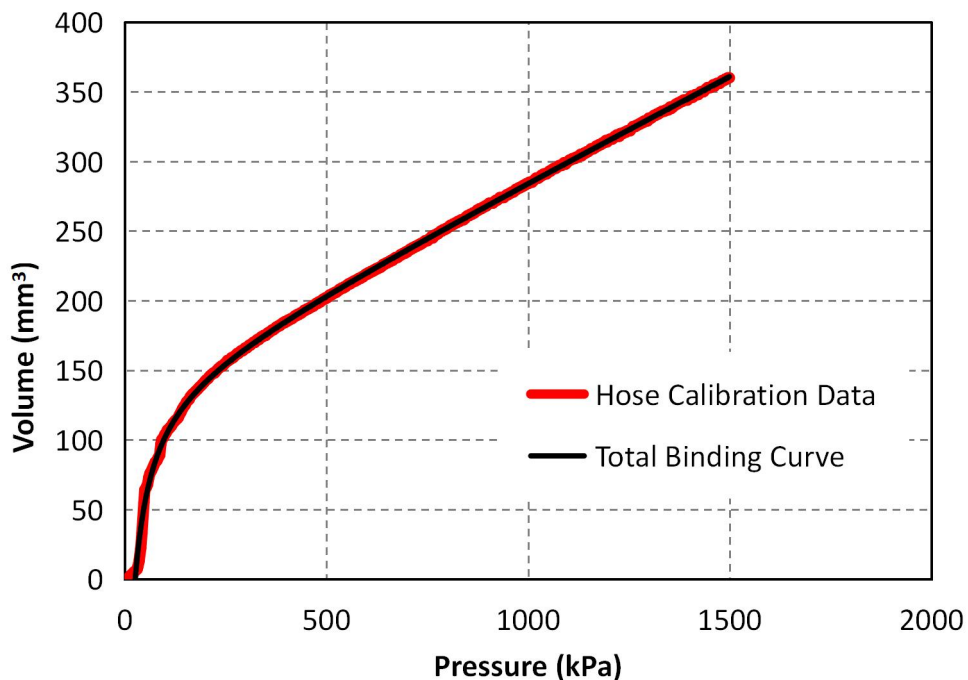


Fig.4.9. Curve fitting for hose calibration data

$$B = 155.9 \text{ mm}^3, C = 39.61\text{kPa}, D=0.1503 \text{ mm}^3/\text{kPa}, E=-17.78 \text{ mm}^3$$

4.1.4.2. Membrane Calibration

During the miniature pressuremeter chamber test, the pressure indicated by the transducer reflects the soil's resistance against probe expansion. However, the stiffness of the probe's membrane also generates resistance against expansion during the test. Both the resistances from the soil and membrane are collectively recorded by the transducer, thus generating an error in the results. Therefore, extra calibration is needed to differentiate the membrane resistance pressure from the soil's resistance pressure. The setup for the calibration of membrane expansion is shown in Figure 4.10. The probe is placed on the vertical stand at the fully unloaded, de-aired, and saturated condition. One cycle of membrane expansion is set up by the control panel of the transducer. The rate of pressurisation is defined by the total test time. As the expansion is fully elastic, any pressure rate should lead to similar test results. It is, however, recommended that one allow more than 20 seconds for expansion to achieve more data readings. To prevent over-expansion, the calibration finishes when the probe reaches 100kPa. This pressure at the final stage gives the membrane a volumetric expansion of around 16% of the probe's total volume. The calibration results are plotted as the pressure in kPa (Y-axis) against volume in mm³ (X-axis), shown in red dots in Figure 4.10.

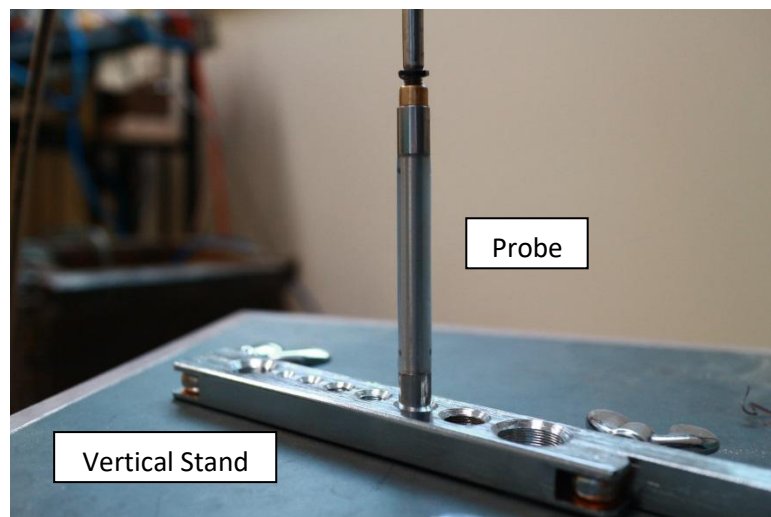


Fig.4.10. Preparation for membrane calibration

The results indicate a linear pressure-volume relationship for the membrane's expansion. There was expansion before 13kPa, meaning the 'lift-up' pressure required to generate initial movement of the membrane was 13kPa. A linear function was fitted

to the graph, as Figure 4.11 shows. With the linear function, any pressure resistance from the membrane due to a specific amount of volumetric expansion can be deducted, and thus excluded from the main pressuremeter test results.

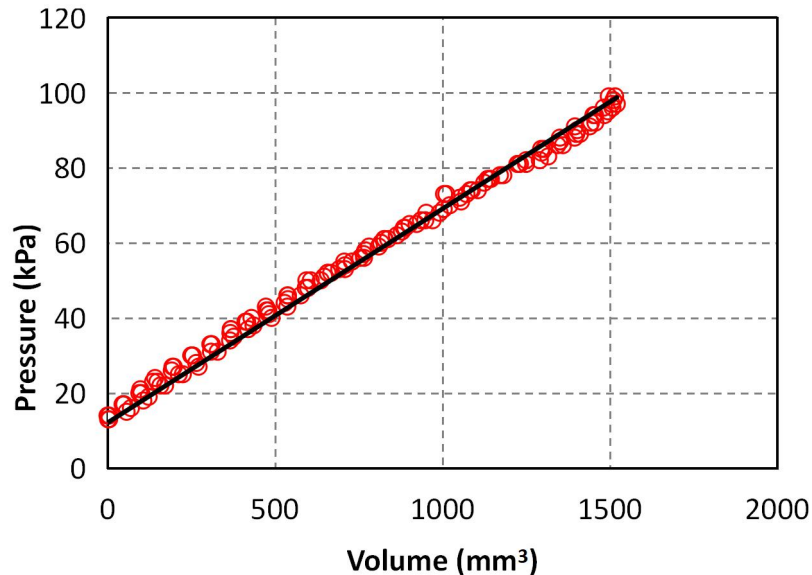


Fig.4.11. Membrane calibration stress-strain

4.1.4.3. Probe Installation

In this step, the de-aired and calibrated probe is installed at the centre of the compacted sand specimen. The installation techniques for the pressuremeter test are described in Chapter 2. As the sandy materials are easy to collapse, the Menard-type pressuremeter probe is not suitable to be used for testing sand. The two appropriate installation techniques for a pressuremeter probe in sandy materials are (1) self-boring installation and (2) push-in installation. The self-boring type of installation requires a rotary cutter to be installed on the probe. In this case, the cutter needs to be very small in order to fit on the general size of the probe. Although the particles of sand are relatively large compared to the size of the probe, the miniature scale cutter would be feeble. Therefore, the application of the self-boring type of installation is unpractical for this chamber test. Instead, installation can be done using the push-in technique to insert the pressuremeter probe into the soil. During the push-in installation of the pressuremeter probe, the local density around the probe may increase. This is especially significant in in-situ pressuremeter test scenario. In this research project, however, since the horizontal confining pressures are not applied during installation, the sand can be regarded as being in un-confining condition. Therefore, the push-in technique would

not increase the local density considerably. Before the installation, the probe connected to the hose needs to go through the small central opening of the top transparent cover and the top webbing of the chamber so that the cover and the frame can be moved to the top of the chamber without disturbing the probe once the installation is done.

There are four principles that need to be taken into account when installing the probe. First, the probe needs to be centralised in the middle of the sand. This is named Horizontal Centralisation. It is achieved by positioning the probe using a concave-corner, square timber block with half of the side length of the sand specimen, as showed in Figure 4.12. The Horizontal Centralization ensures that the top cover and the top webbing can be aligned with the top margin of the chamber correctly. It also ensures that the stress around the probe and the assumed stress distribution of the cavity at the central position of the chamber are uniform.



Fig.4.12. Horizontal centralization of the pressuremeter probe

Second, the probe needs to be inserted up until the middle depth of the sand. This principle is called Vertical Centralisation. Vertical Centralisation ensures that the probe is located at the middle height of the specimen. It is achieved by using a marker to highlight the right length of the hose.

Third, the expansion probe needs to be vertically inserted into the soil. This is done by using a tube level during the installation process, as Figure 4.13 shows.

Maintaining the probe in a vertical position ensures that the stress distribution along the length of the pressuremeter probe is uniform, thus controlling the quality of the test.



Fig.4.13. Vertical probe installation

The fourth principle prevents sand leakage from the top opening of the transparent plate. As described in Section 3.2.6.4, the components on top of the chamber for the vertical confining pressure are the transparent plate and the top webbing. There is an ovoid hole on the transparent plate for probe installation. Therefore, without any sealing, the sand particles would escape through the gap between the probe and the ovoid hole side wall. The remedy for sand leakage is to seal the opening with two metal gaskets. The gaskets are square metal plates as shown in Figure 4.15. Each of the gaskets has one slot that tightly fits the diameter of the hose. Therefore, when the two gaskets are embedded into the hose, they seal the top opening around the hose, while still allowing horizontal movement during the test. For better horizontal flexibility, lubrication is applied between the gaskets and the interface between the top gasket and the plate.

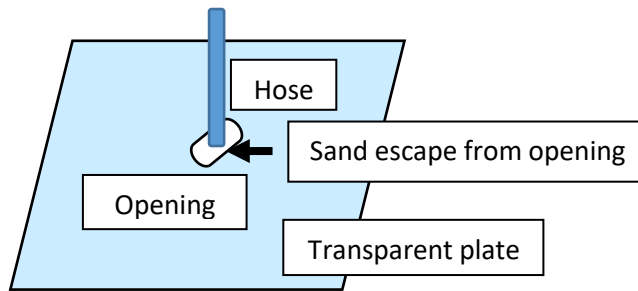


Fig.4.14. Top transparent plate with opening

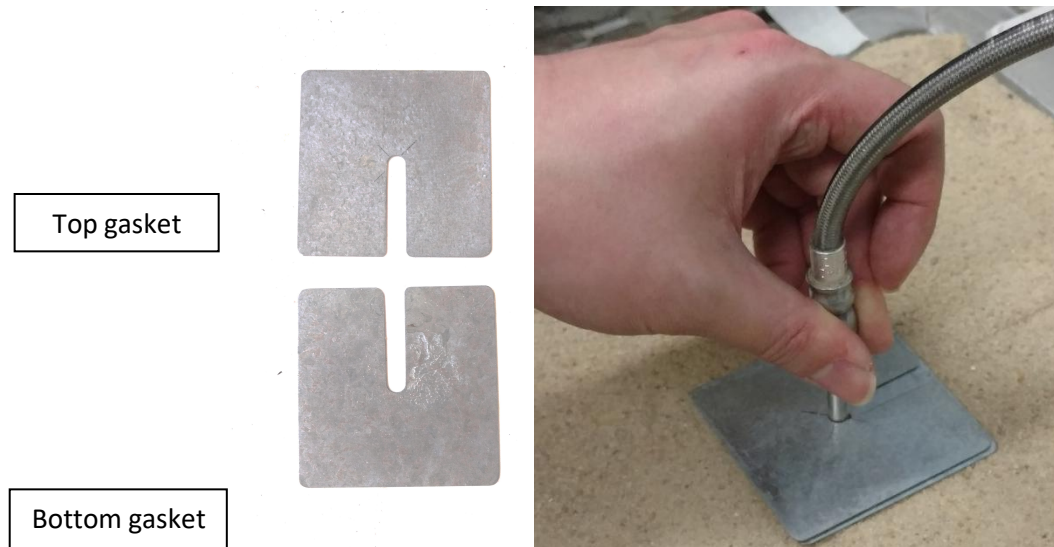


Fig.4.15. Metal gaskets to stop sand leakage from top

4.1.4.4. Top Webbing Installation

Following the placement of the transparent plate, the top webbing is installed on the chamber to reinforce the transparent plate. Since the pressuremeter probe is inserted into the sand specimen without confining pressures, the probe needs to be free from vibrations, rotations, and any other disturbance. The top webbing is fastened by eight metal U-clamps as discussed in Section 3.2.6.5 and shown in Figure 4.16. Once the installation is finished, the sand specimen and the probe can be regarded as well confined with zero pressure and are ready for the chamber pressuremeter test.

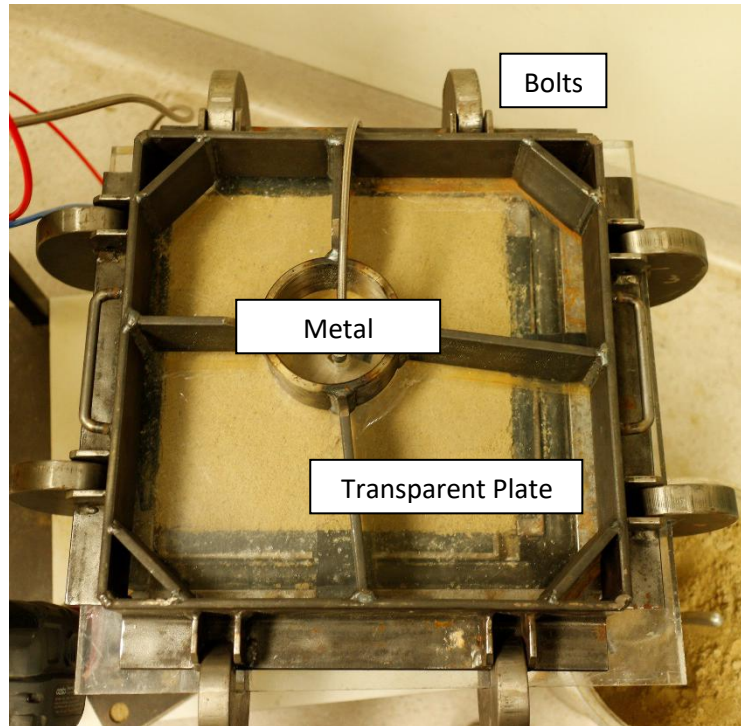


Fig.4.16 Top webbing installation

4.1.5. Pressuremeter Test Procedure

4.1.5.1. Apply Air Pressure

The pneumatic anisotropic pressuremeter chamber requires confining pressure from the external air-supply system. The air supply system is discussed in Chapter 3.2. The air resource comes from the laboratory air compressor. Consequently, the first step to apply air pressure is to open the inlet of the air compressor for pressurised air inflow.

Pressure Regulator System

The air pressure control panel for diverging and adjusting the air pressure is shown in Figure 4.17. The compressed air flow first passes through the main valve V_1 . Then, it is divided by three 'T junctions', J_1 , J_2 , and J_3 , into three embranchments. These three embranchments are controlled by another three valves, V_2 , V_3 , and V_4 . Valve V_2 , which controls the embranchment of the cushion, generates a vertical confining pressure. Valves V_3 and V_4 are for the two air cushions of the horizontal confining pressures. These valves are used to isolate their respective air embranchments. These valves need to be closed under the following conditions: (a) when there is no test running, (b) when the embranchment is not in use during the test (the vertical air channel in this research), or (c) when there is another channel being regulated. The

valves lead the air flows into three electric air pressure regulators, R_1 , R_2 , and R_3 . Each regulator has a digitizer, which displays the output air pressure (in kg/cm^2). The regulators control the actual pressure by changing the input voltages of the regulators using adjustable voltage regulators B_1 , B_2 , and B_3 . The digitizers that are located on the voltage boards display their output voltages to the air regulator. There is another valve on the bottom of the panel, V_5 , which acts as the de-air valve for the whole system. This valve is used after the test to depressurise the system.

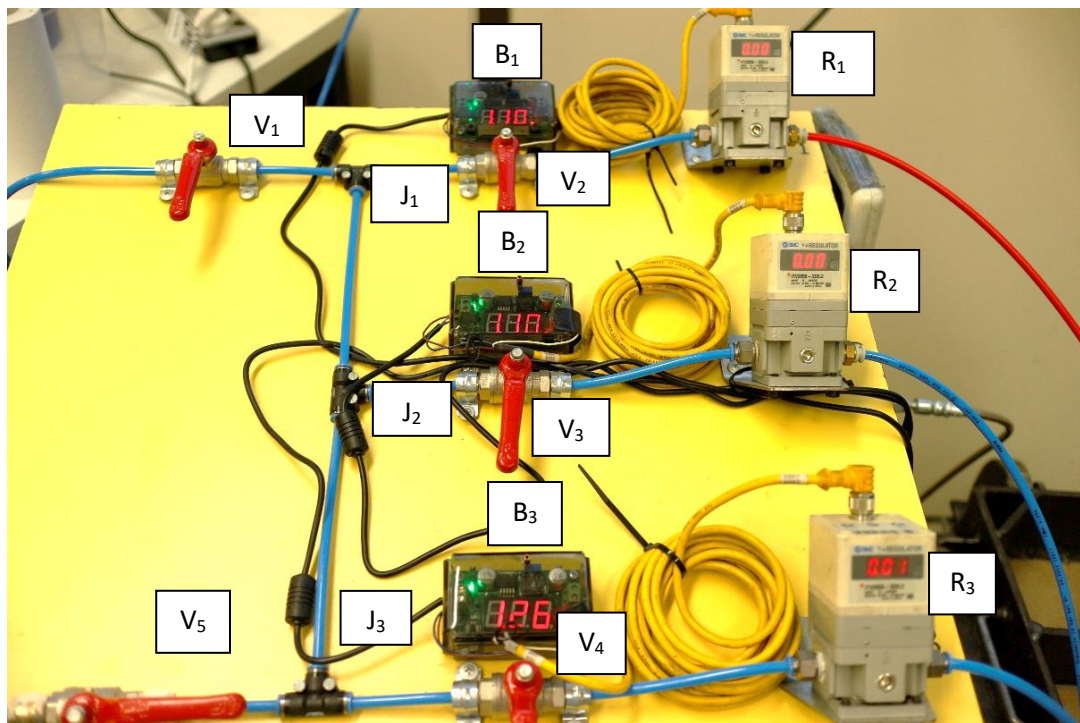


Fig.4.17. Air pressure control panel

Pressure Gauge Setup

Figure 4.18 shows the pressure gauge setup for pressure regulation. The air flows delivered by regulators go into their corresponding cushions through valves V_6 , V_7 , and V_8 . These valves are closed during the regulation process so that the cushions do not generate any pressure to disturb or shear the specimen. There is a pressure gauge connected to the three tubes from the outlet of the three regulators by two T joints with the three valves, V_9 , V_{10} , and V_{11} . The pressure gauge has the accuracy of 1kPa . Valve V_9 governs the air flow from regulator R_1 to the pressure gauge. Valves V_{10} and V_{11} monitor the air pressure from regulators R_2 and R_3 , respectively. With this pressure measurement system, when one of valves V_9 , V_{10} , and V_{11} are open while the other two

valves remain closed, the pressure gauge can measure the air pressure from the channel dedicated to the independent valve.

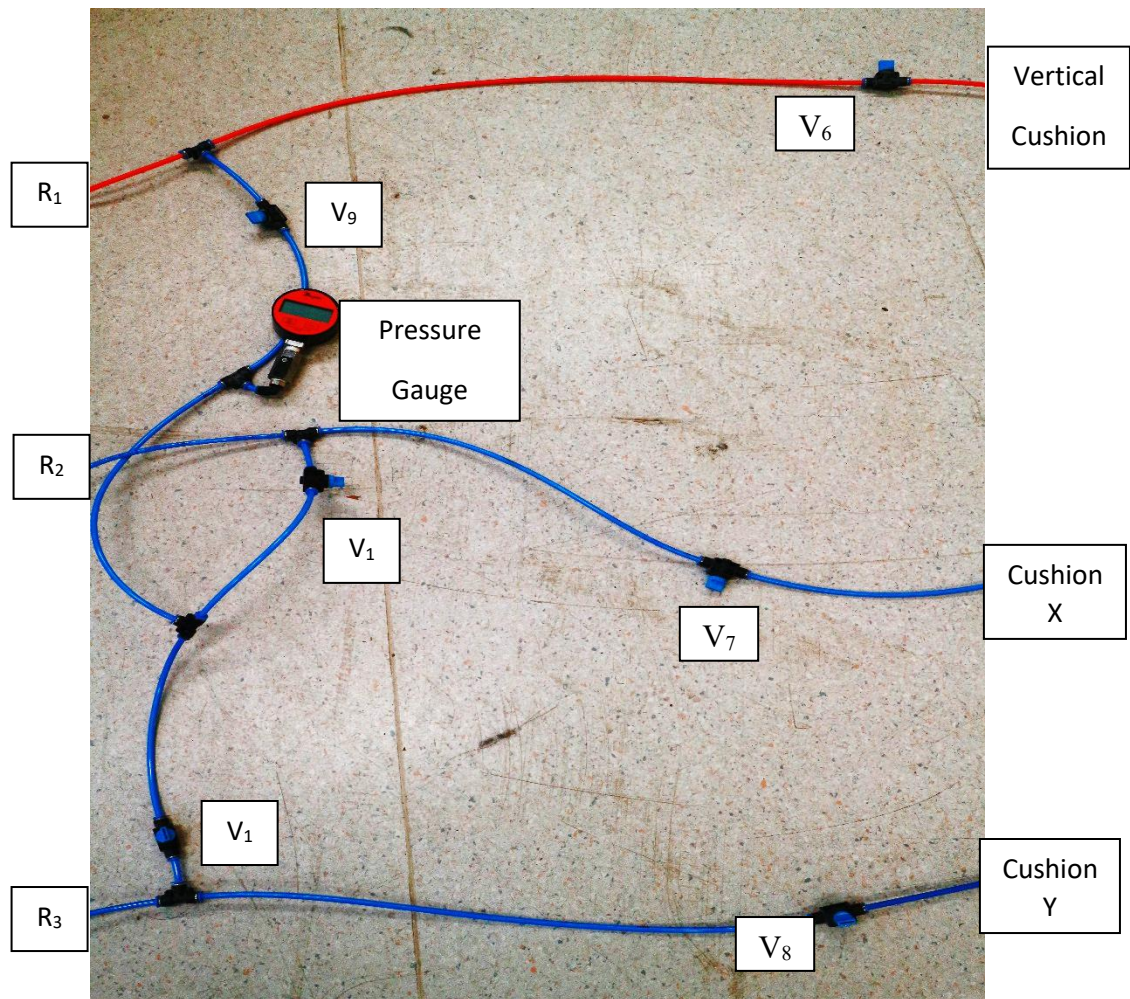


Fig.4.18 Air pressure measurement system

Regulation Steps

Step 1 of pressure regulation is the pre-regulation check. Before the air pressure for each channel is adjusted, the main valve, V_1 , and the valves for each channel, V_2 , V_3 , and V_4 , are closed, the discharge valve, V_5 , needs to be fully opened. This prevents unexpected air pressure from damaging the specimen.

Step 2 is the power connection. There are three power adapters to apply electricity power to the three air-regulating channels in the control panel. Each power adapter is connected with one voltage board and its corresponding electric regulator. In this project, the vertical air channel was abandoned, and therefore, voltage board B_1 had to always be disconnected. Regulation starts with air channel No.2 (corresponding to J_2 -

B₂-V₃-R₂ in Figure 4.17 and R₂-V₁₀-V₇ and Cushion X in Figure 4.18). When the adapter for B₂ and R₂ is plugged in, the channel for air flow No.2 is electrified, and the valve V₃ remains closed. The voltage is indicated by the digitizer on B₂. This voltage is adjusted to a minimum (1.1V) by rotating the switch to ensure that regulation starts at a minimum pressure of 102kPa. As a result, overloading of the regulator is prevented.

Step 3 involves utilizing the pressure gauge setup shown in Figure 4.18 to measure the air pressures during the air regulation. The air flow from R₂ goes to the pressure gauge when valve V₁₀ is opened. The valves for the other channels, V₉ and V₁₁, are closed. It is also important to maintain the valves for the cushions of V₆, V₇, and V₈ closed so that the air pressure adjustment does not generate pressure in cushion Y, as shown in Figure 4.18.

Step 4 introduces compressed air into the air control panel. First, the valve dedicated to regulator V₃ is opened. The main inflow valve, V₁, is opened, and the discharge valve, V₅, is closed. Air regulator R₂ starts releasing air to maintain air pressure. The digitizers on regulator R₂ and the pressure gauge start indicating the pressure value of the air flow. Despite the difference in units (kg/cm² in the regulator, kPa in pressure gauge), the actual pressure should be similar.

Step 5 involves the regulation of air pressure. Regulation is achieved by adjusting the output voltage on voltage board B₂. Regulator R₂ monitors the output air pressure on the pressure gauge. The purpose of regulation is to achieve horizontal confining pressure, P_x , as indicated in the Test Design (Section 4.1.2), based on the correlation between the air pressures in the cushions and the confining pressures of the two principal horizontal confining directions (Section 3.2.9).

Step 6 requires the release of air pressure in preparation for the next regulation. This is done by opening the main discharge valve, V₅, and closing the main inflow valve, V₁. After the pressure reading on regulator R₂ and the pressure gauge become zero, cushion X is deflated. The values of V₃, V₇, and V₁₀ are fully closed. Then, the power adapter for B₂ is unplugged.

For step Step 7, one conducts calibration for air channel No.3 (corresponding to J₃-B₃-V₄-R₃ in Figure 4.17 and R₃-V₁₁-V₈ and Cushion Y in Figure 4.18) by repeating steps 2 to 6, with the valves and voltage board mentioned in Step 7 activated. After the air pressure in cushion Y is adjusted to the specified value from the Test Design (Section 4.1.2) based on calibration in Section 3.2.9, the regulation process is finished.

The air pressure is released from the discharge valve, V_5 . All valves from V_2 to V_{11} are opened, except for the main inflow valve, V_1 , which is closed to prepare the air control panel for the test.

4.1.5.2. Apply Cavity Expansion

Cavity expansion is achieved with the automatic, digital control pressure-volume transducer (Figure 4.19). The main part of the transducer is a cylindrical thick-wall container, which accommodates de-aired water. Two quick-coupling connectors are located at the front of the container. The vertical connector handles water intake. Through this intake, the transducer is filled up with de-aired distilled water from the external water reservoir. Except when filling up the transducer, the intake connector remains closed during the test. The horizontal connector is the water outlet that is connected with the high pressure hose described in Section 4.1.4. Inside the transducer, there is a pressure monitor near the connectors so that the fluid pressure can be monitored by the system. On the back of the container, there is a rotary piston pump. The rotary piston pump is driven by the electric rotary motor attached to the back of the pump. The speed of the rotatory motor can be adjusted to control the pressure and volume of the de-aired water. A detachable control panel sits on the side of the transducer. The control panel has a digitizer and a keypad. The two main functions of the control panel are (1) to control the pre-test process, such as handle zero offsets, empty transducer, fill up transducer, apply instant pressure or volume to the transducer, or stop or pause the test in emergency and (2) to display the real-time water pressure, real-time volume, and test stage. Under the container, there are three cables. The front cable is connected with the control panel for sending commands and real-time reading between the panel and the transducer. The second cable is the data transmitter connected to the computer so that the transducer can operate multi-step, rate-adjustable tests and log the data through the computer program. The last cable is used for the power supply.

During the pressuremeter test, the pressuremeter probe is placed fully inside the specimen. Therefore, the loading and unloading stages and their pressure-volume indications are totally dependent on the transducer. During the loading stage, the transducer discharges de-aired water at a defined rate from its water outlet by the rotary piston pump. The de-aired water goes through the high pressure hose into the probe,

thus generating membrane expansion. The cavity wall of the specimen is expanded by the membrane while resisting against it. The resistance pressure along with the volume change of the transducer is back-fed as a signal to the system. The loading stage then stops when the target pressure or volume change is met. During the unloading stage, the rotary piston pump reverses to decrease the pressure. The transducer withdraws the de-aired water from the probe, thus leading to a shrinkage of the cavity that releases pressure. When the transducer detects that either the fluid pressure or the volume increment has reached pre-defined parameters, the transducer terminates the unloading stage.

Defining and obtaining results from complex tests merely with the control panel is impractical. Therefore, the computer software, GDSLab, is used to program the test. The interface of GDSLab is shown in Figure 4.20. The program was originally designed for the advanced triaxial test that involved the 'cell pressure,' the 'back pressure', and 'axial strain' controls. For the pressuremeter chamber test, the 'cell pressure' column that controls the pressure and volume of the transducer, as shown in Figure 4.20 (a), are the adjusted values. The top dialogue box is used to select the four types of pressurisation. 'Constant' means an instant pressurisation, 'ramp' means the pressurisation is at a constant rate, 'sinusoidal' means the pressure increment is sinusoidal, 'hold volume' means the cell would hold its current volume, regardless of pressure. In this research project, since the pressurisation rate is constant, the 'ramp' type is selected. The next dialogue revolves around selecting whether the target of the test is defined by 'pressure' or 'volume.' The tests use a 'pressure' control type of test. The dialogue box then shows the current pressure and asks to define the target pressure for the stage (all in kPa). For the 'ramp' mode, the total test duration needs to be set in minutes in the last dialogue. In each pressuremeter chamber test in this project, there are usually five stages. The first stage is the idling stage, which applies low pressure (usually 5 kPa) to settle the initial volume of the transducer. The idling stage is followed by four loading stages, which are (1) the first loading stage, (2) the first unloading stage, (3) the second loading stage, and (4) the second unloading stage. For the same group of the test (same confining pressure), the list of program setup stages can be a saved file that can be directly used as the setup for the next test, as Figure 4.20 (b) shows. When 'go to test' is clicked, the test can then be started. The transducer runs the test plan automatically.

There are three factors that needed to be defined in order for the test stages to be set up. These are the limit pressure, the test rate, and the pressure variance of the unload-reload cycle. These factors are discussed in the following paragraphs of this section.

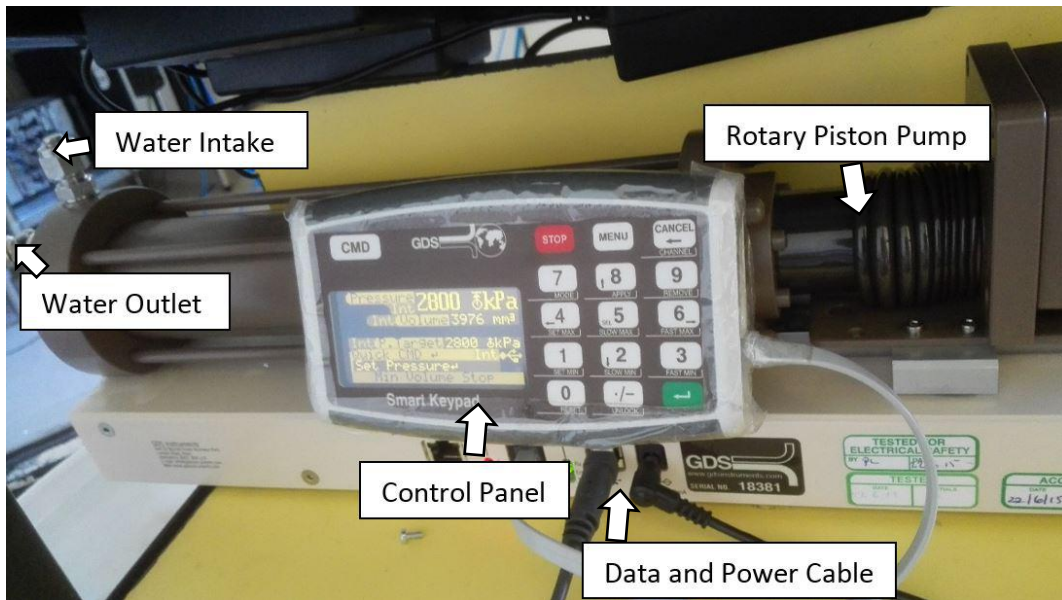
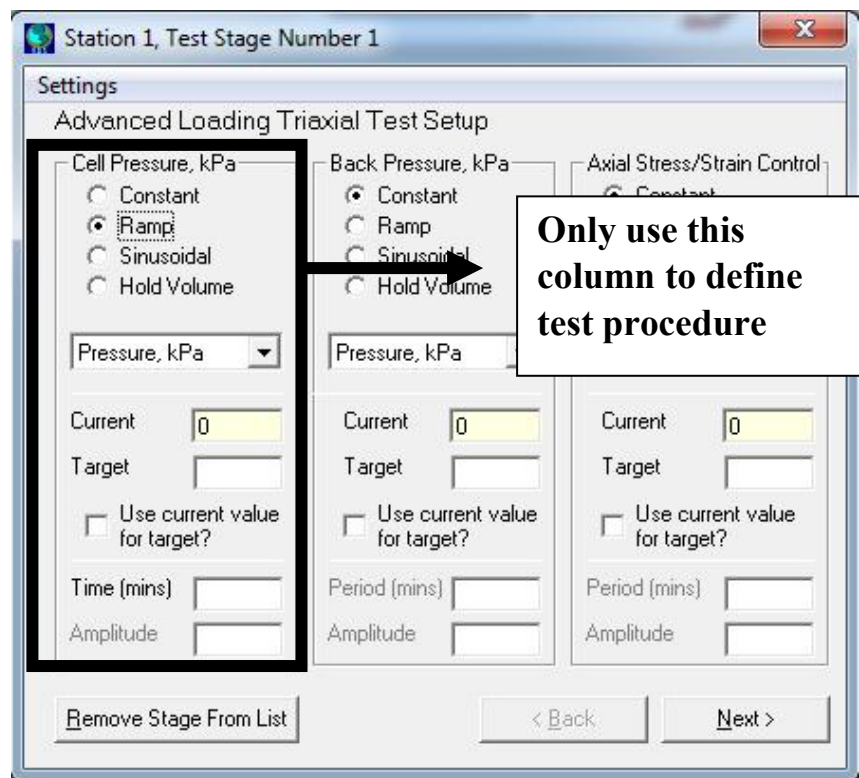
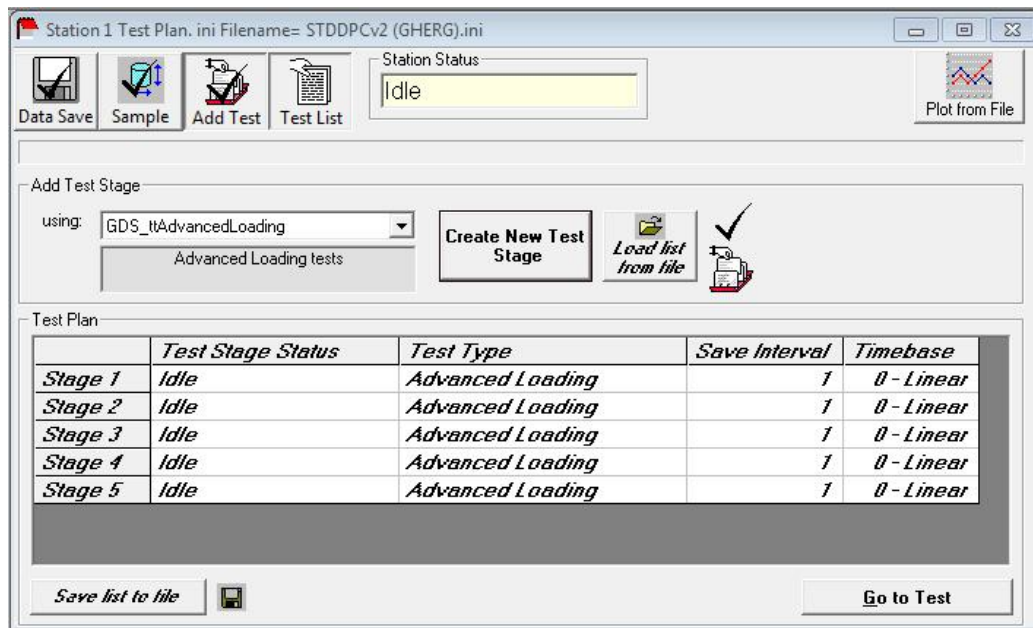


Fig.4.19 Pressure-volume transducer and control panel



(a)



(b)

Fig.4.20. GDSLab software interface of (a) single stage definition and (b) multiple stages assignment

Define the Limit Pressure

The maximum expansion of the probe results from the combined action of both the horizontal confining pressures, P_x , P_y , and the hydraulic limit pressure of the probe, P_{LT} . The horizontal confining pressure (P_x , P_y) for each test is already determined by the applied air pressure discussed in Section 4.1.5.1. The limit pressure (P_{LT}) needs to be defined at this stage. Defining the pressure limit helps to achieve volumetric expansion of around 15% of volumetric strain. The appropriate P_{LT} should also keep the probe from over-expansion. Moreover, as the pressure rate has already been determined, consideration should be given to the total test time (within 20 minutes) to avoid sand creeping.

In this research project, since the unloading-reloading cycle starts at the pressure limit (discussed later in this section), the first and second loading stages have the same target pressure. Therefore, the way to define the pressure limit in the GDSLab interface is to set the limit pressure as the ‘target’ for both loading steps.

The determination of the pressure limit is based on volumetric expansion of the probe. However, the difference in P_{LT} causes different hose expansions. The actual volumetric expansion of the probe can only be obtained when hose calibration is

applied to the test results (as described in Chapter 4.1.4). Therefore, the pressure limits for each confining pressure case need to be estimated. The method applied in this research is the performance of one-step pilot tests for each case of confining pressures. In the pilot tests, the stress-strain relationship is not studied. Instead, the probe is pressurised with high limit pressure (1400kPa) in quick test time (two minutes). The volume change indicated by the software is monitored. Once the volumetric expansion exceeds 20% of the probe's original volume V_0 (4869mm³), the expansion is immediately manually stopped. The test is then repeated with a lower limit of pressure (200kPa less than the previous test). Until the volume change at the pressure limit gets close to 20% of the probe's original volume, the pressure limit value in the pilot test is determined as the pressure limit for the real test. The determined pressure limits all confining pressures in this research, which are shown in Table 4.2.

Table 4.2. Different limit pressure and volumetric strain from pilot tests.

Group	P_x (kPa)	P_y (kPa)	Cavity Pressure (kPa)	Limit Pressure (kPa)	Volumetric Strain (%)
1	150	150	228	600	12
2	225	225	342	800	14
3	300	300	456	1200	16
4	225	150	280	800	16
5	300	150	311	800	12

Define the Pressure Rate

In this research project, the unique pressure rate was used for all the tests. Once the pressure limit is determined, the rate can be defined by assigning a running time (in minutes) for the stage in the GDSLlab programme. Since the pressure rate is constant, the test time for the stage is calculated by the differences of pressures before and after each stage, and the unique pressure rate determined in this section using Equation 4.2.

$$T_S = \frac{|p_{ts} - p_{0s}|}{rate} \quad \text{Eq.4.2}$$

In this equation, T_s (in minutes) is the total time of the test, and P_{ts} is the target pressure of the stage (in kPa), and P_{0s} is the pressure at the start of the stage (in kPa). The rate (in kPa/min) is the defined pressure rate of the test.

The test programme is defined in a way that avoids any over-estimation (too fast) and under-estimation (too slow) of the test rate. Due to the fact that the minimum time interval for the transducer reading is one second, the over-estimation of the pressure rate loosens the data plot. And the over-discrete data plot causes unsmooth curves in the test results so that the transitions of the stress-strain behaviour are overlooked. On the other hand, the under-estimation of the pressure rate may lead to sand creeping. Creeping causes some extra volumetric strains during the test so that the stress-strain relation from the pressuremeter test result is disturbed. Since the in-situ pressuremeter test has a running time for the first loading of 15 minutes and a pressure limit between 800kPa and 1200kPa, the designed pressure rate is 100kPa/min. This pressure rate gives the chamber test 8 to 12 minutes running time for the first loading cycle, and the pressure variation at each time interval is 1.67kPa.

Define Unload-Reload Cycle

Section 2.3 describes the interpretation of the unload-reload stiffness, G_{ur} . Obtaining the G_{ur} requires performing at least one unload-reload loop during the pressuremeter chamber test. The maximum and minimum pressures of the loop need to be determined for each test.

In the present research project, the unload-reload cycles start at the stress level of the pressure limit defined by the pilot tests in Table 4.2. The strain level corresponding to the pressure limit from the pilot tests ensure that the unload-reload cycle is not disturbed by installation. In terms of the pressure variances of the cycles, the empirical function suggested by Mair and Wood (1987) suggests that around 0.6-0.65 of the pressure limit can be regarded as the maximum pressure variance of the unload-reload cycle. The current research applies applies 200kPa as a general pressure variance.

4.1.5.3. Data Acquisition, Corrections, and Post-processing

Data Acquisition

Once the five stages of test procedure are finished, the GDSLlab programme automatically generates a '.gds.' file in the defined directory. The file can be read on

Microsoft Excel. As mentioned in the previous section, the program is designed for tri-axial testing. Therefore, the raw test results are overcomplicated for the pressuremeter test due to the program's multiple functions. The first step of data processing is to simplify the data files. There are three columns of data that need processed. These columns are (1) the 'stage number' to identify the stage of the test, (2) the 'Radial Pressure' (in kPa), and (3) the 'Radial Volume.' The three columns are copied and pasted into a new Microsoft Excel worksheet for processing. The 'Radial Pressure' is converted into '*Pressure*', which indicates the pressure of the system (in kPa). This pressure includes the soil and membrane resistance pressure. The 'Radial Volume' is converted into 'Volume' to indicate the transducer volume during the test (in mm³). This column is then set to zero by removing the pre-test volume of the transducer and is then converted to the '*dV*', which indicates the total volume change of both the hose and the probe (in mm³).

Volume Correction

The volume correction for hose compliance is applied before the pressure correction for membrane resistance. This is due to the fact that hose expansion happens during the membrane calibration test, whereas no membrane resistance happens during the hose calibration. As mentioned in Section 4.1.4.1, the hose calibration test works out a function between the calibrated volume increment of the hose, '*dV_{calibration}*' (in mm³) against '*Pressure*' applied to the transducer (in kPa). Applying this function to the pressure value of the test data can obtain the actual loss of volume due to hose expansion. This is then excluded by the total volume change of the test result and becomes a new value, volume change, '*dV*' (in mm³), for the probe and the soil cavity.

Pressure Correction

Pressure correction for membrane resistance is then applied in accordance with the corrected '*dV*'. The membrane calibration described in Section 4.1.4.2 works out a linear equation that describes the relationship between the resistant pressure (in kPa) and the corresponding volumetric expansion. The actual membrane pressure is applied using this equation with the corrected '*dV*' from the previous step. This pressure is then excluded from the total pressure of the test data and becomes the actual '*Pressure*' of the soil cavity (in kPa).

Initial Volumetric Strain Correction

The corrected ‘ dV ’ is divided by the original probe volume (4869mm^3) to obtain the uncorrected volumetric strain, $\varepsilon_{v(\text{uncorrected})}$. In the monitored test data, the uncorrected volumetric strain starts at the initial value of *Pressure* (5kPa). However, some of the initial volumetric strain is meant to for expand the membrane of the probe to have full contact with the cavity. Generated by the horizontal confining pressures of the chamber, this initial strain happens when the value of *Pressure* is smaller than the cavity pressure, P_{Cavity} (in kPa). To obtain the actual volumetric strain, ε_v , the *Pressure*- ε_v graph needs to be shifted to the left so that

$$\varepsilon_v = \varepsilon_{v(\text{uncorrected})} - \alpha, \quad \text{Eq.4.3}$$

where α (in %) is the volumetric strain corresponding to a *Pressure* less than P_{Cavity} . The graph of *Pressure* against ε_v is then plotted for the interpretation of the unload-reload stiffness discussed in Section 4.1.6.1.

Post Processing

As the total expansion is within a small strain level, probe expansion can be regarded as a cylindrical volumetric expansion. Therefore, the uniform radial strain of the probe also refers to the circumferential strain, ε_c (in %), and is converted from the volumetric strain, ε_v , using the following equation:

$$\varepsilon_c = \frac{\sqrt{\frac{\varepsilon_v}{L}}}{r_0} \times 100 (\%) \quad \text{Eq.4.4}$$

In this equation, L is the length of the expansion portion of the probe (62mm) and r_0 is the original diameter of the probe (5mm). Both the *Pressure* (kPa) and the circumferential strain, ε_c (%) are then converted into the values of the natural logarithm, forming $\text{Ln}(\text{Pressure})$ and $\text{Ln}(\varepsilon_c)$ for the analysis of the frictional angle discussed in Section 4.1.6.2.

4.1.6. Interpretation

4.1.6.1. Unload-Reload Stiffness

The interpretation of G_{ur} is discussed in Section 2.3. In the post-processed test data, the interpretation of G_{ur} requires the corrected *pressure- ε_v* curve from the first unloading stage (stage 3) and the second loading stage (stage 4). During these two stages, the probe's behaviour of shrinkage and expansion is recorded by the *pressure- ε_v* curve, which forms a loop. It is assumed that the soil around the cavity behaves elastic during the loop. Therefore, the elastic response is fitted by a straight line. Figure 4.21 shows one of the fitted straight lines from the test. The slope of the line indicates the unload-reload stiffness, G_{ur} (in MPa).

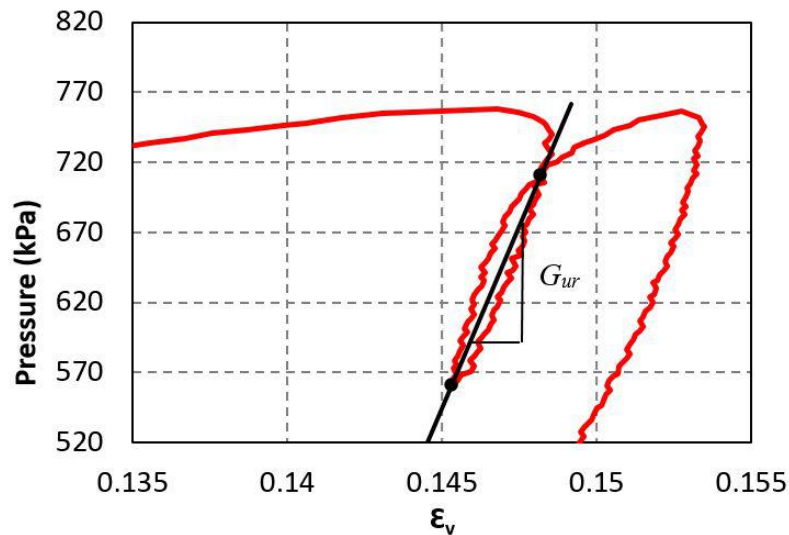


Fig.4.21. Unload-reload stiffness interpretation

4.1.6.2. Friction Angle

Generally, the pressuremeter test is usually used to obtain three parameters of a material's plasticity: the undrained shear strength, the friction angle, and the dilation angle. In this research project, however, the sandy material has no undrained shear strength. Therefore, the friction angle is the most essential interpreted parameter of a material's plasticity based on the anisotropic pressuremeter chamber tests in this research. The interpretation of the friction angle is achieved through a graphical method. It uses the graph of natural logarithm values of *pressure* (in kPa) against the circumferential strain, ε_c (in %). As Figure 4.22 shows, at the high-pressure level, the

natural logarithm graph gradually becomes linear. Assuming the linear portion of the $\text{Ln}(\text{pressure})\text{-Ln}(\varepsilon_c)$ graph can be replaced with a straight line with the slope, S , Huges et al. (1977) suggest that the friction angle, ϕ , become a function of S_i , which is expressed as follows:

$$\phi = a \sin [S / (1 + (S - 1) \times \sin (\phi_{CV})] \quad \text{Eq.4.5}$$

The ϕ_{CV} is the constant volume friction angle of sand. It denotes the angle between normal stress and shear stress on the shear plane of the sand specimen. The value-constant volume friction angle is measured with the direct shear test (described in Section 4.1.7.2) as 32.1° .

Equation 4.5 was further modified by Ajalloeian and Yu (1998), who considered the geometric impact of the pressuremeter probe. The slope, S , was converted into S_d . The relationship between S_d and S is expressed as follows:

$$S_d = S \times (1 - \frac{d}{L}) \quad \text{Eq.4.6}$$

In the equation, d is the diameter of the probe and L is the length of the expansion portion of the pressuremeter probe. The interpretation of friction angle is fully described in Chapter 2.

In mathematical terms, the natural logarithm scale of the pressure-strain graph is becoming closer to the asymptote of $\text{Ln}(\text{pressure}) = \text{Ln}(\varepsilon_c)$, which means that in large strain conditions, S is approximated to 1. The physical explanation is that, when the ideal plane-strain assumption can be applied under infinite strain, the estimated friction angle from the pressure test is equal to the constant volume friction angle, ϕ_{cv} . In reality, however, the probe can only expand under small strain. Therefore, the estimated friction angle, ϕ , is dependent on the actual pressure-strain values applied for defining the slope S .

The starting and ending points of the linear portion of the $\text{Ln}(\text{pressure}) = \text{Ln}(\varepsilon_c)$ graph are two crucial factors in the determination of the slope, S , and the friction angle, ϕ . The ending point of the slope denotes the pressure limit, P_L , and its corresponding circumferential strain (both are in natural logarithm values). The starting point of the slope represents the beginning of plasticity and its corresponding

circumferential strain (both are in natural logarithm values). However, granular material does not follow the linear-elasto-plastic stress strain behaviour. The solution for determining the beginning of plasticity of granular material is to carry out a curve fitted on the non-logarithm form of a *pressure- ϵ_c* curve. The fitting equation is a one-side, total-binding equation, similar to Equation 4.2. This time the binding equation is written as follows:

$$Pressure = B_{max} \times \frac{\epsilon_c}{K_d + \epsilon_c} + NS \times \epsilon_c + Background \quad \text{Eq.4.7}$$

In this equation, the value of B_{max} (in kPa) stands for the maximum specific binding value of *Pressure*. Any pressure that is higher than B_{max} is fully controlled by the strain and the linear regression factor, NS . Therefore, it can be deemed that the *Pressure* represented by B_{max} denotes when sand becomes mostly plastic, which indicates the beginning of plasticity. The beginning of plasticity for each piece of test data is equal to the B_{max} fitted in its total binding curve. This assumption is verified through the interpretation of the results.

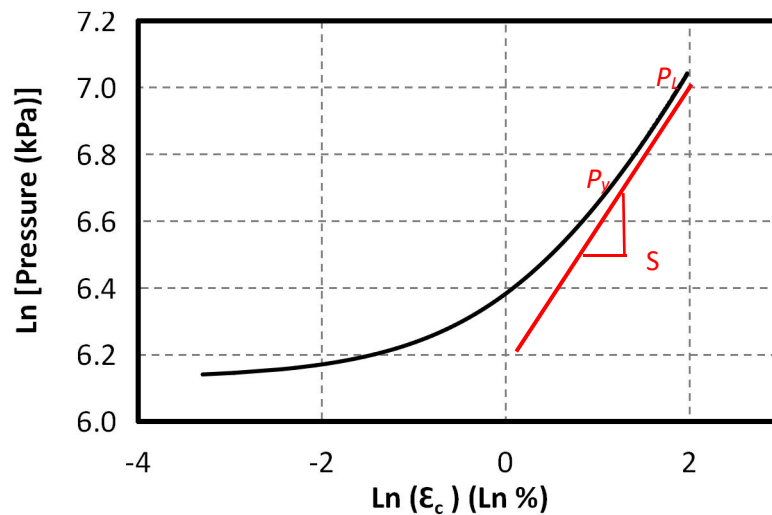


Fig.4.22. Natural logarithm pressure-cavity strain graph

4.1.6.3. Dilation Angle

As described in Section 2.3.1.3, when the sand around the pressuremeter test cavity develops positive volumetric strain, the dilation is considered to occur in the test sand. The intensity of the test sand's dilation is indicated by its dilation angle, ψ . When

the dilation stops, the sand becomes constant in volume, and the friction angle, ϕ , gradually decreases from its peak value to the constant volume friction angle, ϕ_{cv} . The relationship between the dilation angle and the friction angle is defined by Rowe (1962) in Equation 2.15. Using the slope of logarithm *pressure- ε_c* , S in Figure 4.22, the correlation between the dilation angle and the slope S can be expressed as follows:

$$\psi = \text{asin}(S + (S - 1) \times \sin\phi_{cv}) \quad \text{Eq.4.8}$$

4.1.7. Test results

4.1.7.1. Corrected Pressure VS. Volumetric Strain Curves

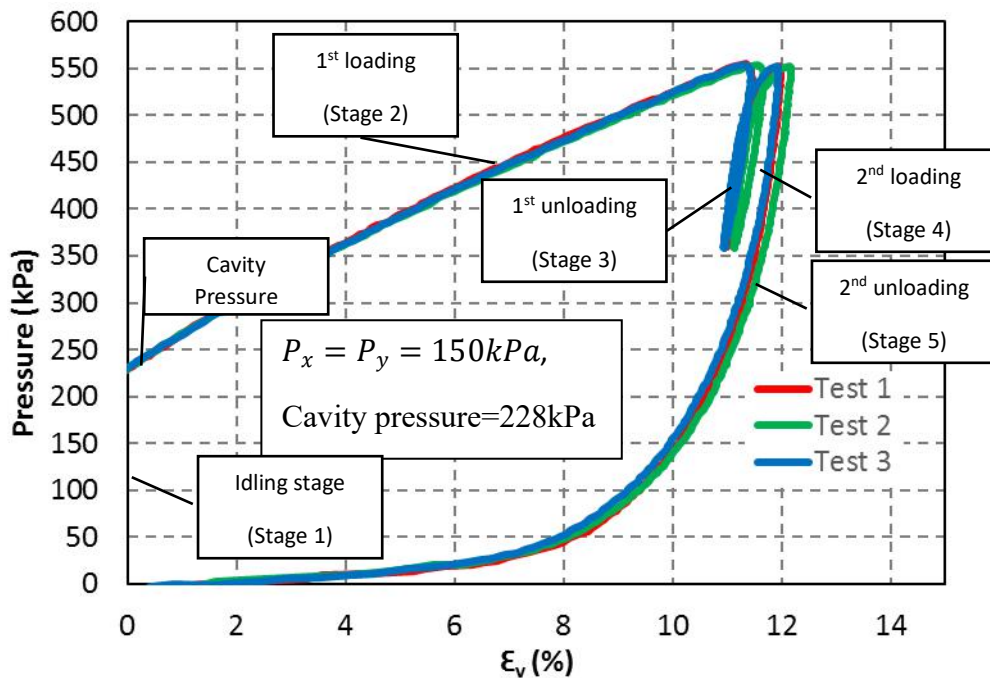
Isotropic Test Results

The results from the three pressuremeter chamber tests applying horizontally isotropic confining pressures to group 1 are shown in Figure 4.23 (a). Three tests were carried out with the lowest horizontal confining pressures: $p_x = p_y = 150\text{kPa}$. The results were corrected and plotted as *Pressure* (kPa) against volumetric strain, ε_v . During the first loading stage (stage 2), the probe pressure started from the minimum pressure of stage 1 (5kPa) and gradually increased at a pre-defined rate (100kPa/min). The initial cavity strain ($\varepsilon_v=0$) started at the time when the probe pressure was greater than the cavity pressure (228kPa). The sand cavity was then pushed by the probe membrane to start the cavity expansion until the probe pressure reached the pre-defined pressure limit (600kPa). After correction, the pressure limits were lowered from a pre-defined 600kPa to roughly 550kPa due to membrane resistance during calibration. The first unloading stages (stage 3) started immediately after pressure limits were reached. These pressure drops were accompanied by a volumetric decrease due to the material's elastic response. After 200kPa of probe pressure was diminished, the second loading stages (stage 4) started to re-expand the cavity back to the pressure limits, generating the unload-reload loop for the test. This was followed by the second unloading stage (stage 5) to depressurise the probe and the cavity. The maximum volumetric strains were around 0.12 (12%) after the application of hose calibration.

The *pressure- ε_v* curves of group 2 (isotropic 225kPa confining pressures) and group 3 (300kPa confining pressure) are shown in Figure 4.23 (b) and Figure 4.23 (c) respectively. Similar to the test results for group 1, the expansions started from the cavity pressure (342kPa for group 2, 456kPa for group 3), then gradually increased to

their corresponding pressure limits. Due to increasing confining pressure, based on the test plan in Section 4.1.2, the limit pressures for group 2 were increased to 800kPa and became roughly 750kPa after membrane calibration. The maximum volumetric strains for group 2 were around 0.13 (13%) after hose calibration. In group 3, the pressure limits in the corrected graph are around 1150kPa, with maximum volumetric strains of 0.16 (16%) approximately.

The three *pressure- ϵ_v* curves for each group are plotted on the same graph for comparison. It can be seen that the pressure-expansion behaviours during the five test stages are comparable. The similarities of the curves indicates the desirable qualities of the specimen compactions and the probe installations.



(a)

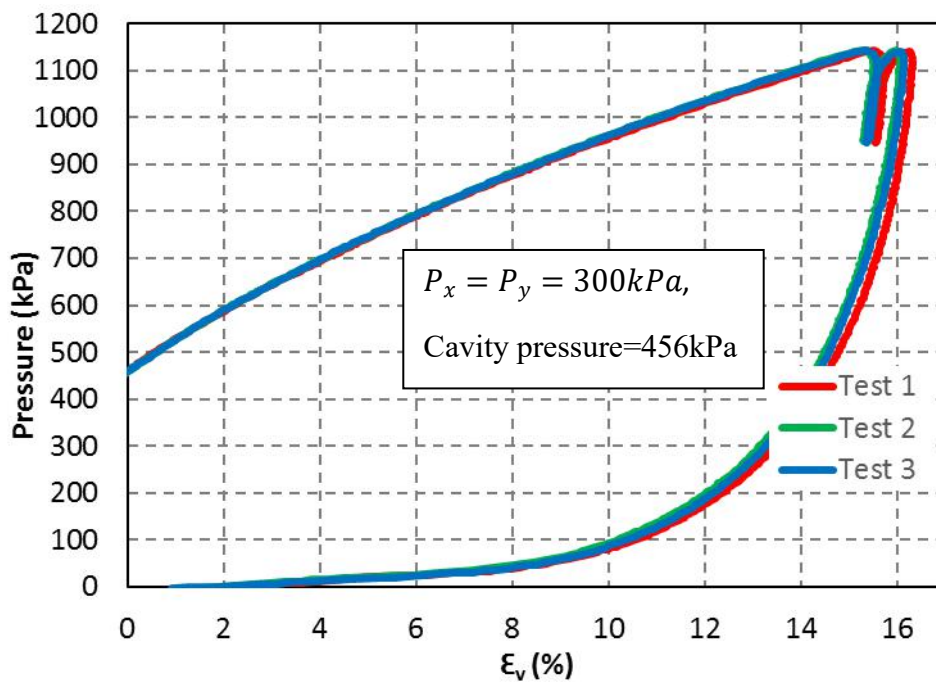
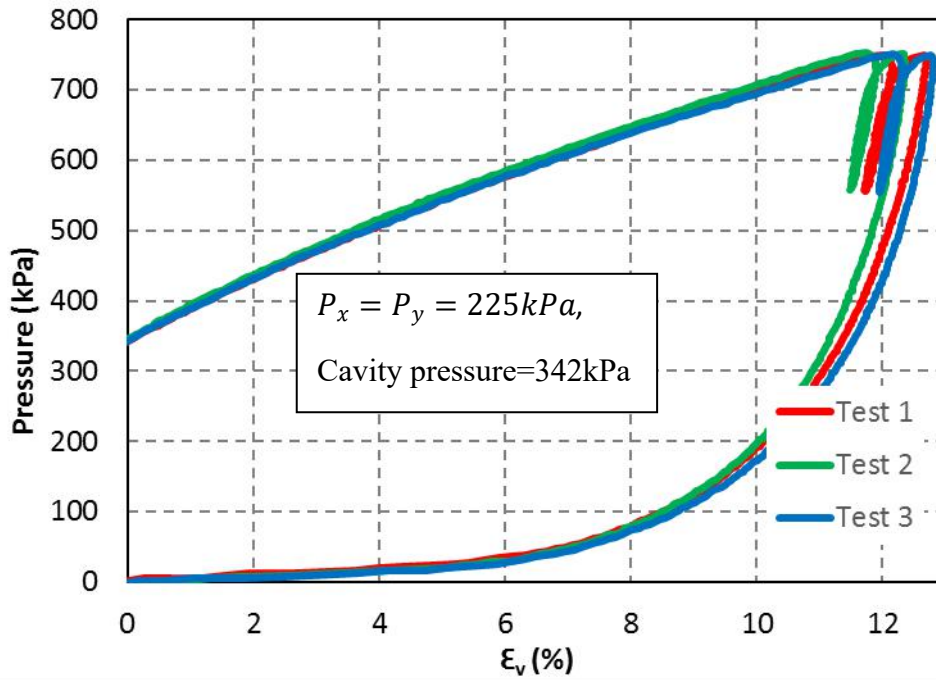
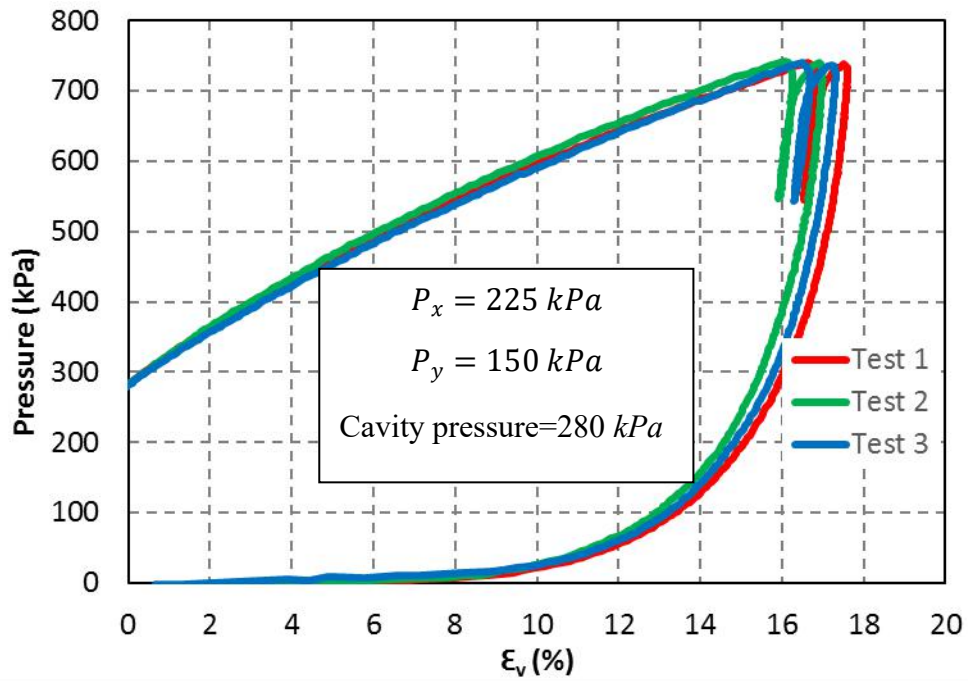


Fig.4.23. Pressure-Volumetric Strain curves comparison for isotropic tests: (a) group 1, (b) group 2, and (c) group 3

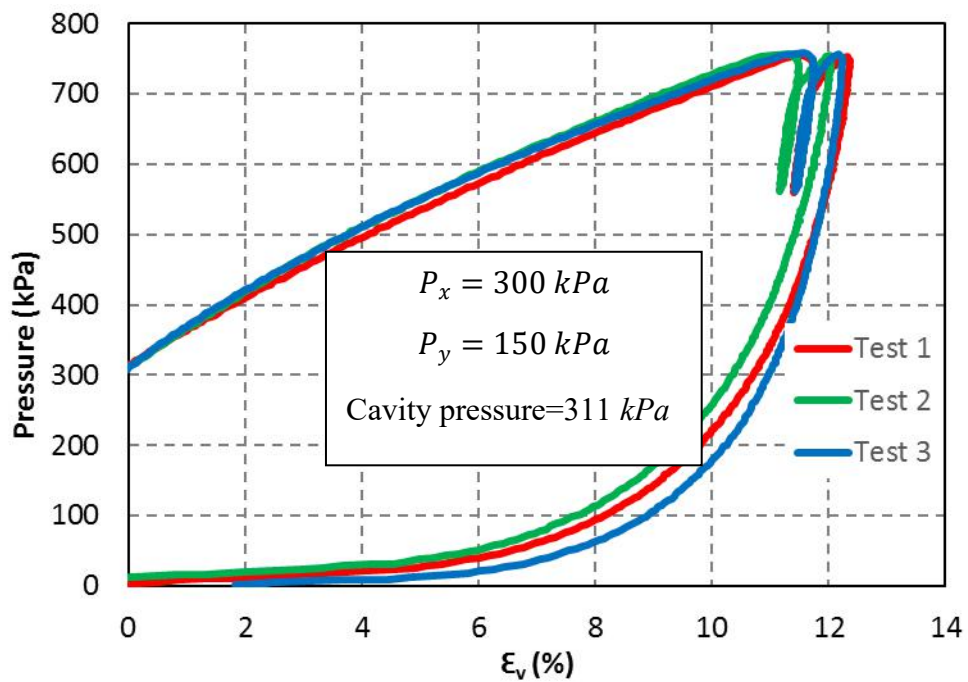
Anisotropic Test Results

The results of the two groups of anisotropic tests (group 4 and group 5) are plotted as Pressure- ϵ_v curves on two graphs based on the different confining pressures (Figure 4.24). Results were plotted from the minimum cavity pressures (280kPa and

311kPa respectively) up to the maximum pressures. The maximum volumetric strains of the curves are around 0.17 (17%) for group 4, and 0.115 (11.5%) for group 5.



(a)



(b)

Fig.4.23. Pressure-Volumetric Strain curves comparison for the anisotropic tests:

(a) group 4 and (b) group 5

4.1.7.2. Interpretation Summary

Based on the interpretation methods discussed in Section 4.1.6, the summary of the unload-reload stiffness, G_{ur} , and the friction angle (corrected by Ajalloeian's method), ϕ , from the 15 tests are presented in Table 4.3. In isotropic conditions, the values of G_{ur} are strongly dependent on cavity pressure, rising up from around 32MPa-36MPa to around 72MPa-86MPa when the cavity pressure increases from 228kPa to 456kPa.

The friction angle is less sensitive to a change in cavity pressures. It exhibited a little drop from around 33°-34° to around 29°-31 ° along with the cavity pressure increase. For the anisotropic conditions, fewer variations were found in the results. The G_{ur} increases from around 43MPa to around 51MPa along with cavity pressure increasing from 280kPa to 311kPa. Regardless of the cavity pressure change, ϕ appears to remain stable . Further graphical analysis and comparison are provided in Section 4.1.8.

Table 4.3 Interpretation summary of pressuremeter chamber tests

Test No.	P_x (kPa)	P_y (kPa)	Cavity Pressure (kPa)	G_{ur} (MPa)	$\phi_{uncorrected}$ (°)	$\phi_{corrected}$ (°)	$\psi_{uncorrected}$ (°)	$\psi_{corrected}$ (°)
1-1	150	150	228	36.88	39.32	34.21	8.87	2.50
1-2				32.2	38.34	32.92	7.63	1.47
1-3				34.78	38.58	34.4	7.92	1.71
2-1	225	225	342	39.08	36.13	31.8	4.86	-0.84
2-2				42.13	35.48	28.55	4.07	-1.50
2-3				46.31	35.41	30.73	3.98	-1.57
3-1	300	300	456	86.59	36.79	32.05	5.68	-0.15
3-2				71.38	35.98	31.3	4.68	-0.99
3-3				72.46	36.39	31.62	5.18	-0.57
4-1	225	150	280	43.15	35.82	32.8	6.71	0.71
4-2				41.2	35.75	32.68	6.71	0.71
4-3				43.02	36.67	33.66	7.95	1.74
5-1	300	150	311	48.38	37.59	32.8	6.69	0.68
5-2				51.82	36.74	31.93	5.62	-0.2
5-3				51.94	36.06	31.80	4.77	-0.91

4.1.8. Comparison and Conclusion

4.1.8.1. Unload-reload Stiffness (G_{ur}) in Isotropic Condition

The interpreted G_{ur} (in MPa) values from the chamber pressuremeter tests under isotropic horizontal confining pressures are plotted against the cavity pressures (in kPa),

as shown in Figure 4.24. When the cavity pressure increases from 228kPa to 342kPa, G_{ur} slightly increases from 32.2MPa - 36.88MPa to between 39.08MPa - 46.31MPa. When the cavity pressure increases from 342kPa to 456kPa, G_{ur} dramatically rises to 71.38MPa – 86.59MPa. Based on the trend line, the intensity of growth of G_{ur} also increases along with the increase of the cavity pressure level. This behaviour shows the stress dependency of the shear modulus in hardening soil materials, such as the tested sand.

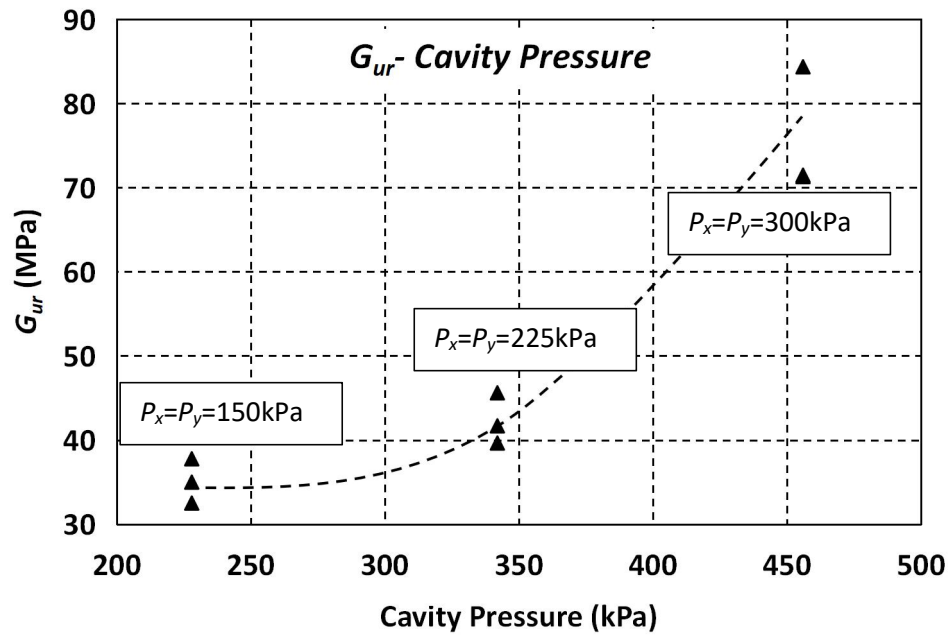


Fig.4.24 Stress dependency of G_{ur} under different cavity pressures from the Isotropic Pressuremeter Chamber Tests

4.1.8.2. Friction Angle (ϕ) in Isotropic Condition

The uncorrected and corrected friction angles ($^{\circ}$) under isotropic confining pressure conditions are plotted against cavity pressure and presented in Figure 4.25. The friction angle without correction, $\phi_{uncorrected}$, at a cavity pressure of 228kPa is around 38.34 $^{\circ}$ -39.32 $^{\circ}$. At 342kPa of cavity pressure, the angle marginally drops to around 35.41 $^{\circ}$ -36.13 $^{\circ}$. The angle under 456kPa of cavity pressure stays at 35.98 $^{\circ}$ -36.79 $^{\circ}$. With the use of the geometry correction from Equation 4.6, the friction angle, $\phi_{corrected}$, starts from 32.92 $^{\circ}$ -34.4 $^{\circ}$ at the lowest pressure level (228kPa) and then decreases to 28.55 $^{\circ}$ -31.8 $^{\circ}$ at 342kPa. Although it slightly increases the cavity pressure of 456kPa, the friction angle stays below 32.05 $^{\circ}$.

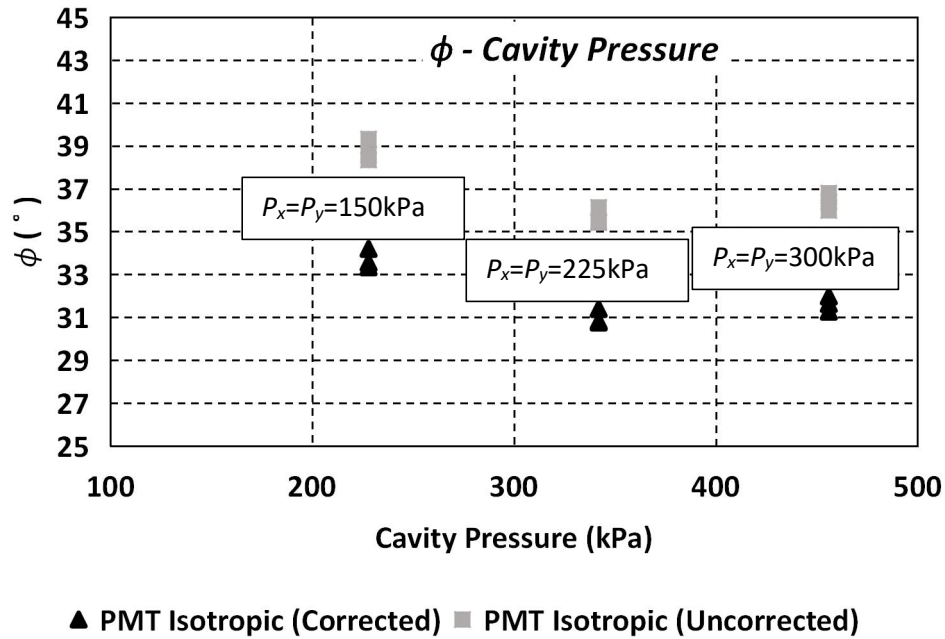


Fig.4.25 ϕ in different cavity pressures in the isotropic pressuremeter chamber tests

4.1.8.3. Dilation Angle (ψ) in Isotropic Condition

Both of the corrected and uncorrected dilation angles are plotted in Figure 4.26. The uncorrected dilation angle, $\psi_{uncorrected}$, is between 7.63° and 8.87° when the cavity pressure is 228kPa. The value drops to around 3.98° to 4.86° at 342kPa of cavity pressure. Then, it stays at around 4.68° to 5.68° for 456kPa cavity pressure. The corrected dilation angle, ψ , exhibits lower values in general. It starts from 1.47° to 2.50° with 228kPa of cavity pressure. When the cavity pressure increases to 342kPa and 456kPa, $\psi_{corrected}$ becomes negligible negative values. These negative values should be regarded as 0 dilations, meaning that the sand around the pressuremeter cavity has reached constant volume state. In general, this figure proves that the dilation angle of the samples at the achieved density and applied stress levels is very small and negligible.

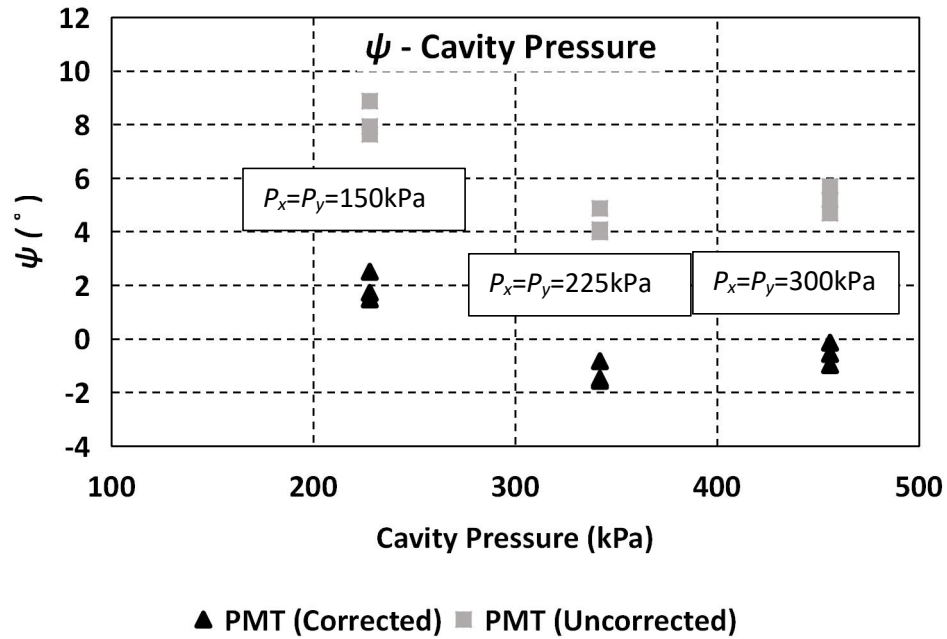


Fig.4.26 ψ under different cavity pressures in the isotropic pressuremeter chamber tests

4.1.8.4. Comparison of ϕ from Isotropic Tests with Direct Shear Tests

Direct Shear Test

The friction angle measured from the pressuremeter tests was verified against the results of the direct shear test. The direct shear test is a standard test to estimate a material's shear strength, including the friction angle and cohesion. This research project applied the direct shear test on the tested material (sand) in order to (1) compare the friction angles of the test sand obtained from the direct shear test and from the interpretation of the chamber pressuremeter test under isotropic horizontal confining pressures; (2) obtain the constant volume friction angle, ϕ_{cv} , for the interpretation of friction and dilation angle based on the pressuremeter chamber test; and (3) describe the friction/dilation angle's dependency on the cavity pressure/horizontal confining pressure.

Preparing the direct shear test in sand starts with placing the material into the 100mm×100mm shear box shown in Figure 4.1. When the box was first filled up, a hummer vibration is applied on the shear box frame. After the sand became denser, the shear box was again topped up with sand. The procedure was repeated until the sand density reaches the density in the pressuremeter chamber test (1922kg/m³). The shear box was then installed into the shear apparatus. Four screws for fastening the top half and the bottom half of the shear box were then removed to allow the specimen shear.

The normal stress, σ_n , was automatically applied to the top of the shear box loading plate by the direct shear apparatus. In accordance with the pressuremeter chamber test plan, 150kPa, 225kPa, and 300kPa of σ_n were applied to three tests in that order. For dry granular materials, the one-dimensional compression finished immediately after the normal stresses were applied. The shear rate was defined as 0.5mm/min, and the total shear distance as 1.5cm.

The direct shear apparatus recorded the shear stress τ against the shear displacement during the test. As Figure 4.26 shows, when sand started to shear, the shear stress reached the maximum value, called the peak shear strength, τ_{peak} . Following the peak stress, the sand same fully plastic until the test finished. The shear stress stayed at a constant while being sheared at a constant volume. This shear stress is called the constant volume shear strength, τ_{cv} . The values of τ_{peak} and τ_{cv} for each σ_n are shown in Table 4.4. In this case, as Figure 4.27 shows that the τ_{cv} at three different σ_n values appear in the same oblique straight line. The angle of this line indicates the uniform ϕ_{cv} value (32.1°). On the other hand, the τ_{peak} at three different σ_n values indicates different lines representing different ϕ_{peak} values (36.29° for $\sigma_n=150$ kPa, 34.74° for $\sigma_n=225$ kPa, and 34.11 for $\sigma_n=300$ kPa).

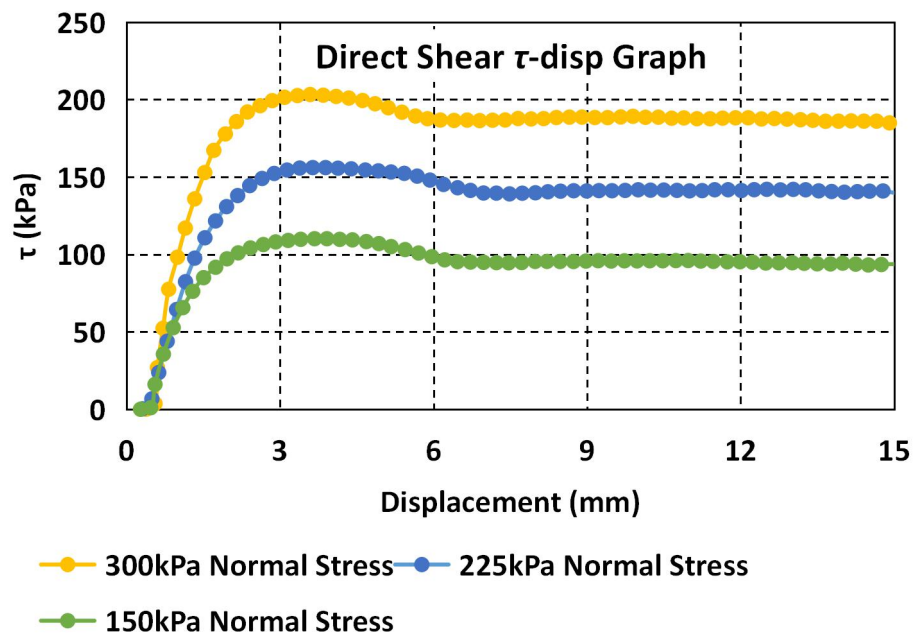


Fig.4.27. Direct Shear Test Result

Table 4.4 Peak and constant volume shear strength

σ_n (kPa)	τ_{peak} (kPa)	τ_{cv} (kPa)
150	110.15	94.49
225	156.05	141.78
300	203.20	187.49

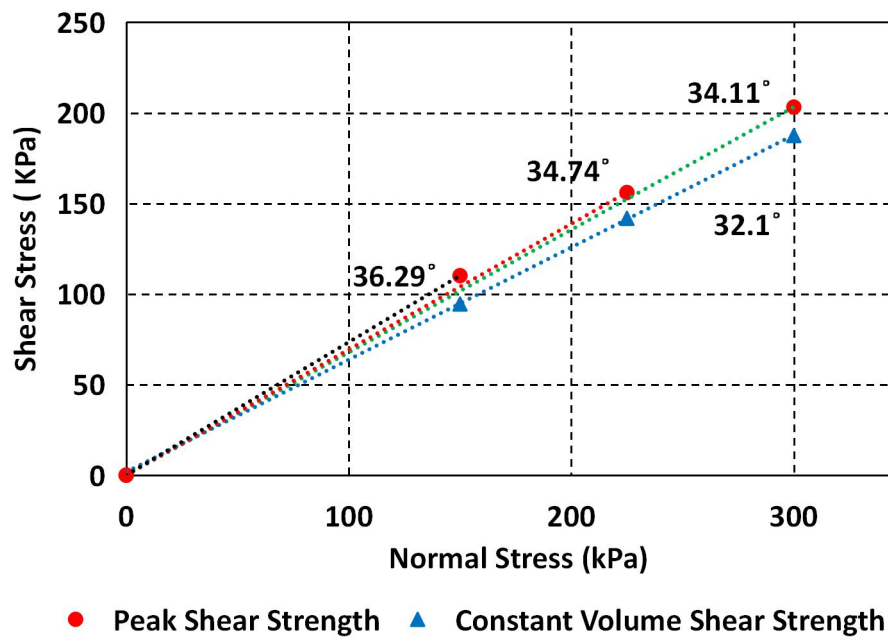


Fig.4.28. Interpretation of ϕ_{peak} and ϕ_{cv}

Results Comparison

The ϕ_{peak} and ϕ_{cv} from the direct shear test results and the ϕ from the isotropic pressuremeter chamber tests were plotted against each other for comparison. The *pressure* (in kPa) indicated on the X-axis is the normal stress for the direct shear tests and the cavity pressure for the pressuremeter chamber tests. The results are shown in Figure 4.29.

Based on the comparison, the corrected friction angle measured from the chamber test is around 2° less than the constant volume friction angle from the direct shear test regardless of the stress level. This phenomenon can be explained by the different constraint conditions of the material during the two tests. In chamber tests, sand particles are more restrained in three dimensions than the particles in direct shear box.

The relative particle movements in direct shear tests may lead to slightly higher friction angle.

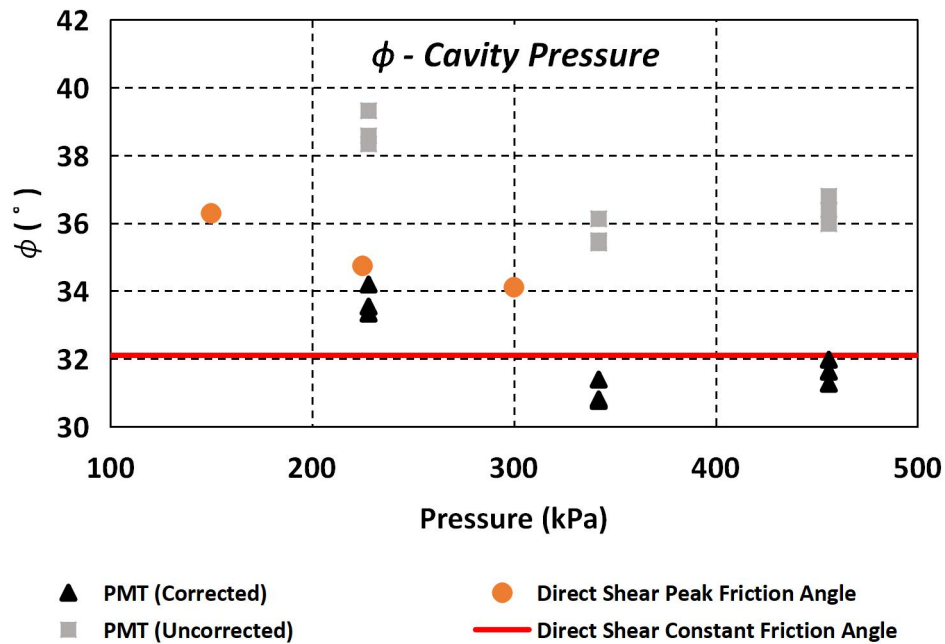


Fig.4.29. Friction Angle Comparison

4.1.8.5. Unload-reload Shear Modulus in Anisotropic Conditions

The unload-reload shear modulus (G_{ur}) from the pressuremeter chamber tests under both anisotropic and isotropic confining conditions were plotted against the cavity pressure, as Figure 4.30 shows. The graphs show that an increase in confining pressure results in the increase of unload-reload shear modulus in both isotropic and anisotropic chamber tests, indicating the stress dependency of the parameter, as demonstrated in Section 2.3.1.5. The impact of anisotropy is also found based on the value of G_{ur} . Since sand is hardening material, the stiffness of sand varies due to different hardening conditions (Schanz 1998). In the isotropic chamber test, the material was stiffened due to isotropic (oedometric) hardening. In the isotropic chamber test, the stress dependency of G_{ur} was only due to isotropic (oedometric) hardening. In the anisotropic chamber test, G_{ur} stiffened because of both isotropic (oedometric) hardening and anisotropic (shear) hardening. As a result, when one of the horizontal confining pressures is 50% higher than the other one, the estimated unload-reload stiffness, G_{urA} , is around 25% higher than G_{ur} , estimated from the trend line of the isotropic test results. In addition, when the anisotropy increases from 50% to 100%, G_{urA} is around 50% higher than G_{ur} .

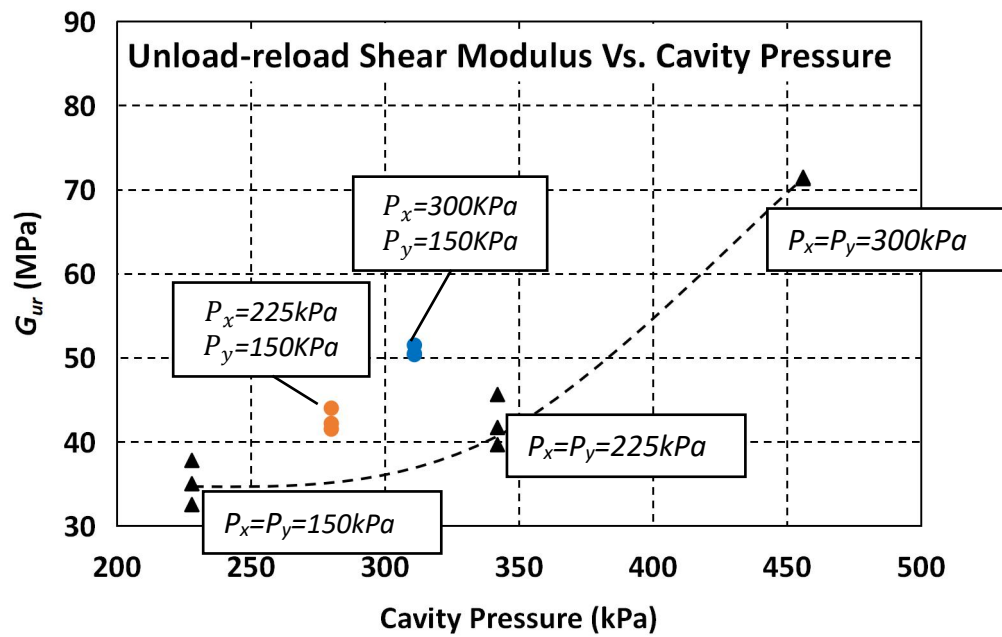


Fig.4.30. G_{ur} from isotropic/anisotropic pressuremeter chamber tests

4.1.8.6. Friction Angle and Dilation Angle in Anisotropic Condition

Results of the corrected friction angle, ϕ , from the anisotropic tests were plotted along with the isotropic tests results in Figure 4.31.

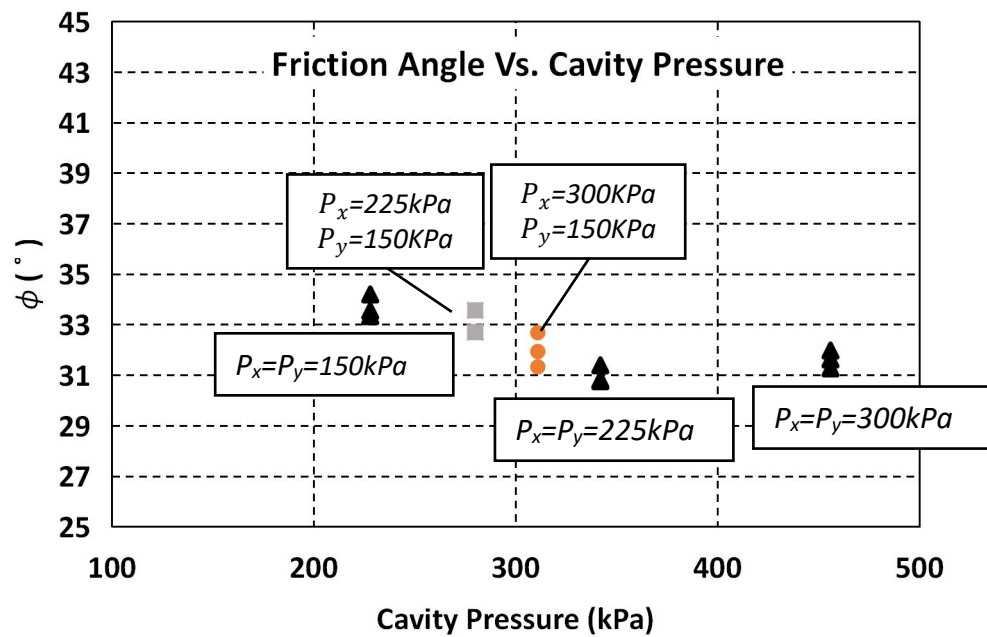


Fig.4.31. ϕ from Isotropic/Anisotropic Pressuremeter Chamber Tests

The result shows that the interpretation of the friction angle was hardly affected by the anisotropy. The relationship between the friction angle and cavity pressure from anisotropic tests perfectly incorporates the relationship from isotropic tests. Since anisotropy does not affect the interpretation of the friction angle, it should have no impact on the interpretation of the dilation angle, meaning that the corrected dilation angles for the achieved density of the applied sand are negligible. This is showed in Figure 4.32.

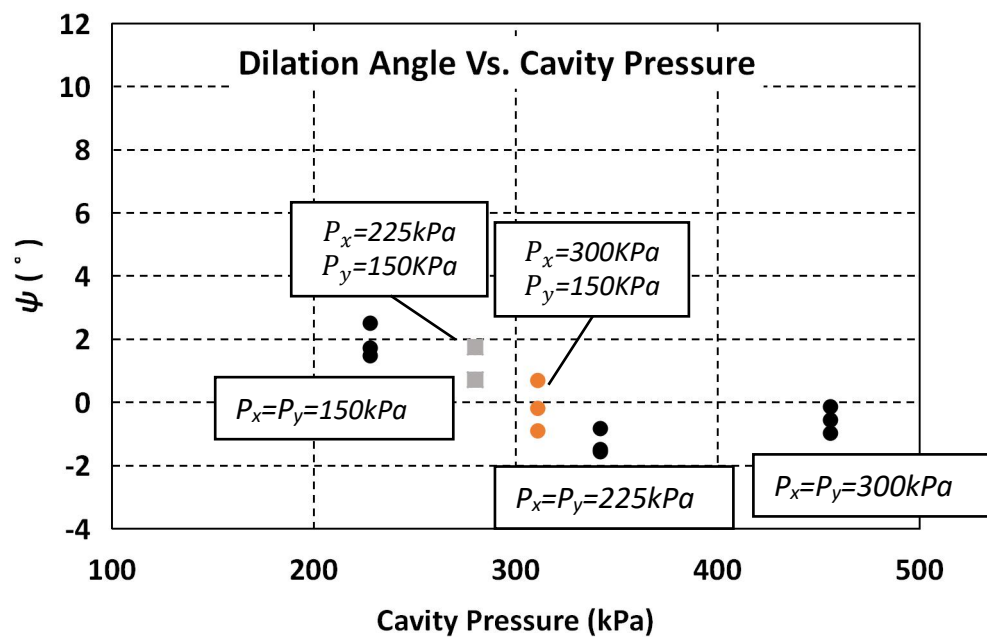


Fig.4.32. ψ from Isotropic/Anisotropic Pressuremeter Chamber Tests

4.2. Unconfined Expansion Test

4.2.1. Introduction

Given the potential for bias of the two major methods for tensile strength measurement described in Section 2.5.2, an alternative method of testing with potentially less bias is presented for application to IGMs. The Unconfined Expansion Test (UET) is based on fracturing a cylinder of the IGM from using an inflatable probe. In this research, UET is performed to find out the tensile strength of brown coal in unconfined cavity expansion condition.

Described in Section 4.2.2, the tensile strength and the undrained shear strength are the parameters defining the tensile and shear failures of IGMs. For insitu PMT test in brown coal, the occurrences of tensile and shear failure depend on the insitu horizontal stress as shown in Figure 4.33. Since the insitu horizontal stress is related to the test depth, the determination of appropriate test depth for insitu PMT in brown coal can be achieved by knowing the tensile strength using the UET.

Test results from a series of tests on brown coal using the UET are presented. The results are also numerically validated through an eXtended Finite Element Method (XFEM) model analysis of the UET procedure using ABAQUS 6.14.

4.2.2. Theoretical Background

The UET employs cylindrical cavity expansion to radially crack an unconstrained cylindrical specimen. The cylindrical cavity is drilled along the axis of the cylindrical specimen. An inflatable probe is inserted into the cavity and expanded hydraulically. The probe hydraulic pressure must be monitored during the test to determine the failure pressure. This pressure can be converted to the tensile strength of the material. Also, the elastic stiffness of the material in tension can be determined by measuring the volume of expansion of the probe.

The theory of cylindrical cavity expansion was originally developed for field scale pressuremeter testing in boreholes (Clarke 1996; Haberfield 1997; Yu 1990). However, pressuremeter testing is usually employed in geotechnical engineering to measure in-situ horizontal stress or fundamental soil properties such as shear modulus or undrained shear strength. Cylindrical cavity expansion has also been used in pavement engineering for determining the shear and compressive properties of asphalt mixtures (Alavi and Monismith 1994; Crockford 1993).

Haberfield (1997) and Ladanyi (1967) showed that cavity expansion inside brittle materials such as rock may initiate radial crack(s) from the cavity wall. Figure 4.33 shows two Mohr circle diagrams illustrating the difference between (a) shear strength, and (b) tensile strength dominated failure in a vertical borehole. The magnitude of the in-situ horizontal stress is the centre of Mohr circles, σ_{h0} . While the cavity is expanding, it generates radial compression stress, σ_r greater than 0 (compression), and circumferential tension stress, $\sigma_\theta < 0$ (tension). The difference between the magnitude of these two principal stresses then defines the shear stress, $\tau = (\sigma_r - \sigma_\theta)/2$. If the shear stress reaches the shear strength of the material, S_u , before the magnitude of the circumferential stress exceeds the tensile strength of the material the failure is compression dominant (Fig. 4.33a). If the magnitude of the circumferential stress exceeds the tensile strength before the shear strength is exceeded then the failure is tension dominated. In a borehole, the likelihood of a tension crack forming will depend on the in situ horizontal stress. In a laboratory, there is no in-situ horizontal stress, so $\sigma_{h0} = 0$. Since the tensile strength of IGMs is usually smaller than their shear strength, $\sigma_t < S_u$, failure occurs when the circumferential stress reaches the tensile strength, $\sigma_\theta = \sigma_t$. Hence, failure of a laboratory specimen of an IGM is typically tension dominant and the maximum pressure measured in UET test can be independent of the material shear strength.

For the UET experiments described in the research, cylindrical brown coal specimens of 75 mm diameter and cavity diameter of 10 mm were used. The cylinders were 71 mm long. The analytical solutions for thick-walled hollow cylinders are applicable in this case.

Knowing the internal applied pressure (p), and the specimen size, the pressure and stress distribution can be computed using the analytical solution for thick-walled cylinders derived by S. P. Timoshenko and Woinowsky-Krieger (1959), given in equation. 4.9 and 4.10.

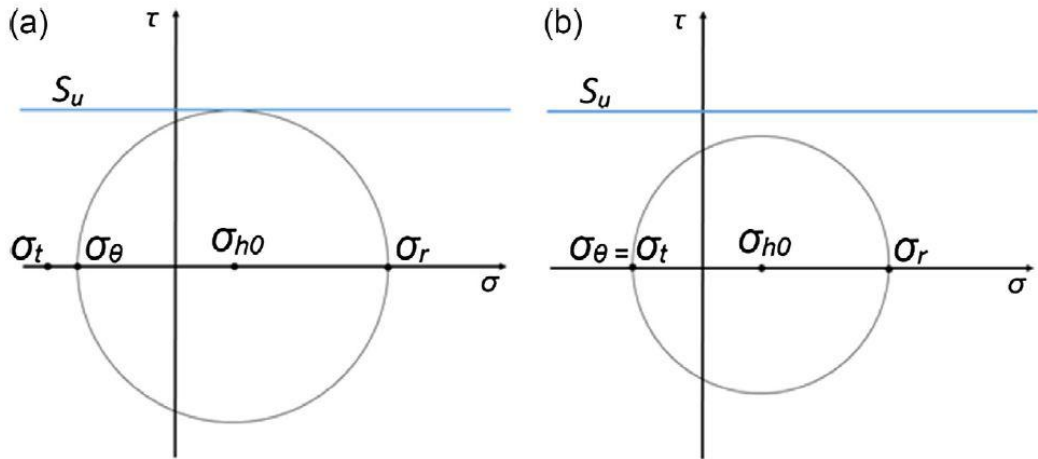


Fig.4.33. Failure due to cavity expansion, (a) compression dominant, (b) tension dominant

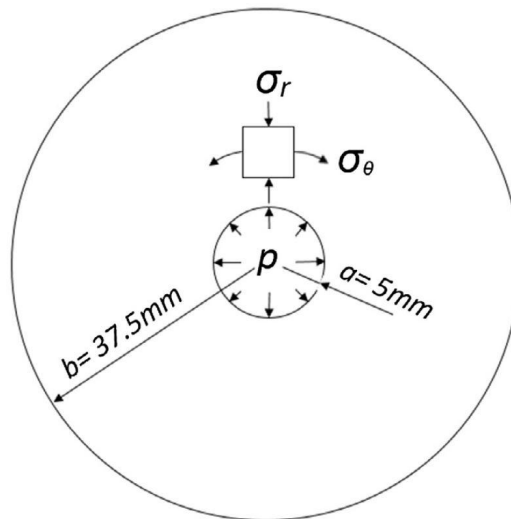


Fig.4.34.Plane view of the specimen

$$\sigma_{\theta} = \frac{a^2 p}{b^2 - a^2} \left(1 + \frac{b^2}{r^2}\right) \quad \text{Eq.4.9}$$

$$\sigma_r = \frac{a^2 p}{b^2 - a^2} \left(1 - \frac{b^2}{r^2}\right) \quad \text{Eq.4.10}$$

where σ_r =radial stress (in compression), σ_{θ} =circumferential or hoop stress (in tension), a =cavity radius, b =specimen radius, r =distance from the centre of the cavity. The maximum tensile stress occurs just on the cavity wall, so by putting $r=a$ in equation 4.9 the maximum tensile stress can be calculated from equation 4.11.

$$\sigma_t = \frac{(b^2+a^2)p}{b^2-a^2} \quad \text{Eq.4.11}$$

Considering the given specimen size (shown in Figure 4.34), and using equation 4.11, the tensile strength of the material for the UETs, can be computed as $\sigma_t=1.036p$.

In addition to the tensile strength of the material, the elasticity parameters (shear modulus and elastic stiffness) can be obtained from the UET if the cavity volume change is measured during the test.

Mair and Wood (1987) showed that the shear modulus (G) can be calculated from the linear part of pressure versus volume change profile for the cavity expanding in a soil (equation 4.12). The elastic stiffness can then be calculated from Hooke's law (equation 4.13), where E is the elastic stiffness, m is the Poisson's ratio, V_0 is the initial volume of the cavity, dp is the pressure change inside the cavity and dV is the volume change of the cavity.

$$G = V_0 \frac{dp}{dV} \quad \text{Eq.4.12}$$

$$E = 2G(1 + \nu) \quad \text{Eq.4.13}$$

4.2.3. Test Material

Victorian brown coal is very light with a typical unit weight of 11.5kN/m³. Its shear strength parameters are about 200kPa cohesion and 30° friction angle. Elastic stiffness and Poisson's ratio are of the order of 10–30MPa and 0.2–0.25, respectively. The brown coal used in the current research was collected from Yallourn mine, which extracts coal from the uppermost seams of the coal sequence. All specimens were extracted from a single 0.4m×0.4m×0.4m intact block of brown coal. The moisture content of the block was measured immediately after collection and was determined to be 182.23%. The block was stored and maintained in a humidity controlled storeroom at 12°C temperature. Test specimens were extracted from the block by drilling. During testing, specimens were well wrapped in a plastic membrane to conserve the moisture content. All tests were performed in a temperature-controlled room at 21°C.

4.2.4. Specimen Preparation

All of the UET specimens were cored from a saturated block of brown coal. Cylindrical specimens were cored with a diameter of 75 mm and length of 66 mm (see Figure 4.38). The specimen length of 66 mm was selected to ensure that the 64-mm expandable part of the probe lay completely inside the specimen and the stresses were essentially uniform along the specimen length. A 10-mm (plus 40–80 μ m soften due to drilling) cylindrical cavity was drilled along the axis of the cylinder. The ratio between the specimen' radius and cavity radius was 7.5 for all tests. The cavity was drilled with care to avoid initial cracking in the specimen. The finished specimens were stored under fully saturated conditions before the UET was performed.

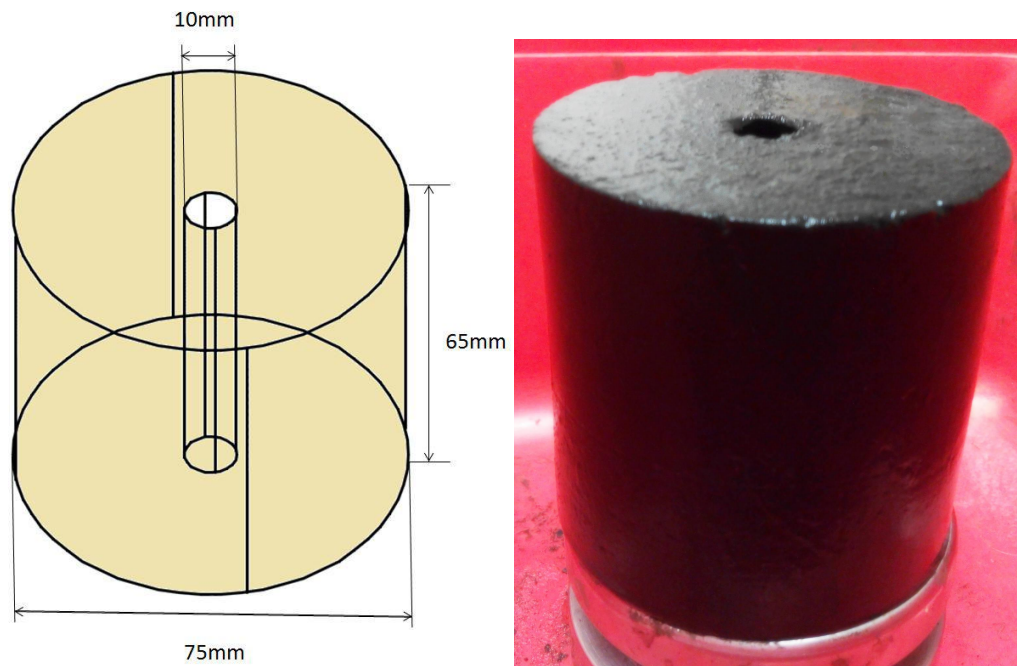


Fig.4.38. UET Specimen

4.2.5. Determination of Loading Rate

Excess pore water pressure caused during cylindrical expansion was a concern during interpretation of the tests. Hence, an appropriate loading was determined rate to minimise excess pore water pressure at the centre of the specimen by carrying out an FEM analysis with Abaqus/Standard 6.14. An effective stress analysis method for fluid-filled porous media available in Abaqus/Standard 6.14 was employed.

The test was modelled by a conventional method that considers the coal as a porous medium and adopts effective stress principles to describe its behaviour. The porous medium modelling provided in Abaqus/Standard considers the presence of two fluids in the pores. One is the wetting phase that is deemed to be incompressible (water in this analysis). The other is typically a gas, which is relatively compressible. Only the wetting phase (water) was used in the analysis. It was assumed that the coal specimen was fully saturated and the voids were completely filled by wetting liquid. The coal hydraulic conductivity and void ratio values were $4 \times 10^7 \text{ mm/s}$ and 1.5, respectively, and the elastic stiffness was varied from 10MPa to 30MPa Tolooiyan et al. (2014).

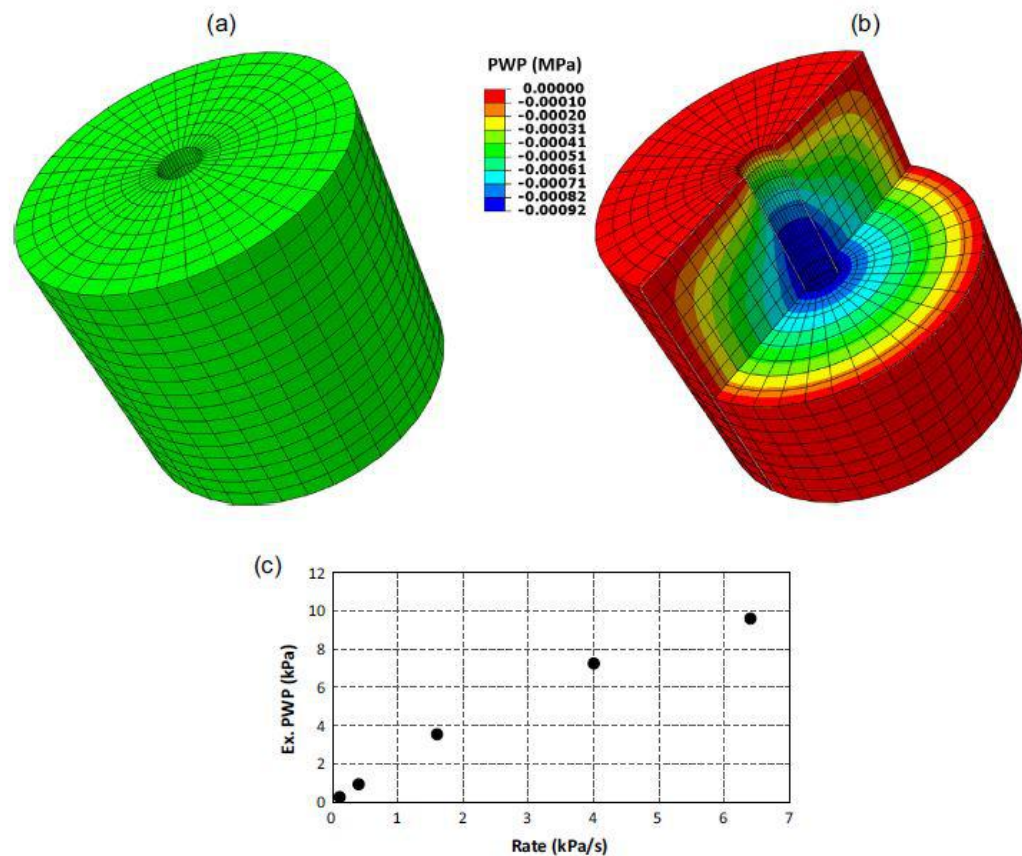


Fig.4.39. (a) 3D FEM geometry, (b) distribution of excess pore water pressure, (c) plotting developed excess pore water pressure against expansion stress rate.

The 3D model finite element geometry is shown in Figure 4.39a, where 5120 eight-node brick, trilinear displacement, trilinear pore pressure elements (type C3D8P) are used to model the test geometry. A pore water pressure boundary condition with zero magnitude was predefined over the external surface of the specimen. The probe

expansion was simulated by applying a cylindrically distributed stress inside the cavity at different rates of change. The maximum excess pore water pressure was investigated when the effective stress reached 180kPa at the centre of the specimen. As shown in Figure 4.39b, the magnitude of excess pore water pressure is less than 1kPa at an effective stress of 180kPa when the cavity expansion stress rate is 0.4kPa/s, hence any rate less than 0.4kPa/s should be fine for this purpose (Note, the model defines positive pressures as negative values, see Figure 4.39a and b). Figure 4.39c shows the sensitivity of the developed excess pore water pressure to the expansion stress rate. The cavity expansion rate of 0.1kPa/s was chosen as the appropriate loading rate for performing the UETs.

4.2.6. UET Setup

To prevent specimen cracking prior to testing the following setup procedure was adopted. The specimen was placed on a horizontal platform before the UET probe was pushed in. The platform had a hole in the centre to let the tip of the probe extend through the specimen. The probe was lubricated with vaseline to ease its insertion into the specimen. When the probe was inserted (see Figure 4.40), the drainage valve of the automated pressure-volume controller was open to prevent any excess initial pressure in the probe. The pore pressure value was monitored after probe placement. When the magnitude of water pressure in the system was back to the initial value (0–5kPa) and was stable, the UET was started immediately to avoid moisture loss.

A target water pressure (400kPa), which is higher than the maximum tensile strength, and a test period of 60min was set to give an applied pressure rate growth of 0.1 kPa/s. The volume change and water pressure were automatically recorded each second and the test was stopped immediately after failure. A video camera was set up over of the specimen to record the specimen failure.



Fig.4.40. Probe is placed inside the specimen

4.2.7. Results

Results for eight UETs on brown coal are shown in Figure 4.41. Each pressure-strain profile consists of three distinct regions. As the internal diameter of the cavity is not exactly 10mm and 20–40 μ m on the sides of the cavity is softened due to both drilling and placement of the probe, the initial curved region (Region 1), is attributed to expansion of the membrane until it comes into full contact with the sides of the cavity. This is similar to the results of typical field scale Menard pressuremeter test in geotechnical materials, Region 2 is approximately linear until the first crack is initiated (primary failure), marking the tensile strength of the brown coal specimen. The primary failure pressure for the tested specimens were found to lie in the range from 110kPa to 150kPa. By applying the correction factor of 1.036 (calculated from equations 4.9-4.11),

the tensile strength of the tested Yallourn brown coal specimens is found to lie in the range from 114kPa to 155kPa. This finding is broadly in agreement with results reported in Tolooiyan et al. (2014), which gave results for the tensile strength between 110kPa and 130kPa for Loy Yang brown coal. The shear modulus and the elastic stiffness of tested specimens can be calculated from the slope of pressure-volume profile by using equation 4.12 and 4.13. By assuming a Poisson's ratio of 0.22 for brown coal, the measured elastic stiffness is in the range of 18–20kPa. Region 3 relates to the process of crack propagation (secondary failure). Figure 4.42 shows a brown coal UET specimen after the end of secondary failure. Since brown coal is considered a brittle material, it can be expected that the specimen fails (secondary failure) immediately after crack initiation (primary failure) with no further pressure increase for crack propagation. However, such a phenomenon was not experienced in any of the performed tests.

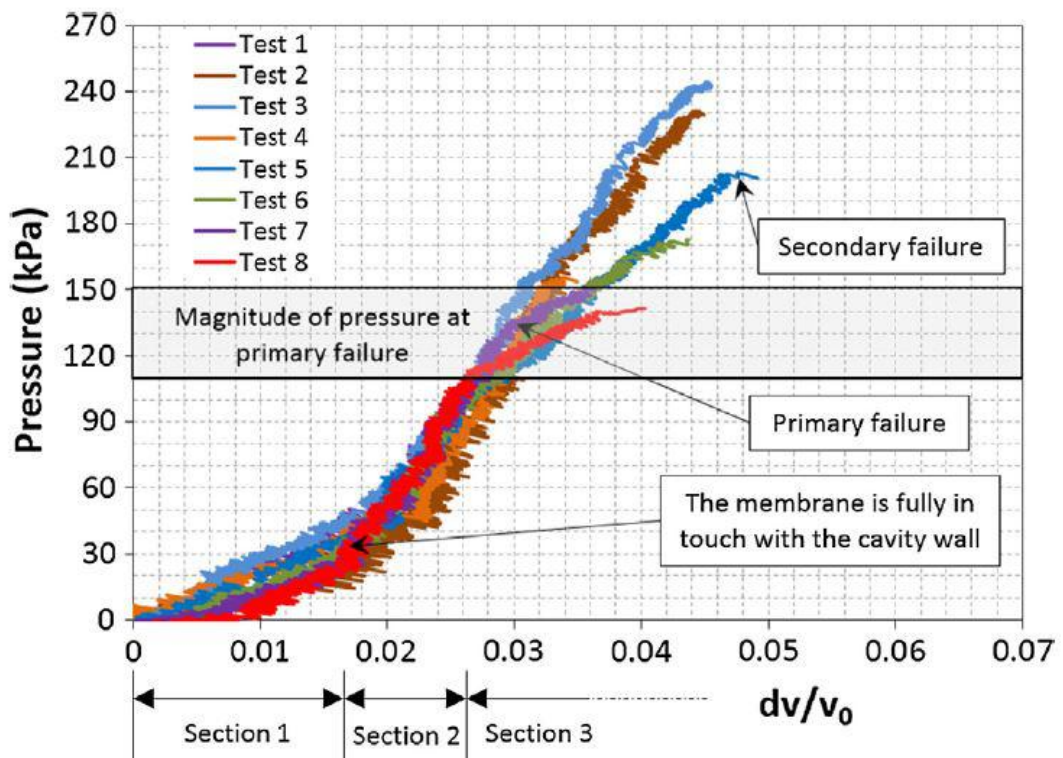


Fig.4.41. 8 test results of UET on brown coal

Two features affect how a crack propagates through a specimen under radial loading during secondary failure. The first is the energy release rate which determines how the forces that cause cracking are dynamically transferred to adjacent material and

the second is the distribution of stresses in the specimen in the direction of crack propagation and how these are modified by the generation of the crack. If the tip of the crack progresses into a region of lower, sub critical, tensile stress then the crack will cease to grow. Describing the contribution of these two components has been examined through further laboratory experiments to quantify the energy release rate and modelling to combine this with the changing stress patterns. A laboratory test was performed to determine the critical energy release rate, and XFEM analysis was performed to check the results.



Fig.4.42. Brown coal UET specimen after the secondary failure

4.2.8. Determination of Energy Release Rate

The critical energy release rate, G_C , is the work required to produce a unit increase in crack area. The crack propagates immediately after initiation if the energy release rate is larger than the critical energy release rate of the material ($G > G_C$). However, if the energy release rate is smaller than the critical energy release rate ($G < G_C$), then the crack is stable and further energy (pressure increase in the case of UET) is needed to propagate the crack. In practice, G_C can be determined from equation 4.17.

$$G_C = \frac{K^2(1-\nu^2)}{E} \quad \text{Eq.4.17}$$

where E is the elastic stiffness of the material, ν is the Poisson's ratio, K is the fracture toughness in Mode I (the tensile stress is normal to the plane of the crack).

Fracture toughness (K) is a property of the material that describes its ability to resist fracture and can be determined experimentally in the laboratory. Semi-Circular Bending tests (SCB) suggested by (Chong and Kuruppu 1984) were performed on brown coal specimens to measure the fracture toughness. Few specimen machining operations and easy test procedures using common testing apparatus are major advantages of the SCB test Ayatollahi and Aliha (2006).

The specimen geometry and the test set-up for the SCB are shown in Figure 4.43. A direct shear box apparatus available in most geotechnical laboratories was modified for this test. The apparatus can apply positive or negative deformation along a predefined horizontal axis. A 5kN S-Beam load cell with an accuracy of 1N was employed to measure the bending load. The shear box was replaced by two aluminium plates, one connected the specimen to the load cell while the other one connected the specimen to the axle through two rollers. Deformation was applied at a slow rate to fail the specimen while avoiding excess pore water pressure. The magnitude of the load at failure (FSCB) was converted to fracture toughness using equation 4.18 and equation 4.19 (Kuruppu and Chong 2012).

$$Y = 5.6 - 22.2\left(\frac{c}{r}\right) + 166.9\left(\frac{c}{r}\right)^2 - 576.2\left(\frac{c}{r}\right)^3 + 928.8\left(\frac{c}{r}\right)^4 \quad \text{Eq.4.18}$$

$$K = \frac{Y \times F_{SCB} \times \sqrt{\pi c}}{2rt} \quad \text{Eq.4.19}$$

where Y is a dimensionless intensity factor, t is the specimen thickness of 30mm.

Determination of the deformation rate was performed by using effective stress analysis for fluid-filled porous media available in Abaqus/Standard 6.14 in the same manner as explained for the determination of the loading rate in UET. The coal hydraulic conductivity and void ratio values were 4×10^{-7} mm/s and 1.5, respectively, and the elastic stiffness was 19MPa. The 3D finite element geometry is shown in Figure 4.44a, where 1050 eight-node brick, trilinear displacement, trilinear pore pressure

elements (type C3D8P) are used to shape the specimen in true scale. The top loading plate and two rollers were modelled as analytical rigid bodies. A pore water pressure boundary condition with zero magnitude was predefined over the external surface of the specimen and inside the initial cut (c). The bending test was simulated by applying deformation over the top loading plate, and maximum, and minimum excess pore water pressures were investigated.

Figure 4.44b shows the simulated pressure distribution for the deformation rate of 0.0002mm/s when the magnitude of the force reacting against the applied deformation reached 30N. The maximum excess pore water pressure and excess pore water suction are 0.47kPa and 0.80kPa, respectively at this load. Since these values are small, 0.0002mm/s was considered a reasonable rate for performing SCB tests on brown coal. The results of the laboratory SCB tests showed that the average F_{scb} value for the brown coal specimens was about 26N when deformation was applied at a rate of 0.0002mm/s implying that pore pressures were acceptable for these tests.

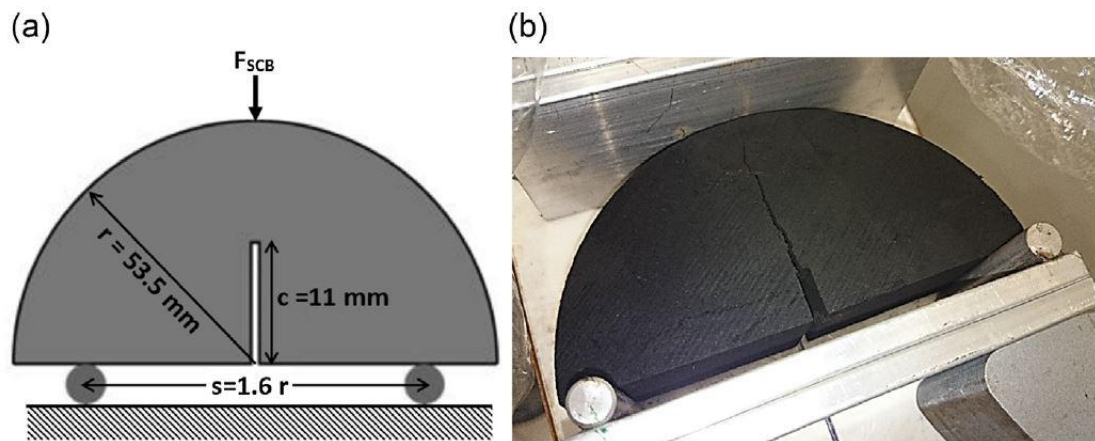


Fig.4.43. SCB specimen and setup, (b) brown coal SCB specimen after failure

Based on the average measured F_{scb} of 26N, a fracture toughness of $6.86\text{kPa}\cdot\text{m}^{1/2}$ was calculated using equation 4.18 and equation 4.19. Inserting this value in equation 4.17 and adopting the average elastic stiffness of 19MPa and Poisson's ratio of 0.22 yields a critical energy release rate of $2.357\text{Pa}\cdot\text{m}$.

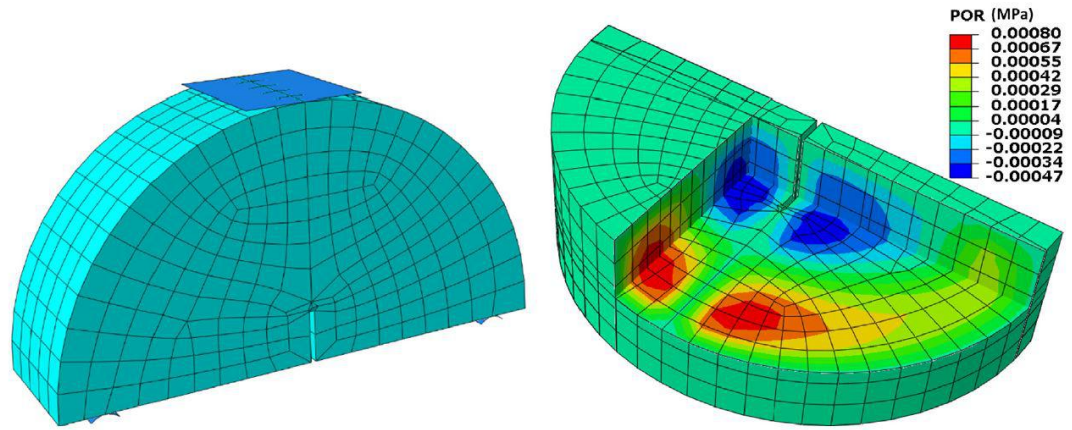


Fig.4.44. (a) The FEM geometry of SCB specimen, (b) distribution of pore water pressure/suction in SCB specimen.

4.2.9. XFEM analysis

The extended finite element method (XFEM) is an effective way to simulate initiation and propagation of a discrete crack and alleviate the shortcomings associated with meshing crack surfaces. This method was first introduced by Belytschko and Black (1999). It is an extension of the conventional FEM and is based on the theory of partition of unity developed by Melenk and Babuška (1996), which allows local enrichment functions to be efficiently incorporated into a FEM approximation. Two special enrichment functions provide for the presence of discontinuities in conjunction with additional degrees of freedom.

For the purpose of fracture analysis, the enrichment functions mostly consist of the near-tip asymptotic functions that capture the singularity around the crack tip and a discontinuous function that represents the jump in displacement across the crack surfaces. The approximation for a displacement vector function u with the partition of unity enrichment is shown in equation 4.20 (V. ABAQUS, 2014).

$$u = \sum_{I=1}^N \underbrace{N_I(X)}_{T1} \left[\underbrace{u_I}_{T2} + \underbrace{H(x)a_I}_{T3} + \underbrace{\sum_{\alpha=1}^4 F_{\alpha}(x)b_I^{\alpha}}_{T4} \right] \quad \text{Eq.4.20}$$

where $N(x)$ is the nodal shape function; u_I is the nodal displacement vector associated with the continuous part of the FE solution; $H(x)$ is the discontinuous jump function across the crack surfaces; a_I is the nodal enriched degree of freedom vector;

$F_\alpha(x)$ is the elastic asymptotic crack tip functions; and b_i^α is the nodal enriched degree of freedom vector. In this function, the terms T1 and T2 apply to all the nodes in the model; the term T3 applies to nodes whose shape function support is cut by the crack interior; and the term T4 applies only to nodes whose shape function support is cut by the crack tip (see Figure 4.45).

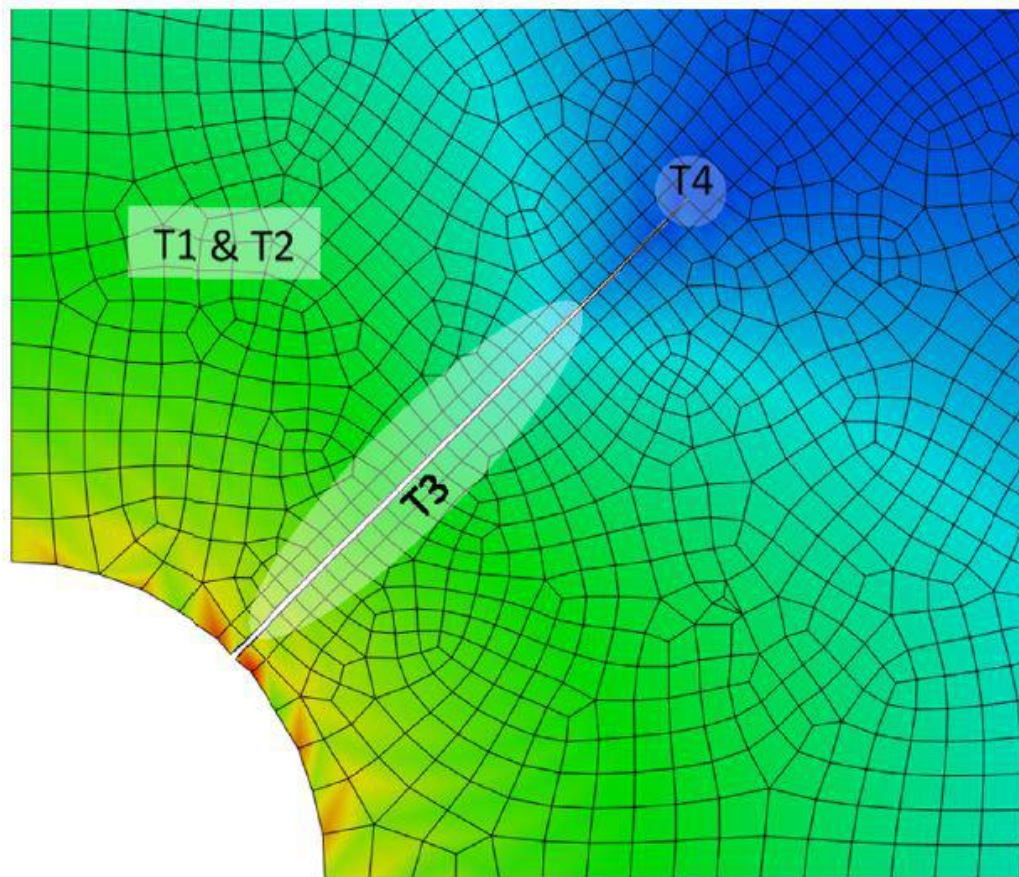


Fig.4.45 The XFEM approximation

Unlike the traditional crack propagation methods that require the failure zone to align with element boundaries and the cracks to develop along a set of predefined paths, the XFEM-based cohesive segments method simulates the crack initiation and propagation along any solution-dependent path in the specimen. For the simulation procedure adopted, the asymptotic crack tip function (Term 4 in equation 4.20) was not required and only the discontinuous jump function across the crack surfaces is defined as described in equation 4.21.

$$H(x) = \begin{cases} 1 & \text{if } (z-z') \cdot m \geq 0, \\ -1 & \text{otherwise,} \end{cases} \quad \text{Eq.4.21}$$

where z is a Gauss point, z' is the closest point to z that is on the crack, and m is the unit outward perpendicular to the crack at z' . It should be noted that, in this method, the crack has to spread across the entire failing element in one time step to avoid the need for the asymptotic crack tip function.

As the trigger for crack initiation, the maximum allowable principal tensile stress was defined as the failure criterion. Thus, crack initiation occurs when the maximum principal stress reaches the predefined critical value that is the average tensile strength of the brown coal specimen (130 kPa). Since the magnitude of crack opening was not measured during the experiments, no traction-separation law was employed to address this in the modelling.

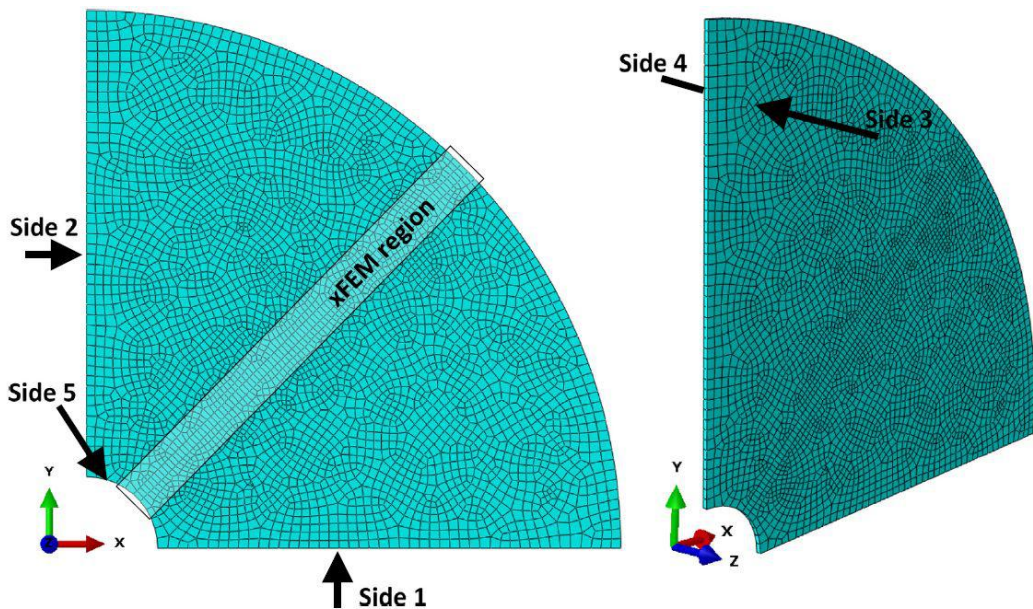


Fig.4.46. The FEM geometry of UET specimen

To minimise the computational cost of numerical analysis, only a thin layer of a quarter of the UET specimen was modelled. The 3D model finite element geometry is shown in Figure 4.46, where 3842 eight-node linear brick, reduced integration, hourglass controlled elements (type C3D8R) are used to define the specimen geometry. To satisfy the required boundary conditions, side 1 was fixed in the Y direction, side 2 was fixed in the X direction, and sides 3 and 4 were fixed in the Z direction. Since the stress was expected to develop uniformly prior to crack initiation/propagation, the XFEM functions were only allocated to the elements located along the central radius

(the XFEM region as shown in Figure 4.46). In this case the crack to initiate and propagate only in this region. A cylindrical pressure was applied on side 5 to simulate the cavity expansion.

Table 4.5. The input parameters for constitutive modelling.

	Tensile strength (kPa)	Poisson's ratio	Critical energy release rate (Pa m)	Elastic Stiffness (MPa)	Friction angle (degrees)	Cohesion (kPa)
value	130	0.22	2.357	19	20	150

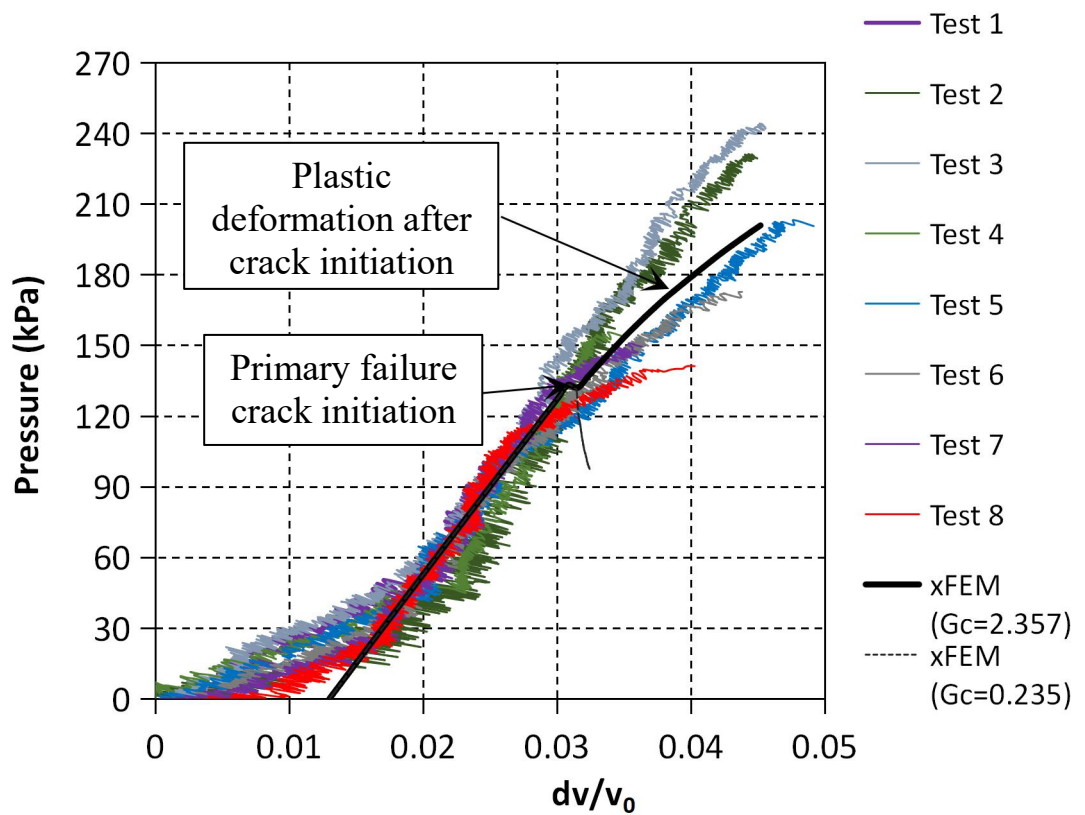


Fig.4.47. UET test on brown coal, the comparison between experiment and XFEM results.

The input parameters for constitutive modelling are given in Table 4.5. It should be noted that, although the maximum principal stress was assigned to trigger the failure in tension, the Mohr-Coulomb model was employed to model the failure in compression, considering that the elements close to the cavity may undergo excessive compression due to the cavity expansion.

Two XFEM analyses were performed to simulate the UET on brown coal. In the first analysis, the actual critical energy release rate of brown coal, $G_c=2.357Pa\cdot m$, was used. In the second analysis a smaller value, $G_c=0.235Pa\cdot m$, was adopted.

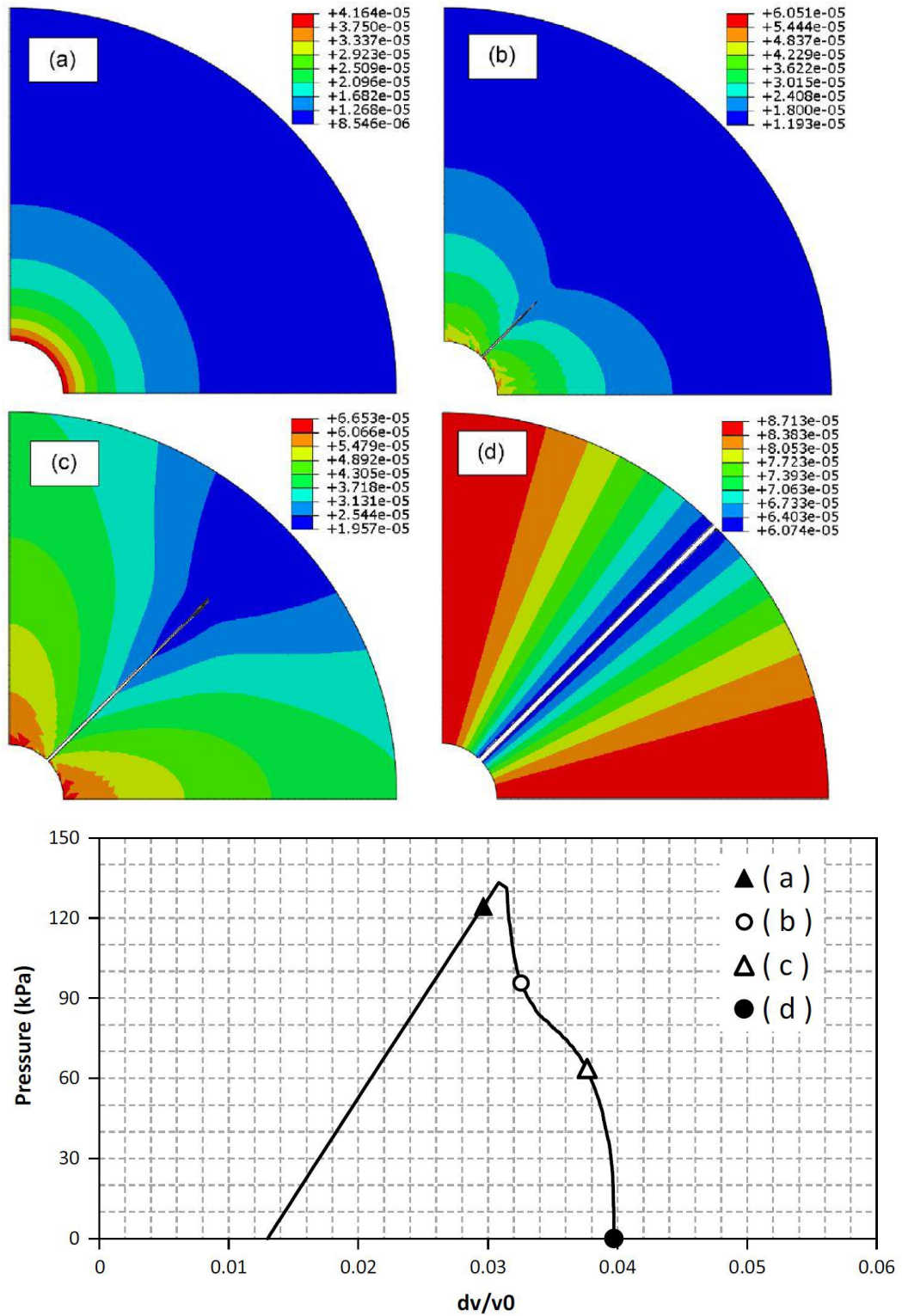


Fig.4.38 Radial deformation in UET specimen (mm)

The goal of the two analyses was to show the effect of the magnitude of critical energy release rate on the behaviour of crack propagation in UET. Results of both analyses are shown in Fig. 15. The initial difference of 30 μ m between cavity and probe radius apparent in the laboratory tests was not considered in the simulation. Hence, the XFEM results are plotted from $dV/V_0 = 0.013$. As shown in Figure 4.47, pressure increases linearly up to critical tensile stress of 130kPa for both analyses. In the analysis using the actual G_c , the energy release after crack initiation (primary failure) does not cause uncontrolled extension of the crack and the pressure increases after crack initiation to extend the crack. With the lower critical energy release rate, the energy release exceeds the critical value and the crack propagates immediately after initiation without further increase in the forcing pressure. Figure 4.48, shows the modelled UET specimen prior, during and after failure.

4.2.10. Comparison with traditional methods

The main objective of developing the UET is to measure the tensile strength of IGMs with a high accuracy while avoiding the biases in the two major methods for tensile strength measurement (DTT and BT) associated with stress concentration, specimen shape and predefined failure plane. Coviello et al. (2005), Yu et al. (2006), Fahimifar and Malekpour (2012) and Tolooiyan et al. (2014) showed that the magnitude of the tensile strength measured by the BT and DTT can be underestimated by more than 5–15% due to the specimen shape and stress concentration around the failure zone. To explore the performance of the UET against the DTT and BT, the constitutive model calibrated during simulation of the UET was employed to simulate the DTT and BT by XFEM (see Figure 4.49). Since the actual tensile strength of 130kPa is used as the input tensile strength in all the simulations, the difference between the specimen's tensile strength as the simulation outputs and the given input tensile strength is indicative of the relative bias of each of the test methods. For the simulation of DTT, seven thousand four hundred eighty-eight linear hexahedron elements (type C3D8R) form each bone-shape end, and 19,742 quadratic tetrahedron elements (type C3D10M) are used to shape the middle part of the specimen. As suggested by Tolooiyan et al. (2014), the shape of the aluminium grips that axially pull the specimen was established to minimise tensile forces within the specimen inside the grip and to produce smoothly varying stress and strain within the gripped region of the

specimen. Since the stiffness of aluminium is much higher than the stiffness of the coal, the two grips are modelled using analytical rigid surfaces to decrease the computational cost. Since the specimen may slide against the aluminium grips during the test, the coal-aluminium interface friction of $\mu=0.55$ is taken into account. For the simulation of the BT, the specimen was modelled with 44,720 linear hexahedron elements (type C3D8R). The aluminium plates that axially push the specimen were modelled using analytical rigid surfaces that account for aluminium coal friction and surface displacement of the coal at the contact surfaces. Please note that since the BT specimen is in compression, the Elastic stiffness of 64MPa is considered instead of 19MPa. For more information regarding the application of DTT and BT for IGMs, please refer to Tolooiyan et al. (2014).

Figure 4.50, compares the magnitude of tensile strength from the simulation of BT, DTT and UET. As shown in this figure, the BT and DTT produce similar values and both underestimate the modelled tensile strength. The UET returns the modelled tensile strength of the specimen.

To investigate the underestimation of the tensile strength by BT and DTT, the effect of stress concentration around the failure zone was investigated. Figure 4.51 shows the stress concentration around the failure zone in DTT, UET and BT, just before crack initiation and failure. The areas indicated in red have reached the principal stress of 100–130kPa and form the failure zone in which the crack initiates. From these figures, it is clear that the principal stress is not developed uniformly on the failure plane of the DTT specimen (see Figure 4.51a). In the BT specimen, only a portion of the specimen's diameter reaches the failure stress at the onset of crack initiation (see Figure 4.51c). However, in BT, the total length of the specimen's diameter is taken into account for the calculation of the tensile strength. As expected from reviewing the work by Coviello et al. (2005), Yu et al. (2006), Fahimifar and Malekpour (2012) and Tolooiyan et al. (2014), the impact of stress concentration around the failure plane and the non-uniform stress distribution along the failure zone caused by DTT and BT introduce a significant bias in the measurement of tensile strength. It is clear that in the UET, the principal stress is developed uniformly around the internal diameter of the specimen where crack initiates (see Figure 4.51b). This is why the measured tensile strength from the XFEM simulation of this test is similar to the given input tensile strength.

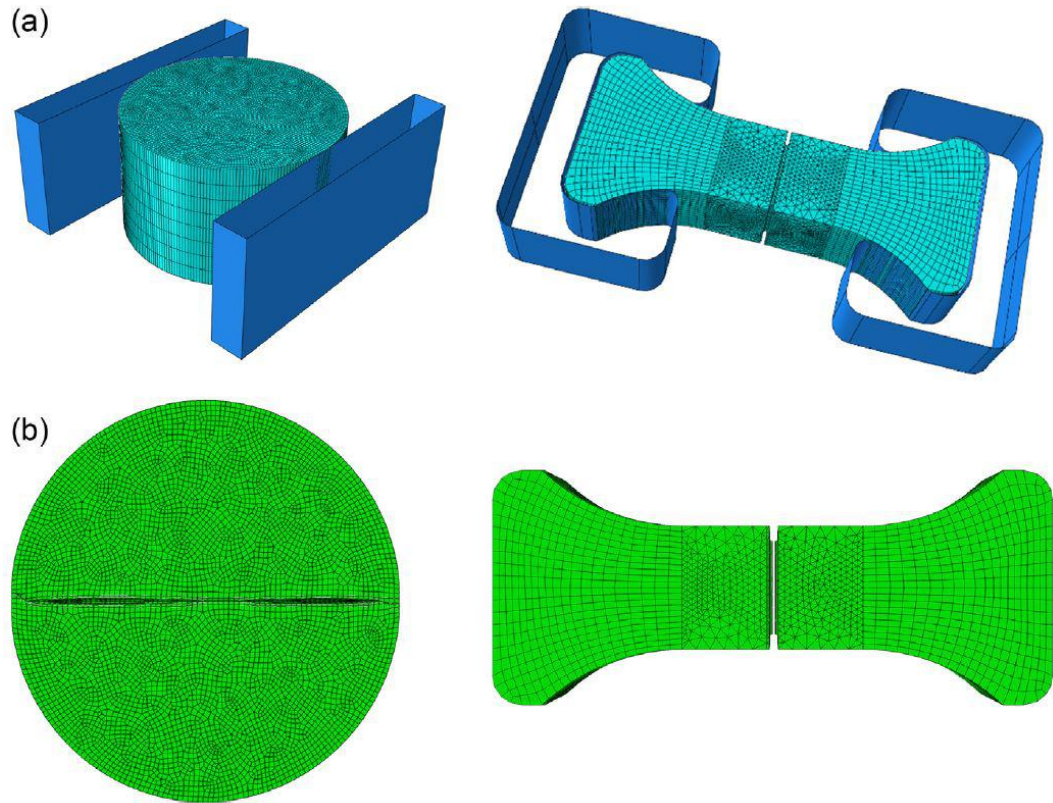


Fig.4.39. Simulation of BT and DTT using XFEM; (a) before failure, (b) after failure.

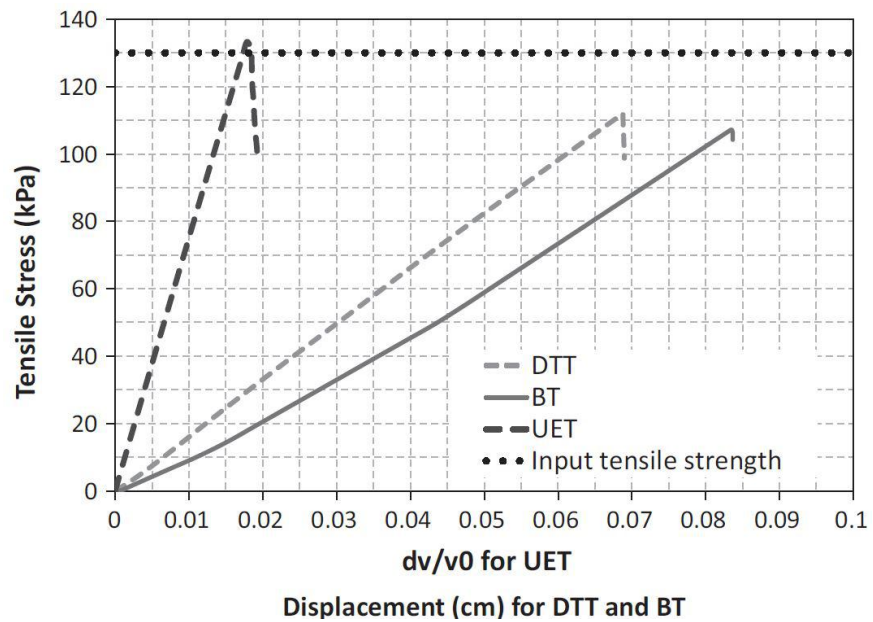


Fig.4.50. Measured tensile strength from simulation of DTT, BT and UET.

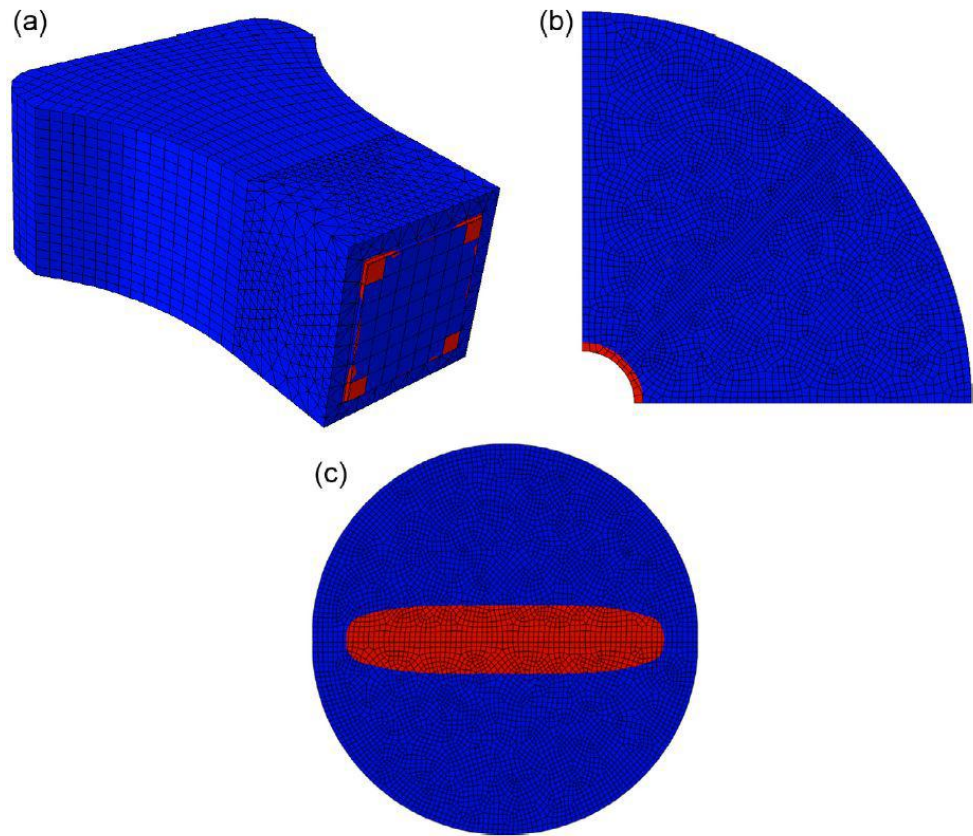


Fig.4.51. Stress concentration just before failure; (a) DTT, (b) UET, (c) BT.

5. Pressuremeter Tests at the Yallourn Open-pit Brown Coal Mine

5.1. Introduction

In-situ Pressuremeter Tests (PMTs) were conducted adjacent to the open-pit batter on the Yallourn brown coal mine in Victoria. The PMT site for this research project is located north-east of the mining field of the Yallourn mine, adjacent to the Latrobe River. The PMTs were performed in the test cavities from two out of three in situ boreholes on the site, as shown in Figure 5.1. The first pressuremeter borehole, PM-1, is located at the mine floor. The second pressuremeter borehole, PM-3 is behind the open-pit batter. Relative to sea level, the Reduced Levels (RL) of the surfaces of PM-1 and PM-3 are -41m and 38.5m, respectively. The batter is approximately 80m high. The purpose of the PMTs is to describe the geotechnical parameters of the ground materials underlying the mining surface.



Fig.5.1. Location of the designed boreholes

5.2. Equipment

The CMR20 radius-measurement pressuremeter probe was used for this research project. The probe was installed by the pre-bored method, as discussed in Section 5.3.

As shown in Figure 5.2, the CMR20 pressuremeter probe is 71mm in diameter and 940mm in total length. The expandable membrane is 426mm in length, which provided a slenderness ratio of 6. The probe is inflated with nitrogen gas. The pressure of the gas is monitored by the pressure gauge at the control unit. The strain measurement of the probe is conducted by four feeler arms. These feeler arms indicate the radial deformations in four directions. The radial deformations are then transmitted to the control unit through the wire harness on top of the pressuremeter probe. The radial and volumetric strains are then calculated based on the average radial deformations. The accuracies of the pressure measurement and the radial deformation measurement (in radial deformation) of the device are $\pm 1\text{Pa}$ and $\pm 1 \times 10^{-6}\text{mm}$, respectively.

The pressuremeter probe was calibrated before the test. The concept of membrane calibration is very similar to the process explained in Section 4.1 for the laboratory pressuremeter probe.

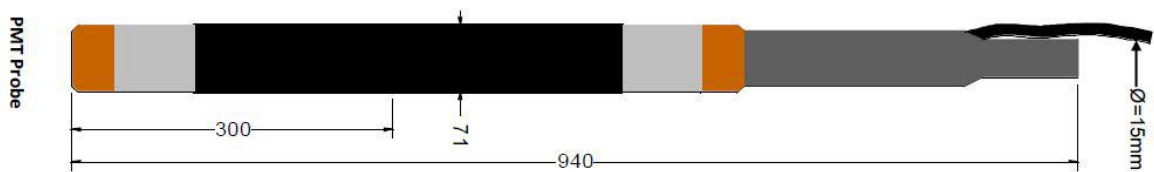


Fig.5.2. Pressuremeter probe diagram

5.3. Borehole Drilling

Two push-in cutting tubes were designed for the creation of the PMT cavities. The two cutting tubes, Cutter 1 and Cutter 2, are shown in Figure 5.3. As found from the UET test, the tensile strength of Yallourn brown coal was found to be around 100-150 kPa (Figure 4.41). Hence, to avoid failure in tension during the field pressuremeter testing, assuming the undrained shear strength of brown coal is around 300kPa to 350kPa, testing depth was designed to be at a minimum of 15 m below the ground level to provide minimum institute stress of 180 kPa when the unit weight of coal is around 12 kN/m^3 . For each PMT test, a borehole was drilled down up to the depth of 2.2m above the testing depth. Following this, Cutter 1 was pushed in by the drill rig to form the initial cavity. Then, Cutter 1 was withdrawn, and Cutter 2 was pushed in to trim the cavity wall and enlarge the cavity to fit the pressuremeter probe. After this, Cutter 2 was withdrawn, and the probe was lowered and placed into the cavity.

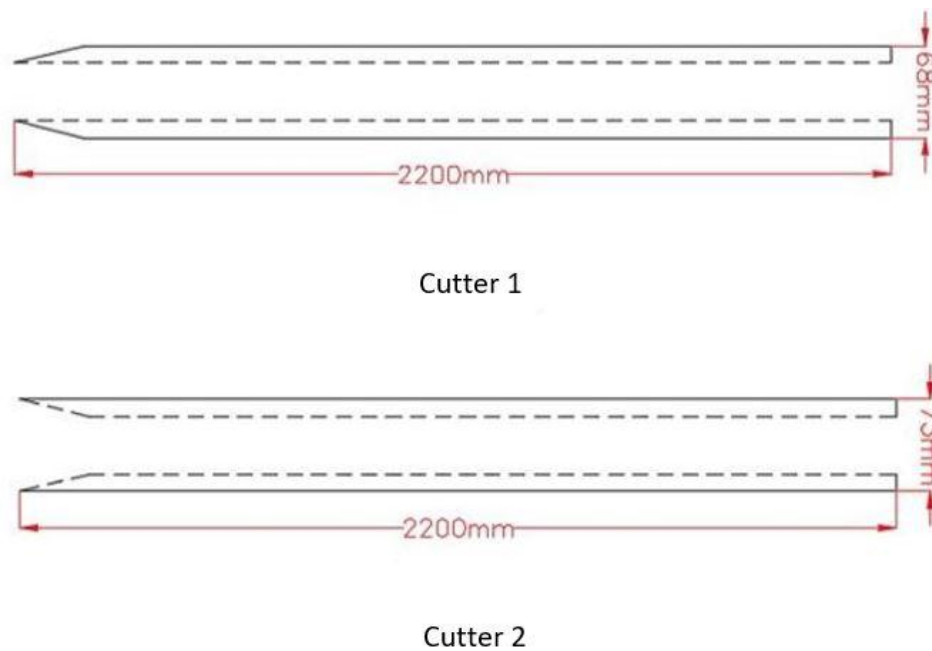


Fig.5.3. Diagram of two cutters

5.4. Pressuremeter Testing

5.4.1. Probe Expansion

Probe expansion was achieved by increasing gas pressure at a rate of 100 kPa/min. During expansion, the radial displacement of all feeler arms was monitored through the control unit over the ground. Since the capacity of the pressuremeter probe is 20MPa, care was taken regarding the magnitude of radial expansion to prevent overexpansion of the membrane. The termination of the test was governed by the maximum radial strain of 25%, which is 8.8mm of radial deformation.

5.4.2. Unload-reload Cycle

The pressuremeter tests applied an unload-reload cycle for the measurement of the (undrained) unload-reload shear modulus, G_{ur} . The strain level at which the first loading stage was terminated was between 7.5% and 10% of cavity strain, ε_c , which is roughly 2.5mm to 3.5mm in radial deformation. The deflating rate during the unloading stage was the same as that of the pressurising stage (100kPa/min). This was ensured in order to prevent the pressure from dropping below the initial cavity pressure at the beginning of the first loading stage.

5.5. Test Results and Parametric Interpretations

5.5.1. Stress-strain Curves

The raw data corrected by the contractor to eliminate errors associated with the system error (host, . The corrected data were then plotted as shown in Figure 5.4. The curves of pressure versus the average radial stain, calculated based on the average displacement of all four filler arms, were used for interpretation of the parameters.

5.5.2. Parameter Interpretations

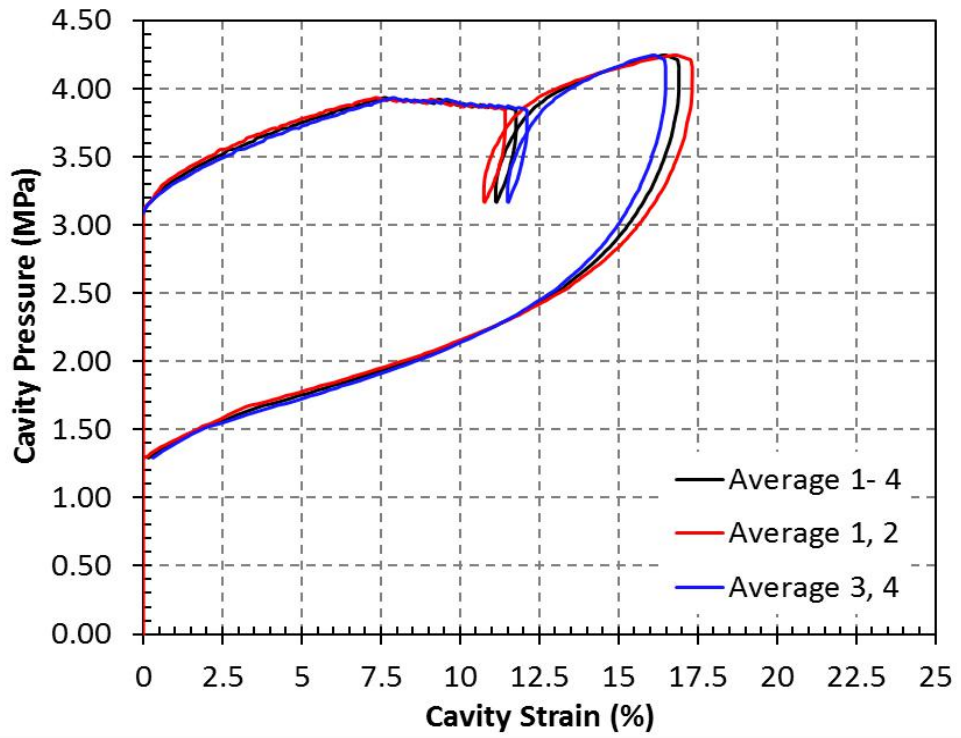
All of the in-situ pressuremeter tests in the present study were performed in cohesive materials (clay and silt) and soft rock (brown coal). As a result, the parameters interpreted from the pressuremeter tests are the total in-situ horizontal stresses, σ_h , the effective in-situ horizontal stress and σ'_h , the unload-reload modulus, G_{ur} , and the undrained shear strength, S_u . The parametric interpretations are reviewed in Section 2.3.2.

5.5.2.1. In-situ Horizontal Stress

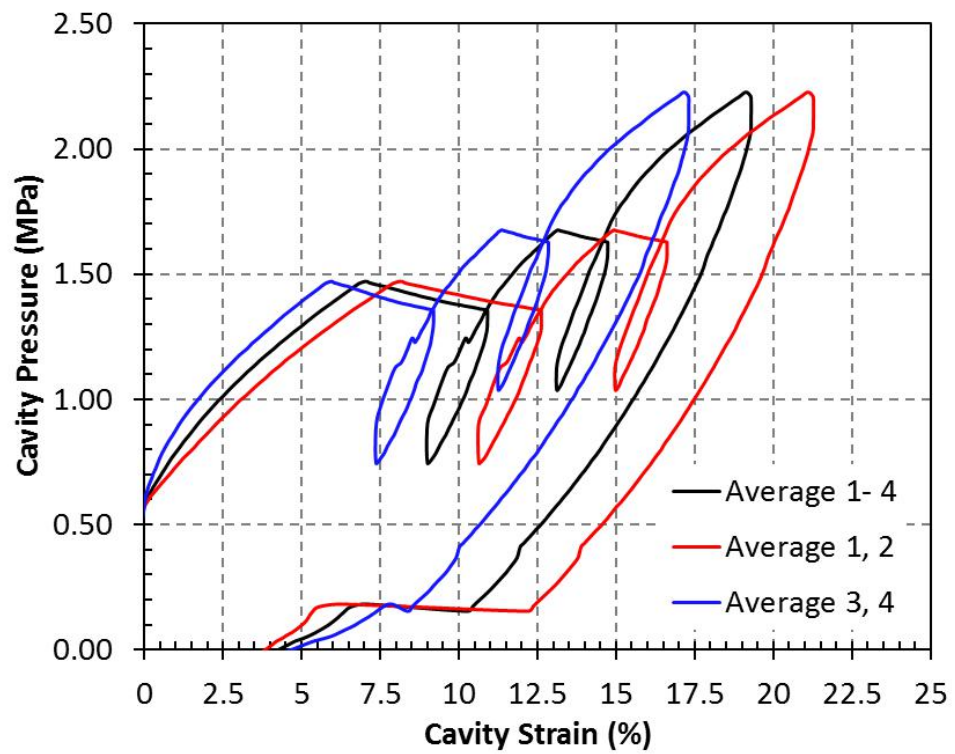
The total of all in-situ horizontal stresses (or so-called the ‘horizontal earth pressure’), σ_h , is derived from the cavity pressure during initiation of cavity expansion (lift-off pressure).

Due to the presence of groundwater, the hydrostatic pressure should be determined based on the horizontal stress values to achieve the effective value of in-situ horizontal stress, σ'_h (see Figure 5.5). Figure 5.6 shows the effective horizontal stresses measured at the two boreholes.

The two boreholes were drilled in different locations (one at the mine floor and one behind the mine batter), and they have different elevation and depths so as to compare the magnitude of in-situ horizontal stresses and describe the horizontal in-situ distribution. For this reason, all the results are plotted against the RL values, as shown in Figure 5.7. As shown in this figure, results from both boreholes are comparable. Additionally, this figure shows how the horizontal in-situ stress behind the batter at the level above the mine floor decreased due to stress relaxation as a consequence of mining.



(a) Depth=117.3m, Material: lignite clay



(b) Depth=39.4m, Material: brown coal

Fig.5.4. Stress-strain curves for two PMTs at borehole PM-3: (a) test in clay (b) test in brown coal

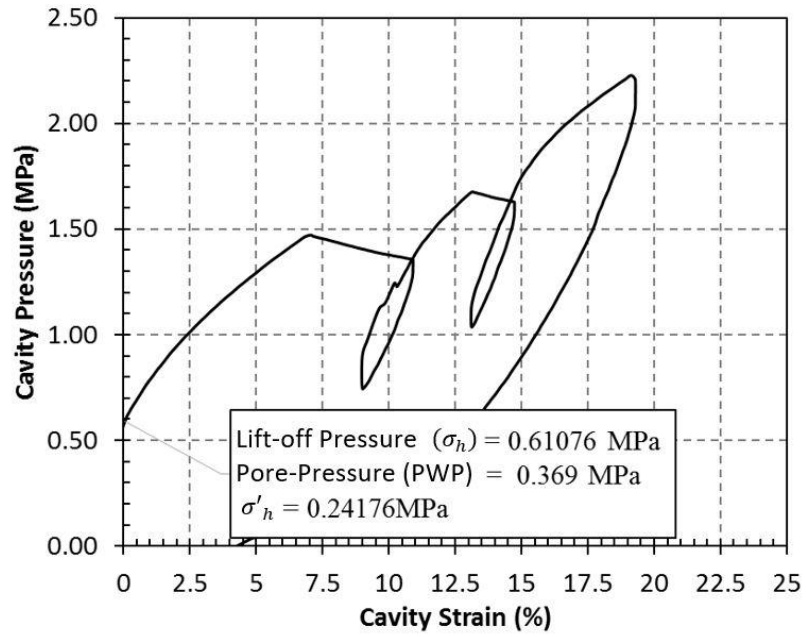


Fig.5.5. Measured effective horizontal stress at 39.4m depth of PM-3

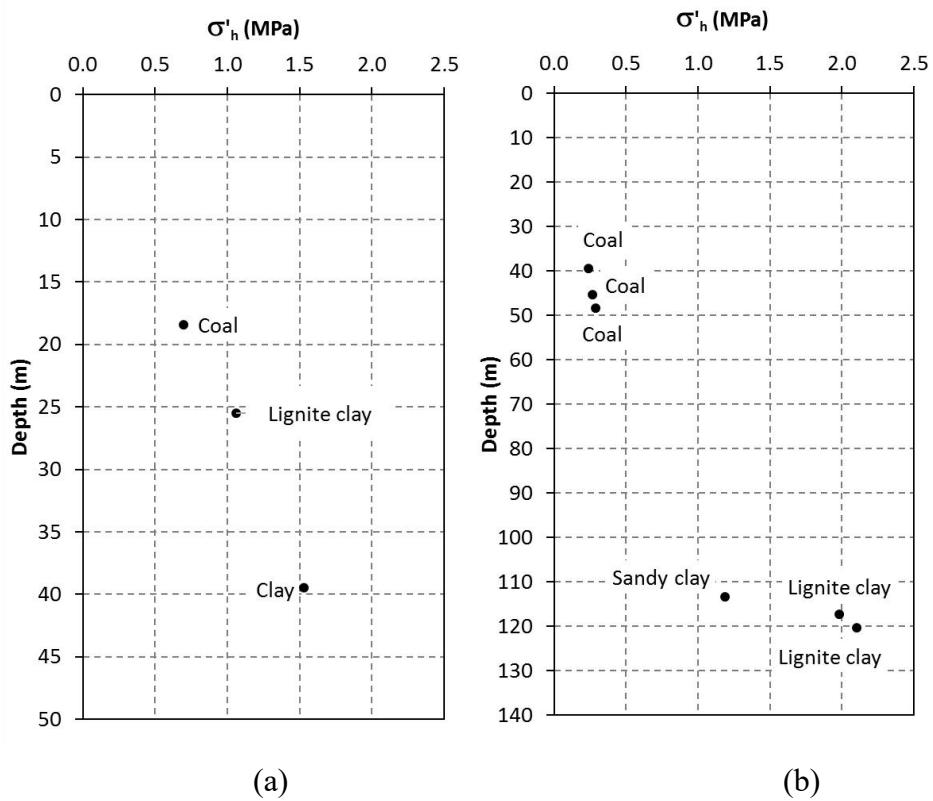


Fig. 5.6. Measured effective horizontal stresses at: (a) PM-1 and (b) PM-3

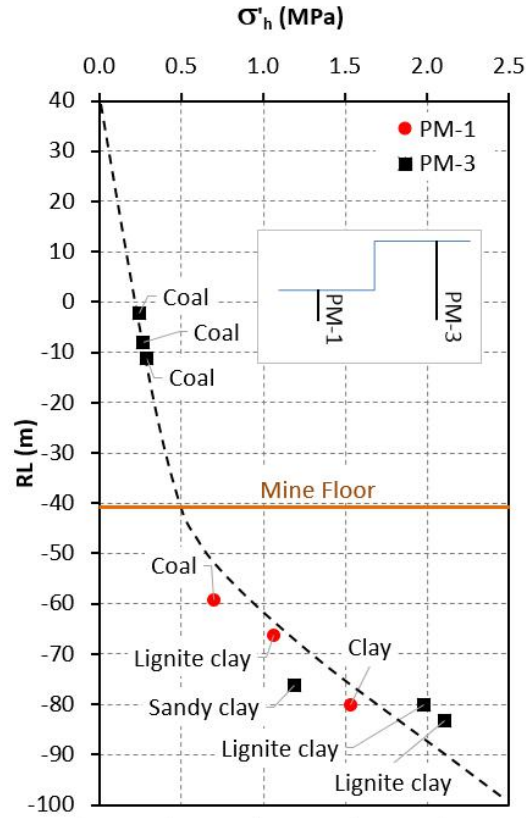


Fig. 5.7. Distribution of effective horizontal stresses at the mine floor and crest

5.5.2.2. Undrained Shear Strength

The estimation of the undrained shear strength, S_u (in MPa), is based on the graphical $p-\ln(\varepsilon_v)$ interpretation method described in Section 2.2.2.3. To apply this method, it is required that one convert the cavity pressure-radial strain ($p-\varepsilon_r$) curves into the cavity pressure-volumetric strain ($p-\varepsilon_v$) curves by applying Equation 2.7. After that, the volumetric strain value should be converted into the natural logarithmic values. The undrained shear strength is thereafter indicated by the slope of the linear part of the $p-\ln(\varepsilon_v)$ curves. An example of the interpretation is shown in Figure 5.8.

The results of the undrained shear strength measured by the pressuremeter tests at the two boreholes are shown in Figure 5.9. As expected, the undrained shear strength of coal was found to be independent of the magnitude of horizontal stress at both the mine floor and mine crest and it falls within the range of 400 to 500 kPa.

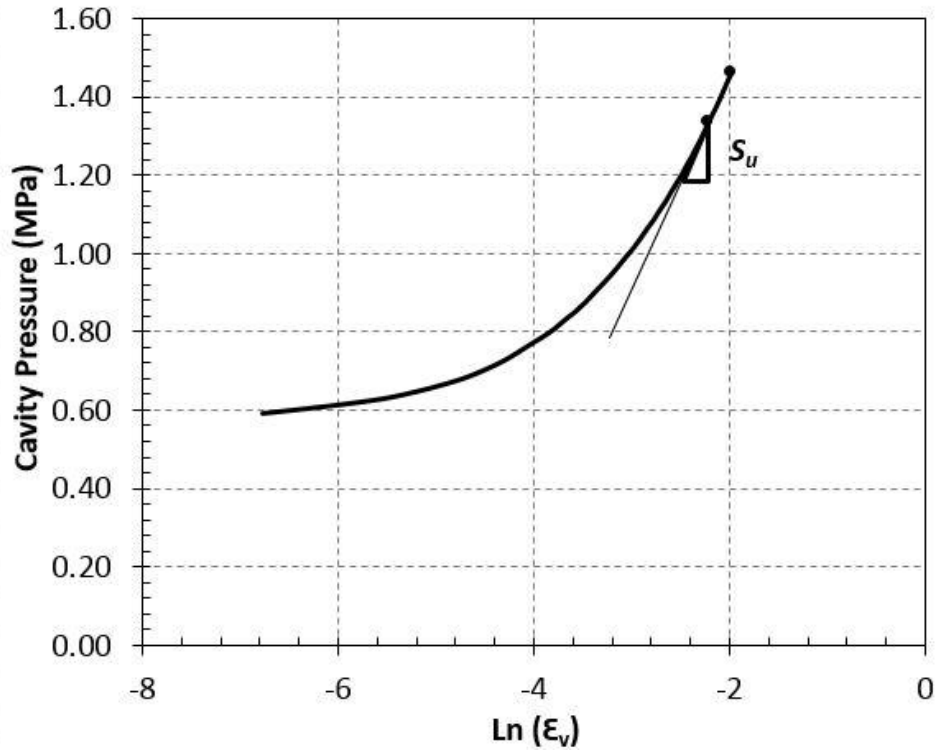


Fig.5.8. Interpreted brown coal undrained shear strength at 39.4m depth of PM-3

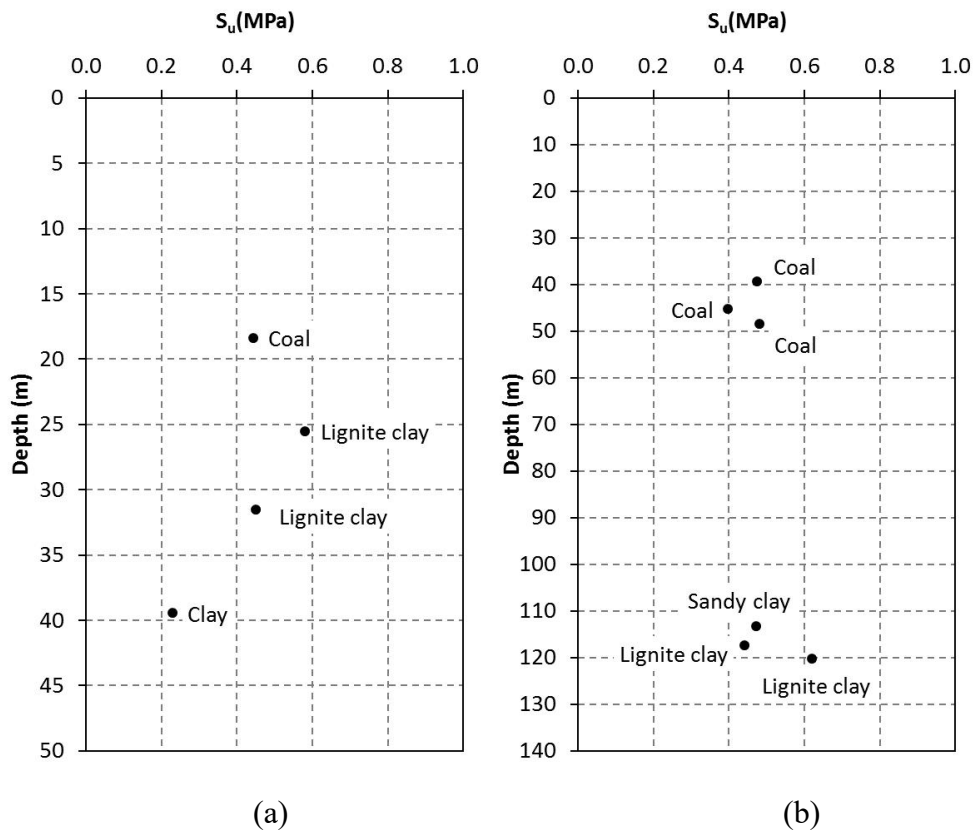


Fig. 5.9. Measured undrained shear strength at: (a) PM-1 and (b) PM-3

5.5.2.3. Unload-reload Shear Modulus

The unload-reload shear modulus, G_{ur} , can be interpreted based on the unload-reload cycles of both the $p-\varepsilon_c$ curves and the $p-\varepsilon_v$ curves. An example of using the $p-\varepsilon_c$ to interpret G_{ur} is shown in Figure 5.10. The intercept and bottom of the unload-reload cycle are connected by a straight line. Since the cavity strain is approximately half of the total volumetric strain during cylindrical cavity expansion, G_{ur} is defined as half of the slope of the straight line.

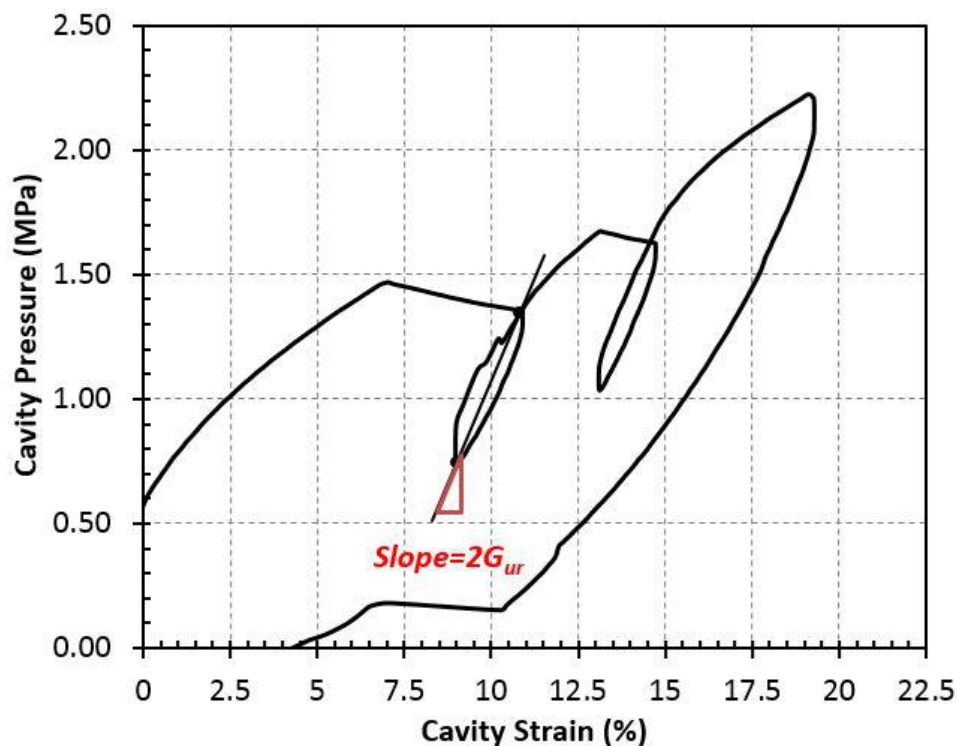


Fig.5.10. Interpreted brown coal unload-reload shear modulus at 39.4m depth of PM-3

For the investigation into the stress dependency of the materials' shear modulus, all the shear modulus results are plotted against the test RL in one graph (see Figure 5.11). As shown in this figure, the shear modulus of coal seems to be slightly dependent on the depth (or the magnitude of in-situ stress) and increases as depth increases. Additionally, the shear modulus of deep non-coal materials were found to be much higher than that of coal. Given that these material are softer than coal at zero confining pressure, this figure indicates the strong stress dependency of the shear modulus of non-coal materials.

One may pay attentions to the differences of ground material in the layer. The clayey content may have changed the stiffness of material. This variation cannot be determined by merely in-situ Pressuremeter Testing. Nevertheless, the trend of shear modulus seems to confirm the trend of measured in-situ horizontal stress as shown in Figure 5.7.

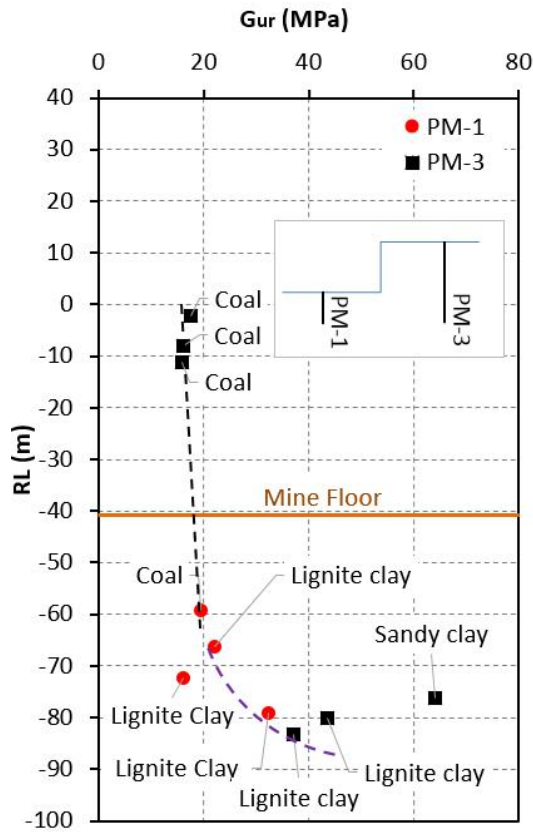


Fig.5.11. Stress (depth) dependency of the measured G_{ur} .

5.6. Conclusion

In-situ pressuremeter tests were carried out near an open-pit batter of Yallourn brown coal mine. The test led to achieve in-situ horizontal stresses at the site and geotechnical parameters (unload-reload shear modulus and undrained shear strength) of brown coal and clay. It can be seen from the results that the in-situ horizontal stresses varies with depth. There is a clear stress relaxation due to mining as shown in Figure 5.7. The interpreted unload-reload shear modulus was found to be strongly dependent to

the in-situ stress conditions, whereas the undrained shear strength value was not affected by the in-situ stresses.

The effect from the stress anisotropy is however unknown. The undrained shear strength is proven by the results to be independent to the variations in-situ stress conditions, and hence stress anisotropy. The unload-reload shear modulus is found to be stress-dependent in both laboratory and in-situ tests. The significance of stress anisotropy has not been detected so as to establish the correlation with the unload-reload modulus.

6. Summary and Recommendations

6.1. Research Conclusion

The in-situ PMT is able to provide useful geotechnical parameters, such as the in-situ horizontal stress, shear modulus and undrained shear strength of the geomaterial in a Victorian brown coal open-pit mine. However, results from a PMT in an open-pit mine may be affected by two main issues: the anisotropy of in-situ horizontal stresses and the tensile failure of brown coal. This research project developed two laboratory tests to better describe the above-mentioned issues. The tests are the Anisotropic Chamber Pressuremeter Test and the UET.

The Anisotropic Chamber Pressuremeter Test was developed to describe the impacts of the anisotropy of in-situ horizontal stress on the interpreted parameters of the PMT. If it exists, the anisotropy of in-situ horizontal stress may have been generated by tectonic activities, dewatering, or mining activities. The impacts of the anisotropy of in-situ horizontal stress on the interpreted shear strength and shear modulus have not been well described in previous research. This is due to the fact that the cylindrical pressuremeter chamber can only generate an isotropic in-chamber confining pressure, which is not able to represent the anisotropy of in-situ horizontal stresses. This research project developed a cubic chamber that can simulate the anisotropy of horizontal stress by the anisotropic confining pressure generated in two principal directions of the chamber. Following the design of the chamber, a series of miniature pressuremeter tests were performed in both isotropic and anisotropic conditions.

The UET for brown coal was developed to describe the true tensile strength of brown coal. Tensile strength can be measured through pre-existing techniques, such as the DTT and BT. However, both the DTT and BT have limitations in performing reliable tensile strength measurements for brown coal. The UET overcomes these limitations by way of tensile stress development using cylindrical cavity expansion. Therefore, the results from the UET on undisturbed brown coal specimens from the site at which the field PMT test were used to determine the coal's tensile strength. Based on the measured values, the minimum depth for the field PMT test was calculated so that tensile failure of the brown coal could be avoided during the field test.

Two numerical modelling techniques were used for the analysis of the laboratory tests. The three-dimensional FEM was used to describe the internal stresses of the

Anisotropic Chamber Pressuremeter Test in both isotropic and anisotropic conditions. The XFEM was used to model tensile failure during the UET. Simulation results from XFEM were compared with the UET results for the verification of the input shear strength, modulus parameters and the critical energy release rate for the fracture simulation. The critical energy rate was calculated based on the fracture toughness obtained from the Semi-Circular Bending (SCB) test at the preliminary stage of the UET analysis.

Following the laboratory tests and numerical simulations, this researcher conducted in-situ PMTs in Yallourn Open-pit Mine. Nine tests were conducted in clay and brown coal in two locations, one located at the mine floor and the other behind the mine batter. Based on the the interpretations of the test results, the in-situ horizontal stresses (σ'_h), the undrained shear strength (S_u) and the unload-reload stiffness (G_{ur}) were obtained.

6.2. Research Findings

6.2.1. Anisotropic Pressuremeter Chamber

A series of isotropic and anisotropic pressuremeter chamber tests were performed on a material that allows test (sand) to study the possible effect of the horizontal stress anisotropy on the material elasticity (unload-reload shear modulus - G_{ur}), material plasticity (shear shear strength by friction angle (ϕ), and dilation angle (ψ)).

As expected, the unload-reload modulus (G_{ur}) from the tests subjected to isotropic horizontal confining pressures demonstrated strong dependencies on the applied confining pressures. At a cavity pressure of 228kPa, G_{ur} is around 35MPa. When cavity pressure increases to 456kPa, G_{ur} increases to 71MPa. Additionally, it was found that the anisotropy of horizontal pressure has significant impacts on the G_{ur} . When the ratio between applied confining pressure (P_x/P_y) is 1.5 and 2, the G_{ur} is 25% and 50% higher than the G_{ur} for the same cavity pressure at isotropic condition. This behaviour is due to the effect of shear hardening when the horizontal stresses are unequal.

The friction angle (ϕ) interpreted from the chamber pressuremeter tests subjected to different isotropic confining pressure levels was maintained at around 32°. This value is comparable to the constant volume friction angle (ϕ_{cv}) estimated from the direct shear tests. The dilation angle (ψ) interpreted from the chamber pressuremeter tests is negligible (0°). This is due to the fact that the interpretation took place at a stage where

the material around the cavity reached a constant volume. Results demonstrated that the values of ϕ and ψ from the tests are not dependent on the stress level. Additionally, the anisotropy of the horizontal confining pressures does not affect these two parameters.

6.2.2. Unconfined Expansion Test

The measured tensile strength from the UET on the Yallourn coal was found to be in the range of 100kPa to 150kPa. The curve fitting from XFEM verified Young's modulus of brown coal at around 17MPa. The fracture toughness measured through parallel Semi-Circular Bending (SCB) was found to be $6.86\text{kPa}\cdot\text{m}^{1/2}$, which provided a critical energy release rate of $2.357\text{Pa}\cdot\text{m}$.

Based on the measured tensile strength of the brown coal (100kPa to 150kPa), the test depths of the in-situ Pressuremeter Test (PMT) on the brown coal open-pit mine were determined at a minimum of 15 m below the ground level. Given that the unit weight of brown coal is around 12 kN/m^3 , in-situ stress of 180 kPa should exist at this depth to avoid the tensile failure of brown coal.

6.2.3. In-situ Pressuremeter Test

Behind the open-pit batter, effective in-situ horizontal stress (σ'_h) measured by PMT stayed between 250kPa to 300kPa. From RL-60m to RL-80m, which is around 20m below the mine floor, σ'_h increased from roughly 700kPa to 2100kPa along with the depth. The significant difference between σ'_h measured at the depth below and above the mine floor is due to stress relaxation as a consequence of mining.

The interpreted undrained shear strength (S_u) is found to be slightly sensitive to the variation of the in-situ horizontal stress (σ'_h). The S_u measured from clay and brown coal falls between the range of 400-500kPa. The unload-reload stiffness (G_{ur}) interpreted from the in-situ PMT is found to be dependant to the in-situ horizontal stress. For brown coal, when σ'_h increases from around 250kPa to 700kPa, G_{ur} increases from around 17MPa to around 20MPa. For clay, the dependency of G_{ur} to σ'_h is more significant, when σ'_h increases from around 1060kPa to 2000kPa, G_{ur} increases from roughly 45MPa to 64MPa.

It is clear that in-situ stress condition have affected the measurement of G_{ur} . However it is believed that this is not the case for the measured S_u values. The effect of in-situ stress anisotropy is remained to be unknown.

6.3. Discussions and Recommendations

Reviewed in Chapter 4.1, the impact of the anisotropy of the confining pressure condition on the interpreted G_{ur} of sand was verified by the Anisotropic Chamber Pressuremeter Test. However, the interference of the anisotropy of σ'_h in the interpreted G_{ur} of clay and brown coal cannot be explicitly determined based on the in-situ test results. Although stress anisotropy is likely to occur behind the mine batter, the intensity of anisotropy and the orientations of the converted principal stresses are unknown. It is recommended that the interference of stress anisotropy on the magnitude of G_{ur} be further studied.

The laboratory test material in the research is dry, medium-dense sand. As a result, test quality can be controlled by merely maintaining material density with repetitive compaction procedure. However, the material selection leads to the fact that undrained shear strength (S_u) cannot be examined in the laboratory test. Alternative material for the chamber tests are clay and brown coal. However, the sample preparations for clay and brown coal chamber tests comprise more complexities. For clay, techniques are required for maintaining moisture content, consolidation and time-dependent behaviour (creep) before the test. For brown coal, excavation and transportation of undisturbed sample in the dimension of the chamber was found to be impossible. The above-mentioned limitations are beyond the scope of the present research. These are recommended to be future research topics.

In addition, the magnitude of σ'_h presented in Chapter 5 was calculated by subtracting the hydrostatic pore water pressure (based on the water level in the PMT borehole) from the total stress measured by the pressuremeter probe. Since the dissipation of tensile and excess pore water pressures generated from mining activities and dewatering may take a few decades, the calculation of active pore water pressure based on the depth of ground water level is not necessarily accurate. Thus, for future studies, it is recommended that one employ (or develop) a pressuremeter probe that allows for the measurement of active pore water pressure during pressuremeter testing. However, accessing or developing such a probe for rock testing might be a challenge.

Reference

- ABAQUS. (2017). SIMULIA User Assistance 2017: Dassault Systems.
- ABAQUS, V. (2014). 6.14 Documentation. Dassault Systemes Simulia Corporation.
- Ajalloeian, R., & Yu, H. S. (1998). Chamber studies of the effects of pressuremeter geometry on test results in sand. *Geotechnique*, 48(5), 621-636.
- Ajaz, A., & Parry, R. H. G. (1974). An unconfined direct tension test for compacted clays. *Journal of Testing and Evaluation*, 2(3), 163-172.
- Alavi, S. H., & Monismith, C. L. (1994). Time and temperature dependent properties of asphalt concrete mixes tested as hollow cylinders and subjected to dynamic axial and shear loads. *Journal of the Association of Asphalt Paving Technologists*, 63, 152-181.
- AlZubaidi, R. M. (2015). A new method for interpreting pressuremeter data to estimate in situ horizontal stress. *Arabian Journal of Geosciences*, 8(7), 5295-5302.
- Anandarajah, A., & Agarwal, D. (1991). Computer-aided calibration of a soil plasticity model. *International Journal for Numerical and Analytical Methods in Geomechanics*, 15(12), 835-856.
- Anderson, J. B. (2001). Finite Element Modeling of Florida Soil with The PENCEL Pressuremeter (Doctoral dissertation, State University System of Florida).
- Arnold, M. (1981). An empirical evaluation of pressuremeter test data. *Canadian geotechnical journal*, 18(3), 455-459.
- Ayatollahi, M. R., & Aliha, M. R. M. (2006). On determination of mode II fracture toughness using semi-circular bend specimen. *International Journal of Solids and Structures*, 43(17), 5217-5227.
- Bacciarelli, R. E. (1985). The Calibration and Use of a High Capacity Pressuremeter to Determine Rock Stiffness. Paper presented at the The Pressuremeter and its Marine Applications: Second International Symposium.
- Baguelin, F. (1978). The pressuremeter and foundation engineering. *Trans. Tech. Publications*, 617.
- Baguelin, F., Jezequel, J. F., Le, M., & Lemehaute, A. (1972). Expansion of cylindrical probes in cohesive soils. *Journal of Soil Mechanics & Foundations Div*, 98(Sm 11).
- Bellotti, R., Ghionna, V., Jamiolkowski, M., Robertson, P., & Peterson, R. W. (1989). Interpretation of moduli from self-boring pressuremeter tests in sand.
- Belytschko, T., & Black, T. (1999). Elastic crack growth in finite elements with minimal remeshing. *International journal for numerical methods in engineering*, 45(5), 601-620.
- Briaud, J. L., & Audibert, J. M. (Eds.). (1986). *The Pressuremeter and Its Marine Applications: Second International Symposium (No. 950)*. ASTM International.
- Briaud, J. L., & Shields, D. H. (1979). A Special Pressure Meter and Pressure Meter Test for Pavement Evaluation and Design. *Geotechnical Testing Journal*, 2(3), 143-151.
- Briaud, J. L. (1989). *The pressuremeter test for highway applications*. Federal Highway Administration.
- Briaud, J. L. (2013). Ménard Lecture: The pressuremeter Test: Expanding its use. In *Proceedings of the 18th International Conference on Soil Mechanics and Geotechnical Engineering*, Paris, France (pp. 107-126).

- Briaud, J. L., Tucker, L. M., & Makarim, C. A. (1985, January). Pressuremeter standard and pressuremeter parameters. In *The Pressuremeter and its Marine Applications: Second International Symposium*. ASTM International.
- Campanella, R. G., Howie, J. A., Hers, I., Sully, J. P., & Robertson, P. K. (1990). Evaluation of cone pressuremeter tests in soft cohesive soils. In *PRESSUREMETERS: Proceedings of the Third International Symposium on Pressuremeters*, organised by the British Geotechnical Society and held at Oxford University, 2–6 April 1990 (pp. 125-135). Thomas Telford Publishing.
- Chong, K., & Kuruppu, M. D. (1984). New specimen for fracture toughness determination for rock and other materials. *International Journal of Fracture*, 26(2), R59-R62.
- Clarke, B. G., & Gambin, M. (1998). Pressuremeter testing in onshore ground investigations. *ISSMGE Technical Committee*, 16.
- Clarke, B. G. (1994). *Pressuremeters in geotechnical design*: CRC Press.
- Clarke, B. G. (1997, January). Pressuremeter testing in ground investigation. Part II-interpretation. In *Proceedings of the Institution of Civil Engineers: Geotechnical Engineering* (Vol. 125, No. 1).
- Colback, P. S. B. (1966, January). An analysis of brittle fracture initiation and propagation in the Brazilian test. In *1st ISRM Congress. International Society for Rock Mechanics and Rock Engineering*.
- Cosentino, P. J., Kalajian, E., Stansifer, R., Anderson, J. B., Kattamuri, K., Sundaram, S., ... & Cottingham, M. A. (2006). Standardizing the pressuremeter test for determining p_y curves for laterally loaded piles.
- Coviello, A., Lagioia, R., & Nova, R. (2005). On the measurement of the tensile strength of soft rocks. *Rock Mechanics and Rock Engineering*, 38(4), 251-273.
- Crockford, W. W. (1993). Role of principal-plane rotation in flexible pavement deformation. *Journal of transportation engineering*, 119(1), 124-141.
- Cunha, R. P., & Campanella, R. G. (1998). Interpretation of selfboring pressuremeter tests using a curve fitting approach. In *Proceedings of the International Conference on Site Characterization, ISC* (Vol. 98, pp. 759-764).
- Cunha, R. P. D. (1994). Interpretation of selfboring pressuremeter tests in sand (Doctoral dissertation, University of British Columbia).
- Drucker, D. C., & W. Prager, 1952, Soil mechanics and plastic analysis or limit design: *Quarterly of applied mathematics*, v. 10, 157-165.
- Durban, D., & Papanastasiou, P. (1997). Cylindrical cavity expansion and contraction in pressure sensitive geomaterials. *Acta mechanica*, 122(1-4), 99-122.
- Eldridge, T. L. (1983). Pressuremeter tests in sand: effects of dilation (Doctoral dissertation, University of British Columbia).
- Fahimifar, A., & Malekpour, M. (2012). Experimental and numerical analysis of indirect and direct tensile strength using fracture mechanics concepts. *Bulletin of Engineering Geology and the Environment*, 71(2), 269-283.
- Fawaz, A., Boulon, M., & Flavigny, E. (2002). Parameters deduced from the pressuremeter test. *Canadian geotechnical journal*, 39(6), 1333-1340.
- Fernando, J., & Nag, D. (2003). A study of internal overburden dump design and stability analysis for Hazelwood Power Mine, Latrobe Valley, Victoria, Australia. Application of Computers and Operations Research in the Minerals Industries, South African Institute of Mining and Metallurgy, 267-274.

- Finn, P., Nisbet, R., & Hawkins, P. (1986). Guidance on pressuremeter, flat dilatometer and cone penetration testing. Geological Society, London, Engineering Geology Special Publications, 2(1), 223-233.
- Foriero, A., & Ciza, F. (2015). Confined Pressuremeter Tests for the Assessment of the Theoretically Back-Calculated Cross-Anisotropic Elastic Moduli. *Geotechnical Testing Journal*, 39(2), 181-195.
- Fyffe, S., Reid, W. M., & Summers, J. B. (1985, January). The Push-in Pressuremeter: 5 Years Offshore Experience. In *The Pressuremeter and Its Marine Applications: Second International Symposium*. ASTM International.
- Gibson, R. E. (1961). In situ measurement of soil properties with the pressuremeter. *Civil Engrg. and Pub. Wks. Rev.*, 56(568), 615-618.
- Goh, A., & Fahey, M. (1996). Measuring the coefficient of consolidation in situ using SBP and piezocone dissipation tests. In *7th Australia New Zealand Conference on Geomechanics: Geomechanics in a Changing World: Conference Proceedings* (p. 915). Institution of Engineers, Australia.
- Haberfield, C. M. (1997, July). Pressuremeter testing in weak rock and cemented sand. In *Proceedings of the Institution of Civil Engineers: Geotechnical Engineering* (Vol. 125, No. 3).
- Henderson, G., Smith, P. D. K., & St John, H. D. (1979, March). The development of the Push-in Pressuremeter for offshore site investigation. In *Mar 1979*, 14 p, Preprints: Offshore Site Investigation Conference.
- Hoek, E., Carranza-Torres, C., & Corkum, B. (2002). Hoek-Brown failure criterion-2002 edition. *Proceedings of NARMS-Tac*, 1, 267-273.
- Houlsby, G. T., & Carter, J. P. (1993). The effects of pressuremeter geometry on the results of tests in clay. *Geotechnique*, 43(4), 567-576.
- Hudson, J. A., Brown, E. T., & Rummel, F. (1972, March). The controlled failure of rock discs and rings loaded in diametral compression. In *International Journal of Rock Mechanics and Mining Sciences & Geomechanics Abstracts* (Vol. 9, No. 2, pp. 241-248). Pergamon.
- Hughes, J. M. O., & Robertson, P. K. (1985). Full-displacement pressuremeter testing in sand. *Canadian Geotechnical Journal*, 22(3), 298-307.
- Hughes, J. M. O., Wroth, C. P., & Windle, D. (1977). Pressuremeter tests in sands. *Geotechnique*, 27(4), 455-477.
- Isik, N. S., Ulusay, R., & Doyuran, V. (2008). Deformation modulus of heavily jointed–sheared and blocky greywackes by pressuremeter tests: Numerical, experimental and empirical assessments. *Engineering Geology*, 101(3-4), 269-282.
- Jaeger, J. C. (1967, April). Failure of rocks under tensile conditions. In *International Journal of Rock Mechanics and Mining Sciences & Geomechanics Abstracts* (Vol. 4, No. 2, pp. 219-227). Pergamon.
- Jaeger, J. C., & Hoskins, E. R. (1966). Rock failure under the confined Brazilian test. *Journal of Geophysical research*, 71(10), 2651-2659.
- Jang, I. S., Chung, C. K., Kim, M. M., & Cho, S. M. (2003). Numerical assessment on the consolidation characteristics of clays from strain holding, self-boring pressuremeter test. *Computers and Geotechnics*, 30(2), 121-140.
- Jefferies, M. G. (1988). Determination of horizontal geostatic stress in clay with self-bored pressuremeter. *Canadian Geotechnical Journal*, 25(3), 559-573.

- Juran, I., & Mahmoodzadegan, B. (1989). Interpretation procedure for pressuremeter tests in sand. *Journal of Geotechnical Engineering*, 115(11), 1617-1632.
- Kondner, R. L. (1963). A hyperbolic stress-strain formulation for sands. In *Proc. 2nd Pan-American Conf. on SMFE (Vol. 1, pp. 289-324)*.
- Kuruppu, M. D., & Chong, K. P. (2012). Fracture toughness testing of brittle materials using semi-circular bend (SCB) specimen. *Engineering Fracture Mechanics*, 91, 133-150.
- Ladanyi, B. (1967, July). Expansion of cavities in brittle media. In *International Journal of Rock Mechanics and Mining Sciences & Geomechanics Abstracts (Vol.4, No.3, pp.301-328)*. Pergamon.
- Ladanyi, B. (1972). In-situ determination of undrained stress-strain behavior of sensitive clays with the pressuremeter. *Canadian geotechnical journal*, 9(3), 313-319.
- Li, D., & Wong, L. N. Y. (2013). The Brazilian disc test for rock mechanics applications: review and new insights. *Rock mechanics and rock engineering*, 46(2), 269-287.
- Lu, N., Wu, B., & Tan, C. P. (2007). Tensile strength characteristics of unsaturated sands. *Journal of Geotechnical and Geoenvironmental Engineering*, 133(2), 144-154.
- Mair, R. J., & Wood, D. M. (1987). *Pressuremeter testing: methods and interpretation*. Construction Industry Research and Information Association.
- Marsland, A., & Randolph, M. (1977). Comparisons of the results from pressuremeter tests and large in situ plate tests in London Clay. *Géotechnique*, 27(2), 217-243.
- Melenk, J. M., & Babuška, I. (1996). The partition of unity finite element method: basic theory and applications. *Computer methods in applied mechanics and engineering*, 139(1-4), 289-314.
- Menard, L. (1957). *Mesures in situ des propriétés physiques des sols*.
- Menard, L. (1975). Interpretation and application of pressuremeter test results. *Soils-Soils*.
- Monnet, J. (2007). Numerical validation of an elastoplastic formulation of the conventional limit pressure measured with the pressuremeter test in cohesive soil. *Journal of Geotechnical and Geoenvironmental Engineering*, 133(9), 1119-1127.
- Monnet, J. (2008). Numerical analysis for an interpretation of the pressuremeter test in cohesive soil. *Studia Geotechnica et Mechanica*, 30(1-2), 41-49.
- Monnet, J. (2012). Elasto-plastic analysis of the pressuremeter test in granular soil—part 2: numerical study. *European journal of environmental and civil engineering*, 16(6), 715-729.
- Hughes, J. M. O., & Robertson, P. K. (1985). Full-displacement pressuremeter testing in sand. *Canadian Geotechnical Journal*, 22(3), 298-307.
- Palmer, A. C. (1971). Undrained plane-strain expansion of a cylindrical cavity in clay: a simple interpretation of the pressuremeter test. *Brown Univ Providence Ri Div of Engineering*.
- Potts, D. M., & Martins, J. P. (1982). The shaft resistance of axially loaded piles in clay. *Geotechnique*, 32(4), 369-386.
- Powell, J. J. M., & Uglow, I. M. (1985). A comparison of Menard, self-boring and push-in pressuremeter tests in a stiff clay till. In *Offshore Site Investigation (pp. 201-217)*. Springer, Dordrecht.
- Prapaharan, S., Chameau, J. L., Altschaeffl, A. G., & Holtz, R. D. (1990). Effect of disturbance on pressuremeter results in clays. *Journal of Geotechnical Engineering*, 116(1), 35-53.
- Randolph, M. F. (1981). The response of flexible piles to lateral loading. *Geotechnique*, 31(2), 247-259.

- Read, J., & Stacey, P. (2009). Guidelines for open pit slope design. CSIRO publishing.
- Rowe, P. W. (1962). The stress-dilatancy relation for static equilibrium of an assembly of particles in contact. *Proc. R. Soc. Lond. A*, 269(1339), 500-527.
- Satapathy, S., & Bless, S. (1995). Cavity Expansion Analysis of Brittle Materials (No. IAT. R-0075). TEXAS UNIV AT AUSTIN INST FOR ADVANCED TECHNOLOGY.
- Schnaid, F. (1990). A study of the cone-pressuremeter test in sand (Doctoral dissertation, University of Oxford).
- Schnaid, F., Ortigao, J. A., Mantaras, F. M., Cunha, R. P., & MacGregor, I. (2000). Analysis of self-boring pressuremeter (SBPM) and Marchetti dilatometer (DMT) tests in granite saprolites. *Canadian geotechnical journal*, 37(4), 796-810.
- Shaban, A. M. (2016). Evaluation of Unbound Pavement Layers Moduli Using the Miniaturized Pressuremeter Test. Florida Institute of Technology.
- Sharo, A. A. (2009). Pressuremeter applications in laterally loaded drilled shaft socketed into transversely isotropic rock (Doctoral dissertation, University of Akron).
- Shuttle, D. A., & Jefferies, M. G. (1996). A practical geometry correction for interpreting pressuremeter tests in clay. In *International Journal of Rock Mechanics and Mining Sciences and Geomechanics Abstracts* (Vol. 2, No. 33, p. 74A).
- Simmons, J. V., & Simpson, P. J. (2006). Composite failure mechanisms in coal measures' rock masses-myths and reality. *Journal-South African Institute of Mining and Metallurgy*, 106(7), 459.
- Singh, R. N., Pathan, A. G., Reddish, D. J., & Atkins, A. S. (2011). Geotechnical appraisal of the Thar open cut mining project.
- Skandarajah, A. (1992). Strain rate and stress relaxation in simulated pressuremeter testing in clays.
- Tan, N. K. (2005). Pressuremeter and cone penetrometer testing in a calibration chamber with unsaturated Minco Silt (Doctoral dissertation).
- Tang, Z., Tolooyan, A., & Mackay, R. (2017). Unconfined Expansion Test (UET) for measuring the tensile strength of organic soft rock. *Computers and Geotechnics*, 82, 54-66.
- Timoshenko, S. (1940). *Strength of materials Part 1*. D. Van Nostrand Co., Inc.
- Timoshenko, S. (1956). *Strength of Materials Part 2: Advanced Theory and Problems*. Van Nostrand.
- Timoshenko, S. P., & Woinowsky-Krieger, S. (1959). *Theory of plates and shells*. McGraw-hill.
- Tolooyan, A., Mackay, R., & Xue, J. (2014). Measurement of the tensile strength of organic soft rock. *Geotechnical Testing Journal*, 37(6), 991-1001.
- Vaziri, H. H., & Wang, X. (1993). Theoretical solutions for the problem of a cylindrical cavity expansion in a Mohr-Coulomb material. *Computers & structures*, 48(5), 961-962.
- Vesga, L. F., & Vallejo, L. E. (2006). Direct and indirect tensile tests for measuring the equivalent effective stress in a kaolinite clay. In *Unsaturated Soils 2006* (pp. 1290-1301).
- Whittle, R. (1999). The myth of the finite pressuremeter geometry correction
- Windle, D., & Wroth, C. P. (1977). The use of a self-boring pressuremeter to determine the undrained properties of clays. *Ground Engineering*, 10(6).
- Wood, D. M. (1990). Strain-dependent moduli and pressuremeter tests. *Geotechnique*, 40(3), 509-512.

- Wroth, C. P. (1982, April). British experience with the self-boring pressuremeter. In Proc. of Int. Symp. Pressuremeter and its Marine Applications, Paris. Chapman & Hall, London (pp. 143-164).
- Wroth, C. P., & Hughes, J. M. O. (1972). An instrument for the in situ measurement of the properties of soft clays. Cambridge Univ., Engineering Department.
- Jaeger, J. (1967). Failure of rocks under tensile conditions. Paper presented at the International Journal of Rock Mechanics and Mining Sciences & Geomechanics Abstracts.
- Yu, H. (1990). Cavity expansion theory and its application to the analysis of pressuremeters. University of Oxford.
- Yu, H. S. (2006). The First James K. Mitchell Lecture In situ soil testing: from mechanics to interpretation. *Geomechanics and Geoengineering: An International Journal*, 1(3), 165-195.
- Yu, H. S. (1994). State parameter from self-boring pressuremeter tests in sand. *Journal of Geotechnical Engineering*, 120(12), 2118-2135.
- Yu, Y., Yin, J., & Zhong, Z. (2006). Shape effects in the Brazilian tensile strength test and a 3D FEM correction. *International journal of rock mechanics and mining sciences*, 43(4), 623-627.
- Zhao, L., & You, G. (2017, July). Cracking Mechanism Along the North Batter of Maddingley Brown Coal Open Pit Mine, Victoria, Australia. In International Congress and Exhibition "Sustainable Civil Infrastructures: Innovative Infrastructure Geotechnology" (pp. 115-129). Springer, Cham.
- Zhou, H., Kong, G., & Liu, H. (2016). Pressure-controlled elliptical cavity expansion under anisotropic initial stress: Elastic solution and its application. *Science China Technological Sciences*, 59(7), 1100-1119.



Research Paper

Unconfined Expansion Test (UET) for measuring the tensile strength of organic soft rock

Mr. Zhan Tang^a, Dr. Ali Tolooiyan^{b,*}, Prof. Rae Mackay^b^aFaculty of Science, Monash University, Australia^bGeotechnical and Hydrogeological Engineering Research Group (GHERG), Federation University Australia, Australia

ARTICLE INFO

Article history:

Received 1 February 2016

Received in revised form 28 September 2016

Accepted 30 September 2016

Available online 10 October 2016

Keywords:

UET

Tensile strength

Extended finite element method

Intermediate geotechnical material

ABSTRACT

An Unconfined Expansion Test (UET) is presented for measuring the tensile strength of Intermediate Geotechnical Materials (IGM). The test is performed by generating radial cavity expansion inside a cylindrical specimen. Pressure redistributes evenly around the cavity wall during the test. Tensile failure initiates on the weakest plane around the cavity and radially propagates across the specimen. By also capturing the stress-strain relationship and deriving the shear modulus, a UET is also capable of measuring the tensile elastic modulus of the material. An eXtended Finite Element Method (XFEM) analysis using Abaqus/Standard has been carried out to verify the UET test results.

© 2016 Elsevier Ltd. All rights reserved.

1. Introduction and background

Ensuring stability of Engineered slopes in excavations is a complex problem that depends on detailed knowledge of the slope materials and ground stresses. For most slope stability analyses, the likelihood of movement is assessed by calculating the ratio of the maximum shear resistance to the magnitude of the driving shear force (the factor of safety) for the worst case slip surface. However, these analyses omit other failure modes that can be more important. Recent research has classified brown coal as an Intermediate Geotechnical Material (IGM) [25]. The failure modes of IGMs include ductile failure and brittle failure. The undrained shear strength is usually greater than tensile strength. Depending on the loading scenario and the field condition, failure may occur once the tensile forces reach the tensile strength of the material.

Measuring the tensile strength in the laboratory can be achieved by imposing a tensile stress directly or indirectly on a specimen through an applied load and establishing the stress required to cause tensile failure. The measured load limit, F , and the failure plane area, A , obtained from the test are used to calculate the tensile strength of the specimen using an equation with

the general form $\sigma_t = \alpha \frac{F}{A}$, where σ_t is the tensile strength, and α is the test shape factor that converts the force into tensile force on the failure surface.

The Direct Tension Test (DTT) is, theoretically, the simplest laboratory test for measuring tensile strength. It has been extensively used to investigate the tensile strength of unsaturated soils, over-consolidated clays, and cemented sands but specimen preparation is not easy for these materials and the design of the test apparatus is a critical problem [1,21,25,26]. The specimen is typically a cylindrical or rectangular bar of the material. The bar is gripped at both ends and the specimen pulled apart at a known rate. Care with the grip and specimen design is essential to ensure a uniform tensile stress across the specimen at the failure location. A difficulty associated with the DTT for IGMs is that the stress can concentrate close to the grips and can lead to unpredictable and non-uniform failure plane locations. This makes it almost impossible to determine the test shape factor, α , required to calculate the tensile strength. Tolooiyan et al. [25] adopted a notch around the midpoint of the specimen to force the specimen to fail on a predefined plane so that α is known. Although this technique produces measurable results, the nature of the result is unclear given the natural heterogeneity of IGMs. Under field conditions tensile failure will preferentially occur on planes of weakness but a predefined failure plane may not capture this tendency and can therefore lead to an overestimation of the effective tensile strength.

The Brazilian Test (BT), also called the indirect tensile test or the splitting tensile test, is an alternative tensile strength

* Corresponding author at: Geotechnical and Hydrogeological Engineering Research Group (GHERG), Federation University Australia, Churchill, VIC 3842, Australia.

E-mail addresses: ali.tolooiyan@federation.edu.au, tolooiyan@gmail.com (A. Tolooiyan).

<http://dx.doi.org/10.1016/j.compgeo.2016.09.016>

0266-352X/© 2016 Elsevier Ltd. All rights reserved.

measurement technique. Cylindrical specimens with a diameter to thickness ratio of 2–2.5 are placed between two flat rigid loading plates that are parallel to the specimen's longitudinal axis. The plates compress the specimen at a specified rate. The compression loading is then converted to tensile stress on a diametric plane perpendicular to the loading plates. For this test, the area, A , is equal to the thickness, t , times the diameter, D . The α factor has been determined to be $2(jk + 1)\pi$, where k is the thickness to diameter ratio and j is an empirical factor [28]. The tensile strength of brittle material is normally smaller than the compressive strength and, therefore, in the BT, tension fails the specimen. Compared with the DTT, the BT is both easier, in a practical sense, and less expensive for specimen preparation. The validity of this test for rock materials has been debated [8,9,15–17]. Recent research confirms that a correction factor should be applied to BT results even for uniform materials [25,28]. It is appropriate to observe here that comparisons of DTT and BT tests for different materials [20] show significant differences between the results of both tests types. In Table 2 of Li and Wong's paper, the BT results both underestimate and overestimate the results from the DTT for different materials even though the correction factors identified by Tolooiyan et al. [25] and Yu et al. [28] suggest that the BT test for uniform materials should always underestimate true tensile strength. This difference may be due to the particular materials considered by Li and Wong [20] or due to differences between the DTT results and the underlying true tensile strengths for these materials. Further studies would be needed to resolve this potential issue. However, it is important to note that the bias identified for the DTT also exists for the BT for fine-grained IGMs with oriented grain structures, as the failure plane is also predefined.

Given the potential for bias of the two major methods for tensile strength measurement described above, an alternative method of testing with potentially less bias is presented for application to IGMs. The Unconfined Expansion Test (UET) is based on fracturing a cylinder of the IGM from within using an inflatable probe. The test form and the theory are described in detail in the following section. Test results from a series of tests on brown coal using the UET are presented. The results have been numerically validated through an eXtended Finite Element Method (XFEM) model analysis of the UET procedure using ABAQUS 6.14.

2. Theoretical background of UET

The UET employs cylindrical cavity expansion to radially crack an unconstrained cylindrical specimen. The cylindrical cavity is drilled along the axis of the cylindrical specimen. An inflatable probe is inserted into the cavity and expanded hydraulically. The probe hydraulic pressure must be monitored during the test to

determine the failure pressure. This pressure can be converted to the tensile strength of the material. Also, the elastic modulus of the material in tension can be determined by measuring the volume of expansion of the probe.

The theory of cylindrical cavity expansion was originally developed for field scale pressuremeter testing in boreholes [7,14,27]. However, pressuremeter testing is usually employed in geotechnical engineering to measure in-situ horizontal stress or fundamental soil properties such as shear modulus or undrained shear strength. Cylindrical cavity expansion has also been used in pavement engineering for determining the shear and compressive properties of asphalt mixtures [2,10].

Haberfield [14] and Ladanyi [19] showed that cavity expansion inside brittle materials such as rock may initiate radial crack(s) from the cavity wall. Fig. 1 shows two Mohr circle diagrams illustrating the difference between (a) shear strength, and (b) tensile strength dominated failure in a vertical borehole. The magnitude of the in-situ horizontal stress is the centre of Mohr circles, σ_{h0} . While the cavity is expanding, it generates radial compression stress, σ_r greater than 0 (compression), and circumferential tension stress, $\sigma_\theta < 0$ (tension). The difference between the magnitude of these two principal stresses then defines the shear stress, $\tau = (\sigma_r - \sigma_\theta)/2$. If the shear stress reaches the shear strength of the material, S_u , before the magnitude of the circumferential stress exceeds the tensile strength of the material the failure is compression dominant (Fig. 1a). If the magnitude of the circumferential stress exceeds the tensile strength before the shear strength is exceeded then the failure is tension dominated. In a borehole, the likelihood of a tension crack forming will depend on the in situ horizontal stress. In a laboratory, there is no in-situ horizontal stress, so $\sigma_{h0} = 0$. Since the tensile strength of IGMs is usually smaller than their shear strength, $\sigma_t < S_u$, failure occurs when the circumferential stress reaches the tensile strength, $\sigma_\theta = \sigma_t$. Hence, failure of a laboratory specimen of an IGM is typically tension dominant and the maximum pressure measured in UET test is independent of the material shear strength.

Analytical solutions are available for cavity expansion in both thick-walled and thin-walled hollow cylinders. Thick-walled cylinders are usually regarded as those having outer (specimen) and inner (cavity) diameter differences of more than 10%. For the UET experiments described in the paper, cylindrical brown coal specimens of 75 mm diameter and cavity diameter of 10 mm were used. The cylinders were 71 mm long. The analytical solutions for thick-walled hollow cylinders are applicable in this case.

Knowing the internal applied pressure (p), and the specimen size, the pressure and stress distribution can be computed using the analytical solution for thick-walled cylinders derived by Timoshenko and Woinowsky-Krieger [24], given in Eqs. (1) and (2).

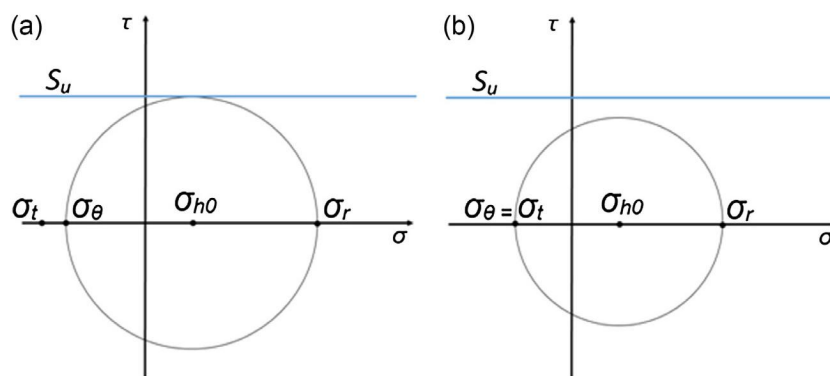


Fig. 1. Failure due to cavity expansion, (a) compression dominant, (b) tension dominant.

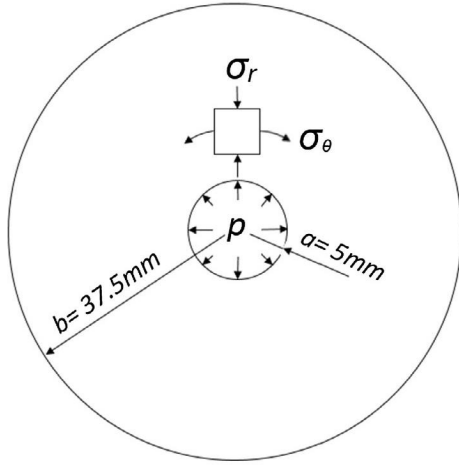


Fig. 2. Plan view of the specimen.

$$\sigma_{\theta} = \frac{a^2 p}{b^2 - a^2} \left(1 + \frac{b^2}{r^2} \right) \quad (1)$$

$$\sigma_r = \frac{a^2 p}{b^2 - a^2} \left(1 - \frac{b^2}{r^2} \right) \quad (2)$$

where σ_r = radial stress (in compression), σ_{θ} = circumferential or hoop stress (in tension), a = cavity radius, b = specimen radius, r = distance from the centre of the cavity.

The maximum tensile stress occurs just on the cavity wall, so by putting $r = a$ in Eq. (1), the maximum tensile stress can be calculated from Eq. (3).

$$\sigma_t = \frac{(b^2 + a^2)p}{b^2 - a^2} \quad (3)$$

Considering the given specimen size (shown in Fig. 2), and using Eq. (3), the tensile strength of the material for the UETs, can be computed as $\sigma_t = 1.036 p$.

In addition to the tensile strength of the material, the elasticity parameters (shear modulus and elastic modulus) can be obtained from the UET if the cavity volume change is measured during the test.

Mair and Wood [22] showed that the shear modulus (G) can be calculated from the linear part of pressure versus volume change profile for the cavity expanding in a soil (Eq. (4)). The elastic modulus can then be calculated from Hooke's law (Eq. (5)), where E is the elastic modulus, ν is the Poisson's ratio, V_0 is the initial volume of the cavity, dp is the pressure change inside the cavity and dV is the volume change of the cavity.

$$G = V_0 \frac{dp}{dV} \quad (4)$$

$$E = 2G(1 + \nu) \quad (5)$$

3. Test material

Victoria's brown coal deposit is the world's largest and represents 23% of world's known brown coal [3]. More than 80% of Victoria's brown coal is located in the Latrobe Valley, 160 km south-east Melbourne [12]. The three Latrobe Valley mines, Loy Yang, Yallourn and Hazelwood supply brown coal to four power stations that supply most of the electricity in Victoria. Exploitation of the brown coal is by open-pit excavation, with mining depths varying from 70 to 250 m; coal seam thicknesses can exceed

100 m. The mines are three of the largest open cut mines in the world and are subject to significant ground movements due to the nature of the brown coal. Therefore, improving understanding of the geotechnical properties of the brown coal is important to ensure ongoing stability of these mines.

Victorian brown coal is very light with a typical unit weight of 11.5 kN/m^3 . Its shear strength parameters are about 200 kPa cohesion and 30° friction angle. Elastic modulus and Poisson's ratio are of the order of 10–30 MPa and 0.2–0.25, respectively. The brown coal used in the current research was collected from Yallourn mine, which extracts coal from the uppermost seams of the coal sequence. All specimens were extracted from a single $0.4 \text{ m} \times 0.4 \text{ m} \times 0.4 \text{ m}$ intact block of brown coal. The moisture content of the block was measured immediately after collection and was determined to be 182.23%. The block was stored and maintained in a humidity controlled storeroom at 12°C temperature. Test specimens were extracted from the block by drilling. During testing, specimens were well wrapped in a plastic membrane to conserve the moisture content. All tests were performed in a temperature-controlled room at 21°C .

4. Test setup

The authors developed an automated mini-pressuremeter probe for performing pressure controlled, hydraulic cavity expansion tests. The test setup includes a mini-pressuremeter, an automated pressure-volume controller, a pore water pressure transducer, a rigid calibration cylinder, a de-airing tank with suction pump, an electro-pneumatic controller, a data acquisition box, a computer and control software.

The geometry and dimensions of the lab scale mini-pressuremeter probe are shown in Fig. 3. The probe comprises a

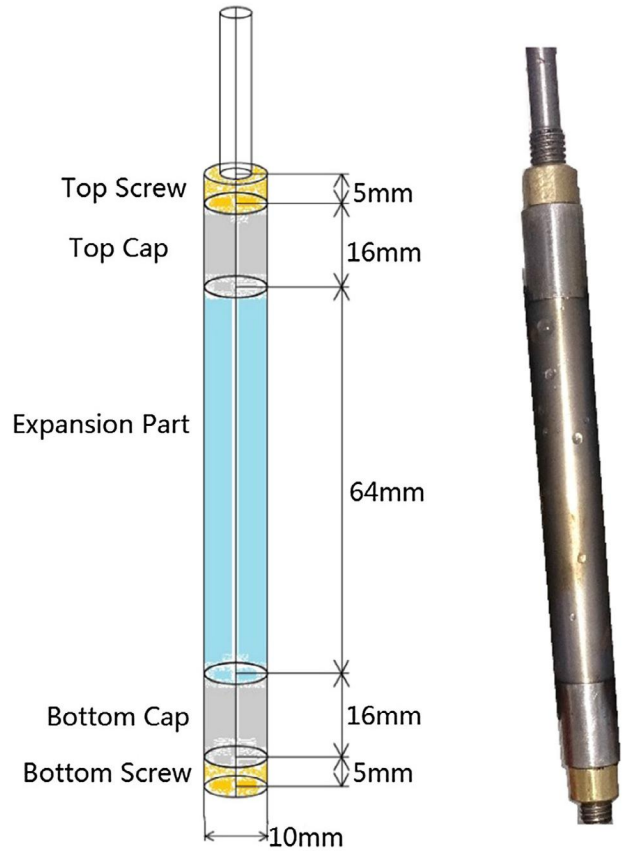


Fig. 3. The mini-pressuremeter probe.

hollow steel tube, a rubber membrane over the steel tube and metal caps fixed at both ends of the tube to hold the rubber membrane. Two holes in the steel tube allow water to be injected into the annular space between the membrane and steel tube to inflate the membrane. The probe diameter is 10 mm and the total length is 103 mm. The length of the expandable section of the membrane is 64 mm. The ratio between expansion membrane length and diameter, L/D , is 6.5, which is similar to field-scale commercial pressuremeter probes.

The probe is connected to a pressure transducer to measure the actual pressure in the membrane. The system is connected to a pressure-volume controller with a high strength tube. The controller is capable of applying pressures up to 1000 kPa with an accuracy of 0.01 kPa. The maximum volume that can be delivered by the pressure-volume controller is 26 ml with an accuracy of $1e-5$ ml. The system is software controlled and allows the user to specify the initial pressure, the target pressure and the test duration.

The volume change measurement is highly sensitive to expansion of the piping, fluid temperature and the occurrence of air in the system. At high pressure, any air in the system will dissolve in the water and generate a bias. Therefore, apart from maintaining the temperature during the test, the system was completely de-aired before each test. The de-airing procedure was achieved by two steps. For the distilled water, a vacuum pump was connected to the de-airing tank to absorb air until no visible air bubbles in the water. Then distilled water from the de-airing tank was used to flush the air bubbles out of the pressure-volume controller, pore water pressure transducer and, pressuremeter probe and the connecting hoses. The de-airing procedure was repeated until there were no visible air bubbles in the transparent water outlet tube. Also, the pressure-volume controller was vibrated while flushing to avoid small air bubbles being trapped. After the de-airing procedure, the apparatus was pressurised with all input and output valves closed to check for any time-dependent volume change.

5. Calibration

Calibration of the system was an essential operation to obtain the precise pressure-expansion probe volume curve. Even a small error in volume change measurement seriously influences the shear/elastic modulus obtained from the test. The calibration procedure took the following errors into account:

Correction 1. The expansion of tubing and the compressibility of membrane.

During the test, the tubing conveying the water to the pressuremeter expands under pressure and the membrane compresses. To identify these components of the volume change measured by the volume controller the probe was inserted into a thick-walled steel calibration cylinder and pressurised (see Fig. 4). The expansion



Fig. 4. The thick-walled steel calibration cylinder.

behaviour of the steel cylinder is minimal and quantifiable. In this case the volume changes recorded are directly related to the piping and membrane materials. Also, any possible leakage of the system can be detected in such a calibration test by maintaining pressure at the target level and monitoring the volume change.

As given in Eq. (6), in the real test, the actual volume change of the specimen due to the cavity expansion (dV) is equal to total measured volume change (dV_{total}) minus the volume change measured through the calibration procedure ($dV_{calibration}$).

$$dV = dV_{total} - dV_{calibration} \quad (6)$$

To apply the above correction, a closed-form equation is required to make a relationship between the applied pressure and the volume change due to the expansion of the tubing and the flexibility of the pressure-volume controller. This equation can be written in the form of one-site total binding equation, as shown in Eq. (7), where B is the maximum specific binding (in ml), C is the equilibrium binding constant (in kPa), D is the slope of nonspecific binding (in ml/kPa) and E is the amount of nonspecific binding (in ml).

$$dV_{calibration} \text{ (ml)} = B \frac{\text{Pressure (kPa)}}{C + \text{Pressure (kPa)}} + D \times \text{Pressure (kPa)} + E \quad (7)$$

Fig. 5a shows the equation fitting parameters for correcting the 1.5 ml volume change error observed due to applying pressures from 0 to 400 kPa pressure.

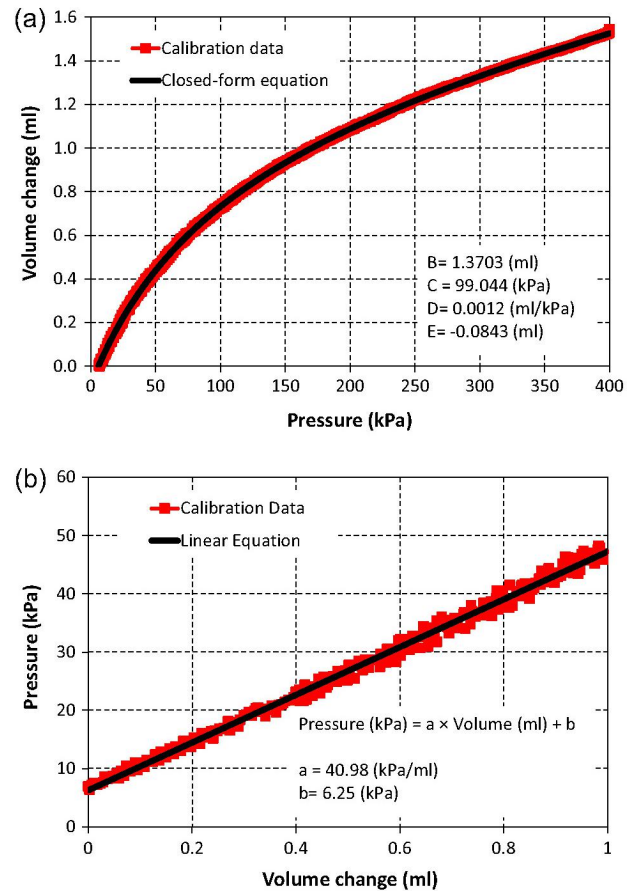


Fig. 5. (a) Nonlinear closed-form equation for correction 1, (b) linear equation for correction 2.

Correction 2. Membrane compliance.

The stiffness of the membrane creates part of the pressure during the test. To overcome the bias generated from membrane resistance, a free expansion calibration was applied. During the calibration, the probe was expanded without confinement. The recorded pressure increase under these conditions is solely due to membrane stiffness. For the real test, the actual contact pressure between the membrane and the cavity wall is then equal to the measured pressure minus the membrane compliance pressure (see Eq. (8)). As shown in Fig. 5b, the relationship between the observed volume change and the pressure bias due to the membrane resistance is linear. Hence, a simple linear equation can be used to apply this calibration.

$$P = P_{total} - P_{membrane\ compliance} \quad (8)$$

These corrections omit second order effects due to the interaction between compliance and membrane compression, which are assumed to be negligible.

6. Specimen preparation

All of the UET specimens were cored from a saturated block of brown coal. Cylindrical specimens were cored with diameter 75 mm and length 66 mm (see Fig. 6). The specimen length of 66 mm was selected to ensure that the 64 mm expandable part of the probe lay completely inside the specimen and the stresses were essentially uniform along the specimen length. A 10 mm (plus 40–80 μm soften due to drilling) cylindrical cavity was drilled along the axis of the cylinder to just take the probe. The ratio between specimen radius and cavity radius was 7.5 for all tests. The cavity was drilled with care to avoid initial cracking in the specimen. The finished specimens were stored under fully saturated conditions prior to performing the UET.

7. Determination of loading rate

Excess pore water pressure caused during cylindrical expansion was a concern for the interpretation of the tests. Hence, an appropriate loading rate to minimise excess pore water pressure at the centre of the specimen was determined by carrying out an FEM analysis with Abaqus/Standard 6.14. The effective stress analysis

for fluid-filled porous media available in Abaqus/Standard 6.14 was employed.

The test was modelled by a conventional method that considers the coal as a porous medium and adopts effective stress principles to describe its behaviour. The porous medium modelling provided in Abaqus/Standard considers the presence of two fluids in the pores. One is the wetting phase that is deemed to be incompressible (water in this analysis). The other is typically a gas, which is relatively compressible. Only the wetting phase (water) was used in the analysis. It was assumed that the coal specimen was fully saturated and the voids were completely filled by wetting liquid. The coal hydraulic conductivity and void ratio values were 4×10^{-7} mm/s and 1.5, respectively, and the elastic modulus was varied from 10 MPa to 30 MPa [25].

The 3D model finite element geometry is shown in Fig. 7a, where 5120 eight-node brick, trilinear displacement, trilinear pore pressure elements (type C3D8P) are used to model the test geometry. A pore water pressure boundary condition with zero magnitude was predefined over the external surface of the specimen. The probe expansion was simulated by applying a cylindrically distributed stress inside the cavity at different rates of change. The maximum excess pore water pressure was investigated when the effective stress reached 180 kPa at the centre of the specimen. As shown in Fig. 7b, the magnitude of excess pore water pressure is less than 1 kPa at an effective stress of 180 kPa when the cavity expansion stress rate is 0.4 kPa/s, hence any rate less than 0.4 kPa/s should be fine for this purpose (Note, the model defines positive pressures as negative values, see Fig. 7a and b). Fig. 7c shows the sensitivity of the developed excess pore water pressure to the expansion stress rate. The cavity expansion rate of 0.1 kPa/s was chosen as the appropriate loading rate for performing the UETs.

8. UET setup

To prevent specimen cracking prior to testing the following setup procedure was adopted. The specimen was placed on a horizontal platform before the UET probe was pushed in. The platform had a hole in the centre to let the tip of the probe extend through the specimen. The probe was lubricated with vaseline to ease its insertion into the specimen. When the probe was inserted (Fig. 8), the drainage valve of the automated pressure-volume con-

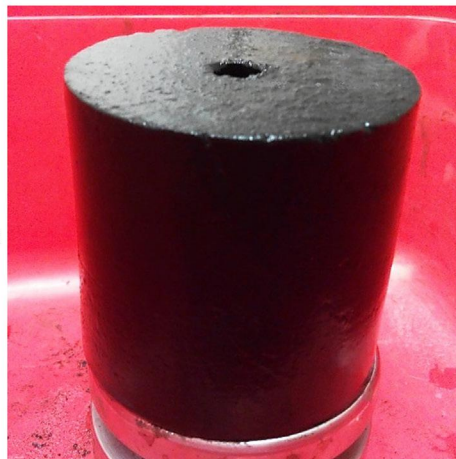
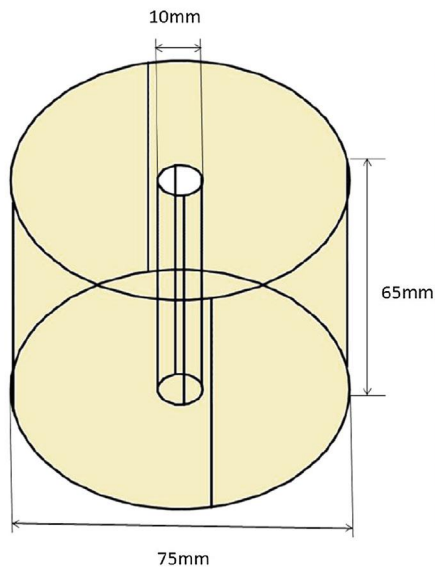


Fig. 6. UET specimen.

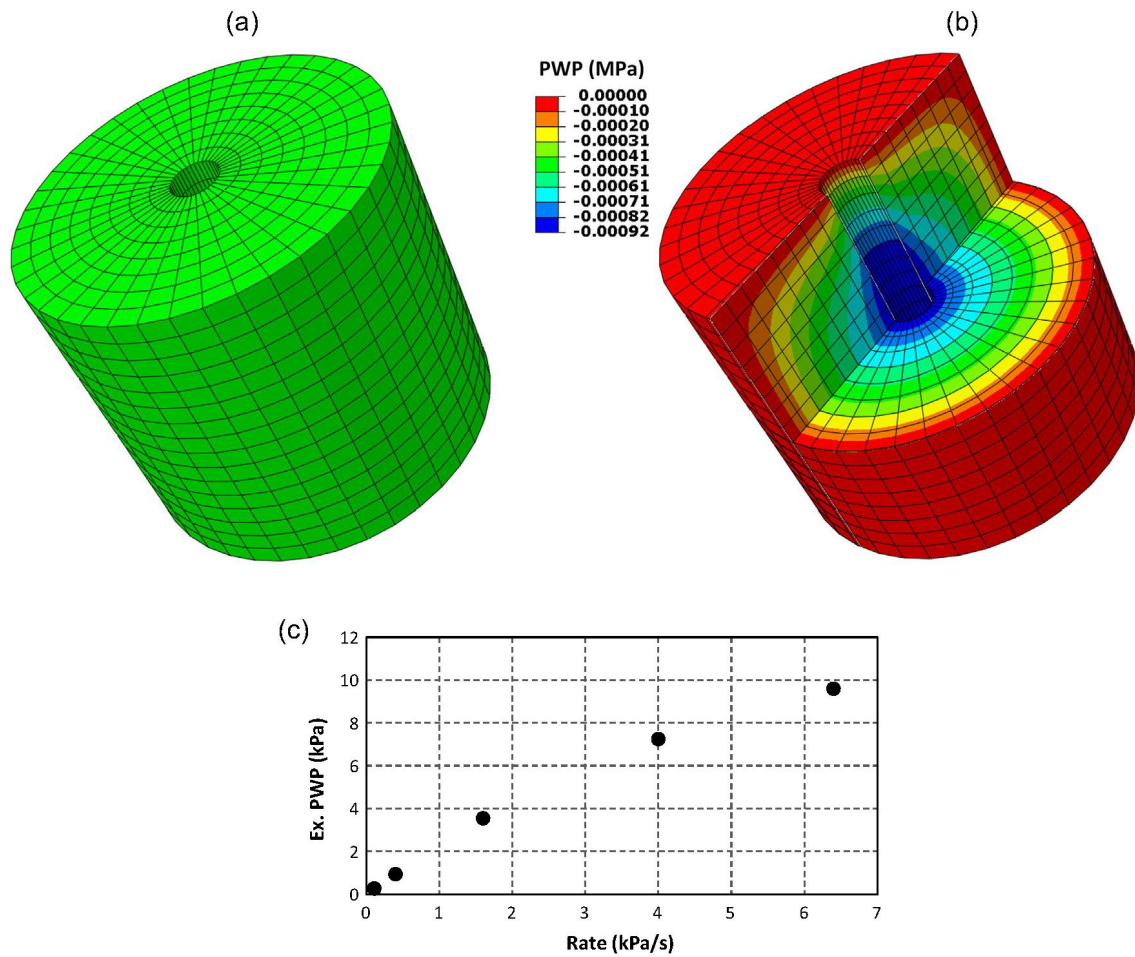


Fig. 7. (a) 3D FEM geometry, (b) distribution of excess pore water pressure, (c) sensitivity of the developed excess pore water pressure to the expansion stress rate.

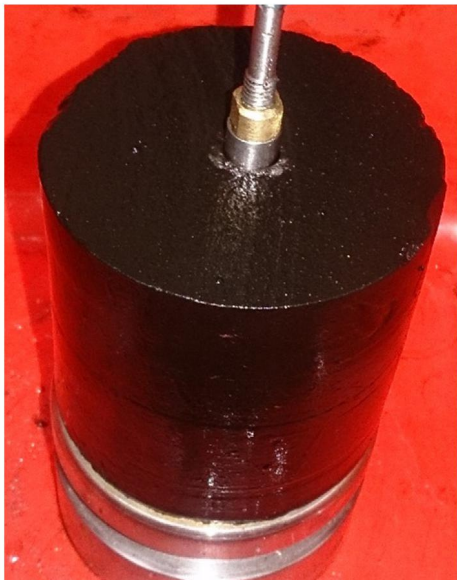


Fig. 8. Probe is placed inside the specimen.

troller was open to prevent any excess initial pressure in the probe. The pore pressure value was monitored after probe placement. When the magnitude of water pressure in the system was back

to the initial value (0–5 kPa) and was stable, the UET was started immediately to avoid moisture loss.

A target water pressure (400 kPa), which is higher than the maximum tensile strength, and a test period of 60 min was set to give an applied pressure rate growth of 0.1 kPa/s. The volume change and water pressure were automatically recorded each second and the test was stopped immediately after failure. A video camera was set up over of the specimen to record the specimen failure.

9. UET results

Results for eight UETs on brown coal are shown in Fig. 9. Each pressure-strain profile consists of three distinct regions. As the internal diameter of the cavity is not exactly 10 mm and 20–40 μm on the sides of the cavity is softened due to both drilling and placement of the probe, the initial curved section (Region 1), is attributed to expansion of the membrane until it comes into full contact with the sides of the cavity. This is similar to the results of typical field scale Menard pressuremeter test in geotechnical materials, Region 2 is approximately linear until the first crack is initiated (primary failure), marking the tensile strength of the brown coal specimen. The primary failure pressure for the tested specimens were found to lie in the range from 110 kPa to 150 kPa. By applying the correction factor of 1.036 (calculated from Eqs. (1)–(3)), the tensile strength of the tested Yallourn brown coal specimens is found to lie in the range from 114 kPa to 155 kPa. This

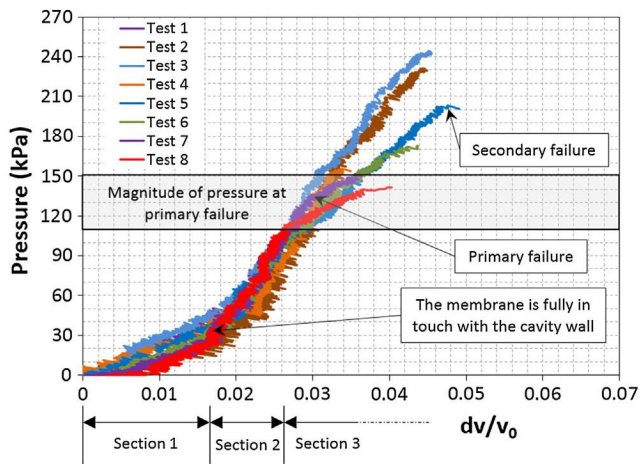


Fig. 9. Results of UET on brown coal.

finding is broadly in agreement with results reported in Tolooyan et al. [25], which gave results for the tensile strength between 110 kPa and 130 kPa for Loy Yang brown coal. The shear modulus and the elastic modulus of tested specimens can be calculated from the slope of pressure-volume profile by using Eqs. (4) and (5). By assuming a Poisson's ratio of 0.22 for brown coal, the measured elastic modulus is in the range of 18–20 kPa. Region 3 relates to the process of crack propagation (secondary failure). Fig. 10 shows a brown coal UET specimen after the end of secondary failure. Since brown coal is considered a brittle material, it can be expected



Fig. 10. Brown coal UET specimen after the secondary failure.

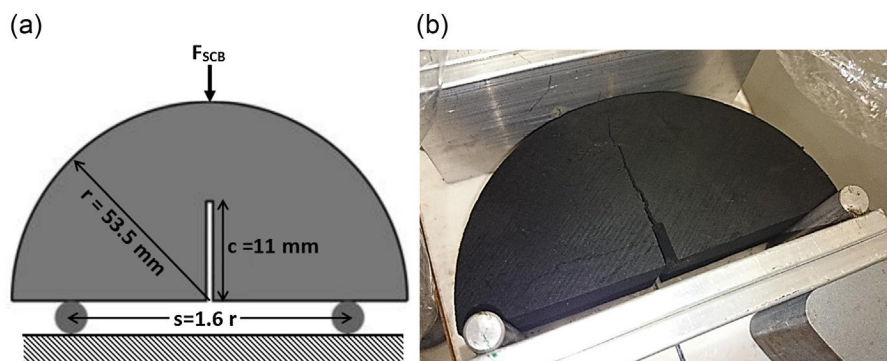


Fig. 11. (a) SCB specimen and setup, (b) brown coal SCB specimen after failure.

that the specimen fails (secondary failure) immediately after crack initiation (primary failure) with no further pressure increase for crack propagation. However, such a phenomenon was not experienced in any of the performed tests. Two features affect how a crack propagates through a specimen under radial loading during secondary failure. The first is the energy release rate which determines how the forces that cause cracking are dynamically transferred to adjacent material and the second is the distribution of stresses in the specimen in the direction of crack propagation and how these are modified by the generation of the crack. If the tip of the crack progresses into a region of lower, sub critical, tensile stress then the crack will cease to grow. Understanding the contribution of these two components has been examined through further laboratory experiments to quantify the energy release rate and modelling to combine this with the changing stress patterns. A laboratory test was performed to determine the critical energy release rate, and XFEM analysis was performed to check the results.

10. Determination of energy release rate

The critical energy release rate, G_c , is the work required to produce a unit increase in crack area. The crack propagates immediately after initiation if the energy release rate is larger than the critical energy release rate of the material ($G > G_c$). However, if the energy release rate is smaller than the critical energy release rate ($G < G_c$), then the crack is stable and further energy (pressure increase in the case of UET) is needed to propagate the crack. In practice, G_c can be determined from Eq. (9).

$$G_c = \frac{K^2(1 - \nu^2)}{E} \quad (9)$$

where E is the elastic modulus of the material, ν is the Poisson's ratio, K is the fracture toughness in Mode I (the tensile stress is normal to the plane of the crack).

Fracture toughness (K) is a property of the material that describes its ability to resist fracture and can be determined experimentally in the laboratory. Semi-Circular Bending tests (SCB) suggested by Chong and Kuruppu [6] were performed on brown coal specimens to measure the fracture toughness. Few specimen machining operations and easy test procedures using common testing apparatus are major advantages of the SCB test [4].

The specimen geometry and the test set-up for the SCB are shown in Fig. 11. A direct shear box apparatus available in most geotechnical laboratories was modified for this test. The apparatus can apply positive or negative deformation along a predefined horizontal axis. A 5 kN S-Beam load cell with an accuracy of 1 N was employed to measure the bending load. The shear box was replaced by two aluminium plates, one connected the specimen

to the load cell while the other one connected the specimen to the axle through two rollers. Deformation was applied at a slow rate to fail the specimen while avoiding excess pore water pressure. The magnitude of the load at failure (F_{SCB}) was converted to fracture toughness using Eqs. (10) and (11) [18].

$$Y = 5.6 - 22.2\left(\frac{c}{r}\right) + 166.9\left(\frac{c}{r}\right)^2 - 576.2\left(\frac{c}{r}\right)^3 + 928.8\left(\frac{c}{r}\right)^4 - 505.9\left(\frac{c}{r}\right)^5 \quad (10)$$

$$K = \frac{Y \times F_{SCB} \times \sqrt{\pi c}}{2rt} \quad (11)$$

where Y is a dimensionless intensity factor and t is the specimen thickness of 30 mm.

Determination of the deformation rate was performed by using effective stress analysis for fluid-filled porous media available in Abaqus/Standard 6.14 in the same manner as explained for the determination of the loading rate in UET. The coal hydraulic conductivity and void ratio values were 4×10^{-7} mm/s and 1.5, respectively, and the elastic modulus was 19 MPa. The 3D finite element geometry is shown in Fig. 12a, where 1050 eight-node brick, trilinear displacement, trilinear pore pressure elements (type C3D8P) are used to shape the specimen in true scale. The top loading plate and two rollers were modelled as analytical rigid bodies. A pore water pressure boundary condition with zero magnitude was predefined over the external surface of the specimen and inside the initial cut (c). The bending test was simulated by applying deformation over the top loading plate, and maximum, and minimum excess pore water pressures were investigated.

Fig. 12b shows the simulated pressure distribution for the deformation rate of 0.0002 mm/s when the magnitude of the force reacting against the applied deformation reached 30 N. The maximum excess pore water pressure and excess pore water suction are 0.47 kPa and 0.80 kPa, respectively at this load. Since these values are small, 0.0002 mm/s was considered a reasonable rate for performing SCB tests on brown coal. The results of the laboratory SCB tests showed that the average F_{scb} value for the brown coal specimens was about 26 N when deformation was applied at a rate of 0.0002 mm/s implying that pore pressures were acceptable for these tests.

Based on the average measured F_{scb} of 26 N, a fracture toughness of $6.86 \text{ kPa m}^{1/2}$ was calculated using Eqs. (10) and (11). Inserting this value in Eq. (9) and adopting the average elastic

modulus of 19 MPa and Poisson's ratio of 0.22 yields a critical energy release rate of 2.357 Pa m.

11. XFEM analysis of UET crack initiation and propagation

The extended finite element method (XFEM) is an effective way to simulate initiation and propagation of a discrete crack and alleviate the shortcomings associated with meshing crack surfaces. This method was first introduced by Belytschko and Black [5]. It is an extension of the conventional FEM and is based on the theory of partition of unity developed by Melenk and Babuška [23], which allows local enrichment functions to be efficiently incorporated into a FEM approximation. Two special enrichment functions provide for the presence of discontinuities in conjunction with additional degrees of freedom.

For the purpose of fracture analysis, the enrichment functions mostly consist of the near-tip asymptotic functions that capture the singularity around the crack tip and a discontinuous function that represents the jump in displacement across the crack surfaces. The approximation for a displacement vector function u with the partition of unity enrichment is shown in Eq. (12) [11].

$$u = \sum_{I=1}^N N_I(x) \left[\underbrace{u_I}_{T1} + \underbrace{H(x)a_I}_{T3} + \sum_{\alpha=1}^4 \underbrace{F_{\alpha}(x)b_I^{\alpha}}_{T4} \right] \quad (12)$$

where $N_I(x)$ is the nodal shape function; u_I is the nodal displacement vector associated with the continuous part of the FE solution; $H(x)$ is the discontinuous jump function across the crack surfaces; a_I is the nodal enriched degree of freedom vector; $F_{\alpha}(x)$ is the elastic asymptotic crack tip functions; and b_I^{α} is the nodal enriched degree of freedom vector. In this function, the terms T1 and T2 apply to all the nodes in the model; the term T3 applies to nodes whose shape function support is cut by the crack interior; and the term T4 applies only to nodes whose shape function support is cut by the crack tip (see Fig. 13).

Unlike the traditional crack propagation methods that require the failure zone to align with element boundaries and the cracks to develop along a set of predefined paths, the XFEM-based cohesive segments method simulates the crack initiation and propagation along any solution-dependent path in the specimen. For the simulation procedure adopted, the asymptotic crack tip function (Term 4 in Eq. (12)) was not required and only the discontinuous jump function across the crack surfaces is defined as described in Eq. (13).

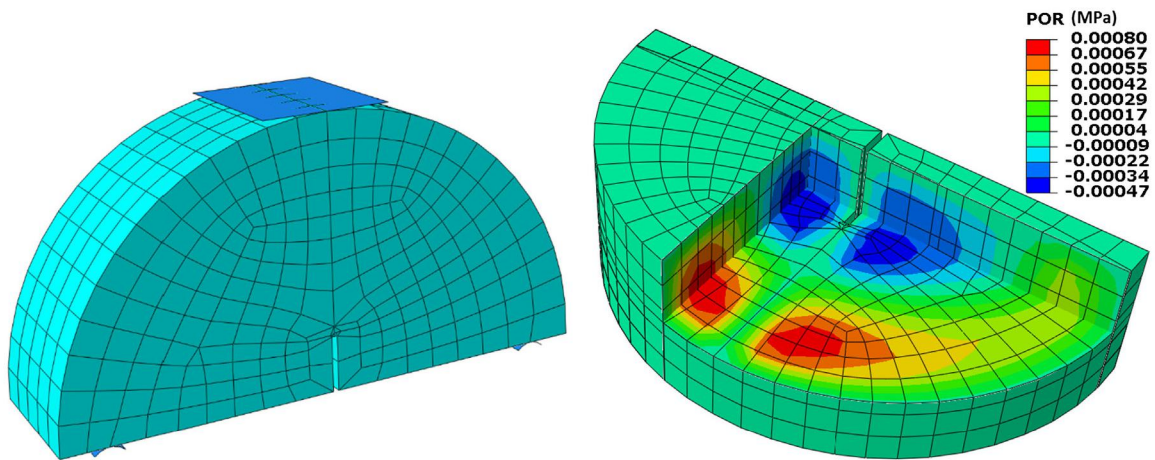


Fig. 12. (a) The FEM geometry of SCB specimen, (b) distribution of pore water pressure/suction in SCB specimen.

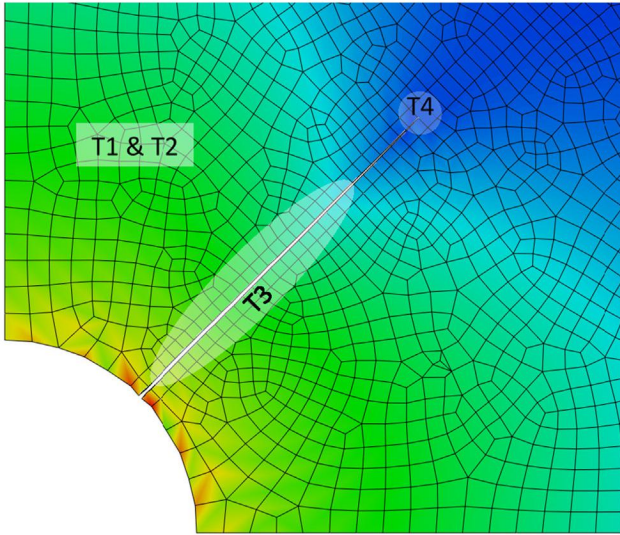


Fig. 13. The XFEM approximation.

$$H(x) = \begin{cases} 1 & \text{if } (z - z') \cdot m \geq 0, \\ -1 & \text{otherwise,} \end{cases} \quad (13)$$

where z is a Gauss point, z' is the closest point to z that is on the crack, and m is the unit outward perpendicular to the crack at z' . It should be noted that, in this method, the crack has to spread across the entire failing element in one time step to avoid the need for the asymptotic crack tip function.

As the trigger for crack initiation, the maximum allowable principal tensile stress was defined as the failure criterion. Thus, crack

initiation occurs when the maximum principal stress reaches the predefined critical value that is the average tensile strength of the brown coal specimen (130 kPa). Since the magnitude of crack opening was not measured during the experiments, no traction-separation law was employed to address this in the modelling.

To minimise the computational cost of numerical analysis, only a thin layer of a quarter of the UET specimen was modelled. The 3D model finite element geometry is shown in Fig. 14, where 3842 eight-node linear brick, reduced integration, hourglass controlled elements (type C3D8R) are used to define the specimen geometry. To satisfy the required boundary conditions, side 1 was fixed in the Y direction, side 2 was fixed in the X direction, and sides 3 and 4 were fixed in the Z direction. Since the stress was expected to develop uniformly prior to crack initiation/propagation, the XFEM functions were only allocated to the elements located along the central radius (the XFEM region as shown in Fig. 14). In this case the crack to initiate and propagate only in this region. A cylindrical pressure was applied on side 5 to simulate the cavity expansion.

The input parameters for constitutive modelling are given in Table 1. It should be noted that, although the maximum principal stress was assigned to trigger the failure in tension, the Mohr-Coulomb model was employed to model the failure in compression, considering that the elements close to the cavity may undergo excessive compression due to the cavity expansion.

Two XFEM analyses were performed to simulate the UET on brown coal. In the first analysis, the actual critical energy release rate of brown coal, $G_c = 2.357 \text{ Pa m}$, was used. In the second analysis a smaller value, $G_c = 0.235 \text{ Pa m}$, was adopted. The goal of the two analyses was to show the effect of the magnitude of critical energy release rate on the behaviour of crack propagation in UET. Results of both analyses are shown in Fig. 15. The initial difference of $30 \mu\text{m}$ between cavity and probe radius apparent in the labora-

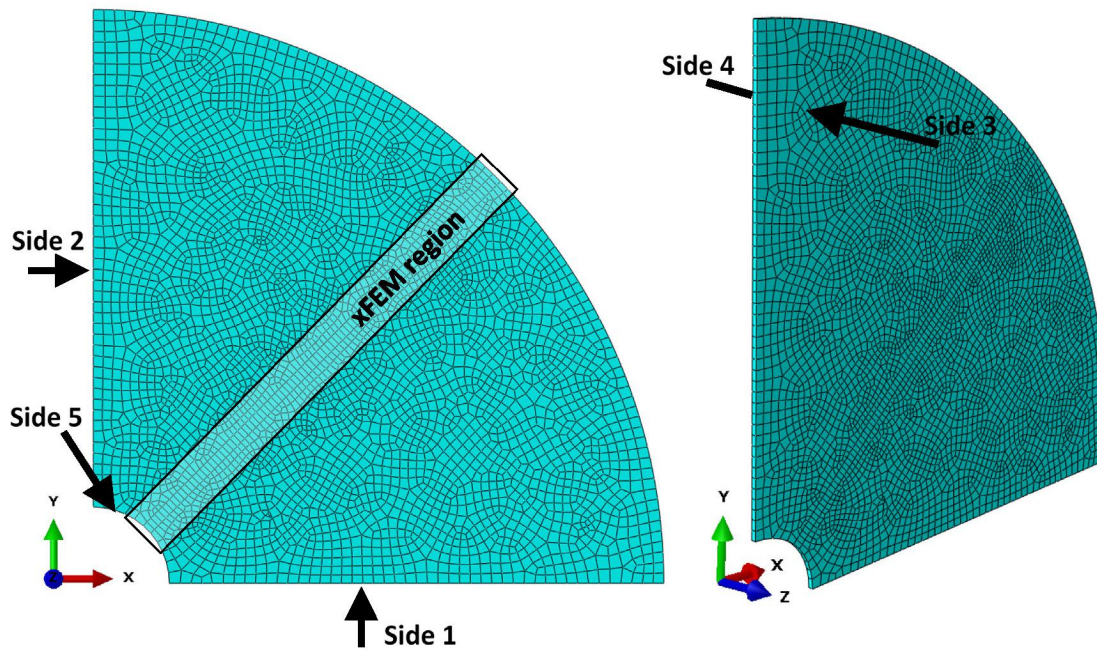


Fig. 14. The FEM geometry of UET specimen.

Table 1
The input parameters for constitutive modelling.

	Tensile strength (kPa)	Poisson's ratio	Critical energy release rate (Pa m)	Elastic modulus (MPa)	Friction angle (degrees)	Cohesion (kPa)
Value	130	0.22	2.357	19	20	150

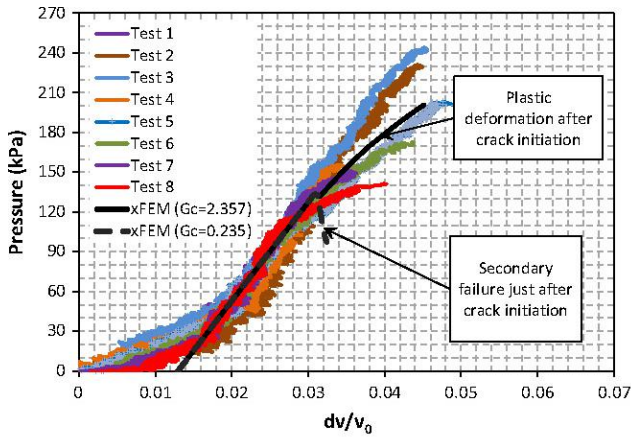


Fig. 15. UET test on brown coal, the comparison between experiment and XFEM results.

tory tests was not considered in the simulation. Hence, the XFEM results are plotted from $dv/v_0 = 0.013$. As shown in Fig. 15, pressure increases linearly up to critical tensile stress of 130 kPa for both analyses. In the analysis using the actual G_c , the energy release after crack initiation (primary failure) does not cause uncontrolled extension of the crack and the pressure increases after crack initiation to extend the crack. With the lower critical energy release rate, the energy release exceeds the critical value and the crack propagates immediately after initiation without further increase in the forcing pressure. Fig. 16, shows the modelled UET specimen prior, during and after failure.

12. Comparison with traditional methods

The main objective of developing the UET is to measure the tensile strength of IGMs with a high accuracy while avoiding the biases in the two major methods for tensile strength measurement (DTT and BT) associated with stress concentration, specimen shape

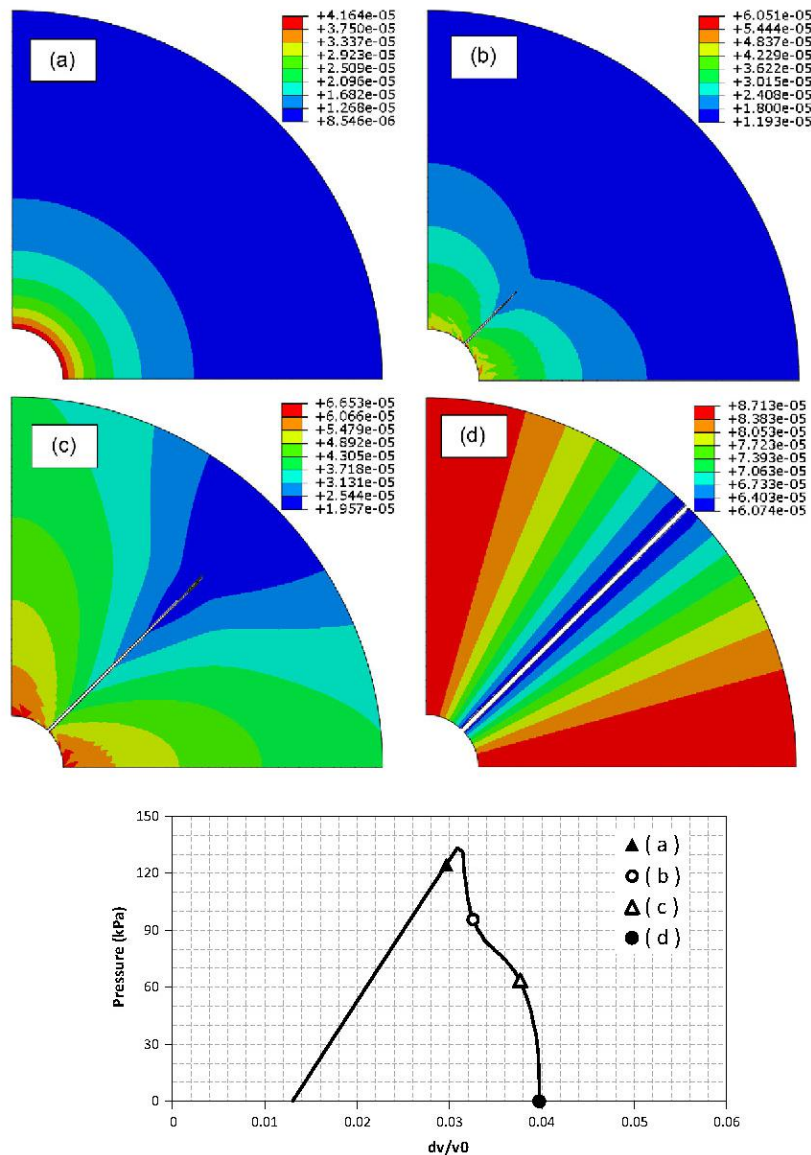


Fig. 16. Radial deformation in UET specimen (mm).

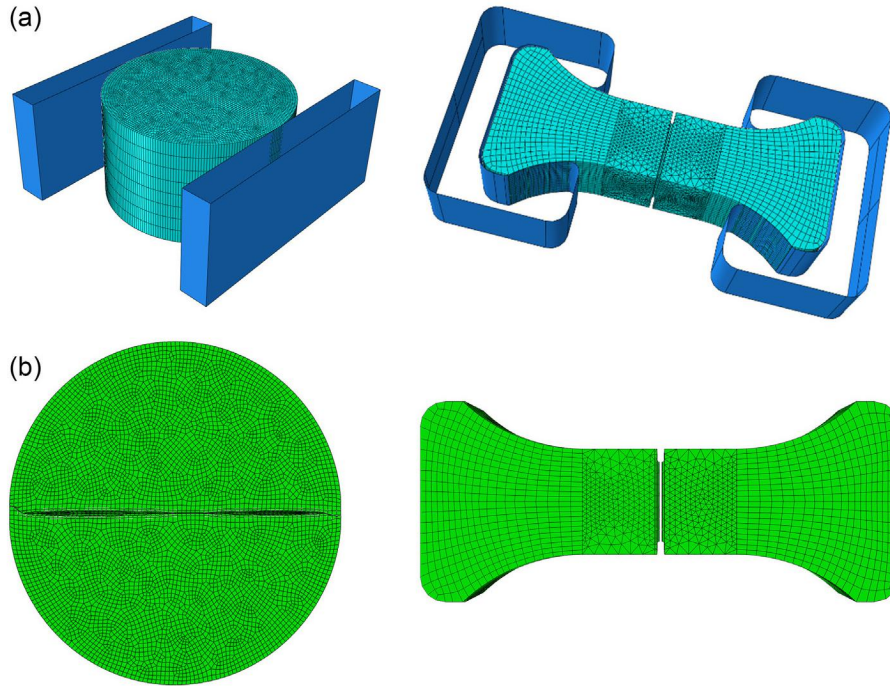


Fig. 17. Simulation of BT and DTT using XFEM; (a) before failure, (b) after failure.

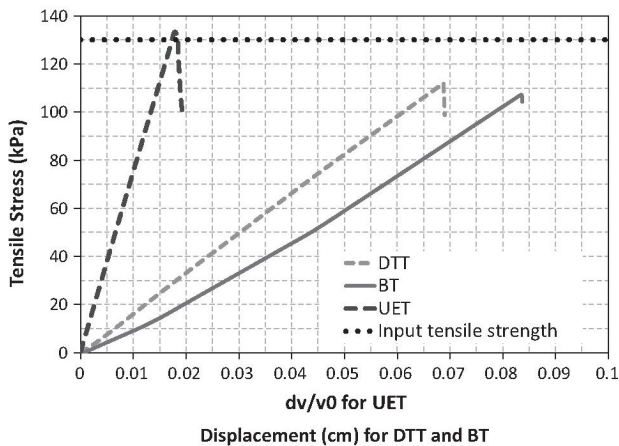


Fig. 18. Measured tensile strength from simulation of DTT, BT and UET.

and predefined failure plane. Coviello et al. [9], Yu et al. [28], Fahimifar and Malekpour [13] and Tolooiy et al. [25] showed that the magnitude of the tensile strength measured by the BT and DDT can be underestimated by more than 5–15% due to the specimen shape and stress concentration around the failure zone. To explore the performance of the UET against the DTT and BT, the constitutive model calibrated during simulation of the UET was employed to simulate the DTT and BT by XFEM (see Fig. 17). Since the actual tensile strength of 130 kPa is used as the input tensile strength in all the simulations, the difference between the specimen's tensile strength as the simulation outputs and the given input tensile strength is indicative of the relative bias of each of the test methods. For the simulation of DTT, seven thousand four hundred eighty-eight linear hexahedron elements (type C3D8R) form each bone-shape end, and 19,742 quadratic tetrahedron elements (type C3D10M) are used to shape the middle part of the specimen. As suggested by [25], the shape of the aluminium grips that axially pull the specimen was established to minimise tensile

forces within the specimen inside the grip and to produce smoothly varying stress and strain within the gripped region of the specimen. Since the stiffness of aluminium is much higher than the stiffness of the coal, the two grips are modelled using analytical rigid surfaces to decrease the computational cost. Since the specimen may slide against the aluminium grips during the test, the coal-aluminium interface friction of $\mu = 0.55$ is taken into account. For the simulation of the BT, the specimen was modelled with 44,720 linear hexahedron elements (type C3D8R). The aluminium plates that axially push the specimen were modelled using analytical rigid surfaces that account for aluminium coal friction and surface displacement of the coal at the contact surfaces. Please note that since the BT specimen is in compression, the Elastic modulus of 64 MPa is considered instead of 19 MPa. For more information regarding the application of DTT and BT for IGMs, please refer to Tolooiy et al. [25].

Fig. 18, compares the magnitude of tensile strength from the simulation of BT, DTT and UET. As shown in this figure, the BT and DTT produce similar values and both underestimate the modelled tensile strength. The UET returns the modelled tensile strength of the specimen.

To investigate the underestimation of the tensile strength by BT and DTT, the effect of stress concentration around the failure zone was investigated. Fig. 19 shows the stress concentration around the failure zone in DTT, UET and BT, just before crack initiation and failure. The areas indicated in red¹ have reached the principal stress of 100–130 kPa and form the failure zone in which the crack initiates. From these figures, it is clear that the principal stress is not developed uniformly on the failure plane of the DTT specimen (Fig. 19a). In the BT specimen, only a portion of the specimen's diameter reaches the failure stress at the onset of crack initiation (Fig. 19c). However, in BT, the total length of the specimen's diameter is taken into account for the calculation of the tensile strength. As expected from reviewing the work by Coviello et al. [9], Yu et al. [28],

¹ For interpretation of color in Fig. 19, the reader is referred to the web version of this article.

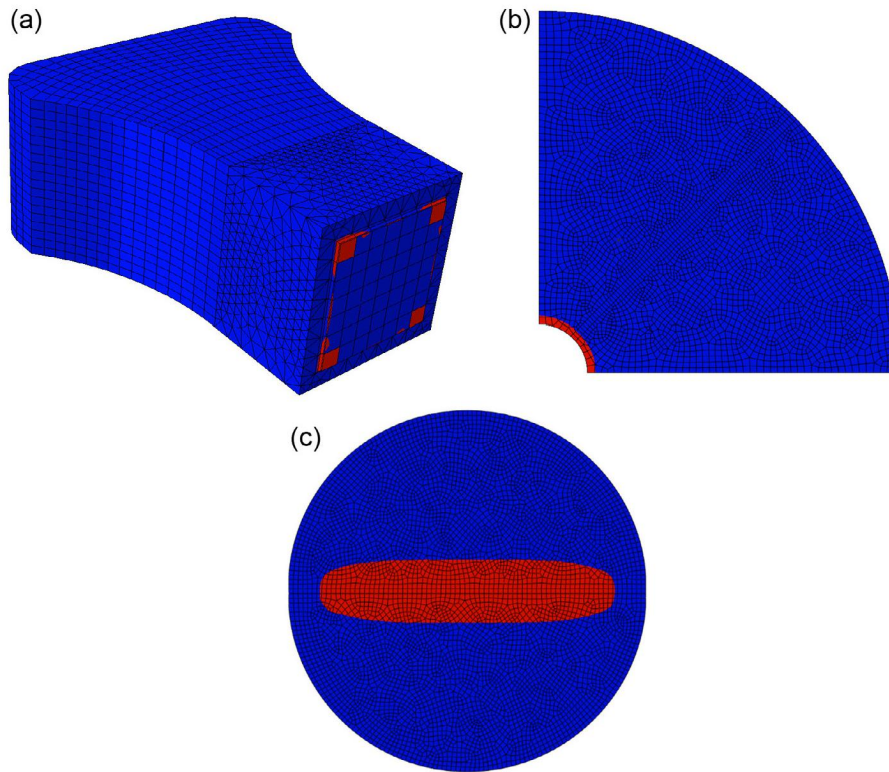


Fig. 19. Stress concentration just before failure; (a) DTT, (b) UET, (c) BT.

Fahimifar and Malekpour [13] and Tolooyan et al. [25], the impact of stress concentration around the failure plane and the non-uniform stress distribution along the failure zone caused by DTT and BT introduce a significant bias in the measurement of tensile strength. It is clear that in the UET, the principal stress is developed uniformly around the internal diameter of the specimen where crack initiates (Fig. 19b). This is why the measured tensile strength from the XFEM simulation of this test is similar to the given input tensile strength.

13. Discussion and conclusion

The cavity expansion test, referred to in this paper as an unconfined expansion test or UET, has been developed for intermediate geotechnical materials to extend the range of methods of laboratory determination of the tensile strength of these materials. As well as the tensile strength the test also allows measurement of the shear modulus and the estimation of elastic modulus, if Poisson's ratio is known. The tensile strength is determined from the cavity pressure required to initiate crack failure of the specimen, while shear modulus and elastic modulus depend on the gradient of volumetric cavity expansion against increasing cavity pressure. In addition to the additional information provided by this test, its advantage over standard tests for tensile strength, the Direct Shear Test and the Brazilian Test, lies in the removal of the restriction on the orientation of the crack direction that is a feature of the standard tests. The new test reduces the potential for bias in the test results arising from predefinition of crack orientation: the crack should always propagate in the orientation of lowest tensile strength.

The test was designed to mimic, at the laboratory scale, pressuremeter testing used for in situ stress and material strength measurements in the field. The theory developed for the interpretation of field scale pressuremeter results has been employed for the analysis of the UET results. Development of the test required the removal of measurement errors introduced by the compliance

of the pipe and membranes used for the construction of the test equipment. Equations for correction of the measurements related to cavity pressure were constructed using two supplementary calibration experiments. A high degree of accuracy in the determination of cavity pressure was achieved.

Eight experiments were performed on brown coal specimens taken from a single block. As brown coal is porous, with high water content and low hydraulic conductivity, care was taken to ensure that pore pressure changes in the specimen during the test were minimal by adopting low time rates of pressure change. The experimental results all showed the same general behaviour for all specimens but with a range of apparent tensile strengths. The initiation of crack failure is directly discernible from the displacement volume versus cavity pressure graph. The obtained tensile strengths were consistent with previous measurements of tensile strength using Direct Tensile and Brazilian tests.

Numerical modelling using ABAQUS 6.14 was undertaken to confirm the test results, as well as to determine the rates of pressure change w.r.t. time to control pore pressures. The model results provide confidence in the validity of the test and test results.

One interesting observation from the test concerned the increase in cavity pressure to propagate the crack after crack initiation. Numerical modelling was undertaken, alongside additional mechanical testing to quantify the critical crack energy release rate for the brown coal, to explain the observed results. The modelling provided direct confirmation that for the given test configuration the energy release rate during cracking was less than the critical release rate and, therefore, cracking failure was progressive rather than instantaneous.

In conclusion, the testing has shown that the UET can be performed to determine tensile strength, shear modulus and elastic modulus in laboratory scale specimens with acceptable accuracy. The testing has also shown that the critical energy release rate on crack formation is important for the determination of the mechanics of crack propagation through brown coal.

Acknowledgements

The authors would like to acknowledge the staff of the Latrobe Valley brown coal mines and Earth Resources Regulation in the Department for Economic Development, Jobs, Transport and Resources of the Victorian Government for their support in undertaking this study. The authors are also grateful for the technical support provided by Wayne Powrie for the high quality construction of the UET equipment used for the study.

References

- [1] Ajaz A, Parry R. An unconfined direct tension test for compacted clay. *ASTM J Test Eval* 1974;2:163–72.
- [2] Alavi SH, Monismith CL. Time and temperature dependent properties of asphalt concrete mixes tested as hollow cylinders and subjected to dynamic axial and shear loads. *J Assoc Asphalt Paving Technol* 1994;63:152–81.
- [3] Australia Mineral Resource. The Australian atlas of mineral resources, mines, and processing centres. Commonwealth of Australia; 2011.
- [4] Ayatollahi MR, Aliha MRM. On determination of mode II fracture toughness using semi-circular bend specimen. *Int J Solids Struct* 2006;43:5217–27.
- [5] Belytschko T, Black T. Elastic crack growth in finite elements with minimal remeshing. *Int J Numer Meth Eng* 1999;45:601–20.
- [6] Chong KP, Kuruppu MD. New specimen for fracture toughness determination for rock and other materials. *Int J Fract* 1984;26:R59–62.
- [7] Clarke BG, Menard. Pressuremeter testing in ground investigation. Part 1 – Site operations. In: *Proceedings of the ICE - geotechnical engineering*. p. 96–108.
- [8] Colback PSB. An analysis of brittle fracture initiation and propagation in the Brazilian test. In: *First congress of the international society for rock mechanics*. Lisbon (Portugal): International Society for Rock Mechanics; 1966. p. 385–91.
- [9] Coviello A, Lagiolo R, Nova R. On the measurement of the tensile strength of soft rocks. *Rock Mech Rock Eng* 2005;38:251–73.
- [10] Crockford WW. Role of principal-plane rotation in flexible pavement deformation. *J Transport Eng* 1993;119:124–41.
- [11] Dassault Systèmes. Abaqus. 6.14 ed. Providence (RI, USA): Dassault Systèmes, Dassault Systèmes Simulia Corp.; 2014.
- [12] DPI. About Victoria's brown coal. Melbourne: Department of Environment and Primary Industries; 2012.
- [13] Fahimifar A, Malekpour M. Experimental and numerical analysis of indirect and direct tensile strength using fracture mechanics concepts. *Bull Eng Geol Environ* 2012;71:269–83.
- [14] Haberfield CM. Pressuremeter testing in weak rock and cemented sand. In: *Proceedings of the ICE - geotechnical engineering*. p. 168–78.
- [15] Hudson JA, Brown ET, Rummel F. The controlled failure of rock discs and rings loaded in diametral compression. *Int J Rock Mech Min Sci Geomech Abstr* 1972;9:241–8.
- [16] Jaeger JC. Failure of rocks under tensile conditions. *Int J Rock Mech Min Sci Geomech Abstr* 1967;4:219–27.
- [17] Jaeger JC, Hoskins ER. Rock failure under the confined Brazilian test. *J Geophys Res* 1966;71:2651–9.
- [18] Kuruppu MD, Chong KP. Fracture toughness testing of brittle materials using semi-circular bend (SCB) specimen. *Eng Fract Mech* 2012;91:133–50.
- [19] Ladanyi B. Expansion of cavities in brittle media. *Int J Rock Mech Min Sci Geomech Abstr* 1967;4:301–28.
- [20] Li D, Wong L. The Brazilian disc test for rock mechanics applications: review and new insights. *Rock Mech Rock Eng* 2013;46:269–87.
- [21] Lu N, Wu B, Tan C. Tensile strength characteristics of unsaturated sands. *J Geotech Geoenviron Eng* 2007;133:144–54.
- [22] Mair RJ, Wood DM. Pressuremeter testing: methods and interpretation. London: CIRIA; 1987.
- [23] Melenk JM, Babuška I. The partition of unity finite element method: Basic theory and applications. *Comput Meth Appl Mech Eng* 1996;139:289–314.
- [24] Timoshenko S, Woinowsky-Krieger S. *Theory of plates and shells*. McGraw-Hill; 1959.
- [25] Tolooiyan A, Mackay R, Xue J. Measurement of the tensile strength of organic soft rock. *Geotech Test J* 2014;37.
- [26] Vesga L, Vallejo L. Direct and indirect tensile tests for measuring the equivalent effective stress in a kaolinite clay. In: *Unsaturated soils 2006*. p. 1290–301.
- [27] Yu HS. *Cavity expansion theory and its application to the analysis of pressuremeters*. University of Oxford, St. Anne's College; 1990.
- [28] Yu Y, Yin J, Zhong Z. Shape effects in the Brazilian tensile strength test and a 3D FEM correction. *Int J Rock Mech Min Sci* 2006;43:623–7.



Use of stochastic XFEM in the investigation of heterogeneity effects on the tensile strength of intermediate geotechnical materials

Ashley P. Dyson^a, Zhan Tang^b, Ali Tolooiyan^{a,*}

^a Geotechnical and Hydrogeological Engineering Research Group (GHERG), Federation University Australia, Gippsland Campus, Victoria, Australia

^b Faculty of Science, Monash University, Australia

ARTICLE INFO

Keywords:

Intermediate geotechnical material
Fracture mechanics
Stochastic methods
Extended finite element method
Unconfined expansion test

ABSTRACT

The numerical simulation of an Unconfined Expansion Test (UET) is presented with tensile strength fracture criteria assigned by stochastic methods to take into account material heterogeneity. Tests are performed by producing radial cavity expansion models of thinly sliced cylindrical specimens. The introduction of element-wise allocation of fracture parameters generates instances of specimen failure without the requirement of predefined fracture zones, permitting discontinuities to form naturally within zones containing weak strength parameters. The parallel application of an in-house Python scripts and eXtended Finite Element Method (XFEM) facilitates the investigation of heterogeneity effects on the tensile strength of intermediate geotechnical materials.

1. Introduction and background

Conventional numerical modelling methods such as the Finite Element Method (FEM) often perform poorly in approximation of solutions with non-smooth characteristics in the modelling domain, for example near discontinuities, crack initiation/propagation, and singularities. The eXtend Finite Element Method (XFEM) developed by Belytschko and Black [1] is an effective method to simulate discontinuities and crack opening by enabling a local enrichment of approximation spaces. With the additional degrees of freedom from special enrichment functions, once the failure criteria are fulfilled, cracks are allowed to initiate in local enrichment regions and to propagate based on the energy release criteria without the need for conventional re-meshing. Due to the absence of remeshing requirements, XFEM has become one of the choice methods for modelling fracture of cohesive materials [2–5].

Theoretically, the simplest laboratory testing method for the measurement of tensile strength is the Direct Tension Test (DTT). The method has been extensively implemented in the investigation of the tensile strength of over-consolidated clays, unsaturated soils, and cemented sands. However, the complicated process of specimen preparation is a significant obstacle [6,7]. Coupled with potential bias when compared with the Brazilian Testing method [8], Tang et al. [9] developed an XFEM model using Abaqus code [10] to simulate crack opening and tension failure in Unconfined Expansion Testing (UET) in order to analyse both

the stress distribution of the test and to examine fracture parameters. UET (as seen in Fig. 1) is a newly designed test that aims at measuring the tensile strength of intermediate geotechnical materials (IGM) such as soft rocks. A cylindrical cavity is drilled along the axis of a cylindrical specimen, then, based on Timoshenko's thick wall cylinder expansion theory [11] the UET method is able to create circumferential, uniformly-distributed tensile stresses around the sample cavity by the inflation of an expandable probe. Therefore, an arbitrary crack path is created when natural weaknesses of the sample approach the material's tensile strength. XFEM simulation results confirm an agreement with theoretical assumptions in both pre-failure stress distribution and tensile strength [9]. As stresses evenly develop inside the geometry, a radial XFEM region must be predefined within the geometry to overcome the computational ambiguity of crack opening when XFEM is specified over the full domain.

Of particular interest in the study of UETs is the impact of material heterogeneity. This can be achieved by interpolating XFEM with material variability and performing probabilistic analyses. Probabilistic analysis of heterogeneous brittle materials has continued to gain significant attention [2,12,13]. Understanding of the relationship between heterogeneity and UET test results has two benefits. For materials with known heterogeneity, the method can be applied to determine the test quality and possible error. For unknown heterogeneous materials, engineers can back-estimate the material's heterogeneity by performing a large number

* Corresponding author.

E-mail addresses: a.dyson@federation.edu.au (A.P. Dyson), zhan.tang@monash.edu (Z. Tang), ali.tolooiyan@federation.edu.au (A. Tolooiyan).

<https://doi.org/10.1016/j.finel.2018.03.003>

Received 17 October 2017; Received in revised form 16 February 2018; Accepted 14 March 2018

Available online 27 March 2018

0168-874X/© 2018 Elsevier B.V. All rights reserved.



Fig. 1. UET probe placed within a brown coal specimen, Tang et al. [9].

of tests.

This paper introduces the existing uniform XFEM simulation of UET but without a predefined fracture zone. Commencing with the theory of discontinuity simulation by XFEM for implementation of UET modelling, comparisons of scenarios with and without the predefined XFEM region are produced. The process of random variable parameter assignment is detailed, followed by XFEM simulation results. With the aforementioned approach, the goal of this research is to allow fracture to form naturally without predefined XFEM zones, by the process of random variable assignment of element parameters. Furthermore, this paper presents the effects of this process on material strength, such that stochastic models incorporating variation of material characteristics can be calibrated to align with observed laboratory UET results, while also producing numerical results to develop conclusions about empirical UET parameter variability.

2. The extended finite element method overview

The extended finite element method is an indispensable tool for modern numerical simulation of crack initiation, propagation, and coalescence. Initially developed by Belytschko and Black [1,15], XFEM supplements the classic finite element method with local enrichment functions applied to finite element approximation spaces. Alternative existing techniques for fracture simulation include boundary element methods [16,17], continual re-meshing FEM [18], and mesh-free methods [14,19]. However, XFEM exhibits a wide range of beneficial attributes; without the enrichment properties of the extended method, conventional FEM requires appreciable mesh refinement in the neighbourhood of discontinuity tips. Discrete crack propagation phenomena are often modelled efficiently with XFEM without the constraint of extensive re-meshing, a crucial property for computationally expensive non-linear systems. XFEM incorporates the added benefit of integrating readily available codes to existing finite element algorithms and framework.

2.1. Theory

In the extended finite element method, the span of functions for the element-free Galerkin method of Fleming, Chu [19] is implemented utilising Partition of Unity (PU) theory developed by Melenk and

Babuška [20], and Duarte and Oden [21]. The PU method provides analysis of material behaviour characteristics throughout element geometries, rather than exclusively at element nodes. Consequently, mesh and discontinuity alignments are nonessential. Additional degrees of freedom produce near crack tip nodes by enrichment functions. The displacement approximation u , with the partition of unity enrichment is expressed in Equation (1) [10].

$$\mathbf{u}^h = \sum_{i \in I} \mathbf{u}_i \phi_i + \sum_{j \in J} \mathbf{b}_j \phi_j H(x) + \sum_{k \in K} \phi_k \left(\sum_{l=1}^4 \mathbf{c}_k^l F_l(x) \right) \quad (1)$$

where the first contributing part \mathbf{u}_i corresponds to the classical FEM approximation of the displacement field, ϕ_j is the shape function for the j th node whose support is cut by the crack face (but not the crack tip), \mathbf{b}_j is the crack face j th nodal displacement vector; $H(x)$ is the modified Heaviside function (Equation (2)), $F_l(x)$ are the elastic asymptotic crack tip functions (Equations (3)–(6)); \mathbf{c}_k^l is k th nodal enriched degree of freedom vector of the asymptotic crack tip and ϕ_k is the shape function for the k th node whose support is cut by the crack tip. The nodal displacement term \mathbf{u}_i applies to all nodes, while the Heaviside term contributes only to nodes whose support is cut by the crack interior. The final term of Equation (1) is applied only to the nodes whose support is cut by the crack tip.

$$H(\mathbf{x}) = \begin{cases} 1 & \text{if } (\mathbf{x} - \mathbf{x}^*) \cdot \mathbf{m} \geq 0, \\ -1 & \text{otherwise} \end{cases} \quad (2)$$

where, \mathbf{x} is a Gauss point, \mathbf{x}^* is the projection of \mathbf{x} onto the crack line, and \mathbf{m} is the unit outward normal to the crack at position \mathbf{x}^* .

$$F_{l=1}(x) = \sqrt{r} \sin \frac{\theta}{2} \quad (3)$$

$$F_{l=2}(x) = \sqrt{r} \cos \frac{\theta}{2} \quad (4)$$

$$F_{l=3}(x) = \sqrt{r} \sin \frac{\theta}{2} \sin \theta \quad (5)$$

$$F_{l=4}(x) = \sqrt{r} \cos \frac{\theta}{2} \sin \theta \quad (6)$$

Where, (r, θ) form the polar coordinate system with the crack tip at the origin.

2.2. Extended finite element simulations with predefined enrichment zones

The numerical fracture simulations of Tang et al. [9] provides an innovative technique for the modelling of the tensile strength of organic soft rock cored specimens. Utilising the XFEM in Abaqus 6.14 FEM code, Tang et al. [9] produced a quarter annulus shaped membrane (Fig. 2) with spatially homogeneous material properties shown in Table 1. As shown in Fig. 2, a predefined thin enrichment XFEM region is extending radially from a centre cavity. Due to the expectation of stress developing uniformly through the model geometry, crack initiation and propagation are exclusively allowed to develop within the desired XFEM region.

To trigger the crack initiation, the failure criterion was defined by a Maximum Principal Stress Failure Criteria (MPSFC) of 130 kPa, suitably modelling failure under tension. Conversely, the deviatoric stress criterion modelled failure in compression, as expected in elements close to the annulus cavity wall, where aperture expansion may cause excessive compression.

In preference to implementing a computationally expensive full three-dimensional model, a thin layer consisting of 3842 eight-node linear brick reduced integration elements (ABAQUS type C3D8R) was deemed a suitable specimen geometry for initial analysis. A thin 3D layer was chosen in preference to a 2D plane-strain model, due to the contact

formulation of the inner cavity. Abaqus 3D shell elements (S4R 4-node reduced integration) were chosen due to the number of contact elements, in comparison with the Abaqus beam elements (B31) of 2D plane-strain simulation.

Boundary conditions illustrate side 1 as fixed in the Y direction, side 2 fixed in the X direction, and sides 3 and 4 fixed in the Z direction (Fig. 2). Isotropic cylindrical pressure applied to side 5 simulated the expansion of the internal cavity, providing conditions to trigger fracture initiation. The full dimensions of the UET sample and the quarter annulus considered for modelling are given in Fig. 3.

2.3. Heterogeneous XFEM model without predefined enrichment zone

The model described above constitutes a powerful technique for the simulation of cracked specimens mimicking unconfined expansion tests. However, the prescription of a defined failure region (XFEM region in Fig. 2) represents an unrealistic system. In the paper presented, methods permit solution dependent fracture paths to develop, without the need to predefine the failure region.

In the absence of heterogeneous material characteristics in numerical simulation of isotropic loading scenarios such as UET, homogeneous parameters of elastic modulus and maximum tensile strength are allocated to all specimen elements. Hence, fractures are unable to differentiate strong and weak zones and propagate uniformly, making numerous fractures developing radially from the inner cavity (Side 5). This method of homogenous crack initiation and propagation is not only unrealistic but also causes the solution to fail after a few unconverged iteration (see Fig. 4). To solve this limitation, material variability should be introduced in numerical modelling. The maximum principal stress crack initiation criteria which is available in Abaqus enhanced with the addition of heterogeneous strength parameters allows cracks to initiate naturally, meaning no initial fractures were designed within the Finite Element geometry. Instead, cracks form without predefined orientations, locations and dimensions, with crack characteristics determined by the cavity expansion applied to the unique instance of the of material's maximum principal stresses. Due to the energy release rate and the material strength values, cracks propagate orthogonal to the orientation of the internal cavity.

3. Assign material variation into XFEM

3.1. Definition of model variability

It is widely accepted that computational methods aid the construction

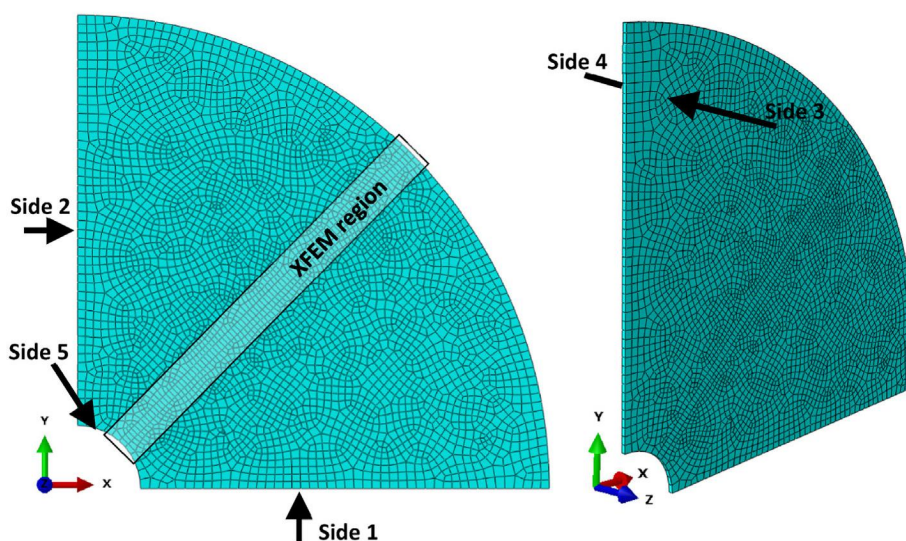


Fig. 2. XFEM geometry of Tang et al. [9].

Table 1
Input parameters of initial quarter annulus model.

Tensile strength (kPa)	Poisson's ratio	Critical energy release rate (Pa m)	Elastic modulus (MPa)	Friction angle (degrees)	Cohesion (kPa)
130	0.22	2.357	19	20	150

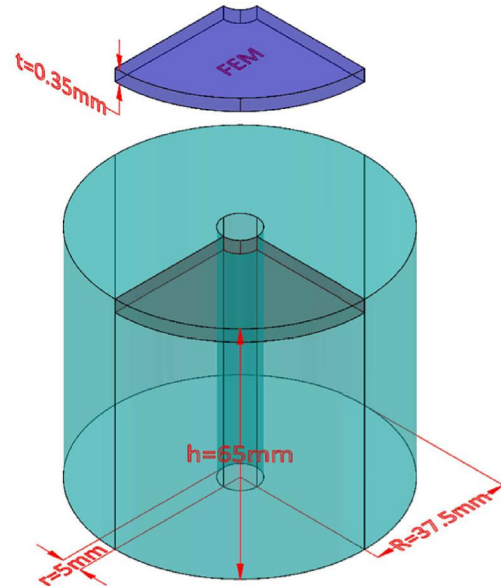


Fig. 3. Quarter annulus of UET sample used for FEM modelling.

and analysis of engineering systems ranging from the nano-scale to the macro-scale. Inherent material uncertainties and their influence on system behaviour have led to an increase in stochastic methods applied to geotechnical problems of high complexity. Numerical simulations containing stochastic and heterogeneous soil models are gaining attention in broad range of geotechnical engineering fields, from slope stability analysis [22,23] to discrete fracture networks [24]. Heterogeneous characteristics may be applied to include Poisson's ratio, elastic modulus, yield stress, methods of loading, etc. Heterogeneities are often generated by means of statistics and probability theory, with resulting behaviour

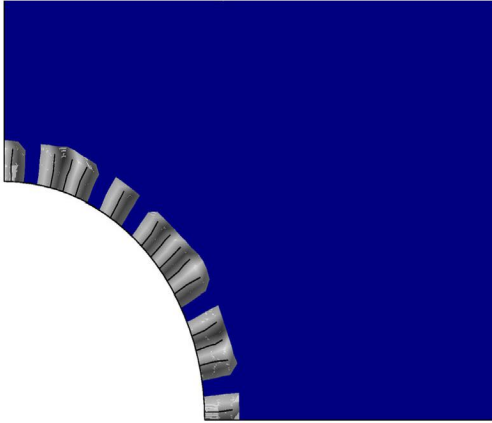


Fig. 4. Multiple cavity fractures caused by material homogeneity.

that cannot be achieved by classical deterministic approaches.

3.2. Numerical definition of material variation

Due to the Central Limit Theorem (CLT), sufficiently large random samples of a population of finite variance, produce sample means approximately equal to the mean of the population. Furthermore, sample means will follow an approximately Gaussian distribution, with sample variances mirroring the population variance. Although uncertainties in soil mechanics may follow non-Gaussian distributions, stationary Gaussian random fields are routinely assumed for the sake of simplicity and due to a lack of knowledge regarding experimental data. This paper concentrates exclusively on the normal (Gaussian) distribution for the variation of element maximum principal stress failure criteria and element elastic modulus. The fluctuations in these properties suggest an approach for the production of spatial variation in crack initiation and propagation. As the objective of this research is to naturally produce fracture by material strength parameter variation, the analysis of non-Gaussian distributions is deemed beyond the scope of this paper. Spatially random variables without a spatial correlation length have been implemented in this research, as spatial correlation parameters are not required to produce the goal of fracture initiation.

Material properties are varied as a percentage of their mean value (Fig. 5). As maximum principal stress and elastic modulus variables permit only non-zero values, random variables outside the range of $[0, 2\mu]$ were rejected and given random normal values within the

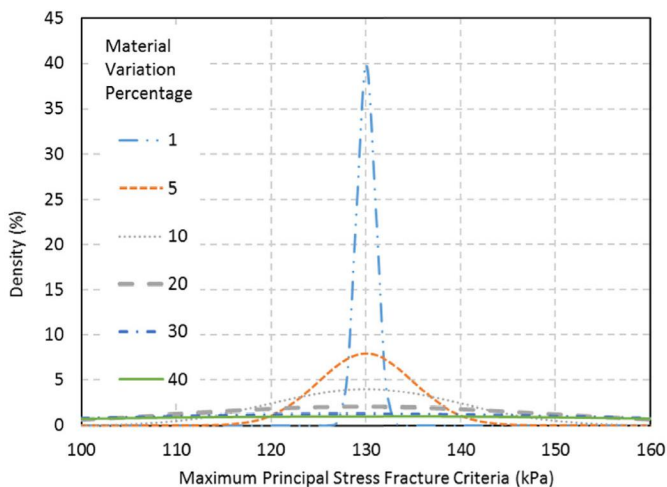


Fig. 5. Distribution of maximum allowable principal stress in tension (fracture initiation criteria).

permissible domain. This process produced a truncated Gaussian distribution free from skew.

3.3. Simulation methodology

The proposed method is specified by the following procedure and in Fig. 6.

- (1) Meshing the domain with Abaqus CAE to create an input (inp) file. A fine mesh is required to ensure crack paths are modelled with satisfactory resolution;
- (2) Generating normally distributed tensile strength and elastic modulus parameters for each finite element using in-house Python scripts;
- (3) Assigning material element properties to finite elements, indexed within input files generated by Abaqus;
- (4) Implementing Abaqus standard solver, running cavity expansion simulation (UET) and producing pressure-volume curves and Abaqus ODB files;
- (5) Exporting pressure-volume data to a spreadsheet;
- (6) Repeating steps (2–5) for a sufficient number of random initial configurations, as required by the Monte Carlo simulation method. This process is automated by the creation of a batch file;
- (7) Determining cavity strength parameters immediately prior to specimen failure;
- (8) Conducting statistical analysis using the statistical package R [27].

This procedure is implemented to produce spatially dependent crack initiation and propagation, unachievable in spatially uniform and homogeneous materials.

To determine the impact of fluctuating tensile strength and elastic modulus, a one-factor-at-a-time sensitivity analysis was conducted consisting of the variation of four parameters:

- 1) Impact of mean tensile strength fracture initiation criteria Element Maximum Principal Stress Failure Criteria (MPSFC) values

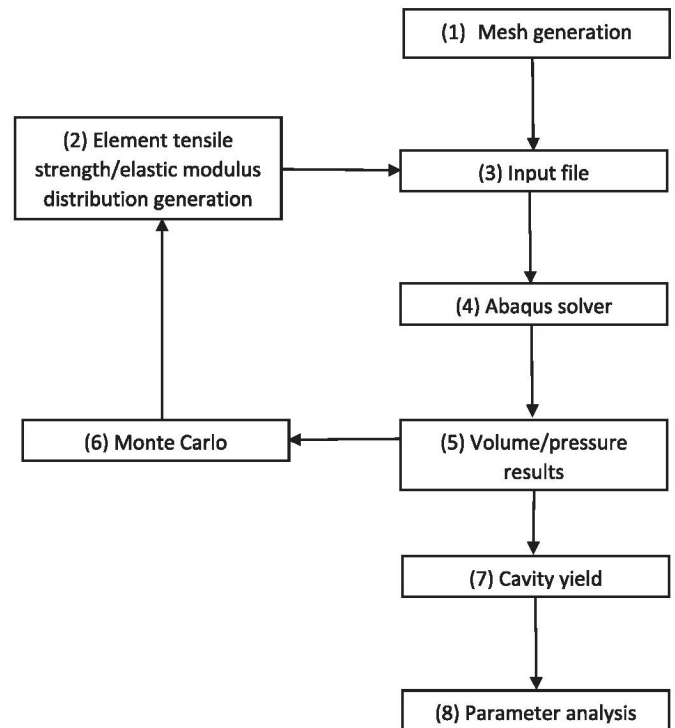


Fig. 6. Analysis procedure flowchart.

for XFEM crack initiation were generated with distribution means of 104, 117 and 130 kPa, each with a spread of 20% of the mean strength value. The spread is expressed such that three standard deviations each side of the mean contains stress values within 20% of the mean principal stress. The variation of cavity pressure at initial fracture is then determined in terms of mean and percentage spread of yield pressure mean.

2) Impact of tensile strength fracture initiation criteria spread

Element MPSFC values are generated with a mean of 130 kPa and a spread of 1, 5, 10, 20, 25, 30 and 40% of the MPSFC mean. Similarly, cavity yield pressure mean and percentage spreads are determined.

3) Impact of elastic modulus distribution mean

Elemental elastic modulus values are generated with a mean of 15.2, 19 and 22.8 MPa and 20% mean elastic modulus variation. From the cavity pressure-strain curve, the elastic modulus can be determined from the linear component of the pressure versus change volumetric strain, as shown by Wood [25] (Equation (7)). This is then used to calculate a mean output elastic modulus for the model from Hooke's law (Equation (8)). Output elastic modulus mean and percentage material spreads are then determined.

$$G = V_0 \frac{dp}{dV} \tag{7}$$

$$E = 2G(1 + \nu) \tag{8}$$

where, G is shear modulus, V_0 is initial volume of the cavity, E is elastic modulus, and ν is Poisson's ratio of the UET sample.

4) Impact of elastic modulus distribution spread

Elemental elastic modulus values are generated with a mean of 1.9 MPa and spreads of 1, 10, 20 and 30%. The yield elastic modulus mean and percentage material spreads are then determined using the same method as in procedure (3) detailed above.

4. Results

Examples of element variation are shown in Fig. 7. Four instances of crack propagation of the elemental MPSFC with Gaussian distribution ($\mu = 130000$, $\sigma = 4333.33$) are presented in Fig. 8 with contour fields signifying displacement magnitude. As expected, element heterogeneity

of fracture criteria allows crack paths to develop nonuniformly, radially extending from the interior cavity. Although the samples in 7(a) and (c) produced a solitary fracture, 7(b) and (d) indicate that multiple fractures are capable of forming.

As the goal of producing spatially nonuniform cracks has been achieved, analysis of the strength properties of heterogeneously distributed element characteristics is investigated using the methods detailed above.

4.1. Impact of mean tensile strength fracture initiation criteria

When assessing the impact of tensile strength initiation criteria variation (Table 2, Figs. 9 and 10), suggests Gaussian MPSFC distributions with 20% spread have the impact of producing a material that will fail at a cavity pressure (primary failure) slightly lower than the mean MPSFC (between 2% and 3% lower). This is to be expected as crack paths will propagate through weak zones while avoiding regions of high tensile strength. Thus cavity pressures less than the mean MPSFC cause the sample to fracture.

Similarly, yield cavity pressures spreads are smaller than the MPSFC variation of 20% for each of the mean MPSFC values tested. While the percentage differences between mean MPSFC and cavity yield pressure seem mostly unaffected by MPSFC means, the percentage change in spread parameters is more varied. Of particular interest is the narrowing of the distribution of yield cavity pressures, compared with MPFSC variation. This suggests that widely varying MPSFC elements produce a much narrower band of yield pressures (observed between 38% and 47% less). As the initial difference of 30 μm between the cavity and probe radius observed in laboratory testing was not considered for this simulation, the XFEM results are plotted from $dv/dv_0 = 0.013$ (Fig. 9). The whisker plot of Fig. 10 details similar variation for each distribution of MPSFC with increasing mean strength.

4.2. Impact of tensile strength fracture initiation criteria spread

The impact of the distribution spread for a fixed mean MPSFC of 130 kPa is detailed in Table 3. As expected, increased MPSFC element variation produces a wider range of cavity yield pressures, as shown in Fig. 11. It is immediately obvious that variation of input MPSFC parameters does not produce equal yield cavity pressure spreads. For low

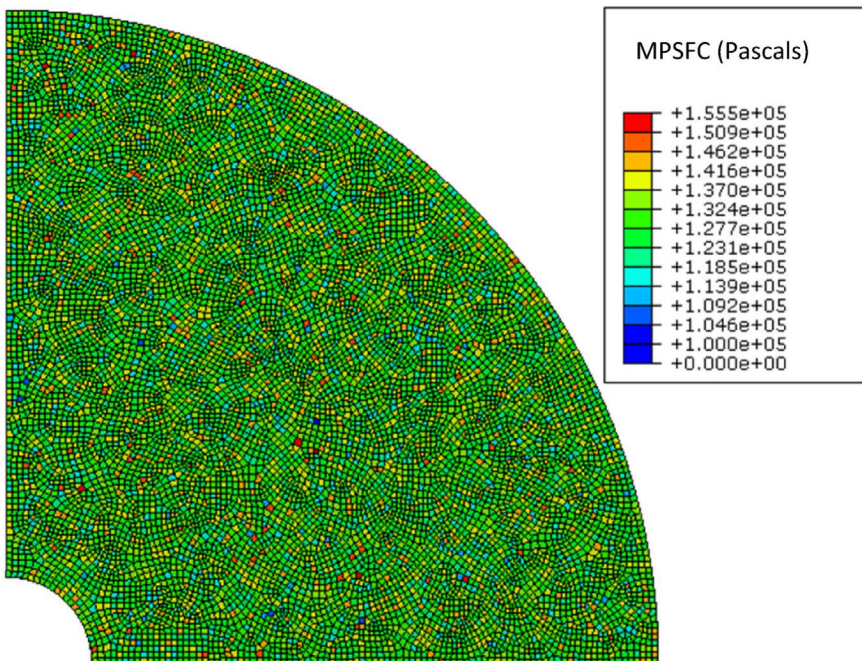


Fig. 7. Specimens with heterogeneous maximum principal strength fracture initiation criteria.

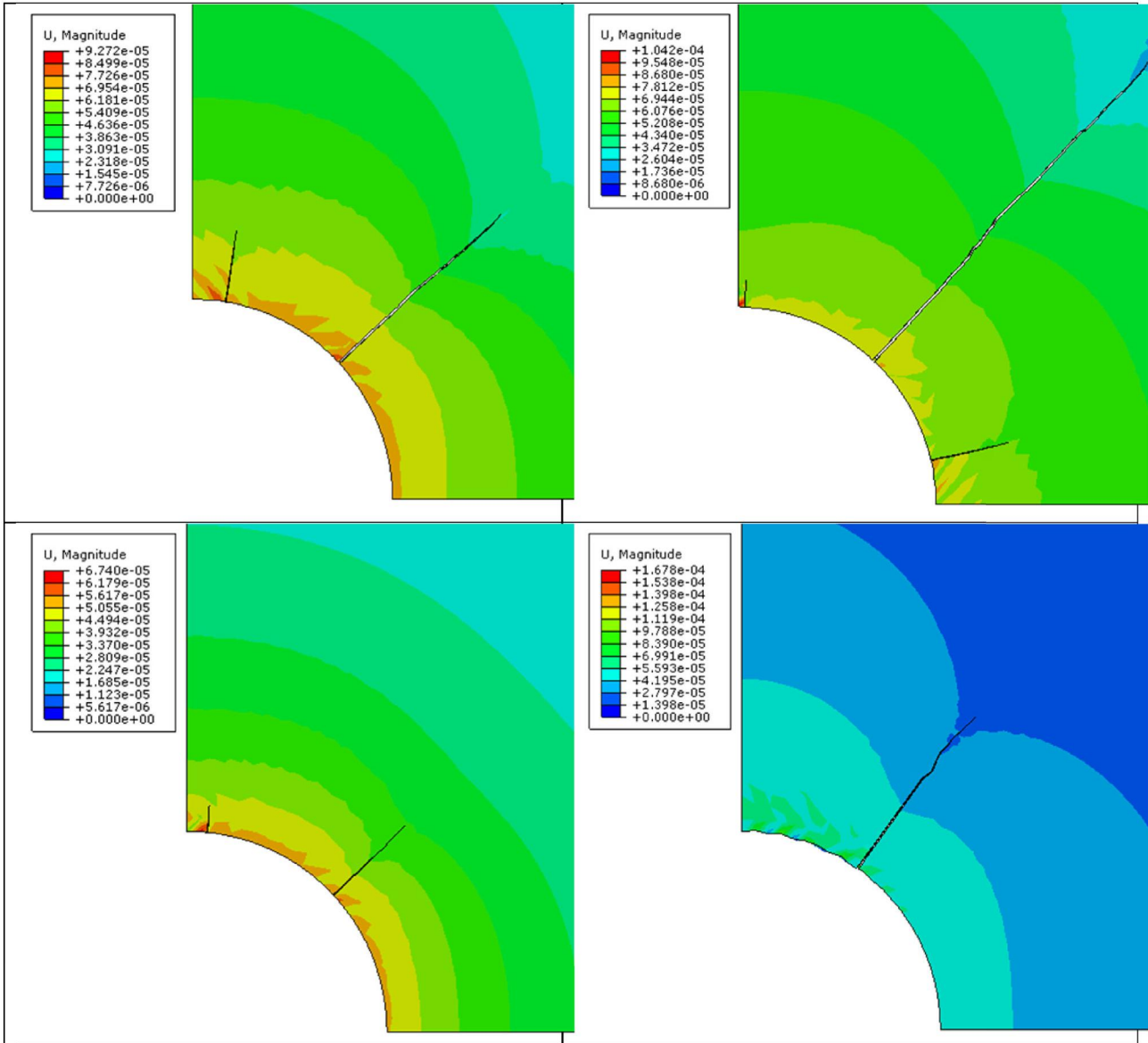


Fig. 8. Four crack propagation instances ($\mu = 130000$, $\sigma = 4333.33$).

Table 2
Variation of mean tensile strength fracture initiation criteria.

Mean elemental MPSFC (kPa)	Mean cavity yield pressure (kPa)	Percentage change in mean parameters	MPSFC variation (%)	Yield cavity pressure variation (%)	Percentage change in spread parameters
104	100.8	-3.07692	20	11.56	-42.2
117	113.1	-3.33333	20	12.38	-38.1
130	127.2	-2.15385	20	10.51	-47.45

MPSFC spreads, the material requires cavity pressures above the MPSFC mean to initiate fracture. Further increasing the spread weakens the material such that cavity pressures well below the mean tensile strength initiation criteria produce cracks.

It is noted MPSFC spread variation has a much greater impact on cavity yield pressure spread than mean cavity yield pressure, especially for small spread values. For small input spreads, the cavity pressure spread increases above the input spread, before drastically narrowing.

Several outliers are observed however, their removal impact is deemed minimal.

To produce models for tensile strength of Loy Yang brown coal between 110 kPa and 130 kPa as reported by Tolooiyan, Mackay [26], a MPSFC mean of 130 kPa with a spread of 40% (Table 3) are proposed. These parameters produce a material with a tensile strength of 119.3 kPa and spread between 110.64 kPa and 127.96 kPa. This range lies within the primary failure zone detailed by Tang et al. [9] for Yallourn brown coal.

4.3. Impact of elastic modulus distribution mean

Investigation of varying element mean elastic modulus values (Fig. 12 and Table 4) indicate that the element mean elastic modulus does not substantially impact the output elastic modulus variation. It is noted in the whisker plot of Fig. 12 that the mean output elastic modulus is minutely diminished compared to the elemental elastic modulus mean. Despite a variation of 20% on the element elastic modulus spread, the output elastic modulus spread is particularly narrow (less than 1.5%)

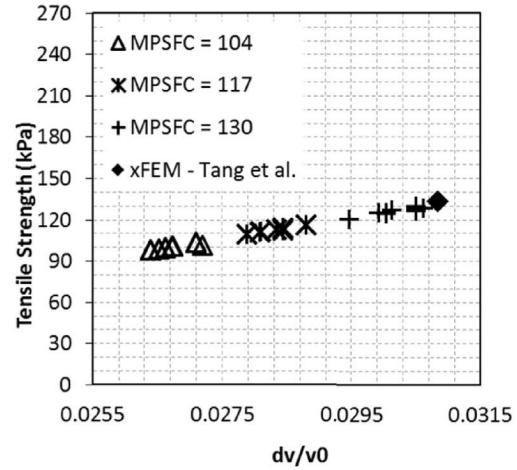
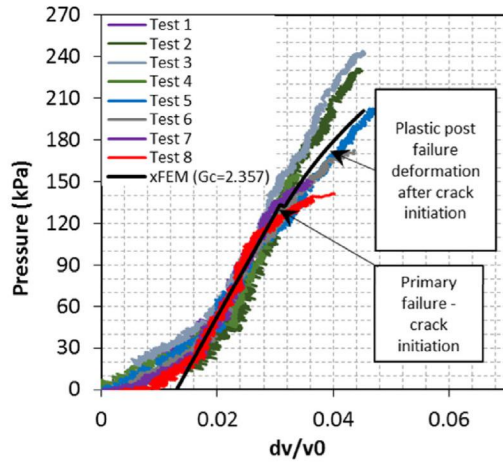


Fig. 9. Variation of yield pressures (primary failure) compared with experimental results produced by Tang et al. [9].

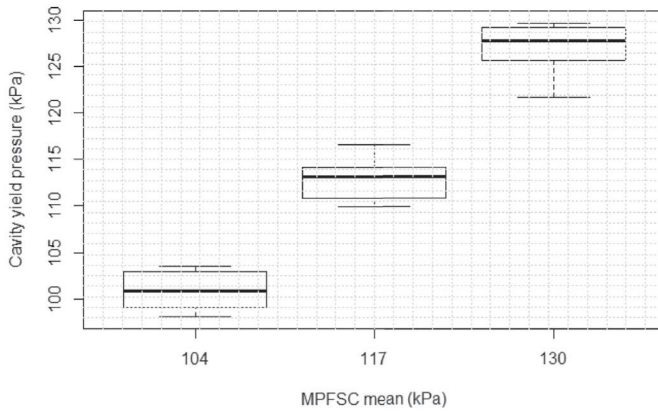


Fig. 10. Whisker plots of mean tensile strength fracture initiation criteria.

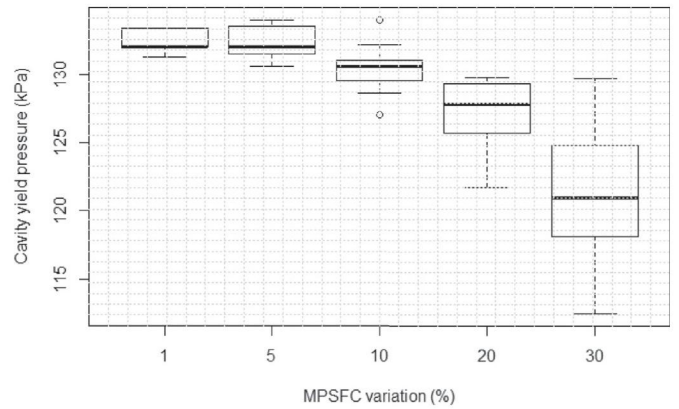


Fig. 11. Whisker plots of tensile strength fracture initiation criteria spread.

Table 3
Tensile strength fracture initiation criteria spread.

Mean elemental MPSFC (kPa)	Mean yield cavity pressure (kPa)	Percentage change in mean parameters	MPSFC spread (%)	Cavity yield pressure spread (%)	Percentage change in spread parameters
130	132.5	1.92	1	3.44	244
130	132.2	1.69	5	5.25	5
130	130.4	0.31	10	7.42	-25.8
130	127.2	-2.15	20	10.51	-47.5
130	123.0	-5.38	25	17.74	-29.0
130	121.4	-6.62	30	21.09	-29.7
130	119.3	-8.23	40	17.32	-56.7

compared with MPSFC variation (Table 2). It is noteworthy that the effects of element elastic modulus variation related to output elastic modulus mean and deviation are considered negligible.

4.4. Impact of elastic modulus distribution spread

Variation of element elastic modulus spread (Table 5 and Fig. 13) shows little impact on mean output elastic modulus values while output elastic modulus spreads remain close to constant. This suggests that probabilistic variation of elastic modulus values is an unnecessary parameter for the variation of output elastic modulus.

5. Discussion and conclusion

The simulations described were designed to mimic the uncertainty and variation of strength inherent in specimens of Victorian brown coal as a non-textbook geotechnical material, by the assignment of Gaussian random variables to individual finite elements. Four sets of experiments were performed to determine the sensitivity of heterogeneous XFEM fracture to the distributed parameters of maximum principal stress failure criteria and elastic modulus. Of particular interest was the negligible impact of elastic modulus variation played on failure characteristics. Parameters were determined to accurately simulate brown coal specimen characteristics in alignment with previous test results.

The approach of varying element properties by random variable sampling for extended finite elements lends itself to expanded analysis of full three-dimensional models given sufficient computational resources. The technique accommodates the future study of a wider range of varied model parameters and random variable distributions commonly used in soil mechanics. The addition of spatial correlation length scales provide a supplementary layer of complexity for future implementation.

The results presented in this paper propose that probabilistic distributions of fracture initiation criteria can be applied to XFEM elements to allow fracture initiation and propagation with comparable behaviour to UET testing of laboratory specimens, without the requirement of pre-defined failure zones. The simulations have demonstrated the impact of heterogeneity in maximum principal stress failure criteria and elastic modulus for the understanding of fracture mechanics in brown coal and intermediate geotechnical material.

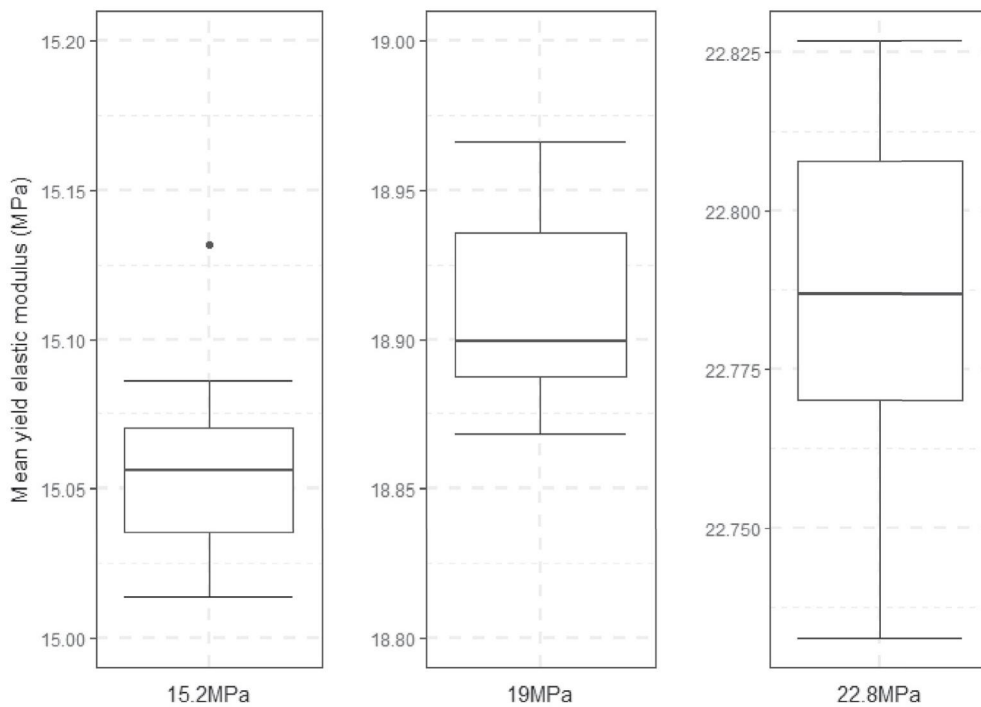


Fig. 12. Whisker plots of elastic modulus distribution mean values.

Table 4
Elastic modulus distribution mean values.

Mean elemental elastic modulus (MPa)	Mean output elastic modulus (MPa)	Percentage change in mean elastic modulus	Elastic modulus spread (%)	Elastic modulus spread (%)	Percentage change in elastic modulus spread
15.2	15.06	-0.95	20	1.21	-93.95
19	18.91	-0.47	20	0.95	-95.25
22.8	22.78	-0.07	20	0.71	-96.45

Table 5
Impact of elastic modulus distribution spread.

Mean elemental elastic modulus (MPa)	Mean output elastic modulus (MPa)	Percentage change in mean elastic modulus	Element elastic modulus spread (%)	Output elastic modulus spread (%)	Percentage change in elastic modulus spread
19	18.91	-0.47	1	0.063026	-93.70
19	18.91	-0.47	10	0.58813	-94.12
19	18.91	-0.47	20	1.050684	-94.75
19	18.89	-0.58	30	0.957721	-96.81

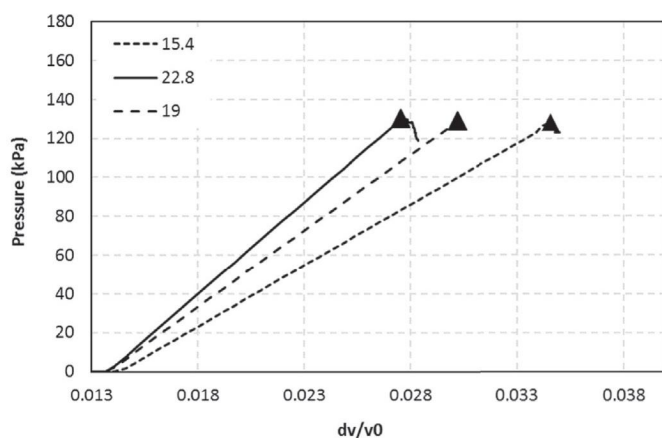


Fig. 13. Primary failure locations.

Acknowledgements

Financial support for this research has been provided by Earth Resources Regulation of the Victorian State Government Department of Economic Development, Jobs, Transport and Resources. The authors would like to thank Mr. Wayne Powrie, who prepared the equipment and specimens for this research. The assistance of Energy Australia is also acknowledged for their support and help with sample collection. The first author is funded by the Australian Government Research Training Program (RTP) and the GHERG scholarship programme and the second author is funded by the GHERG scholarship programme.

References

- [1] T. Belytschko, T. Black, Elastic crack growth in finite elements with minimal remeshing, *Int. J. Numer. Meth. Eng.* 45 (5) (1999) 601–620.
- [2] H. Liu, F. Alonso-Marroquin, D. Williams, Three-dimensional modelling of the rock breakage process, in: *ISRM Regional Symposium-EUROCK 2009*, International Society for Rock Mechanics, 2009.
- [3] S. Salimzadeh, N. Khalili, A three-phase XFEM model for hydraulic fracturing with cohesive crack propagation, *Comput. Geotech.* 69 (2015) 82–92.
- [4] Y. Xie, P. Cao, J. Liu, L. Dong, Influence of crack surface friction on crack initiation and propagation: a numerical investigation based on extended finite element method, *Comput. Geotech.* 74 (2016) 1–14.
- [5] J. Pogacnik, D. Elsworth, M. O'Sullivan, J. O'Sullivan, A damage mechanics approach to the simulation of hydraulic fracturing/shearing around a geothermal injection well, *Comput. Geotech.* 71 (2016) 338–351.
- [6] A. Ajaz, R.H.G. Parry, Unconfined direct tension test for compacted clays, *J. Test. Eval.* 2 (3) (1974) 163–172.
- [7] N. Lu, B. Wu, P. Tan Chee, Tensile strength characteristics of unsaturated sands, *J. Geotech. Geoenviron. Eng.* 133 (2) (2007) 144–154.
- [8] D. Li, L.N.Y. Wong, The Brazilian disc test for rock mechanics applications: review and new insights, *Rock Mech. Rock Eng.* 46 (2) (2013) 269–287.
- [9] Z. Tang, A. Tolooiyani, R. Mackay, Unconfined Expansion Test (UET) for measuring the tensile strength of organic soft rock, *Comput. Geotech.* 82 (2017) 54–66.
- [10] D. Systèmes, Dassault Systèmes, Abaqus, 6.14 ed., 2014. Providence (RI, USA).
- [11] S. Timoshenko, S. Woinowsky-Krieger, *Theory of Plates and Shells*, McGraw-Hill, New York, 1959, 1959.
- [12] I. Kolo, R.K. Abu Al-Rub, R.L. Sousa, Computational modelling of fracture propagation in rocks using a coupled elastic-plasticity-damage model, *Math. Probl Eng.* 2016 (2016) 15.
- [13] X.T. Su, Z.J. Yang, G.H. Liu, Monte Carlo simulation of complex cohesive fracture in random heterogeneous quasi-brittle materials: a 3D study, *Int. J. Solid Struct.* 47 (17) (2010) 2336–2345.
- [14] T. Belytschko, Y. Krongauz, D. Organ, M. Fleming, P. Krysl, Meshless methods: an overview and recent developments, *Comput. Meth. Appl. Mech. Eng.* 139 (1–4) (1996) 3–47.

- [15] N. Moes, J. Dolbow, T. Belytschko, A finite element method for crack growth without remeshing, *Int. J. Numer. Meth. Eng.* 46 (1) (1999) 131–150.
- [16] A.L. Saleh, M.H. Aliabadi, Crack growth analysis in concrete using boundary element method, *Eng. Fract. Mech.* 51 (4) (1995) 533–545.
- [17] W. Wendland, T.A. Cruse, Boundary element analysis in computational fracture mechanics, *Math. Comput.* 55 (192) (1990) 870.
- [18] D.V. Swenson, A.R. Ingraffea, Modeling mixed-mode dynamic crack propagation using finite elements: theory and applications, *Comput. Mech.* 3 (6) (1988) 381–397.
- [19] M. Fleming, Y.A. Chu, B. Moran, T. Belytschko, Enriched element-free Galerkin methods for singular fields, *Int. J. Numer. Meth. Eng.* 40 (8) (1997) 1483–1504.
- [20] J.M. Melenk, I. Babuška, The partition of unity finite element method: basic theory and applications, *Comput. Meth. Appl. Mech. Eng.* 139 (1–4) (1996) 289–314.
- [21] C.A. Duarte, J.T. Oden, Hp clouds-an hp meshless method, *Numer. Meth. Part. Differ. Equ.* 12 (6) (1996) 673–706.
- [22] D. Griffiths, G.A. Fenton, Probabilistic slope stability analysis by finite elements, *J. Geotech. Geoenviron. Eng.* 130 (5) (2004) 507–518.
- [23] S.E. Cho, Probabilistic assessment of slope stability that considers the spatial variability of soil properties, *J. Geotech. Geoenviron. Eng.* 136 (7) (2009) 975–984.
- [24] Q. Lei, J.-P. Latham, C.-F. Tsang, The use of discrete fracture networks for modelling coupled geomechanical and hydrological behaviour of fractured rocks, *Comput. Geotech.* 85 (2017) 151–176.
- [25] R.J.M.D.M. Wood, R.J. Mair, D.M. Wood, *Pressuremeter Testing: Methods and Interpretation*, first ed. ed. London: CIRIA.
- [26] A. Tolooiyan, R. Mackay, J. Xue, Measurement of the tensile strength of organic soft rock BT - measurement of the tensile strength of organic soft rock, *ASTM Geotech. Test. J.* 37 (6) (2014).
- [27] Release 3.4.3, R: A Language and Environment for Statistical Computing, 2017, <http://www.R-project.org/>.